

High Resolution Multi-Wavelength Study of Active Galaxies

Inaugural-Dissertation
zur
Erlangung des Doktorgrades
der Mathematisch-Naturwissenschaftlichen Fakultät
der Universität zu Köln

vorgelegt von
Melanie Krips
aus Köln

Köln 2005

Tag der mündlichen Prüfung: 03.Februar 2005

1.Gutachter: Prof. Dr. Andreas Eckart

2.Gutachter: Prof. Dr. Claus Kiefer

Abstract

This PhD thesis presents a study of active galaxies carried out from cm- to mm-wavelengths with high angular resolution. The mechanism of the activity in these objects is supposed to be strongly correlated with the accretion of matter onto a super-massive black hole in their centres. One approach to increase the understanding of the nature of these highly interesting sources is to observe and analyse the molecular gas. The characteristics of its distribution and dynamics are indispensable diagnostic tools to investigate the accretion processes at different angular scales. A second approach can be found in the study of emission that originates in the direct vicinity of the black hole, such as non-thermal radio emission, for instance.

To account for different activity levels, five objects were chosen ranging from nearby, Low Luminosity Active Galaxies (LLAGs; NGC 3718 at a redshift¹ of $z = 0.003$ and NGC 1068 at $z = 0.004$) to higher redshifted, High Luminosity Active Galaxies (HLAGs; HE 1029-1831 at $z = 0.039$, 3C48 at $z = 0.367$, and Q0957+561 at $z = 1.414$). The first two sources are part of the so called NU(clei of)-GA(laxy) project, that aims at analysing the distribution and kinematics of the molecular gas at high angular resolution/sensitivity in a sample of in total 30 nearby LLAGs. HE 1029-1831 is part of a complementary sample of nearby HLAGs with similar aims. All sources were observed in carbon-monoxide (CO), known to be a good molecular gas tracer, with the IRAM Plateau de Bure Interferometer (PdBI) providing high sensitivity and high angular resolution. CO emission was detected in all five galaxies. In NGC 3718, for instance, the molecular gas disk, having a mass of $2.4 \times 10^8 \mathcal{M}_\odot$, is highly warped from ~ 20 kpc down to ~ 200 pc. The distribution of the gas also reveals large scale asymmetries witnessing a possible tidal tail interaction with its close companion NGC 3729, and as well small scale asymmetries most likely tracing accretion onto the nucleus. The appearance of the molecular gas in NGC 1068 is quite complex, too. Besides two spiral arms at a radius of ~ 1 kpc and a nuclear bar with a length of roughly 2 kpc, a nuclear ring becomes visible. Furthermore, indications for a strongly rotating and compact nuclear gas component are found in the maps, thus supporting previous findings. As a byproduct, new information on the 3 mm and 1 mm continuum was gained indicating a turnover in the Spectral Energy Distribution (SED) between 3 mm and 1 mm similar to what is detected for the central source of our own galaxy, Sgr A*. HE 1029-1831 appears to be a gas rich host galaxy with a barred gas distribution and gas mass of $\sim 8 \times 10^9 \mathcal{M}_\odot$. The striking velocity gradient across the bar indicates a bar-driven gas inflow in this system. The CO emission in 3C48 gives further evidence for a merger hypothesis that was strongly debated in the past. The IRAM PdBI maps show two distinct dynamical systems of which one is centered almost on the nucleus itself and the second one closer to a second bright component that was recently also detected in the Near-Infrared and can be likely associated with a second nucleus. Finally, also in the highest redshifted object of this study, Q0957+561, CO emission was detected towards both lensed images. This is the second system at the redshift range of 1-2 in which CO emission was found. The CO emission is associated with a rotating gas disk of mass $5 \times 10^{10} \mathcal{M}_\odot$. As a further gas tracer, HCN was observed in a subsample of the NUGA survey. CO, although being a good gas tracer, preferentially measures low to moderate gas densities and is thus not well suited for comparisons with stellar characteristics such as star formation. HCN, however, is supposed to trace denser parts of the gas. To obtain hence a more complete picture, IRAM 30m observations were carried out to detect HCN in the NUGA galaxies which are regarded as a first step for follow-up interferometric observations.

¹The redshift of an object is defined as: $z = \nu_{\text{em}}/\nu_{\text{obs}} - 1$; ν_{em} = emitted frequency at the rest-frame of the object, ν_{obs} = observed frequency at the instrument.

A strong correlation between the Far-Infrared luminosities, being a diagnostic tool for star formation, and HCN luminosities is found in this sample consistent with other studies.

To investigate the emission of the central most parts in LLAGN at radio wavelengths and their differences or similarities to HLAGs, snap-shot observations of seven NUGA galaxies with local interferometers (MERLIN) and Very Long Baseline Interferometers (VLBI) were conducted at two different wavelengths (18 cm and 6 cm). The results for the LLAGs are similar to what is usually found for HLAGs supporting the idea that LLAGs might only be scaled down HLAGs in terms of activity, i.e. the responsible physical processes are similar. Besides compact radio emission, also extended and diffuse emission, including jets, were detected. Furthermore, a strong correlation between radio and X-ray luminosities was found indicating connected emission processes. The radio emission (at the core) is mainly produced by (optically thick) synchrotron radiation which can be (inverse) Compton-scattered towards higher energies, thus explaining the observed correlation. This set of radio observations is so far the most sensitive (~ 0.1 mJy) study with the highest angular resolution of such weak radio LLAGs.

Zusammenfassung

Obwohl aktive Galaxien schon seit mehr als 40 Jahren bekannt sind und unzählige Studien über sie durchgeführt wurden, geben sie noch immer große Rätsel auf. Vor allem die Natur ihrer (nuklearen) Aktivität bleibt weitestgehend unverstanden. Die enormen Energien, die in diesen Galaxien freigesetzt werden, können nicht, wie in nicht aktiven Galaxien, durch die in ihnen enthaltenen Sterne produziert werden, soweit diese zumindest einer normalen Entwicklung folgen. Wie bereits angedeutet, entstehen die enormen Leuchtkräfte in den Kernen (d.h. bei Radien von kleiner als 0.1 pc)² dieser Art von Objekten. Nicht selten werden bolometrische³ Leuchtkräfte von bis zu $10^{12} L_{\odot}$ gemessen. Über die sogenannte Eddingtonleuchtkraft, die auf einem Gleichgewicht zwischen Strahlungs- und Gravitationsdruck beruht, kann die erforderliche Mindestmasse ausgerechnet werden. Bei einer Leuchtkraft von $10^{12} L_{\odot}$ müsste die zentrale Masse einen Wert von ca. $3 \times 10^7 M_{\odot}$ erreichen, damit der Strahlungsdruck nicht zu einem Hinausschleudern der Materie führt. Die hellsten Sterne können Massen von bis zu $100 M_{\odot}$ annehmen, d.h. innerhalb von 0.1 pc müsste es alleine 3×10^5 massereiche Sterne geben. Zum Vergleich, die Sternendichte im Milchstraßenzentrum besitzt einen Wert von $10\text{-}100 \cdot 10^6$ Sternen pro pc^3 (e.g., Genzel et al. 2003). Zusammen mit der Entdeckung von massiven schwarzen Löchern in einem Großteil der Galaxien (z.B., Sgr A* in unserer Milchstraße), setzte sich die Hypothese durch, dass sich aktive Galaxien von nicht aktiven durch die Akkretion von Materie auf das zentrale schwarze Loch unterscheiden. Dabei können in der Tat die beobachteten Energien freigesetzt werden. Ein weiterer Erklärungsansatz ist eine stark erhöhte Sternentstehung, da junge Sterne während ihrer Bildungsphase am leuchtkräftigsten sind.

Diese Doktorarbeit befaßt sich nun mit der Untersuchung von aktiven Galaxien unter zwei verschiedenen Blickwinkeln. Molekulares Gas trägt einen signifikanten Teil zu der Materie bei, die dem schwarzen Loch für die Akkretion zur Verfügung steht. Damit ein kontinuierliches Füllen gewährleistet ist, muß dauerhaft Energie, d.h. Drehmoment, vernichtet werden, da das molekulare Gas im allgemeinen in einem dynamisch stabilen System gebunden ist, z.B. in Form einer Gasscheibe. Auch bedarf die Akkretion einer Initialzündung, die z.B. durch Galaxienwechselwirkung hervorgerufen werden kann. Allerdings wurden viele aktive Galaxie als isolierte Objekte beobachtet, was im Widerspruch zu dieser Hypothese steht. Wie die Akkretion nun von den äußeren Bereichen bis hinunter zum schwarzen Loch am Leben gehalten wird, wirft ebenfalls noch viele Fragen auf. Eine Möglichkeit, ein wenig Licht in das "Akkretionsdunkel" zu bringen, besteht darin, das molekulare Gas in aktiven Galaxien bis hinunter zu den kleinsten möglichen Skalen zu beobachten und in seiner Verteilung wie auch Dynamik zu analysieren. In diesem Zusammenhang wurden insgesamt 5 aktive Galaxien untersucht, die nicht nur bei unterschiedlichen Entfernungen sind, sondern auch verschiedene Aktivitätslevel zeigen. Diese 5 Quellen sind: NGC 3718, eine als schwach aktiv (LINER) klassifizierte Galaxie bei einer Entfernung von 13 Mpc ($z = 0.003$), NGC 1068, eine etwas aktivere (Seyfert) Galaxie bei einer vergleichbaren Entfernung von 14.4 Mpc ($z = 0.004$), HE 1029-1831, ein sehr aktiver QSO bei 150 Mpc, 3C48, ein möglicher Merger bei einer Distanz von 850 Gpc ($z = 0.0367$), und schließlich Q0957+561, ein gelinster, extrem heller Quasar bei einer Entfernung⁴ von 1.6 Gpc⁵ ($z = 1.414$). Die

² $1 \text{ pc} \equiv 3.26 \text{ Lichtjahre} \equiv 3.084 \cdot 10^8 \text{ cm} \equiv 2.07 \cdot 10^5 \text{ Astronomische Einheiten}$.

³ d.h. über das gesamte elektromagnetische Spektrum

⁴ Die hier erwähnten Entfernungen beziehen sich auf den über den Winkeldurchmesser (angular size) definierten Abstand (D_A) und nicht auf den über die Leuchtkraft bestimmten (D_L). Beide hängen jedoch über folgende Beziehung zusammen $D_L = (1 + z)^2 D_A$, wobei z die Rotverschiebung ist, sind also äquivalent gebrauchbar.

⁵ Für eine Hubblekonstante von $H_0 = 75 \text{ km s}^{-1} \text{ Mpc}^{-1}$.

ersten beiden Systeme gehören zu einer größeren Studie, dem sogenannten NU(clei of)-GA(laxy) Projekt. Diese internationale Studie hat sich zum Ziel gesetzt, die Akkretionsmechanismen in einer Stichprobe von insgesamt 30 nahen, eher schwach bis moderat aktiven Objekten (d.h. Seyfert und LINER Galaxien) auf den kleinsten Skalen zu untersuchen, um aufgrund der statistischen Basis der Vielfalt der beobachteten Eigenschaften von aktiven Galaxien gerecht zu werden. HE 1029-1831 zählt ebenfalls zu einer größeren Stichprobe, dem Cologne Nearby QSO Sample, die komplementär zu NUGA die gleichen Ziele anstrebt, jedoch für die aktiveren Gegenstücke. Diese Quelle ist einer der am nächsten bekannten QSOs und wurde als einziger bisher aus diesem Sample in seinem molekularem Gas kartiert. Die beiden letzten Galaxien stellen sehr interessante, individuelle Studienobjekte dar, 3C48, wegen seiner vermuteten Mergerstruktur, und Q0957+561, bei dem als zweites Objekt dieser Distanz (d.h. einer Rotverschiebung⁶ zwischen 1 und 2) erst überhaupt molekulares Gas detektiert werden konnte.

Molekulares Gas wird in erster Linie über Kohlenmonoxid nachgewiesen, das einfacher zu beobachten ist, als molekularer Wasserstoff, der aufgrund seines Dipolmomentes bei den herrschenden Bedingungen nur sehr schwer anregbar und daher schwer detektierbar ist, obwohl er den Hauptbestandteil des molekularen Gases ausmacht. Kohlenmonoxid hat jedoch auch einen wesentlichen Nachteil, und zwar, dass es eher weniger dichte Gasregionen kartiert und ein schlechter Indikator für dichtere Bereiche ist, d.h. die für Sternentstehung interessanten Gebiete. Um also ein möglichst vollständiges Bild zu erhalten, wurde in den NUGA Quellen nach sogenannten "dichteren-Gas-Messern", wie z.B. HCN, erfolgreich gesucht. Dies ist als erster Schritt für die Kartierung des dichteren Gases anzusehen. Die Beobachtungen des molekularen Gases durch CO wurde mit dem IRAM Plateau de Bure Interferometer (PdBI) in den französischen Alpen durchgeführt, wohingegen für die Detektierung des HCN das IRAM 30 m Teleskop in der spanischen Sierra Nevada benutzt wurde. Das IRAM PdBI ermöglicht Auflösungen von $\sim 0.5\text{--}7''$, d.h. im Falle von NGC 1068 z.B. erhält man so Informationen über die Gasverteilung bis runter zu einem Radius von ca 50 pc. Einige der Ergebnisse werden hier exemplarisch zusammengefasst.

Die räumliche Verteilung und Dynamik von CO in NGC 3718 zeigt ganz deutlich, dass die Gasscheibe bis in den zentralen Bereich (~ 2000 pc) der Galaxie hinein deformiert ("gewarped") ist. Dies konnte bisher nur von großen Radien (~ 20 kpc) über HI (Schwarz 1985) bis zu einem Radius von 1 kpc über CO gezeigt werden (Pott et al. 2004). Das Kohlenmonoxid folgt sehr schön der Staubverteilung (Fig. 1.1) und enthüllt sowohl auf größeren wie auch auf kleineren Skalen eine starke Asymmetrie der Verteilung. Wie die nahe Begleitgalaxie NGC 3279 vermuten läßt, spricht die großräumige Asymmetrie, die sich in einer NGC 3279 zugewandten Region befindet, für eine signifikante Gravitationswechselwirkung mit diesem Objekt. Die kleinskalige Asymmetrie, die innerhalb der zentralen 2-3'' Bogensekunden gefunden wurde, deutet als eine wahrscheinliche Erklärung auf Akkretion hin.

In NGC 1068 konnte zum ersten Mal Kontinuumsstrahlung bei 1 mm nachgewiesen werden, die im Rahmen der CO Beobachtungen als Nebenprodukt abfielen. Sowohl bei 1 mm als auch bei 3 mm sieht man neben der kompakten Komponente auf dem Nukleus einen Jet (Fig. 1.2). Der Gegenjet ist nur bei 3 mm und höheren Wellenlängen sichtbar. Zusammen mit den Informationen bei 1 mm, 3 mm und bei Radiowellenlängen von Gallimore et al. (1996, 2004), ist eine Umkehrung des Spektrums zwischen 3 mm und 1 mm sichtbar⁷, die, obwohl Auflösungseffekte nicht ganz ausgeschlossen werden können, höchstwahrscheinlich real ist. Eine solche Umkehrung des Spektrum hat man auch schon bei Sgr A*, dem schwarzen Loch unserer Milchstraße, sehen können, und deutet sich ebenfalls bei einer weiteren NUGA Quelle an (NGC 3147), die NGC 1068 schon in ihrer Gasverteilung sehr ähnelt, d.h. als ihr möglicher Zwilling angesehen werden kann. Neben diesen neuen Resultaten konnte die Empfindlichkeit bisheriger CO Beobachtungen mit denen in dieser Arbeit analysierten Messungen signifikant verbessert werden. So war die Echtheit einer stark rotierenden und sehr kompakten Komponente in $^{12}\text{CO}(2-1)$ nur mit einer 3σ -Detektion bestimmt. Die neuen Daten zeigen diese Komponente unabhängig mit einem Signal zu Rauschen von knapp 5. Auch kommt die Ringstruktur der $^{12}\text{CO}(2-1)$ Linie in den Inneren 150 pc sehr viel deutlicher zum Vorschein als bisher. Messungen der $^{13}\text{CO}(1-0)$, einem weiteren Indikator für dichtere Gasbereiche, zeigen, dass das dichtere Gas sehr viel stärker und symmetrischer mit dem Balken verknüpft zu sein scheint als das "dünnere" $^{12}\text{CO}(1-0)$ Gas. Dieses Resultat ist in Einklang mit Ergebnissen für andere Galaxien.

Bislang ist noch sehr wenig über HE 1029-1831 bekannt. Die neuen IRAM PdBI Beobachtungen enthüllen

⁶Maß zur Entfernungsbestimmung; definiert als $z = \nu_{\text{em}}/\nu_{\text{obs}} - 1$; ν_{em} = emittierte Frequenz im Bezugssystem des Objektes, ν_{obs} = beobachtete Frequenz am Instrument.

⁷d.h., eine Zunahme des Flusses von höheren Wellenlängen zu 3 mm hin mit einem anschließenden Flußabfall zwischen 3 mm und 1 mm.

eine sehr gasreiche Galaxie (Gasmasse von ca. $8 \times 10^9 M_{\odot}$). Das molekulare Gase ist sehr stark mit dem Balken assoziiert und nur ganz wenig mit den im Optischen angedeuteten Spiralarmlen. Es erscheint subthermisch angeregt und kalt. Ein starker Geschwindigkeitsgradient konnte quer zum Balken nachgewiesen werden, der basierend auf einem Balkenmodell von Roberts et al. (1979) mit einem nach innen gerichteten Gasfluß in Verbindung gebracht werden kann.

Die Hypothese, ob 3C48 ein Mergersystem ist oder nicht, ist eine lang debatierte Frage. Zuther et al. (2004) haben kürzlich eine zweite Komponente im Nah-Infraroten messen können, deren mögliche Interpretation die eines zweiten Nukleus ist. Nun zeigen die neuen Beobachtungen das Gases durch CO zwei anscheinend unabhängige kinematische Systeme, von denen das ausgedehntere näher an dieser zweiten NIR-Komponente zu finden, wohingegen das zweite, kompaktere Gasreservoir auf dem QSO selber zentriert ist. Außerdem sind auch im 1 mm Kontinuum, das bislang noch nicht kartiert war, eine Ausdehnung in Richtung der zweiten nuklearen Komponente und eine in Richtung bzw. Verlängerung des Radiojets erkennbar. Diese Tatsache könnte dem Gegenargument für die Zweite-Nukleus-Hypothese die Grundlage nehmen, dass die zweite NIR Komponente ein Zeichen für eine Interaktion des Jets mit dem umgebenden interstellaren Medium ist. Die Ergebnisse der IRAM PdBI Beobachtungen favorisieren also im stärkeren Maße die Mergerhypothese.

Q0957+561 stellt die am weitesten entfernte Galaxie in dieser Arbeit dar. Basierend auf Vorarbeiten im Rahmen meiner Diplomarbeit wurden neue Beobachtungen der CO Emission in diesem Objekt durchgeführt, um die Detektion einer rotierenden (scheinbaren) Gasscheibe zu festigen. Auch die Simulationen mit einem Gravitationslinsenprogramm wurden erweitert, um Aussagen über die Struktur der Gasemission machen zu können. Q0957+561 wird durch eine Vordergrundgalaxie in zwei Bilder abgebildet. Mit den neuen Beobachtungen konnte bei dem südlicheren Bild ein einfaches Linienprofil mit nur einer Linie und ein Doppellinienprofil bei dem nördlicheren Bild bestätigt werden (Fig. 1.1). Die Erklärung für den Unterschied zwischen beiden Bildern ist in der speziellen Konfiguration zwischen Linse und Q0957+561 verborgen. Ein Teil der Galaxie liegt in einem Bereich, in dem das Linsenpotential noch stark genug ist, zwei Bilder zu produzieren, während sich der andere Teil schon außerhalb dieser Region befindet, und somit nur einmal verstärkt wird. Stützend auf einen Vergleich mit optischen Bildern von Q0957+561, die in gutem Einklang mit den Ergebnissen über das Gas stehen, und basierend auf detaillierten Simulationen, wird hier die Hypothese der rotierenden Gasscheibe bevorzugt.

HCN konnte in sieben der zwölf beobachteten NUGA Quellen nachgewiesen werden. Die Ergebnisse für diese HCN Beobachtungen stimmen hervorragend mit den Resultaten aus anderen Studien über aktive Galaxien überein. Es wurde ebenfalls eine starke Korrelation zwischen der HCN Leuchtkraft, die die Masse des dichten Gases mißt, und der Fern-Infrarot Leuchtkraft gefunden, die ein Maß für Sternentstehung ist.

Als zweiter Teil dieser Arbeit, der einen anderen Blickwinkel auf aktive Galaxien ermöglicht, wurden Beobachtungen des Radiokontinuums in 7 NUGA Quellen vorgenommen mit Hilfe von hochauflösenden Radiointerferometern wie VLBI⁸ und MERLIN⁹. Diese erreichen räumliche Auflösungen von einigen Millibogensekunden, d.h. im Falle von NGC 3718 sind damit Strukturen von bis 0.1 pc erkennbar. Das Radiokontinuum ist mit nicht-thermischen Energieprozessen verbunden, die in direkter Umgebung des schwarzen Loches stattfinden. Einer der Hauptprozesse ist hierbei die Synchrotronstrahlung, d.h. Strahlung die bei der Beschleunigung eines Elektrons in einem Magnetfeld frei wird. Diese Strahlung ist messbar in ausgedehnteren, optisch dünnen Radiokomponenten, den sogenannten Jets, aber auch in sehr kompakten, optisch dicken Radiokomponenten, den sogenannten Cores oder Kernen. Nach solch ausgedehnten und kompakten Strukturen wurde in sieben NUGA Quellen bei zwei verschiedenen Wellenlängen (18 cm und 6 cm) und verschiedenen räumlichen Auflösungen erfolgreich gesucht. Die sieben untersuchten Objekte zeigen ausgedehnte und diffuse Strukturen, die sich in einer Abnahme des Radioflusses mit steigender Auflösung widerspiegeln. Interferometer lösen mit steigender räumlicher Auflösung ausgedehnte Strukturen auf und sind nur noch empfindlich gegen kompaktere Komponenten der Strahlung. Daneben konnte in einigen Objekten auch Jets nachgewiesen werden. Diese sind zwar, verglichen mit den Radiojets in Quasaren, ihren leuchtstärkeren Gegenparts, nur kleine Glühwürmchen, aber dennoch vorhanden. Dies nährt die Hypothese, dass die weniger aktiven Galaxien, wie die NUGA Quellen, nur herunterskalierte Versionen der massiv aktiven Galax-

⁸Very Long Baseline Interferometrie

⁹Lokales Interferometer in England

ien, wie Quasare, sind. Die verschiedenen Aktivitätslevel innerhalb der aktiven Galaxien mag daher nur durch die Effizienz und Rate der Akkretion bestimmt sein. Ein weiteres Argument für diese Theorie findet sich in einer sehr starken Korrelation zwischen Radio und Röntgenfluss, die für Quasare schon seit längerem bekannt ist und nun erstmals auch für solch radioschwache Objekte (Größenordnung $\sim 0.5-10$ mJy) bestätigt werden kann. Eine solche Beziehung zwischen Radio und Röntgenemission für die kompakten Komponenten ist auch zu erwarten, da die Synchrotronstrahlung unter der Annahme eines Spektrums mit negativer Steigung (d.h., optischer dünner Synchrotronstrahlung) hin zu höheren Energien extrapoliert und dann durch (inverse) Compton-Streuprozesse weiter zu Röntgenwellenlängen hin übertragen werden kann. Bisherige Radiostudien dieser Klasse von aktiven Galaxien beruhten entweder auf Stichproben mit erheblich geringeren räumlichen Auflösungen, oder bei vergleichbarer Auflösung mit einer geringeren Anzahl (~ 3) von Objekten bzw. sehr viel stärkeren Radiostrahlern, d.h. die hier präsentierte Studie ist meiner Kenntnis nach die bisher empfindlichste Analyse über solch radioschwache Galaxien.

Contents

1	Introduction	15
I	Active Galactic Nuclei (AGN)	19
2	Theory and Models	21
2.1	Introduction	21
2.2	Classification of different types of AGN	23
2.2.1	BL Lac (blazars)	25
2.2.2	Quasars/QSOs	25
2.2.3	Seyferts	26
2.2.4	LINERs	26
2.3	Accretion models for HLAGN	26
2.4	Accretion models for LLAGN	27
2.5	Weighing nuclear black holes	28
3	AGN Surveys and Samples	31
3.1	The NUGA project	31
3.1.1	Introduction	31
3.1.2	The NUGA sources	32
3.1.3	First results of CO observations with PdBI	32
3.2	The Cologne nearby QSO sample	38
3.2.1	Introduction	38
3.2.2	Observations	38
II	Observational techniques at radio and mm wavelengths	41
4	Instruments at radio and mm wavelengths	43
4.1	Single-Dish telescopes	43
4.1.1	IRAM 30m telescope	44
4.2	Interferometers	44
4.2.1	IRAM PdBI	45
4.2.2	MERLIN	47
4.2.3	VLBI/EVN	47
4.3	Calibration of interferometric data	47

III Observations I: Molecular gas traced by CO	49
5 NGC 3718	51
5.1 Introduction	51
5.2 Observations	52
5.2.1 Central pointing	52
5.2.2 Mosaic	53
5.3 The data	54
5.3.1 Central emission	54
5.3.1.1 Continuum	54
5.3.1.2 Line	56
5.3.2 Overall emission	59
5.3.3 PdBI-only data	59
5.3.4 PdBI+30m data: short spacing correction	59
5.4 Modeling the CO distribution	62
5.4.1 The model	62
5.4.2 Simulating the short-spacing correction	63
5.4.3 Model versus Data	64
5.5 Discussion	69
6 NGC 1068	71
6.1 Introduction	71
6.2 Observations	73
6.3 The data - first results	73
6.3.1 Continuum emission	76
6.3.1.1 3 mm	76
6.3.1.2 1 mm	77
6.3.2 $^{13}\text{CO}(1-0)$ line emission	77
6.3.3 $^{12}\text{CO}(2-1)$ line emission	80
6.4 Gas and dynamical masses	84
6.5 Estimating the magnetic flux density around the black hole	87
6.6 Summary and Outlook	87
7 HE1029-1831	89
7.1 Introduction	89
7.2 Observations	89
7.3 The data - results	90
7.3.1 CO emission	90
7.3.2 Continuum emission	94
7.4 Summary and Conclusions	94
8 3C48	99
8.1 Introduction	99
8.2 Observations	100
8.3 The data	101
8.3.1 Continuum	101
8.3.1.1 3.5 mm	101
8.3.1.2 1.2 mm	104
8.3.2 Line emission	104
8.3.3 $^{12}\text{CO}(1-0)$	104

8.3.3.1	3C48A	106
8.3.3.2	QSO-red/QSO-blue	107
8.3.4	Earlier vs new data set	107
8.3.5	$^{13}\text{CO}(3-2)$	110
8.4	Gas and dynamical mass in 3C48	110
8.5	3C48 versus the Antennae galaxies and Arp220	113
8.6	Summary and Conclusions	114
9	Q0957+561	117
9.1	Introduction	117
9.2	Observations	118
9.2.1	Data taken in 1998	118
9.2.2	Data taken in 2003	119
9.3	The data	119
9.3.1	Continuum emission	119
9.3.1.1	3.1 mm	119
9.3.1.2	1.3 mm	121
9.3.2	Line emission	121
9.3.2.1	CO(2-1)	121
9.3.2.2	CO(5-4)	121
9.4	Modelling Q0957+561	122
9.4.1	Line emission	122
9.4.1.1	The blueshifted line	128
9.4.1.2	The redshifted line	129
9.4.2	Radio continuum	130
9.5	Discussion	131
9.6	Conclusions	134
IV	Observations II: Molecular gas traced by HCN	135
10	NUGA: IRAM 30m observations of HCN	137
10.1	Introduction	137
10.2	Observations	139
10.3	Results	139
10.4	Summary and Outlook	140
V	Observations III: Radio emission	145
11	NUGA sources	147
11.1	Introduction	147
11.2	Observations	148
11.3	Observational results	148
11.3.1	General results	148
11.3.2	Results for individual galaxies	149
11.3.2.1	NGC 1961	149
11.3.2.2	NGC 2782	151
11.3.2.3	NGC 3147	151
11.3.2.4	NGC 3718	153

11.3.2.5 NGC 4579	153
11.3.2.6 NGC 5953	156
11.3.2.7 NGC 7217	156
11.4 Spectral Energy Distribution	157
11.5 Radio versus X-ray luminosity and black hole mass	159
11.6 Summary and Conclusion	161
VI Summary, Conclusions and future prospects	163
12 Summary and Conclusions	165
12.1 NGC 3718	165
12.2 NGC 1068	166
12.3 HE 1029-1831	166
12.4 3C48	166
12.5 Q0957+561	167
12.6 Dense gas in 12 NUGA galaxies	167
12.7 Radio emission in 7 NUGA galaxies	167
12.8 General remarks and future prospects	168
Appendix	171
A Warps	173
B Emission processes in the radio and X-ray domain	175
B.1 Synchrotron radiation	175
B.2 Compton scattering	178
C Velocity channel maps of HE1029-1831	179
D HCN and ¹²CO(1–0) spectra of the NUGA core sample	183
Bibliography	186
List of figures	195
List of tables	199
Table of Abbreviations	201
Acknowledgements	203
Curriculum Vitae	207

Chapter 1

Introduction

Observations in the past years provide strong evidence for the majority of galaxies hosting a super-massive black hole in the nuclear region (e.g., Kormendy and Gebhardt 2001). A hot matter of current debate is the question whether the possibility of feeding the nuclear super-massive black hole by gas¹ from the host galaxy determines the difference between active, quiescent and pure starburst galaxies. Also the efficiency of the gas accretion seems to play a dominant role since different levels of activity are observed, ranging from so called Low-Luminosity Active Galactic Nuclei (LLAGN) to High-Luminosity Active Galactic Nuclei (HLAGN). The effective mechanisms transporting the gas from outer regions of the host galaxy down to the nucleus and removing surplus angular momentum still remain far from being understood. On large scales (≥ 3 kpc), galaxy interactions are supposed to trigger the infall of gas onto the centre although a significant fraction of active galaxies appear to be isolated with no sign for interaction at all (e.g. Bahcall et al. 1997, de Robertis et al. 1998, Surace et al. 2001). On small scales (< 3 kpc), the processes at play are even less clear. Asymmetrical perturbations, such as nested bars, lopsidedness and warped nuclear disks (e.g. Shlosman & Noguchi 1993, Schinnerer et al. 2000) are among the prime candidates for keeping accretion alive on these scales.

The NUclei of GALaxy (NUGA) project aims at studying the small scale asymmetries of the molecular gas in a survey of in total ~ 30 nearby Low-Luminosity Active Galaxies (LLAGs). Two of these objects, NGC 3718 (Krips et al., 2005a, Fig. 1.1) and NGC 1068 (Fig. 1.2), were analysed in the framework of this PhD thesis. Besides the study of LLAGs, also HLAGs², such as quasars, are an important piece to unpuzzle the nature of these objects. Therefore, 3 sources classified as QSOs/quasars have been included in this work: HE 1029-1803, 3C48 (Krips et al., 2005b) and Q0957+561 (Krips et al. 2004a,b). Molecular gas consists mainly of molecular hydrogen (H_2) but H_2 cannot be directly observed, unfortunately, due to the low gas temperatures which are in general of the order of 10-100K. Since the electric dipole moment vanishes in the equilibrium state of H_2 due to its symmetric diatomic structure, the next measurable transition needs excitations temperatures of ~ 500 K. Also, its rotational-vibrational lines are excited at very high temperatures of 2000-3000K. Another good gas tracer is carbon monoxide (CO) that can be excited via collisions with H_2 at these low temperatures (i.e., needs ~ 6 K for the lowest state). While the analysis of the accreted matter through ^{12}CO emission is a first and important step to improve the knowledge about the distribution and kinematics of the gas, it cannot, however, give a priori a complete picture of all different gas properties. Therefore, other gas tracers have to be taken into account additionally. ^{12}CO is known to trace regions with rather low to moderate gas densities ($n(H_2) \geq 200 \text{cm}^{-3}$). Denser gas ($n(H_2) \sim 10^5 \text{cm}^{-3}$) measurable through HCN for instance is not only found to be stronger correlated to star formation but seems to be also

¹Typical gas masses (atoms+molecules) range from roughly 10^8 - $10^9 M_\odot$ for lower active galaxies (e.g., Seyfert galaxies such as NGC 3718 and NGC 1068) to roughly 10^9 - $10^{10} M_\odot$ for higher active galaxies (e.g., quasars such as 3C48 and Q0957+561). This is $\lesssim 1$ -10% of the total mass of a galaxy which is rather dominated by the stellar mass.

²High-Luminosity Active Galaxies

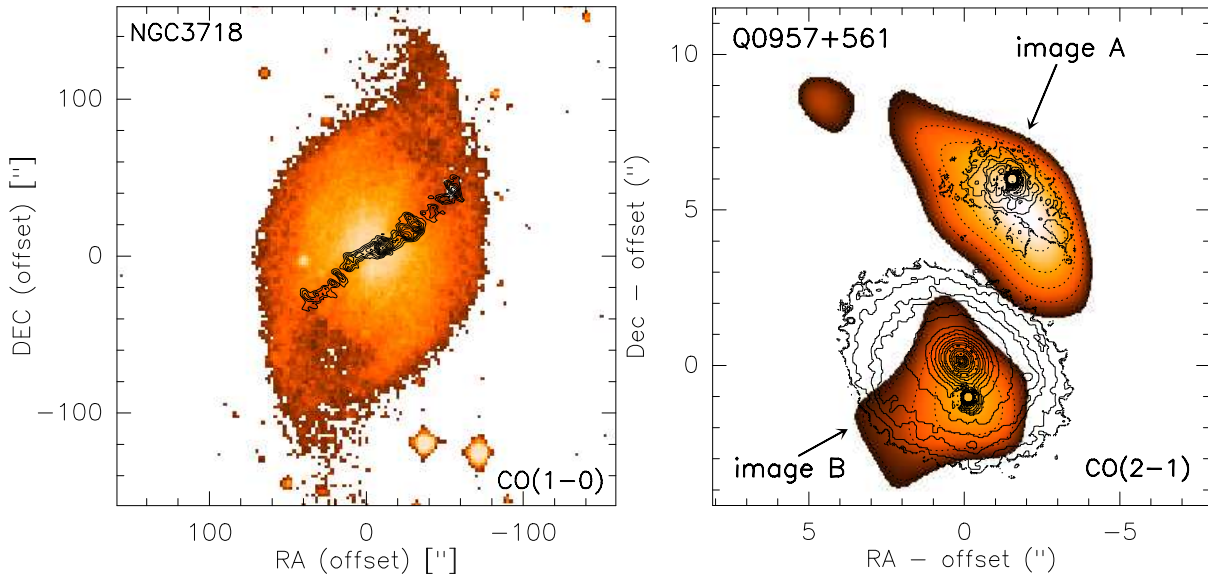


Figure 1.1: *Left*: Optical image (taken from the DSS survey) superimposed with the integrated CO(1–0) contours (black) obtained at the IRAM PdBI (see Chapter 5). The warped molecular gas emission nicely follows the dust lane. Contour levels as in Fig.5.13). *Right*: Integrated CO(2–1) line emission of Q0957 overlaid with (black) contours of the optical images (the lensing galaxy is also visible at $(0'', 0'')$). The lensing effect produces here two images of Q0957+561. For more details see Chapter 9.

more concentrated in the nuclear regions of active galaxies than gas detected by ^{12}CO (Tacconi et al. 1996; Helfer & Blitz 1997). Thus, molecules such as HCN are a further, complementary and necessary diagnostic tool to investigate the gas in active galaxies. Also in terms of the connection and/or discrimination between pure starburst-powered and pure accretion-powered active galaxies, higher gas density tracers are an essential piece of information since starbursts typically and preferentially occur in denser parts of the gas. Therefore, HCN emission has been observed in the NUGA targets using the IRAM 30m telescope as a first step for follow-up interferometric observations.

Besides studying the accretion processes via the molecular gas, the diversity between low and high LAGN can also be investigated on the basis of emission that is directly associated with the central engine, such as the non-thermal radio continuum for instance. HLAGN are often strong radio continuum emitters showing besides compact (sub-parsec) cores also extended structures like jets. The radio emission is supposed to be mainly dominated by synchrotron processes³ providing also an explanation for the strong correlation between radio and X-ray fluxes found in active galaxies. In the compact part of the jet, the electrons, which are accelerated in the magnetic field, produce the synchrotron radiation, and later scatters the emitted low energy photons towards higher energies, resulting in a synchrotron self (inverse) Compton process with high energy (X- and γ -) rays as output.

In recent studies (e.g. Ulvestad & Wilson 1984, Pedlar et al. 1993, Falcke et al. 2000), one suspects that LLAGN might also contain non-thermal radio emission in form of jets and/or compact sources even if much less powerful than observed in HLAGN (Fig. 1.2). Jets are highly correlated with accretion processes onto compact objects (e.g. Pringle 1993, Blandford 1993) and are thus signatures for accretion-powered AGN. Therefore, LLAGN might be only scaled down versions of HLAGN in terms of activity while the effective processes remain the same. As mentioned above, the low luminosity would be caused by either low or inefficient accretion. In this context, a subsample of the NUGA survey, consisting of seven galaxies, were observed with MERLIN and

³Optically thin in jets and optically thick, i.e. self absorbed, in the compact cores

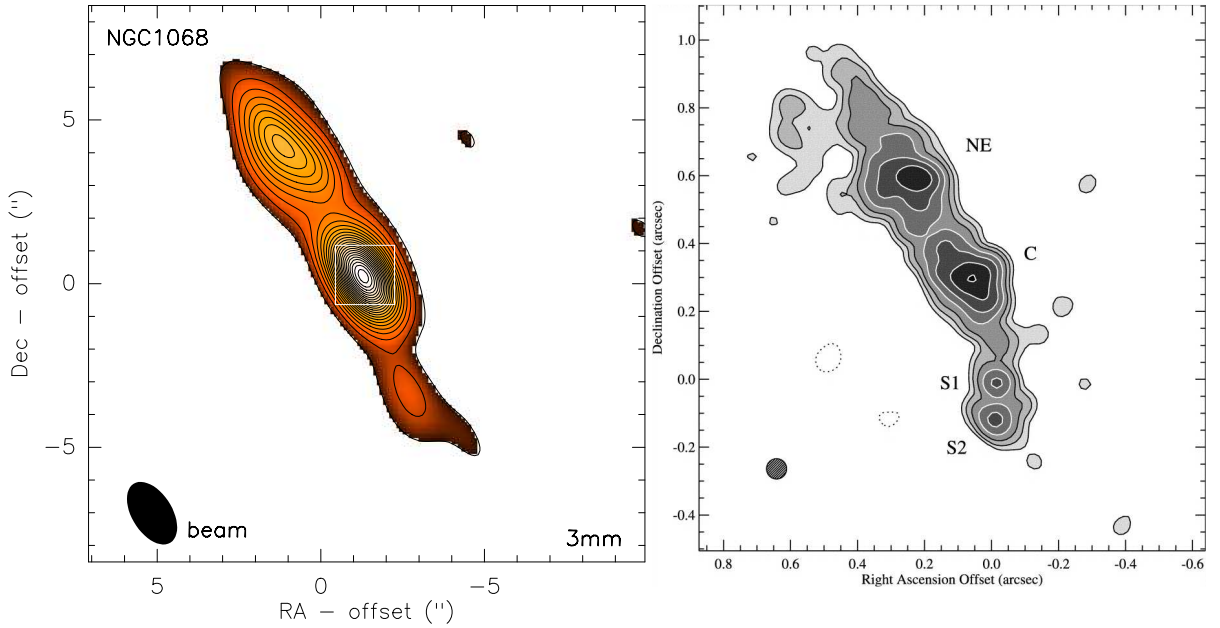


Figure 1.2: Continuum map of NGC 1068 at 3 mm (*left*) and at 6cm (*right*). Contour levels are from $3\sigma=1.1$ to 25.3 mJy/beam in steps of 3σ at 3 mm. The beam size is indicated as filled black ellipse in the lower left corner. The small white box in the left map indicates the field of view of the map at the right. The MERLIN 6cm map is taken from Gallimore et al. (2004).

VLBI at 18cm and 6cm to reveal the nature of non-thermal radio emission in these radio weak galaxies and their difference or similarity to the emission observed in HLAGN (Krips et al. 2004d, 2005c).

All data presented in this PhD thesis, if not otherwise marked⁴, have been observed, reduced, simulated and analysed by myself including, where possible, an active participation at the following observations:

IRAM PdBI (Section 4.2.1, Fig. 1.3):	NGC 3718	$^{12}\text{CO}(1-0)$, $^{12}\text{CO}(2-1)$, 3 mm & 1 mm continuum
	NGC 1068	$^{13}\text{CO}(1-0)$, $^{12}\text{CO}(2-1)$, 3 mm & 1 mm continuum
	HE 1028-1831	$^{12}\text{CO}(1-0)$, $^{12}\text{CO}(2-1)$, 3 mm & 1 mm continuum
	3C48	$^{12}\text{CO}(1-0)$, $^{13}\text{CO}(2-1)$, 3 mm & 1 mm continuum
	Q0957+561	$^{12}\text{CO}(2-1)$, $^{12}\text{CO}(5-4)$, 3 mm & 1 mm continuum
IRAM 30m (Section 4.1.1):	NUGA survey	$^{12}\text{CO}(2-1)$, $^{12}\text{CO}(5-4)$, HCN(1-0)
MERLIN (Section 4.2.2):	7 NUGA sources	18 cm, 6 cm
EVN (Section 4.2.3):	7 NUGA sources	18 cm, 6 cm

The thesis⁵ is structured as following: in Part I basic theories and models for active galaxies are discussed. Some of the studied objects in this PhD thesis belong to larger, statistical samples which are also briefly presented. Part II summarizes the observational techniques used to obtain the data. In Parts III, IV and V, the results of the different

⁴In the cases of NGC 3718, NGC 1068, 3C48 and Q0957+561, new data is compared and merged with earlier data obtained by other groups, where possible and reasonable. This guaranteed a higher sensitivity and also a higher quality for the interpretation of the data.

⁵Throughout the thesis a flat cosmology with $H_0=75 \text{ km s}^{-1} \text{ Mpc}^{-1}$ (if not otherwise stated) and $q_0=0.5$ ($\Omega_M=0.3$, $\Omega_V=0.7$) will be assumed.



Figure 1.3: Picture of the IRAM Plateau de Bure Interferometer (private communication).

observations are described, starting with the observations of the molecular gas traced by CO using the IRAM Plateau de Bure Interferometer, followed by those of gas traced by HCN and carried out with the IRAM 30m telescope, and finishing with the observations of the radio continuum emission in the NUGA survey. All results are summarized in the last Part including conclusions and future prospects.

Part I

Active Galactic Nuclei (AGN)

Chapter 2

Theory and Models

2.1 Introduction

The phenomenon of active galaxies has first been reported in the early 1960s. Unusually bright and compact objects were discovered which were first misleadingly classified as quasi-stellar-objects (quasar/QSO), such as 3C273 for instance (Greenstein et al. 1964). As soon as their distances were derived, the preliminary theories about these sources, being an exotic and so far unknown stage of stellar evolution within the galaxies, had to be discarded. Their redshifts excluded a position within the Milky Way showing that they were external objects, i.e. peculiar galaxies, and even more luminous than previously assumed. Not only that these objects reveal strong emission at one frequency but they also emit strongly over the whole electromagnetic spectrum. Their bolometric¹ luminosities do not seldomly reach $\sim 10^{12} L_{\odot}$. Astonishingly, almost the whole observed energy is related to the very nucleus of these objects outshining in many cases their surrounding host galaxies. This explains their first classification since only the bright nuclei were detected while the host galaxies remained invisible. The compact and very active nuclei in this type of galaxies are hence labeled as Active Galactic Nuclei (AGN). Until now, innumerable observations and studies at all possible frequencies have been conducted to understand the nature of these highly interesting sources. However, a unified theory explaining all different aspects and characteristics of AGN has so far not been found or established due to the huge variety of observed properties. It is not even clear if the AGN phenomenon can be related to only one single basic model and its variants or if different mechanisms have to be considered. Among the candidates for the effective processes of the huge energy release are the accretion of matter onto a super-massive central black hole and enhanced nuclear starbursts. The past decades of research have given significant evidence for most of the galaxies hosting supermassive black holes, i.e. at least those with central bulges (Kormendy & Richstone 1995; Richstone et al. 1999; Kormendy & Gebhardt 2001, Schödel et al. 2002). Magorrian et al. (1998) reported as one of the first groups on a tight correlation between bulge and central black hole masses indicating a similar formation and evolution of both. Gebhardt et al. (2000a), Ferrarese & Merritt (2000) and Shields et al. (2003) found an even tighter correlation between the stellar velocity dispersion in the bulge and the central black hole mass supporting a fundamental link between them. Although super-massive black holes constitute a potential central engine, only a small fraction ($\sim 10\%$; Almaini & Fabian 1997) of the large group of galaxies with a central black hole shows enhanced nuclear activity in the present universe. This fraction increases towards higher redshifts reaching its maximum at $z=2-3$ (e.g., Fan et al. 2001). Recent model calculations, carried out by Yu & Tremaine (2002), support that the supermassive black holes accumulate the majority of their mass in the same redshift range, implying a link between nuclear activity and accretion mechanisms. Thus, the fueling of the central engine with matter seems to be a promising approach and could at the same time also explain the difference of active to quiescent galaxies. One hypothesis is that the accretion process in active galaxies has been initialised and boosted by gravitational interaction with another galaxy while quiescent objects have never undergone a significant

¹i.e., over the whole electromagnetic spectrum

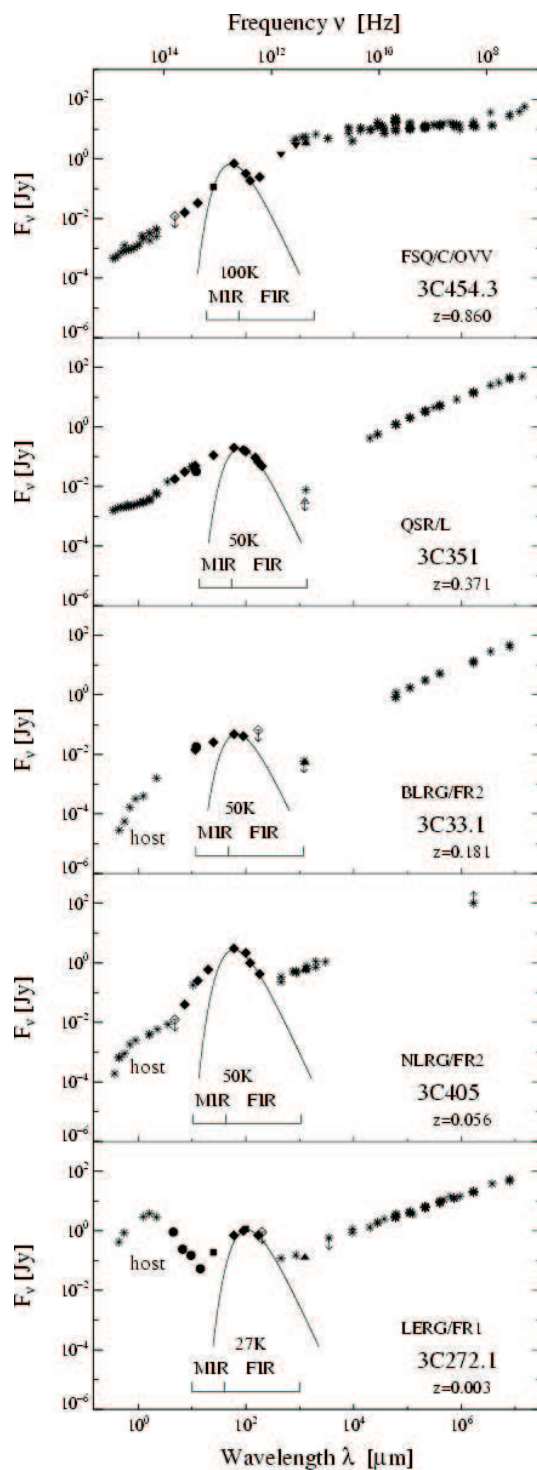


Figure 2.1: Representative SEDs at infrared to radio frequencies of some quasars taken from Haas et al. 2004.

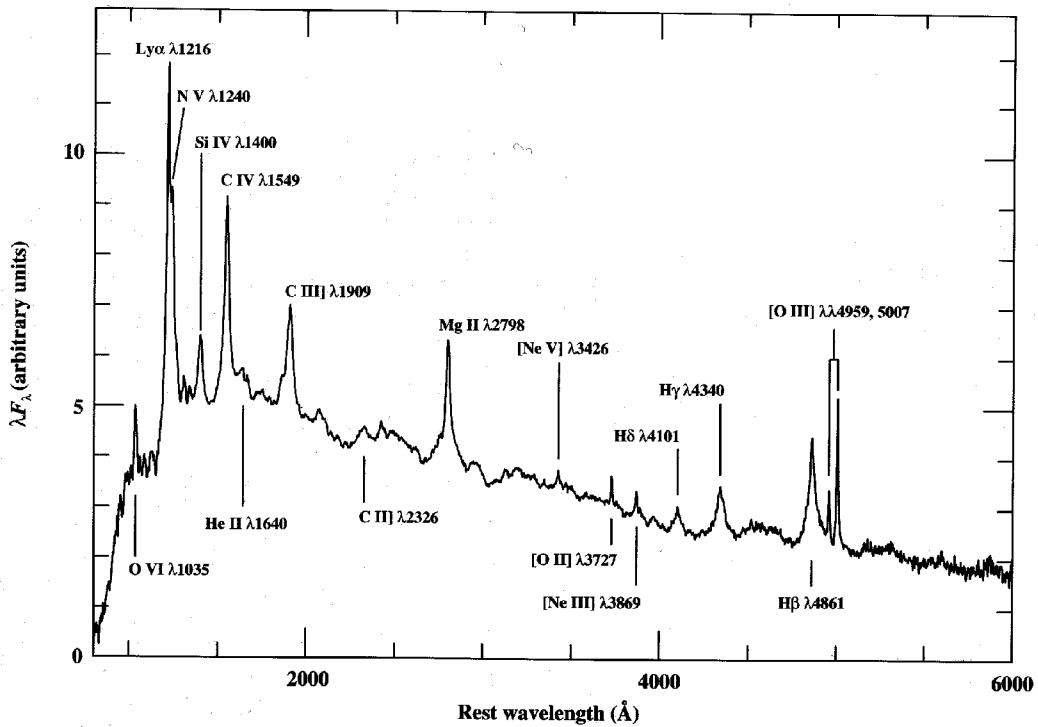


Figure 2.2: Mean optical spectrum of quasars (Francis et al. 1991, Bradley 1997).

collision or merger with a close galaxy which would have enabled a fueling process. However, not every active galaxy is found to have a companion galaxy or shows signs for an ongoing or recent interaction. Besides the difference between quiescent and active galaxies, another pending question is the effective mechanism producing the huge variety of activity levels found among the group of AGN. Here, one distinguishes between so called High Luminosity Active Galactic Nuclei (HLAGN) and Low LAGN (LLAGN). The next sections will present in more detail the different classes of AGN and also the various models proposed to explain them.

2.2 Classification of different types of AGN

The large diversity of observed active galaxies led to a wealth of different classifications. The first detected active galaxies were found to have strong radio emission so that they were hence characterized as quasi-stellar-radio-sources, or shorter, quasars. Their radio quiet counterparts were named quasi-stellar-objects, or QSOs. A less powerful variant of quasars/QSOs were discovered by Carl Seyfert, therefore labeled as Seyfert galaxies. They are somewhat less luminous (a factor of ~ 100) than quasars/QSOs so that their nuclei do not outshine their host galaxies. Still less luminous than Seyfert galaxies are the so called LINERs, Low Ionisation Nuclear Emission Regions. Another class of active galaxies are BL Lac, strongly variable sources. Similar to quasars they were first misleadingly supposed to be stars. A certain class of variable stars are designated as BL Lacertae thus motivating the classification as BL Lac.

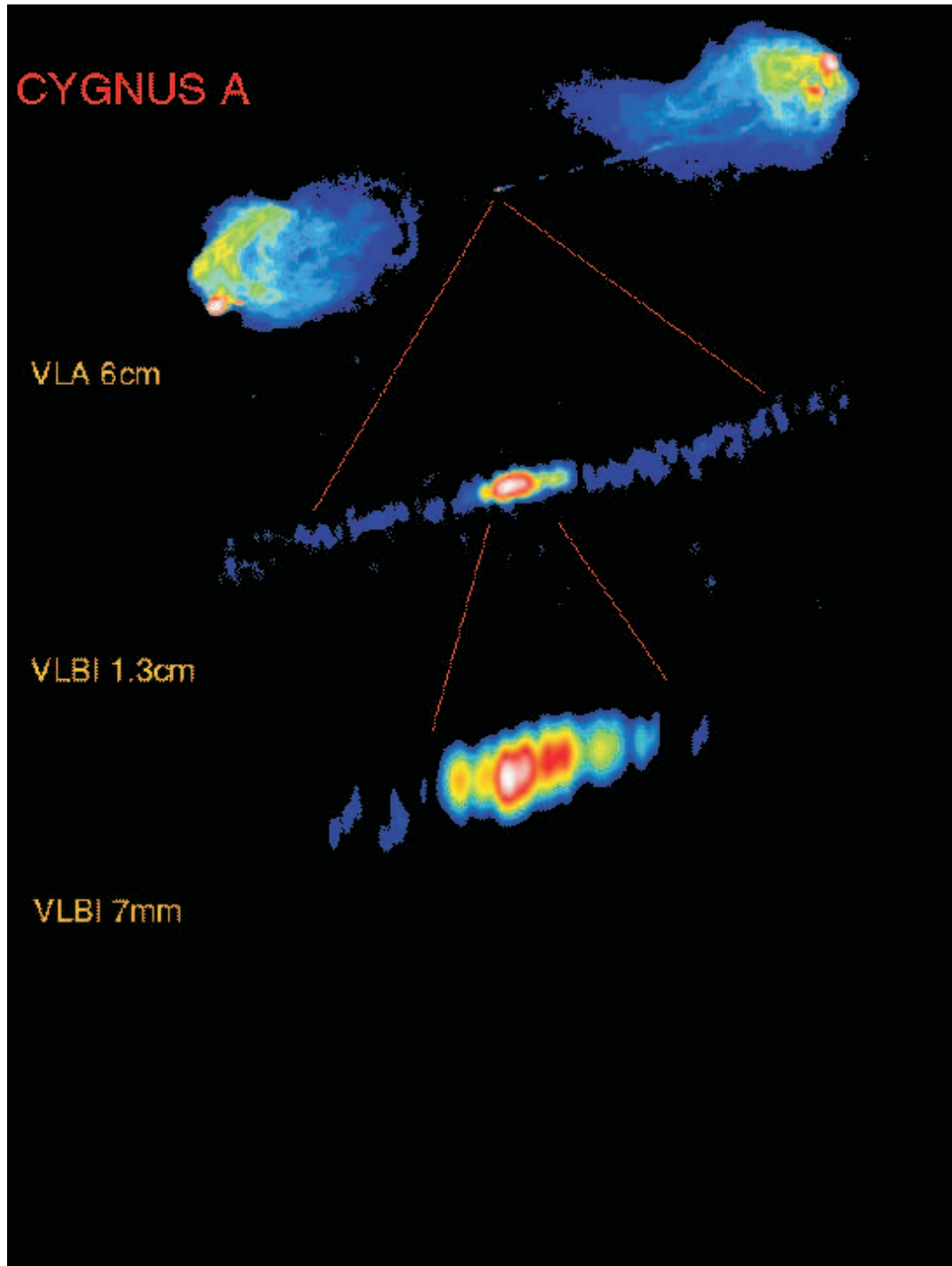


Figure 2.3: An example of a quasar (Cygnus A) with strong core, jet and lobe emission at different radio wavelengths (Krichbaum et al. 1998, Perley et al. 1984).

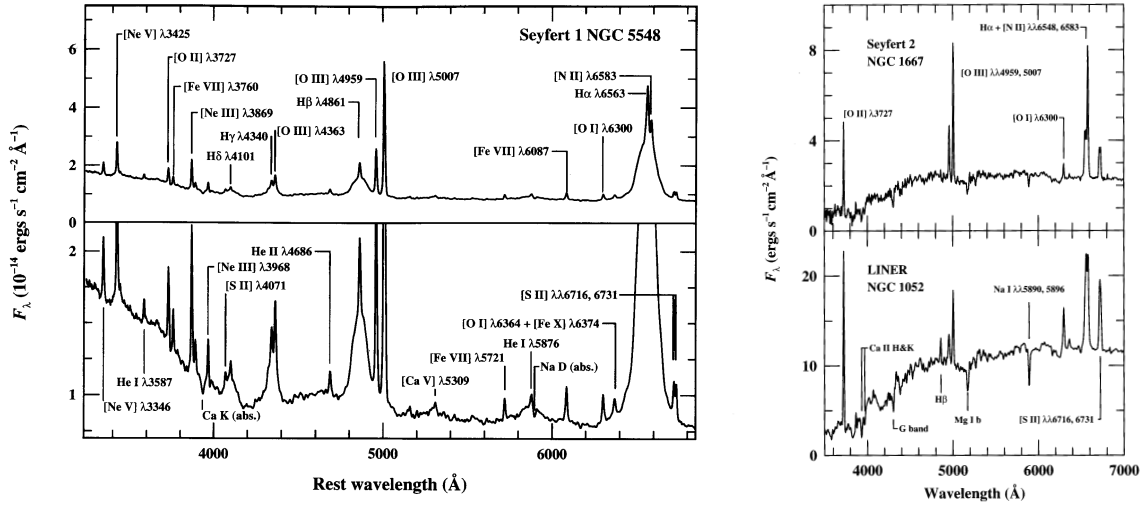


Figure 2.4: Optical spectrum of a Seyfert type 1 (*left*) and type 2 (*right*) galaxy taken from Bradley 1997. While the $H\alpha$ line is broadened in the Seyfert type 1 spectrum (*left*), it is rather narrow in the Seyfert type 2 spectrum (*right*).

2.2.1 BL Lac (blazars)

BL Lac objects show a strong flux variability at almost all frequencies thus being probably the most extreme cases of active galaxies. The observed fluxes can indeed vary on timescales as short as hours. BL Lacs apparently have only weak emission lines but also quasars with stronger emission lines and strong variability have been found as well, called thus Optically Violent Variables (OVVs). Both types of objects are thus often summarized as blazars. Urry & Padovani (1995, and references therein) propose in terms of a unified model that blazars are objects seen close to the axis of a powerful relativistic jet. Thus, apparent superluminal motions are often detected in these systems (e.g. Jorstad et al. 2001).

2.2.2 Quasars/QSOs

Quasars are extremely strong radio galaxies (radio luminosities up to $10^{12}L_{\odot}$) in which the nucleus outshines the host galaxy thus appearing as very compact sources at almost all wavelengths. Besides the compact emission, also twin-like lobe structures and jets are observed at radio and also optical frequencies in these objects (see Fig.2.3). In quasars, the lobes can reach dimensions of up to several Mpc. The radio spectra derived for each component also show different shapes. While the jet and the lobes are supposed to have optically thin synchrotron emission and thus steep spectra (see Fig.2.1), i.e. fluxes that increase with wavelength, the core has a rather flat spectrum produced by optically thick synchrotron emission coming from the base of a jet for instance. Typical optical spectra are shown in Fig.2.2. Continuum emission and strong emission lines from hydrogen for instance are visible (see also Section 2.2.3). A widely accepted explanation for the huge emission at all wavelengths in quasars is the accretion of matter onto a supermassive black hole. As quasars are usually found at higher redshifts², they can also teach us something about the evolution of galaxies.

²These sources are one of the few highly-redshifted systems which are powerful enough to be detected.

2.2.3 Seyferts

One of the strongest characteristics of Seyfert galaxies are their nuclear broad emission lines from ions which cannot be explained by excitation through photons coming from young stars. The energy produced by them would not be sufficient so that other nuclear processes have to be at play. Again, the infall of gas onto a central black hole seems to be the most promising approach. Most of the Seyferts are found to be spiral galaxies although exceptions with an elliptical morphology (e.g. NGC 1275) are also known. In contrast to the stars in Seyferts which typically have speeds of only a few hundred km s^{-1} , the gas moves much faster indicated by the broad line widths between 1000 and 10000 km s^{-1} . This range of line widths motivated to further divide Seyfert galaxies into Seyfert type 1 and type 2 as well as Seyferts falling in between these two extremes hence named type 1.9 or 1.8, for instance (Fig. 2.4). Seyferts of type 1 are those objects with the broadest line widths, i.e. of up to 10000 km s^{-1} , while Seyferts of type 2 have all widths of roughly $\sim 1000 \text{ km s}^{-1}$. Type 1.9 etc. show intermediate velocities. Among the emission lines detected in the optical and ultraviolet spectrum of Seyferts 1, the following ionized species can for instance be identified: the Lyman and Balmer lines of hydrogen, or other species like MgII, NV or OVI. These spectra are quite similar to the “average” spectrum of quasars (see Fig. 2.2 and 2.4). In general, due to the different line widths, spectra of Seyferts 2 do not a priori resemble those of Seyferts 1. However, the spectra determined from *polarised* light reveal a significant similarity to those obtained from Seyfert 1 (e.g. NGC 1068 and NGC 4258; Miller & Antonucci 1983, Antonucci & Miller 1985, Krolik & Kallman 1987, Wilkes et al. 1995). This led to a so called “unified” interpretation of the different Seyfert types. Fig.2.5 illustrates a scenario explaining the differences found between the respective Seyferts. It appears most likely that the different types of Seyfert galaxies are only seen from different viewing angles, i.e. the nucleus of a galaxy classified as Seyfert 1 is not significantly hidden by any material but directly observable while the emission from the Broad Line Region (BLR) in a Seyfert 2 galaxy is covered by the accretion torus. Thus, only reflected light from the nucleus by dust grains can reach the observer in a case of Seyfert type 2 galaxies. Reflected light is generally polarised, mostly due to Thomson scattering, so that the spectrum of polarised emission should indeed have similar characteristics as Seyfert type 1 objects. Besides the broad lines, also narrow lines (line width $< 1000 \text{ km s}^{-1}$) appear, such as forbidden transitions of oxygen (e.g. [OII] and [OIII]). Forbidden lines are possible only if the density is below a certain critical value ($n_{\text{H}} \lesssim 10^8 \text{ atoms cm}^{-3}$). In such an environment³, excitation of the ions by collisions is significantly reduced. While the continuum and broad line emission are often found to be variable, the narrow lines have so far not given any evidence for variability. This nourishes the hypothesis that the Narrow Line Region (NLR) cannot be as close to the central engine as the BLR.

2.2.4 LINERS

LINERs, i.e. Low Ionisation Nuclear Emission Regions, are even less luminous than Seyfert (type 2) galaxies and also detected mainly in spiral galaxies. LINERs occur more frequently than Seyferts. While Seyferts roughly contribute with 10% to all known spiral and S0 galaxies, LINERs already amount to a fourth of all spiral galaxies. The observed lines in a LINER spectrum (e.g. [OI] or [SII]) indicate a rather low-powered nucleus since their excitation does not require such high energies as in Seyferts. Thus, besides accretion processes also enhanced starburst can be made responsible for the observed activity in this class of AGN.

2.3 Accretion models for HLAGN

In the case of HLAGN, the accreting gas is supposed to be located in a thin disk in which the gas can efficiently cool through radiation. This theory was first proposed by Shakura & Sunyaev (1973). A byproduct of the cooling process is the fact, that the temperature of the gas is lower than the virial temperature so that vertical motions are mostly suppressed and the gas remains in a very thin disk. The gas now stays sufficiently long enough in the disk before it drops into the black hole and can thus be cooled down via radiation within the disk.

³NLR have typical particle densities of $n_e = 10^3 \text{ cm}^{-3}$, whereas the one of BLR increase up to $n_e = 10^{11} \text{ cm}^{-3}$.

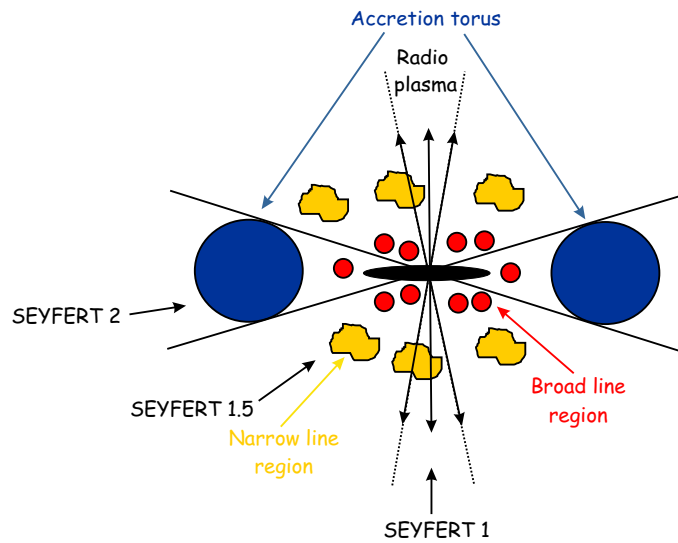


Figure 2.5: A standard schematic model of an active nucleus indicating the unification hypothesis.

2.4 Accretion models for LLAGN

One approach to explain the difference between LLAGN and HLAGN is believed to lie in lower accretion rates on the one hand but also in the efficiency of the accretion of matter onto the AGN on the other hand. In this picture, the lower luminosities ($L \ll 0.1\dot{M}c^2$) in LLAGN with respect to HLAGN could be traced back by radiatively inefficient accretion flows (RIAFs) as summarized in Quataert et al. (2003) or Eckart, Schödel and Straubmeier (2004). In particular, besides the already low accretion rates, only a small fraction of the available gravitational potential energy of the accreting gas is released through radiation and almost everything is converted into thermal energy. Thus, the gas turns into a very hot plasma and the thermal energy will mainly be stored by protons rather than electrons since the latter have a much lower mass. A coupling between protons and electrons through Coulomb collision is unlikely since the timescale for the particles to fall into the black hole is much shorter than the timescales for the collision process and the gas densities are low. Therefore, a two temperature gas is the inevitable result with the protons being hotter than the electrons (by up to two orders of magnitudes). The electrons can radiate much easier and on much shorter timescales than the protons. The latter are swallowed by the black hole before the cooling process through radiation takes over. They carry more than 99% of the energy so that only less than 1% is emitted and can be observed. Several models have been proposed for the dynamics of RIAFs, i.e. for how the plasma falls into the nucleus. State-of-the-art models are the Bondi-Hoyle description (Melia & Falcke 2001), ADAFs⁴ (e.g. Narayan et al. 1995), CDAFs⁵ (Ball et al. 2001), ADIOS⁶ (Blandford & Begelman 1999), jet models (Falcke & Markoff 2000), quasi-monoenergetic electron distributions (Beckert & Duschl 1997) and each combination such as RIAF plus jet emission (e.g. Yuan et al. 2002). Some of these will be presented in the following.

The Bondi-Hoyle approach assumes a spherical accretion of the plasma onto the black hole. The timescales for the protons to be advected into the black holes are much shorter than those for the cooling process via radiation. Thus, only the electrons have enough time to radiate but they carry only a tiny fraction of the available energy.

ADAFs are so called Advection Dominated Accretion flows. They are quite similar to the Bondi-Hoyle description but put more importance onto the angular momentum and viscosity of the plasma. If the cooling of the

⁴Advection Dominated Accretion Flows

⁵Convection Dominated Accretion Flows

⁶Advection Dominated Inflow Outflow Solutions

accreting gas through radiation cannot follow efficiently the heating, the accreting material will inevitably become hotter and the vertical, i.e. local motions increase significantly. As a consequence, the accretion disk will be thickened and the vertical scales are not longer negligible to the radius but rather are of the same order resembling the case of a Bondi-Hoyle Sphere. As another result of the disk thickening, the gas density decreases so that again the probability of cooling through collisions falls as well as the timescale for the gas to arrive at the event horizon of the black hole. The latter becomes comparable to the free-fall time scales. Therefore, the gas has less and less time to cool efficiently and most of the viscously released energy disappears with the protons in the black hole.

Both models presented so far predict quite high densities in the vicinity of the black hole ($\rho \propto r^{-3/2}$, with $r \equiv$ radius (r small) and $\rho \equiv$ gas density). However, as in the case of Sgr A*, for instance, the center of our Milky Way, the observed gas densities are found to be much lower than determined in ADAFs or Bondi-Hoyle models (Aitken et al. 2000 and Bower et al. 2004). Thus, further models were developed such as CDAFs and ADIOS (Blandford & Begelman 1999). CDAF means Convection Dominated Accretion Flow and was discussed by Ball et al. (2001). Analytical calculations and numerical simulations have shown that in an ADAF convection would be unstable (e.g. Igumenshchev et al. 1996 and Igumenshchev & Abramowicz 1999, 2000). However, Igumenshchev & Abramowicz (1999, 2000) also report that the stability of the convection depends on the viscosity parameter α . For small values of α , i.e. $\alpha \lesssim 0.1$, convection becomes stronger so that the gas does not simply fall into the black hole but flows again outwards through long-wavelength convective fluctuations. This leads to a significantly different structure than found in ADAFs or Bondi-Hoyle models. The gas densities are estimated to scale as $r^{-1/2}$, i.e. predict a much lower density at small radii than in ADAF or Bondi-Hoyle models. Narayan et al. (2000) showed that the strong convection process transports angular momentum inward balancing the energy which is moved outwards by convective fluctuations. As a consequence, the gas statically circulates and is not as strongly accreted as in ADAFs or Bondi-Hoyles, i.e. CDAFs predict even lower mass accretion rates.

Similar to CDAFs, the Advection Dominated Inflow-Outflow Solution (ADIOS) assumes that a majority of the infalling gas is actually not accreted by the black hole. In the case of an ADIOS, the gas is rather blown away through winds or outflows due to the energy that is released by the gas which is transported inwards but then not taken over by the black hole. Again the densities at small radii are lower than in ADAFs or Bondi-Hoyles and scale as $r^{-3/2+p}$ with $p \in (0.5, 1)$.

Another explanation of the nuclear mechanisms at play in LLAGN are jets. The bases of jets could appear compact and also have flat spectra since their emission at these small scales would be expected to be optically thick synchrotron emission rather than optically thin (e.g. Falcke & Markoff 2000). Also combinations of ADAFs and jets are discussed (e.g. Yuan et al. 2002). In these scenarios, a small part of the accretion flow is boosted outwards into a small jet resulting in an observable spectrum that is merged from emission coming from the ADAF and the jet at the same time. It is so far almost impossible to distinguish between the core emission from a jet and the very centre of ADAFs. At least, the jet emission becomes optically thin the farther it is ejected from the nucleus so that the flux decreases with decreasing wavelength. As a consequence, the different parts of the jet can be probed by observations at different wavelengths.

2.5 Weighing nuclear black holes

To determine the mass of the nuclear black hole, a few independent methods can be used. One approach is to investigate the dynamics of stars and gas moving in the gravitational field of the black hole. By knowing the velocities of stars and/or gas at a given radius R , one can estimate the dynamical mass that must be located inside R . However, due to the significant distances of galaxies and thus limited angular resolutions and sensitivity for the observations of gas and stars, the radius to which the enclosed dynamical masses can be derived is also limited. The smallest available radius to determine the (molecular) gas velocities of a galaxy at a distance of ~ 5 Mpc, for instance would already be ~ 10 pc assuming angular resolutions of $0.5''$ (e.g. at the IRAM PdBI). In the central 1 pc of our Milky Way the contribution of the stellar masses to the enclosed dynamical mass within this radius is roughly of the order of the central black hole, i.e. a few million solar masses (e.g. Eckart, Schödel & Straubmeier et al. 2004 and references therein). Thus, this first method can only provide an upper limit of the

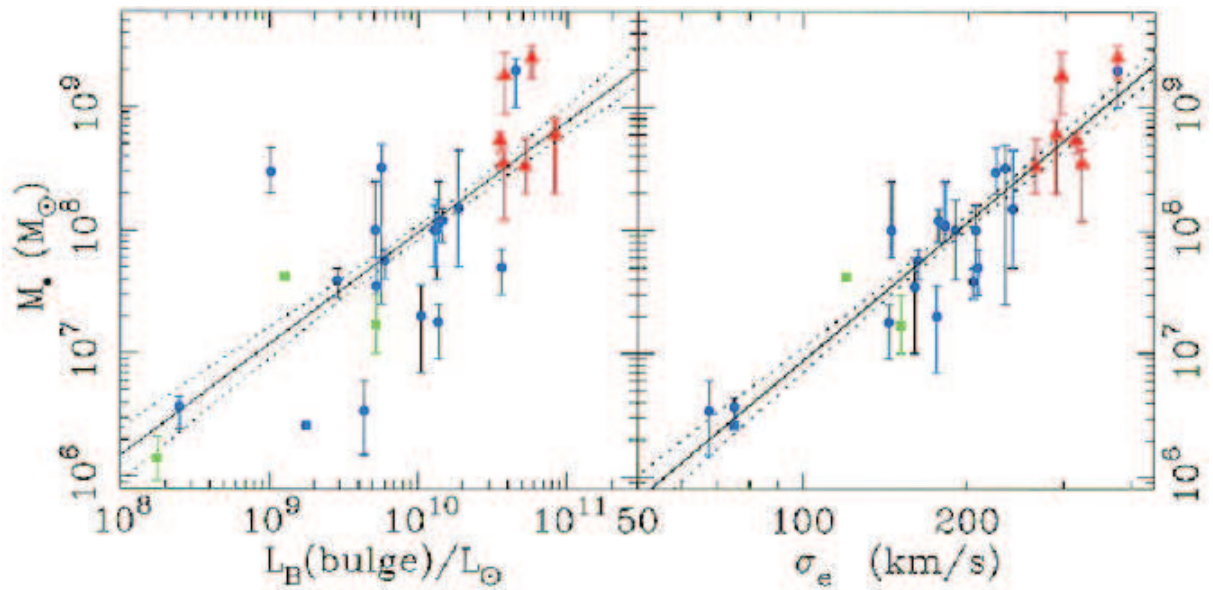


Figure 2.6: Correlation between the luminosity of the bulge and the central black hole mass (M_{\bullet} ; *left panel*), and between the stellar velocity dispersion of the bulge and M_{\bullet} (*right panel*). The plots were taken from Gebhardt et al. 2000.

black hole mass in external galaxies since it is still significantly biased by stellar mass. Another method which is only feasible for Sagittarius A*, the black hole in the centre of the Milky Way, due to its unsurpassable proximity, is to fit the stellar orbits in the direct vicinity of the black hole (e.g. Eckart, Schödel and Straubmeier et al. 2004 and again references therein). This results in an estimate of the black hole mass of Sgr A* with an error of only $\leq 20\%$ (e.g. Ghez et al. 2003, Schödel et al. 2003). Of course, stellar orbit fitting is, at least so far, unrealistic for extragalactic objects due to missing angular resolutions. However, also for extragalactic sources possibilities exist to encircle the black hole mass by using the bulge-to-black-hole correlation (e.g. Magorrian & Fabian 1998, Falcke & Hehl 2003, Shields et al. 2003). In all bulge systems, i.e. galaxies containing a bulge, studied with high spatial resolution supermassive black holes were found. Thus, the evolution of both must be somehow connected. Indeed, Magorrian & Fabian 1998 discovered a correlation between bulge and central black hole masses which turned out to have still a large scatter. Gebhardt et al. (2000a), Ferrarese & Merritt (2000) and Shields et al. (2003) found a much tighter correlation with a significant smaller scatter between the stellar line-of-sight velocity dispersion in the bulge (at radii outside the gravitational influence of the black hole) and the black hole mass (Fig. 2.6). The stellar velocity dispersion can be derived via the [OIII] line width that turned out to be a reliable surrogate for it (Nelson 2000). The black hole mass can also be estimated via reverberation mapping in nearby galaxies (e.g. Netzer & Peterson 1997). Due to the variability of the continuum and emission line fluxes in the BLRs of active galaxies, both emission types, i.e. continuum and line, can be more easily compared with each other. Although a strong correlation between both can be proven, a time lag between the continuum and line emission was observed. The time delay is interpreted in terms of different light travel times allowing in turn to estimate the size of a BLR. Under the assumptions of Keplerian dynamics, the respective line width can be taken as surrogate for the velocities providing again information of the enclosed dynamical mass. With this method, the black hole masses of various quasars and Seyfert 1 galaxies could be determined (e.g. Kaspi et al. 2000) although indications exist that this reverberation method yields systematically low values (Wandel 1999; Ho 1999). However, these variability studies reveal a strong correlation between the independently determined velocity dispersion and black hole mass

of

$$M_{\text{bh}} \simeq a_i \times 10^8 \mathcal{M}_{\odot} \left(\frac{\sigma}{200 \text{km s}^{-1}} \right)^{b_i} \quad (2.1)$$

with $a_i = (a_1, a_2, a_3) = (1.4, 1.2, 1.0)$ and $b_i = (b_1, b_2, b_3) = (4.8 \pm 0.5, 3.8 \pm 0.3, 4.0)$ corresponding to different fits of the correlation (i=1: Ferrarese & Merritt 2000, i=2: Gebhardt et al. 2000, i=3: Shields et al. 2003).

Chapter 3

AGN Surveys and Samples

3.1 The NUGA project

The NUClei of GALaxies (NUGA) project (García-Burillo et al. 2003a) is an international collaboration¹ that aims at establishing a high angular resolution ($\sim 0.5''$ - $1''$) and high sensitivity CO survey of twelve galaxies² with low luminosity Active Galactic Nuclei (AGN) in the Local Universe (distance < 80 Mpc or $z < 0.02$ equivalently). The sample covers the full sequence of activity types including Seyfert 1 and Seyfert 2 galaxies as well as LINERs and transition objects. NUGA is focussed on studying systematically the kinematics and distribution of molecular gas on pc-scales to improve the understanding of the different gas accretion mechanisms onto the AGN. The fueling processes are supposed to play a key role in powering the enormous activity observed in this type of galaxies.

3.1.1 Introduction

The transport of gas from the outer regions of the host galaxy down to the active nucleus requires a significant loss of angular momentum and the effective mechanisms still remain far from being understood. In contrast to large scales (≥ 3 kpc) where dynamical perturbations like galaxy collisions, mergers, or mass accretion (Heckman et al. 1986) as well as bars, spirals and their gravity torques (Combes 1988) enable the infall of gas, the processes responsible for removing angular momentum at small scales (\sim pc-kpc) escape still our comprehension. Various scenarios invoking nested mini-bars (e.g., Shlosman et al. 1993), mini-spirals (e.g., Martini & Pogge 1999), warped nuclear disks (Schinnerer et al. 2000a,b), and lopsidedness or other instabilities (Kormendy & Bender 1999; García-Burillo et al. 2000) have been proposed. So far, no survey of a significant number of active galaxies based on high angular resolution/high sensitivity data has ever been conducted to tackle these open questions. The first projects that aimed at mapping the CO content in a large sample of galaxies, not coercively including objects with AGN, have been carried out with Single-Dish telescopes thus lacking spatial resolution (e.g., Young et al. 1995, Kenney & Young 1988, Braine et al. 1993 and Casoli et al. 1996). However, recent interferometric surveys indeed exist, such as the NRO+OVRO survey (Sakamoto et al. 1999) and the BIMA-Song survey (Thornley et al. 1999), but they are focussed on *normal*, and not on active galaxies. Furthermore, the galaxies taken out of these surveys were only observed with a maximum angular resolution of $\sim 4''$ (corresponding to 300 pc at a distance

¹List of members: S. García-Burillo(1), F. Combes(2), A. Eckart(3), R. Neri(4), S. Leon(5), L.K. Hunt(6), A.J. Baker(7), L.J. Tacconi(7), E. Schinnerer(8), F. Boone(9), P. Englmaier(10) and M.Krips(3,4). (1): Observatorio Astronómico Nacional (OAN)-Observatorio de Madrid, Spain; (2): Observatoire de Paris, LERMA, France; (3): I.Physikalisches Institut, Universität zu Köln, Köln, Germany; (4) IRAM Grenoble, France; (5) Instituto de Astrofísica de Andalucía (CSIC), Granada, Spain; (6) Istituto di Radioastronomia/CNR, Sez. Firenze, Italy; (7) Max-Planck-Institut für extraterrestrische Physik (MPE), Garching, Germany; (8) National Radio Astronomy Observatory, Socorro, USA; (9) Max-Planck Institut für Radioastronomie (MPIfR), Bonn, Germany; (10) Astronomisches Institut, Universität Basel, Binningen, Schweiz

²This is referred to the *core sample*. In total, the NUGA supersample comprises ~ 30 objects. The not mentioned 18 remaining galaxies have already available or even published CO data. Except NGC 1068, they will not be taken into account in the following.

of 15Mpc) and a moderate sensitivity (detectability threshold of $> 180M_{\odot} \text{pc}^{-2}$). Surveys covering exclusively active galaxies can also be found in the literature (Heckman et al. 1989, Meixner et al. 1990, Vila-Vilaro et al. 1998, Tacconi et al. 1997, Baker 1998). Again, they are either hampered and constrained by insufficient angular resolution to confidentially analyse the small scale structures or, from a statistical point of view, the samples are simply too small to allow more general interpretations. Recent improvements in millimeter interferometry now allow qualitative studies of molecular gas emission in these galaxies with sub-arcsecond spatial resolution, high spectral resolution (\sim a few km s^{-1} per channel) and high sensitivity (detectability thresholds $\sigma_{\text{gas}} \sim$ a few tens $M_{\odot} \text{pc}^{-2}$). Thus, the CO observations for the NUGA survey have been conducted with the IRAM Plateau de Bure Interferometer (PdBI: Guilloteau et al. 1992), which currently provides the highest sensitivity and angular resolution for the study of the distribution and dynamics of molecular gas in the nuclei of these galaxies. Besides case by case analyses and simulations of each object (García-Burillo et al. 2003b, Combes et al. 2004 and Krips et al. 2004c, 2005a), the collected data will also be used for a first-order approach to a statistical study of how gas flows into nuclei and the different mechanisms that account for further accretion inward. The observations will also be complemented by N-body simulations of the gas or other developed analysis tools (e.g., Sempere et al. 1995; Englmaier & Shlosman 2000, Schinnerer et al. 2000a,b, García-Burillo et al. 2003, Combes et al. 2003 and Krips et al. 2004c, 2005a). The NUGA project is not restricted to the investigation of the gas, but observations at other wavelengths, mainly in the optical/NIR and radio domain, are carried out as well to obtain a complete picture of these galaxies. Besides information on the stellar content of the NUGA sources gained by HST and ground-based optical/NIR images, properties of the central engine via its radio continuum emission are investigated as well (Part V).

3.1.2 The NUGA sources

The NUGA galaxies were selected via the following criteria:

- The $^{12}\text{CO}(1-0)$ emission in the nuclei of all galaxies has been detected in single dish surveys made at FCRAO³, NRO⁴ and IRAM with T_a^* ranging from 40-140 mK.
- Galaxies are close enough to have a high spatial resolution in pc, namely $V_{\text{sys}} < 4000 \text{ km s}^{-1}$; typical spatial scale ranges from $1'' = 30 \text{ pc}$ - 100 pc for most of the galaxies (total range $1'' < 300 \text{ pc}$).
- Inclinations lie between $\sim 30^\circ$ and $\sim 60^\circ$ which enables the study of velocity fields and nuclear morphology. The declination of galaxies are $> 10^\circ$ in order to allow for almost circular beams.
- Optical and/or NIR high resolution images either with HST⁵ or with Adaptive Optics are available for all galaxies in the sample.

Some basic characteristics of the twelve core NUGA sources are summed up in Table 3.1. To increase the statistical means of the survey, the NUGA core sample has been also extended to a so-called NUGA supersample including galaxies which fulfill the above criteria as well but have already accessible interferometric data (e.g., NGC 1068). As summarized in Table 3.1, the core sample contains very different types of active galaxies, among them Seyfert as well as LINER galaxies and also transition objects.

3.1.3 First results of CO observations with PdBI

The integrated CO intensities from the first PdBI observations are shown in Fig. 3.1 to 3.3. Estimated CO fluxes (integrated) and molecular gas masses are presented in Table 3.2. The maps of the molecular gas distribution reveal very different morphologies (Table 3.3). Besides spiral arms (e.g., NGC 1961, NGC 3147, NGC 4826

³Five College Radio Astronomy Observatory

⁴Nobeyama Radio Observatory

⁵Hubble Space Telescope

Name	RA (J2000)	DEC (J2000)	v_{hel} [km s^{-1}]	i^a ($^\circ$)	Host type	Nuclear type
NGC1961	05:42:04.8	69:22:43.0	3934	49	SAB(rs)c	L2
NGC2782	09:14:05.1	40:06:49.0	2562	42	SAB(rs) pec	H
NGC3147	10:16:53.6	73:24:03.0	2820	26	SA(rs)bc	S2
NGC3627	11:20:15.0	12:59:29.0	727	62	SAB(s)b	T2/S2
NGC3718	11:32:35.3	53:04:01.0	994	60	Sa pec	L1.9
NGC4569	12:36:49.8	13:09:46.0	-235	62	SAB(rs)ab	T2
NGC4579	12:37:43.4	11:49:05.0	1519	37	SAB(rs)b	S1.9/L1.9
NGC4826	12:56:43.7	21:40:52.0	408	57	(R)SA(rs)ab	T2
NGC5953	15:34:32.4	15:11:39.0	1965	36	SAa pec	S2
NGC6574	18:11:52.2	14:58:55.0	2282	38	SAB(rs)bc	S
NGC6951	20:37:14.5	66:06:20.0	1424	35	SAB(rs)bc	S2
NGC7217	22:07:52.4	31:21:33.0	952	35	(R)SAB(rs)a	L2
<i>NGC1068^b</i>	<i>02:42:40.71</i>	<i>-00:00:47.8</i>	<i>1137</i>	<i>32</i>	<i>(R)SA(rs)b</i>	<i>S1.9</i>

Table 3.1: Basic properties of the NUGA sources. ^a $i \equiv$ inclination of the galaxy ^b does not belong to the *core* NUGA sample but to the *supersample*. H=HII-region, S = Seyfert, L=LINER and T=transition object.

(García-Burillo et al. (2003) and NGC 6951), we find rings (e.g., NGC 7217 (Combes et al. 2003)), bars (e.g., NGC 2782) and still compact components (e.g. NGC 1961, NGC 3147, NGC 7217) in each galaxy. Not only symmetric structures appear but also asymmetric ones are present as lopsided components (e.g., NGC 3718 (Krips et al. 2005a and Chapter 5). Some of the first results published for NGC 4826 (García-Burillo et al. 2003) and NGC 7217 (Combes et al. 2004) will be briefly presented in the following.

NGC 4826 is a counter-rotating LINER galaxy. The CO maps obtained with the IRAM PdBI reveal an inner molecular gas disk with a radius of ≤ 700 pc and a total molecular gas mass of $3.1 \times 10^8 \mathcal{M}_\odot$. The gas disk can be further divided into a lopsided nuclear disk of 40 pc radius with a mass of $\sim 0.5 \times 10^8 \mathcal{M}_\odot$, and into two spiral arms at different radii. The molecular gas dynamics appear to have $m=1$ perturbations caused by streaming motions. Two different types of these streaming motions are found: a *fast* and a *slow* wave. The first is traced back to a trailing wave starting outside the corotation within the inner $m=1$ instability while the latter is rather associated with the outer $m=1$ spiral indicating that a fueling of the AGN is rather unlikely and hampered at the current epoch. This and the fact that the observed gas properties, i.e. the $m=1$ perturbations, are also seen in the stellar components, suspect that the AGN in this galaxy does not generously accrete material at present.

NGC 7217 also contains a LINER nucleus. A nuclear molecular gas ring with a 0.8 kpc radius and molecular gas mass of $\sim 3 \times 10^8 \mathcal{M}_\odot$ is detected in the IRAM PdBI maps and found to reach farther out than the stellar/H α ring indicating that star formation must be stronger towards the inner edge. While the CO(1–0) emission reveals stronger emission in the circular ring, the CO(2–1) emission is more concentrated in the centre with a molecular gas mass of $\sim 5 \times 10^5 \mathcal{M}_\odot$ correlated to circumnuclear ionized gas and a spiral dust lane. N-body simulations carried out by Combes et al. (2004) favours a bulge-dominated model, causing a mild oval distortion, to explain the nuclear ring. In these scenarios, only a weak bar was developed with only a short life time so that it is not visible anymore. Star formation, however, was rather concentrated at the gas density peaks at the inner edge of the ring explaining the observed thinner stellar ring. Again, no clear indications are found for an ongoing accretion onto the nucleus but rather evidences for an outward flow of the gas in the ring.

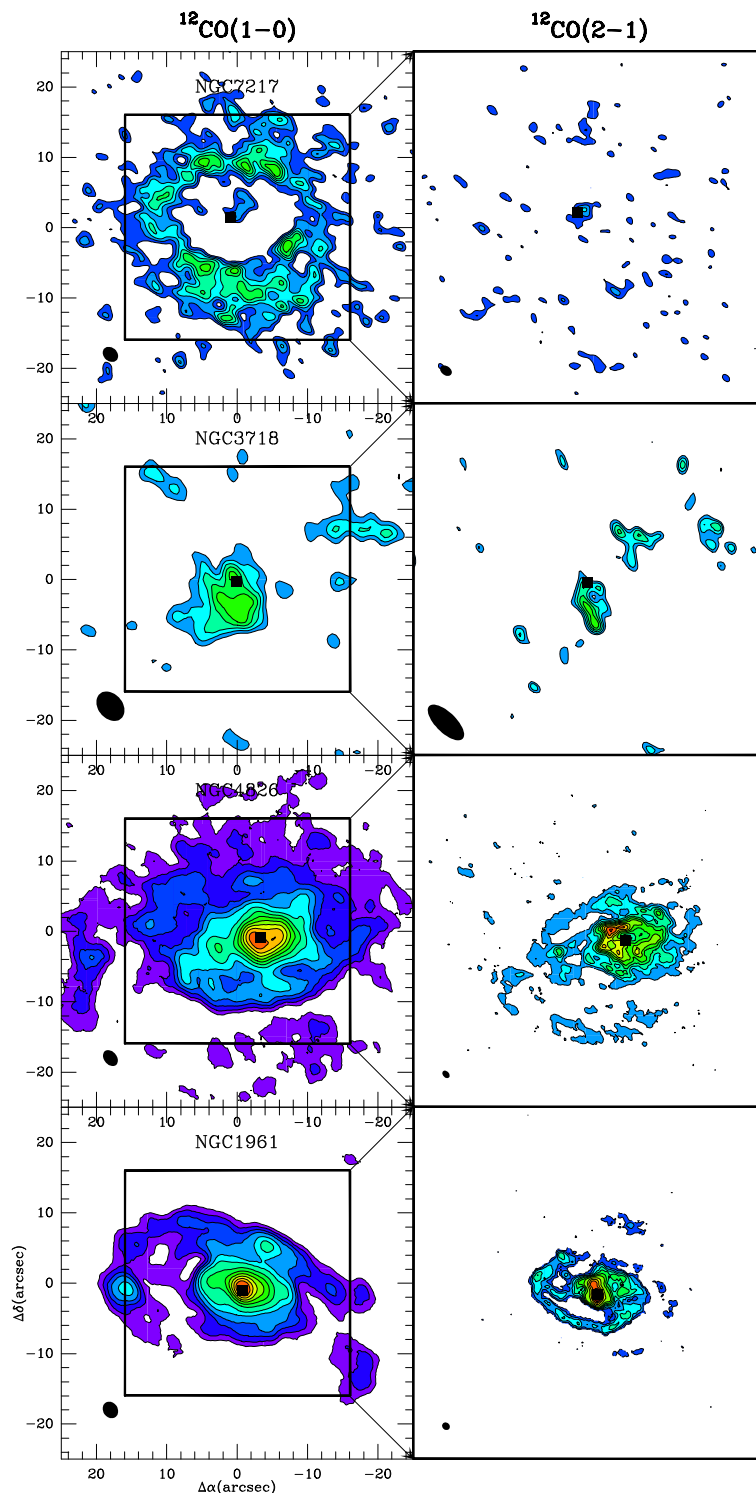


Figure 3.1: Velocity integrated CO(1–0) (*left*) and CO(2–1) (*right*) maps of 8 NUGA sources observed with PdBI. The respective synthesized beams are shown in the lower left corner of each map. Images taken from García-Burillo et al. (2004c). The boxes left mark the field of view of the images on the right. Please note that the images of NGC 3718 have significantly improved due to a revised data reduction and thus this image of NGC 3718 differs slightly from those shown in Chapter 5.

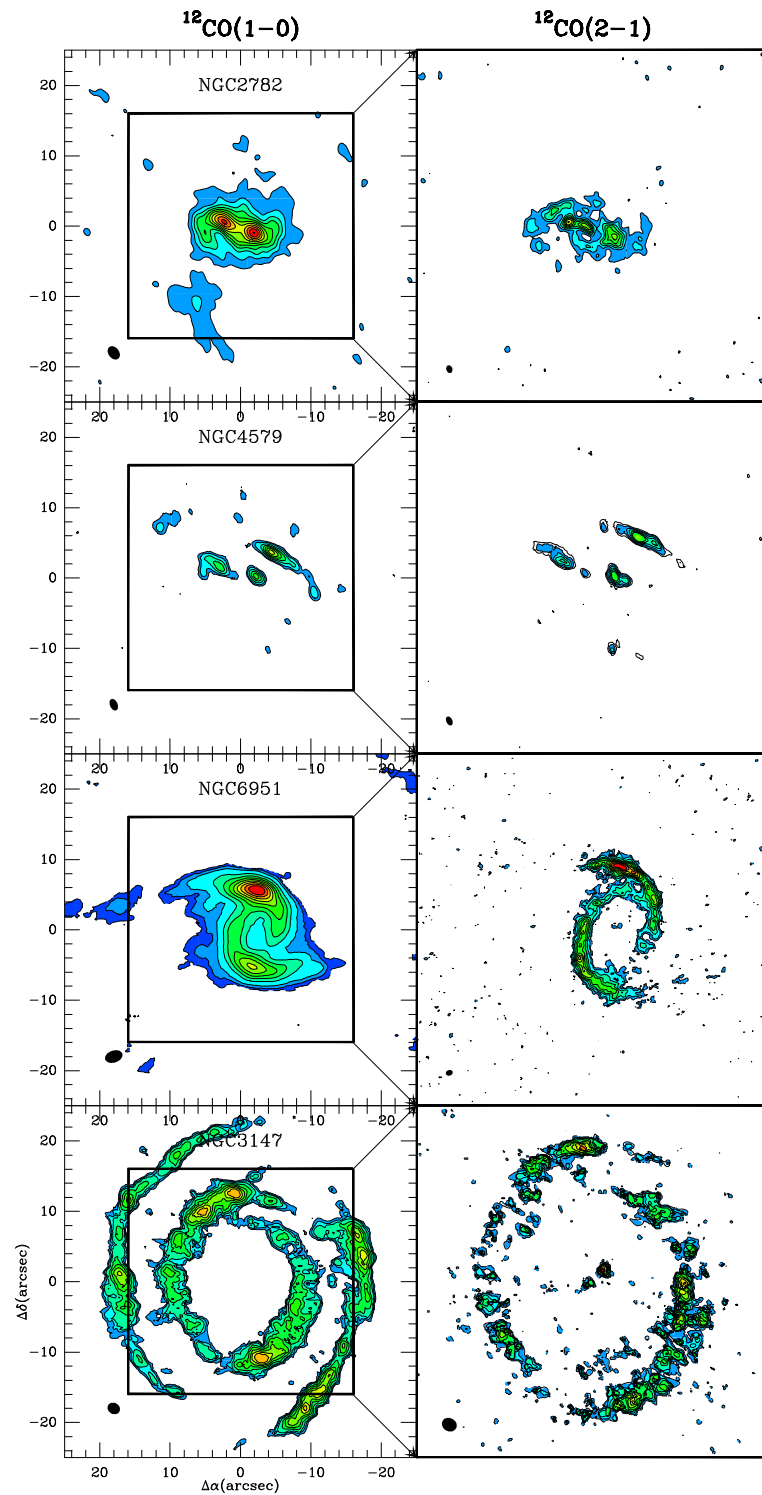


Figure 3.2: Continuation of Fig. 3.1.

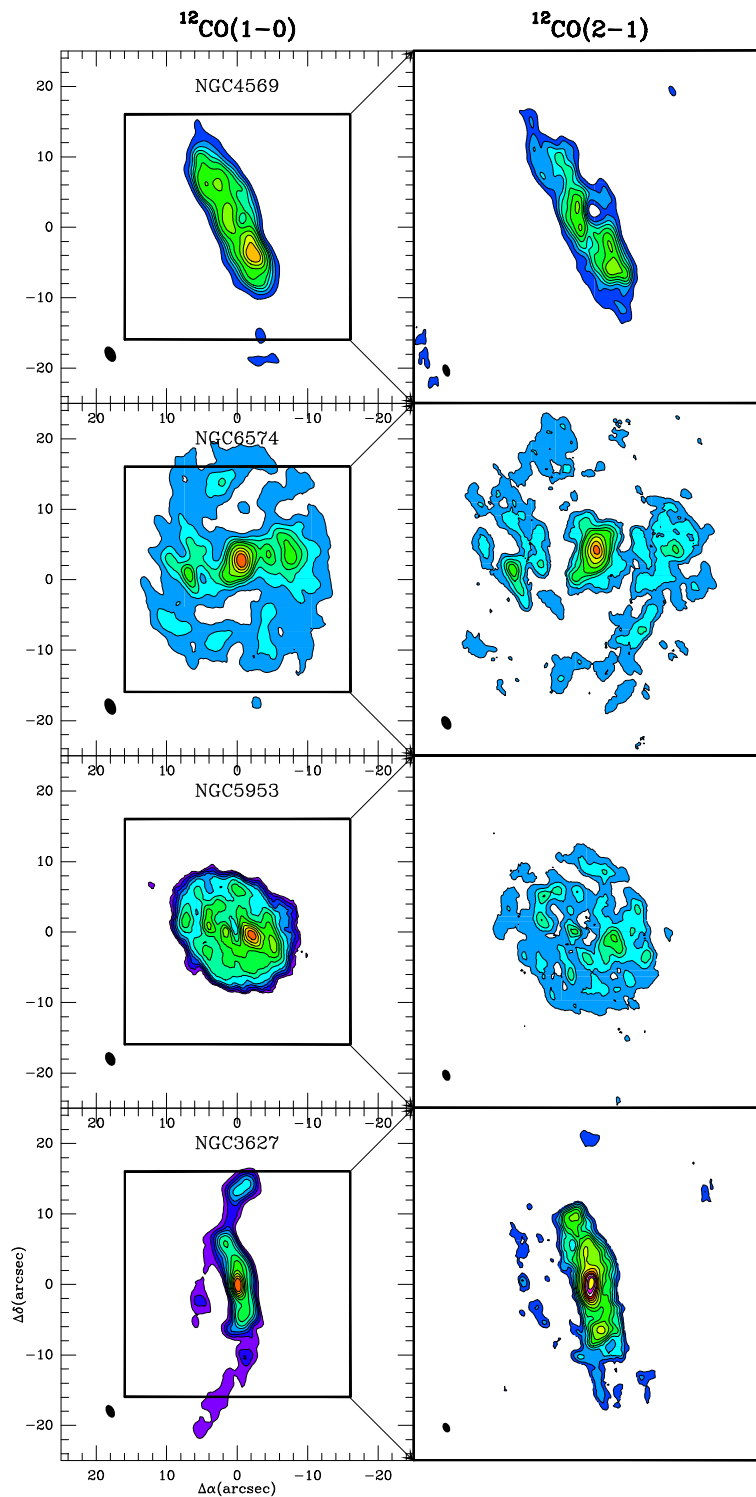


Figure 3.3: Continuation of Fig.3.2.

Name	$\bar{S}_{\text{CO}(1-0)} \Delta v$ (Jy beam $^{-1}$ km s $^{-1}$)	D (Mpc)	\bar{M}_{gas} ($10^8 \mathcal{M}_{\odot}$)
NGC 1961	170	52	53
NGC 2782	60	35	8
NGC 3147	90	38	15
NGC 3627	-	-	-
NGC 3718	10	15	0.1
NGC 4569	-	-	-
NGC 4579	40	20	2
NGC 4826	160	5	0.5
NGC 5953	-	-	-
NGC 6574	-	-	-
NGC 6951	180	19	8
NGC 7217	60	13	1
<i>NGC1068^a</i>	670	14	10

Table 3.2: Velocity integrated CO(1–0) intensities and molecular gas masses of the NUGA core sources from PdBI observations (summed up over the respective emission region in the PdBI maps). The galaxies of figure 3.3 have so far only available integrated maps without any further information on fluxes etc. since their PdBI observations were only recently finished. Please note that missing short-spacing effects and thus possibly missing extended flux have not been taken into account here (cf. Chapter 5, Chapter 10 and Table 10.2). ^a from the extended NUGA sample.

Name	gas morphology and modes
NGC 1961	m=1 inner and outer spirals, compact unresolved source on AGN
NGC 2782	m=2 inner spiral and gaseous bar centered on AGN
NGC 3147	nested m=2 spirals and compact unresolved source on AGN
NGC 3627	bar and spiral structure
NGC 3718	warped disc and inner lopsided structure (see Chapter 5 and Krips et al. 2005b)
NGC 4569	barred and asymmetric
NGC 4579	m=1 lopsided instability, not linked with AGN
NGC 4826	2 m=1 spirals and inner lopsided instability (García-Burillo et al. 2003)
NGC 5953	disk-like asymmetric structure
NGC 6574	spirals, symmetric structure
NGC 6951	m=2 spiral and hole near the AGN
NGC 7217	gas(+stellar) ring and compact unresolved source on AGN (Combes et al. 2003))
<i>NGC1068^a</i>	<i>m=2 outer spirals, bar and nuclear ring (Schinner et al. 2000a,b and Chapter 6)</i>

Table 3.3: Molecular gas morphology of the observed NUGA core sources. Classification partially based on talk given by García-Burillo during a NUGA Meeting in 2002. ^b from NUGA supersample. In terms of N-Body simulations, the modes m (i.e, the number of spiral arms) are correlated with the resonance frequencies between the rotation frequency of a particle (Ω) and the epicycle frequency κ . If the pattern of the potential (e.g., spiral arms), in which the particle is captured, has a pattern speed of Ω_p than resonances will occur at $\Omega=\Omega_p$ (corotation) and $\Omega - \Omega_p = \pm\kappa/m$ (Lindblad resonances). Two spirals would mean m=2, and is the most general case. For a more detailed description see Combes et al. (1995).

3.2 The Cologne nearby QSO sample

3.2.1 Introduction

The ~ 60 sources of the Cologne nearby QSO sample were selected from the Hamburg/ESO survey for bright QSOs and the Véron-Cetty and Véron quasar catalogue via their low redshifts of $z < 0.06$ providing the possibility of observations on the smallest available angular scales and the accesibility of several important diagnostic lines in the NIR (e.g., the CO(2-0) rotation vibrational band head absorption line). A multi-wavelength study of these objects will add - as a final goal - to a systematic study of the different mechanisms of gas fueling into active galactic nuclei (AGN). Together with the NUGA PdBI survey containing Seyfert and LINER galaxies (García-Burillo et al. 2003a,b, Combes et al. 2004, Krips et al. 2005b) this study will span the whole activity sequence of AGN. Especially, the role of nuclear embedded bars, rings, spirals as well as mini-spirals, warps and micro-warps in the fueling process is an important and interesting issue in order to investigate a possible link between different nuclear disk morphologies and activity types.

3.2.2 Observations

Almost 30 objects were observed with the SEST telescope resulting unfortunately in a low detection rate of only $\sim 10\%$ (Bertram et al. in prep.). This is most likely due to uncertainties in the given redshifts which are based on optical observations. Two QSOs, HE 1029-1831 and HE 1136-2304, were additionally observed with the BIMA and IRAM PdBI arrays but only the first one could be detected and mapped. HE 1136-2304 most likely lacks an exact redshift, too. The IRAM PdBI observations will be presented and discussed in Chapter 7. As complementary observations, also MPE⁶ SHARP⁷ data are available which are currently being analysed (Fischer et al. in prep.). These data will allow to constrain further the classification of these objects.

⁶Max-Planck institute for Extraterrestrial physics

⁷NIR Speckle camera at the New Technology Telescope (NTT) operated by the European Southern Observatory (ESO) in La Silla, Chile.

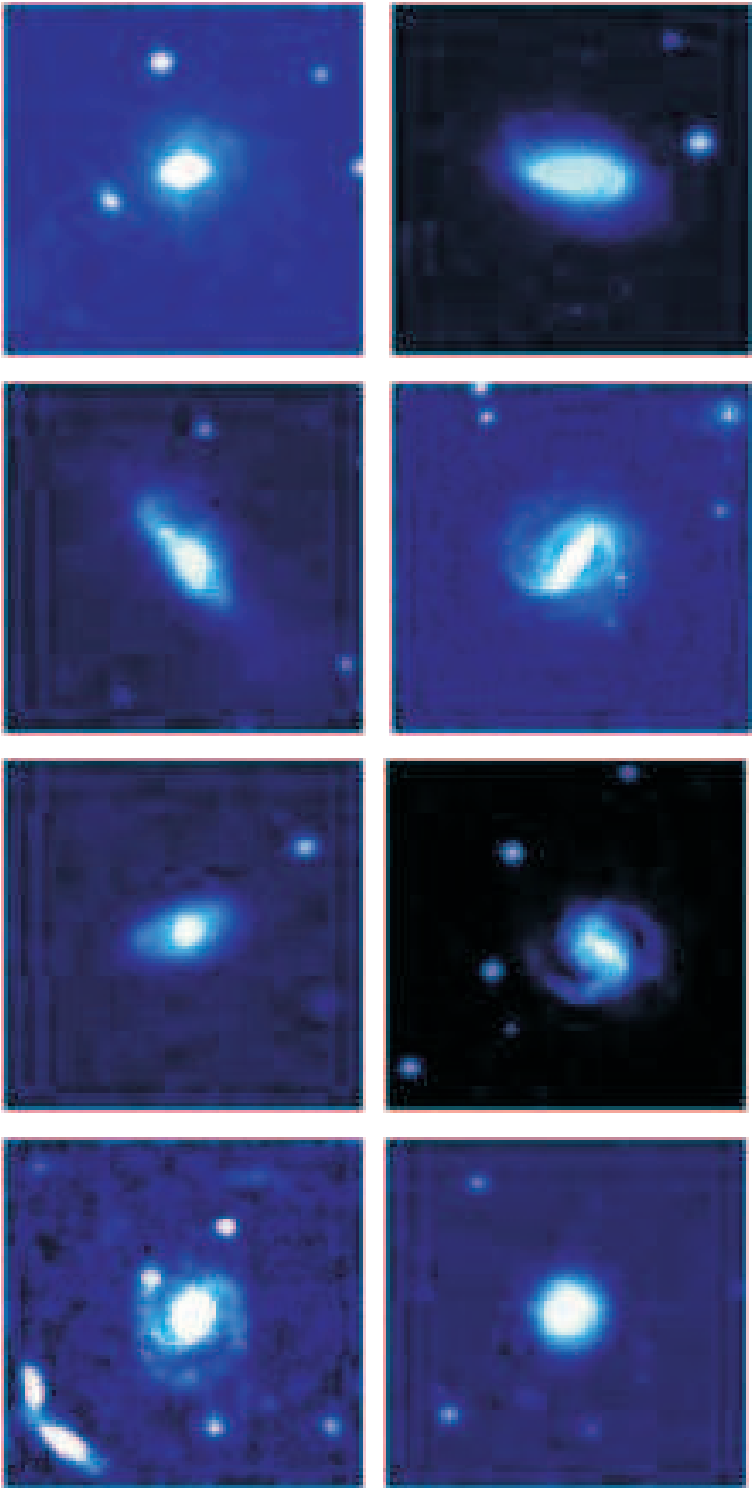


Figure 3.4: Optical images of some selected QSOs taken from the Cologne nearby QSO sample.

Part II

Observational techniques at radio and mm wavelengths

Chapter 4

Instruments at radio and mm wavelengths

Radiation at radio to mm wavelengths is mainly gathered with heterodyne and bolometric receivers. The first type down converts the signal to a lower frequency with a local oscillator (from ~ 1 -100GHz to ~ 100 -600MHz approximately) while the latter directly detects the signal at the observed frequency with a very large bandwidth. Also the collecting areas can be divided into two different systems: single dish telescopes and interferometers. While the first are very limited in angular resolution ($\geq 10''$) the latter provide angular resolutions down to $0.001''$. Freely steerable telescopes can only be built up to a diameter of ~ 100 m. Antennae with larger diameters undergo too strong gravitational deformations so that the requirements for the surface accuracy can no longer be fulfilled. Thus, several smaller antennae are connected with each other to synthesize one big telescope. The longest baseline, i.e. separation between the respective telescopes, determines then the angular resolution. Both types of instruments will be shortly presented in the following. A more detailed description can be found in Krips (2001; diploma thesis), Perley et al. (1994), Thompson et al. (1986) and the IRAM interferometer school.

4.1 Single-Dish telescopes

Based on diffraction theory, the angular resolution of a single dish telescope, defined as the full width at half maximum (FWHM) of the peak power of the antenna beam (θ_{FWHM}), is characterized through the telescope diameter D and the observed wavelength λ as following:

$$\theta_{\text{FWHM}} = 1.03 \times \frac{\lambda}{D} \quad (4.1)$$

In the simplest case, the telescope is a Hertz dipole but parabolic dishes are favoured to increase the collecting area. Following the reciprocity theorem, telescopes can be treated as transmitting system as well as a receiving device. This facilitates an analytical approach. The power is then given by:

$$P = A(\nu, \theta, \phi) I(\nu, \theta, \phi) \Delta\nu \Delta\Omega \quad (4.2)$$

where $A(\nu, \theta, \phi)$ is the effective collecting area, i.e. reception or power pattern, $\Delta\nu$ the bandwidth, $I(\nu, \theta, \phi)$ the source brightness and $\Delta\Omega$ the solid angle. Normalizing $A(\nu, \theta, \phi)$ with A_0 , i.e. $\mathcal{A} = A(\nu, \theta, \phi)/A_0$, the beam solid angle can be defined as:

$$\Omega_A = \int \int_{\text{all sky}} \mathcal{A}(\nu, \theta, \phi) d\Omega \quad (4.3)$$

A_0 is the response at the centre of the main lobe of $A(\nu, \theta, \phi)$ and is often called the effective area in the case of a parabolic telescope while $A(\nu, \theta, \phi)$ is the physical area ($=\pi(D/2)^2$). Here, the ratio between both is called the

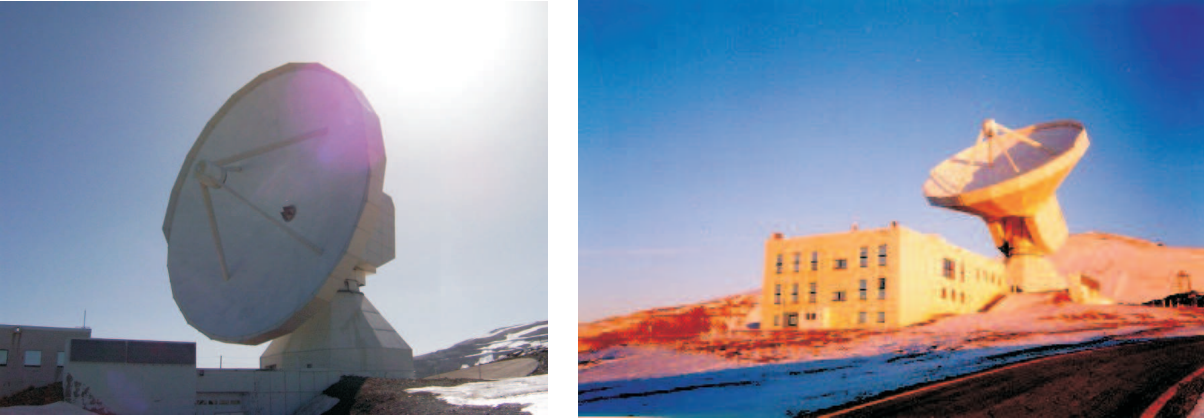


Figure 4.1: Pictures of the IRAM 30m telescope at the Pico Veleta in the Sierra Nevada, Spain.

aperture efficiency η . A fundamental relation between the effective area and the beam solid angle is given by the Antenna theorem (Kraus 1986):

$$A_0 \Omega_A = \lambda^2 \quad (4.4)$$

This relationship implies that an improvement of sensitivity by increasing the collecting area forfeits at the same time field of view.

4.1.1 IRAM 30m telescope

The IRAM 30m telescope is located at the Pico Veleta in the Sierra Nevada in Spain and has been used in the framework of this PhD-thesis. As its name indicates, the diameter amounts to 30m. It is operated at frequencies 80-115.5 GHz, 130-183 GHz and 197-266 GHz or 241-281 GHz, depending on the used receiver. The maximum bandwidth available can reach 2GHz. Besides normal heterodyne receivers also a bolometer (MAMBO) is accessible and in the near future also a polarimeter. The angular resolutions range from $\sim 10''$ at 1 mm to $\sim 20 - 30''$ at 3 mm. The weather conditions are quite stable during the winter period but are less stable during summer due to an increased amount of water vapor in the atmosphere.

4.2 Interferometers

An interferometer consists of several small telescopes which either are locally mounted with baselines of a few hundred meters/kilometers or spread over several continents (Very Long Baseline Interferometry, VLBI) with baselines up to several thousands of kilometers. An interferometer does not directly measure the intensity distribution $I(x, y)$ but its Fourier transformation $V(u, v)$, where x and y are coordinates in the sky and u and v the coordinates of the projected baseline for each telescope pair seen from the source (see Fig4.2). The intensity distribution can then be determined by an inverse Fourier transformation:

$$I(x, y) = \iint e^{-2\pi i(xu+yv)} V(u, v) du dv \quad (4.5)$$

Theoretically, the integrals have to be taken from $-\infty$ to $+\infty$, but practically, the integration interval corresponds only to the solid angle of the primary beam. In practice, the integral has to be transformed into a discrete sum since an interferometer has always a limited number of telescope so that the uv -plane is only discretely sampled. The so derived intensity distribution does not yet represent the pure structure of the target since it is still convolved with

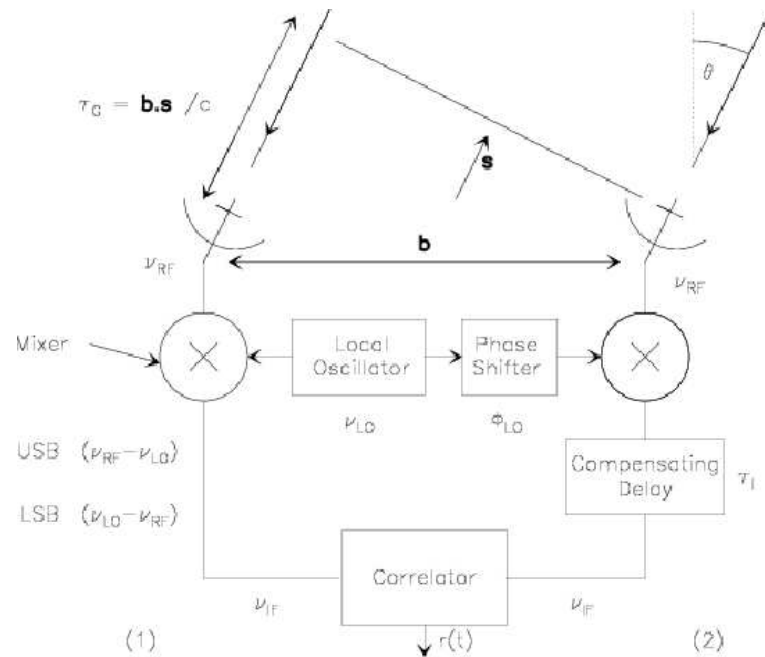


Figure 4.2: Schematical picture of a two-element interferometer (taken from the IRAM Interferometry School).

the so called dirty beam of the interferometer. The latter corresponds to the response of the interferometer to a point source which would result in a constant visibility function. Consistent with the dirty beam, $I(x, y)$ is called dirty map at this stage. To obtain a cleaned map, $I(x, y)$ has to be deconvolved with the dirty beam.

A significant disadvantage of the discrete sampling of the uv -coverage are short-spacing effects. The smallest available baseline of an interferometer is always limited by the size of the used telescopes. Since the longest baseline determines the angular resolution of the instrument, i.e. the smallest resolvable size of the target, the smallest baseline corresponds equivalently to the largest size that can be seen with an interferometer. That means, all structures which are bigger than the sizes characterized by the smallest baseline are missed by the interferometer. An increase of angular resolutions always goes along with a loss of extended and diffuse emission. One method to reduce possible artefacts that might occur in the interpretation of interferometric data is to add the missing short spacings with data obtained with a Single-Dish telescope, i.e. the small baseline are filled up with the missing information. Such a method has been applied in the case of NGC 3718 and will be presented in more detail in Chapter 5.

4.2.1 IRAM PdBI

The IRAM Plateau de Bure Interferometer (Fig.4.3) is located at the Plateau de Bure (2552m above sealevel) in the french Alps, almost 100 km away from the operating institute (Institut for Radio Astronomy at Millimeter wavelength, or briefly IRAM) in Grenoble, France. It consists of 6 antennae meanwhile and can observe frequencies in the range of 82-115 GHz (3 mm) and 205-245 GHz (1 mm) simultaneously. A third (heterodyne) receiver operating at ~ 2 mm is also planned for the near future. The longest possible baselines amount at the moment to 408 meters but an extension of the array has been decided already. Angular resolutions range from $\sim 8''$ down to $\sim 0.5''$ depending on the frequency and array configuration, currently making this instrument the most sensitive interferometer with the highest available angular resolution at these frequencies. Most of the data analysed in this PhD thesis were observed with the IRAM PdBI comprising also a one year stay at IRAM with experiences as Astronomer on Duty at the PdBI.

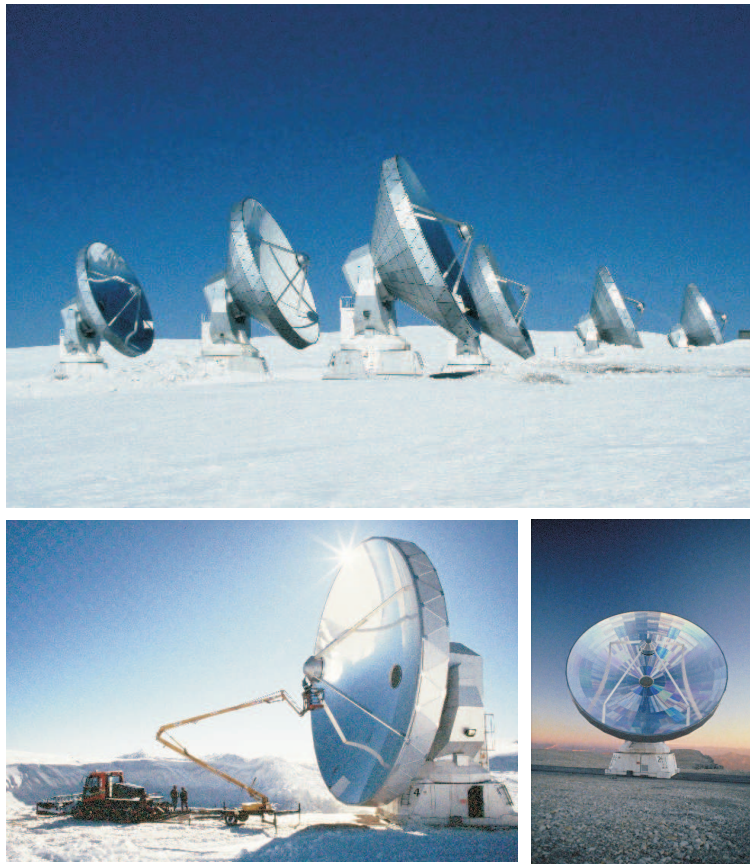


Figure 4.3: Pictures of the IRAM Plateau de Bure Interferometer in the french Alps.

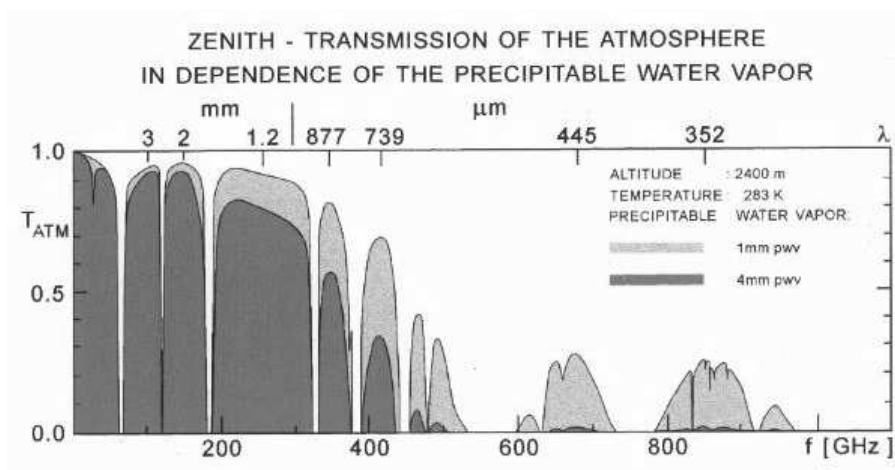


Figure 4.4: Transparency of the earth's atmosphere at different wavelengths (taken from the MPIfR homepage).



Figure 4.5: Picture of the distribution of the MERLIN telescopes (taken from the MPIfR homepage).

4.2.2 MERLIN

MERLIN means Multi-Element Radio Linked Interferometer Network and consists of several radio telescopes spread over the United Kingdom (Fig.4.5). The longest baselines reach up to 217 km providing angular resolution down to $0.05''$. The instrument is operated at frequencies from 151 MHz to 24 GHz corresponding to cm wavelengths. A part of the radio observations of the NUGA sources were conducted with MERLIN (see Chapter V). Contrary to mm-interferometers, radio-, i.e. cm-interferometers can be also located at sealevel since radio emission is much less affected by atmospheric absorption (see Fig.4.4).

4.2.3 VLBI/EVN

VLBI, i.e. Very Long Baseline Interferometry, is a technique that synthesizes radio telescopes spread over the whole world thus resulting in baselines of thousands of kilometers (Fig.4.6). At radio wavelengths VLBI provides so far the highest available angular resolutions down to $0.001''$. EVN is a smaller part of VLBI, called the European VLBI Network with telescopes only in Europe and Asia. Some of the participating antennae are shown in Fig.4.6. A critical point in VLBI is to acquire the data synchronously since they cannot be stored instantaneously to the same medium (in the past years large magnetic tapes were used but since this year the storage went over to hard-discs due to significantly increased storage capabilities). Thus, also exact time information have to be written onto the storage medium. This is generally realised with maser clocks.

4.3 Calibration of interferometric data

The complex visibility function $V(\nu, t) = V_0(\nu, t) e^{i\phi(\nu, t)}$ is measured as phase $\phi_V(\nu, t)$ and amplitude $V_0(\nu, t)$ in a two-element interferometer. In the case of a point source, $V_0(\nu, t)$ is expected to be constant and $\phi_V(\nu, t)$ should be zero, i.e. a complex, extended intensity distribution of a target is characterized by variations of $\phi_V(\nu, t)$ and $V_0(\nu, t)$. However, since real observations are never carried out with ideal instruments and under ideal conditions, $\phi_V(\nu, t)$ and $V_0(\nu, t)$ will also be different from zero or not constant due to atmospheric fluctuations, receiver noise and other causes. For an extended source, the intrinsic shapes of $\phi_V(\nu, t)$ and $V_0(\nu, t)$ corresponding to characteristics of the targets are thus washed out if not totally superimposed. Thus, atmospheric and instrumental effects have to be removed from the observed source data via adequate calibration methods. Also, an interferometer can

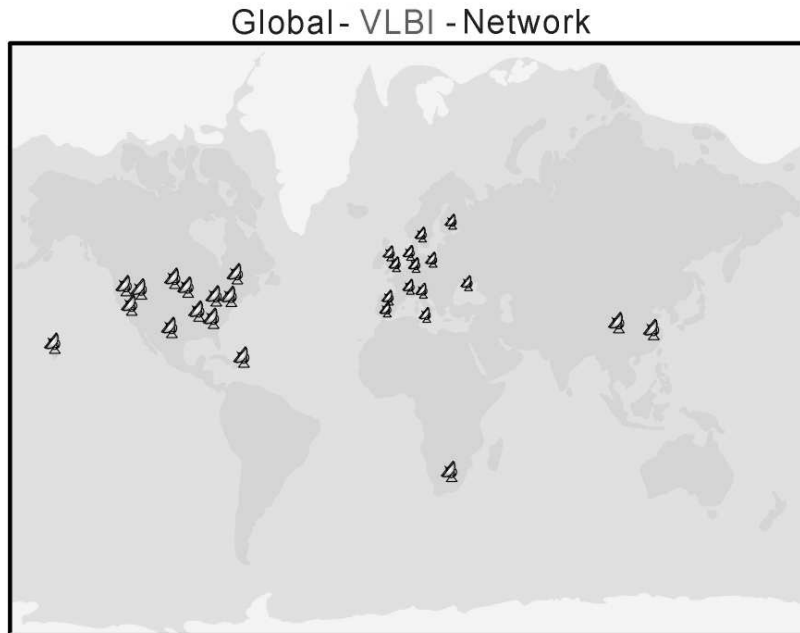


Figure 4.6: Picture of the distribution of the VLBI telescopes (taken from the MPIfr homepage).

only measure relative amplitudes, not absolute ones. Therefore, a so called calibrator is alternately observed with the target during an observation run. One has to distinguish between two different calibrators: phase and amplitude calibrators correcting artefacts that occur time dependent and so called bandpass calibrators which correct effects depending on frequency. The most important difference between both is that phase and amplitude calibrators must be in the vicinity of the target (within a few degrees) to assure a switching between the target and calibrator with a minimum of time loss so that almost equivalent conditions are guaranteed while a bandpass calibrator can also be located farther away. Both types of calibrators should be as strong as possible so that in a minimum of time good signal to noise ratios are achieved. Preferred calibrators at PdBI but also for VLBI are pointlike, strong quasars, such as 3C273 and 3C84 for instance. The alternating observations of a target and a pointlike calibrator allow to fit a curve to the calibrator points and subtract them from the source data assuming that conditions did not significantly change between two calibrator points. A more detailed description of the calibrations process can be found in Krips 2001 (diploma thesis) or the IRAM interferometer school for instance.

Part III

Observations I: Molecular gas traced by CO

Chapter 5

NGC 3718

In this chapter, the first interferometric observations of CO(1–0) and CO(2–1) line emission from the warped LINER NGC 3718 (Krips et al. 2004c, 2005a) will be presented, obtained with the IRAM Plateau de Bure Interferometer (PdBI). This LINER type 1.9 galaxy has a prominent dust lane and on kiloparsec scales, a strongly warped atomic and molecular gas disk. The molecular gas is closely associated with the dust lane across the nucleus and its kinematic center is consistent with the millimeter continuum AGN. A comparison of our interferometric mosaic data, which fully cover the ~ 9 kpc warped disk, with a previously obtained IRAM 30 m single dish CO(1–0) map shows that the molecular gas distribution in the disk is heavily resolved by the PdBI map. On the nucleus the interferometric maps alone contain less than one third of the single dish line flux, and the overall mosaic accounts for about a tenth of the total gas mass of $\sim 2.4 \times 10^8 M_{\odot}$. After applying a short-spacing correction with the IRAM 30 m data to recover the missing extended flux, in total six main source components are found within the dust lane: one associated with the nucleus, four symmetrically positioned on either side at galactocentric distances of about 1.3 kpc and 4.0 kpc from the center, and a sixth on the western side at ~ 3 kpc with only a very weak eastern counterpart. In the framework of a kinematic model using tilted rings, the five symmetric source components are interpreted as locations of strong orbital crowding. Furthermore, the warp is found to appear not only on kpc scales down to ~ 500 pc, but continues down to radii of ~ 100 pc. Besides the sixth feature on the western side, the lower flux (a factor of ~ 2) of the eastern components compared to the western ones indicates an intrinsic large scale asymmetry in NGC 3718 that cannot be explained by the warp. Indications for a small scale asymmetry are also seen in the central 600 pc. These asymmetries might be evidence for a tidal interaction with the companion galaxy (*large scales*) and gas accretion onto the nucleus (*small scales*). Our study of NGC 3718 is part of the NUClei of GALaxies (NUGA) project that aims at investigating the different processes of gas accretion onto Active Galactic Nuclei (AGN) (Section 3.1).

The chapter is outlined as following: Section 5.2 describes the observations. In section 5.3, the results from the observations are presented. A kinematic model is outlined in section 5.4. The chapter finishes with a discussion.

5.1 Introduction

Knowledge of the distribution and kinematics of the circumnuclear molecular gas in active galaxies is essential for understanding the fueling of the central engine and the role of gas and dust in obscuring the active nucleus (AGN). As described in Chapter 3.1, the NUGA project aims at analysing in a case by case study as a first step the molecular gas properties in the host galaxies of each of the NUGA sources. One of these objects is NGC 3718 (Fig. 5.1), a peculiar Sa galaxy at a distance of 15 Mpc (Pott et al. 2004; Schwarz 1985). Together with its companion NGC 3729 it belongs to the Ursa Major group. So far, there were only very weak signatures of a gravitational interaction between these two galaxies. A large warped dust lane runs across the entire stellar bulge of NGC 3718 having a width of $< 2''$ at the center and diverging into several smooth filaments across the bulge ($\sim 1''$ corresponds

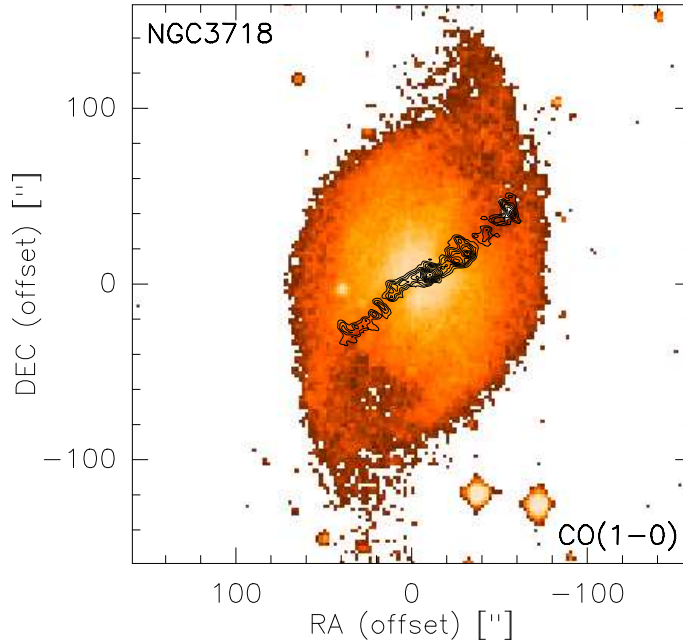


Figure 5.1: Optical image (taken from the Digital Sky Survey (DSS) survey) superimposed with the integrated CO(1–0) contours (black) obtained at the PdBI, with added short spacings from the IRAM 30 m telescope (see section 5.4.2 & 5.4.3). Contour levels as in Fig. 5.13.

to ~ 64 pc for NGC 3718). At a radius of about $1.5'$ from the center, the dust lane bends by almost 90 degrees towards the north and south. This warp signature is also observed in the cold gas distribution, with the HI line emission tracing it out to a radius of more than $6'$ (24 kpc) and CO line emission tracing it towards the center ($\sim 20''$: Pott et al. 2004). The outer parts of the warp were kinematically modeled by Schwarz (1985), while the inner parts down to $\sim 20''$ were modelled by Pott et al. (2004).

NGC 3718 is classified as a LINER of type 1.9 galaxy (Ho et al. 1997). Weak, broad H α emission with FWHM 2350 km s^{-1} is emitted from the nucleus as well as strong [O I] $\lambda=6300\text{\AA}$ with FWHM 570 km s^{-1} indicative of a hidden AGN (Filippenko et al. 1985; Ho et al. 1997). So far no ultraviolet emission has been detected towards NGC 3718 (Barth et al. 1998), probably due to obscuration of the nucleus by dust, whereas a radio source has been confirmed at the position of the nucleus (Burke & Miley 1973; Nagar et al. 2002). In the next sections, the single field and mosaic data obtained with the PdBI at an angular resolution of $\sim 4''$ are analysed.

5.2 Observations

NGC 3718 was observed with the IRAM PdBI in two different modes: *central pointing* (one single field on the center) and *mosaic* (seven fields across the dust lane).

5.2.1 Central pointing

During winter 2000/2001, the CO(1–0) and CO(2–1) lines were mapped in a single field centered at the position of the AGN radio source in NGC 3718, i.e., $\alpha_{2000} = 11^{\text{h}}32^{\text{m}}34.840^{\text{s}}$ and $\delta_{2000} = 53^{\circ}04'04.90''$ (see section 5.3.1.1). The PdBI was at this time deployed in the CD set of configurations with 5 antennae. The bandpass calibrator was 3C273, while the phase and amplitude calibration were performed on 1150+497. Fluxes have been calibrated relative to CRL618 and MWC349. The frequencies were centered on the redshifted $^{12}\text{CO}(1-0)$ line in the USB at

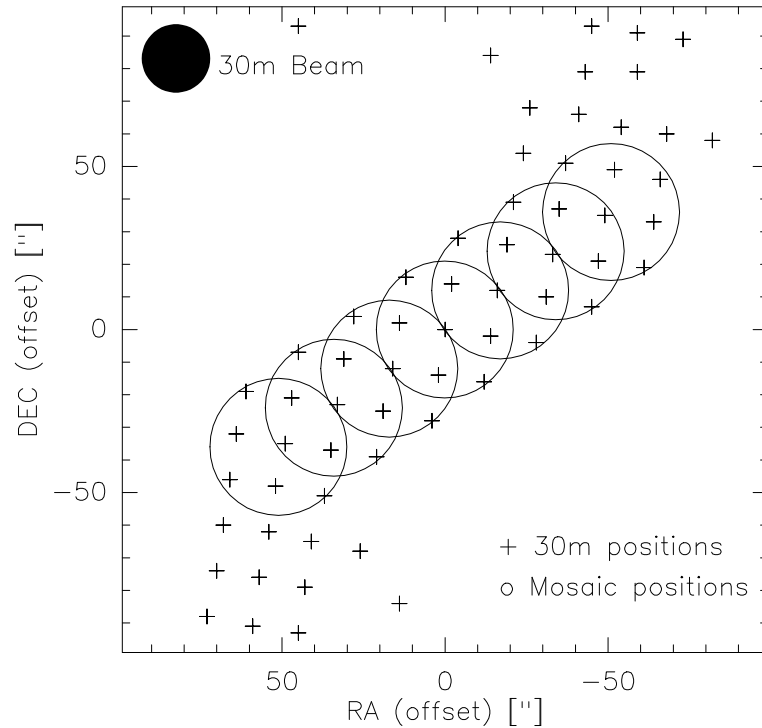


Figure 5.2: Positions of the IRAM 30 m observations are plotted with black crosses, and mosaic fields of the PdBI observations are shown as circles indicating the $42''$ primary beam size for each observing field. The 30 m beamsize is shown in the upper left.

3 mm and on the redshifted $^{12}\text{CO}(2-1)$ line in the LSB at 1 mm. For each line, the total bandwidth was 580 MHz and the spectral resolution 1.25 MHz. The integration time for the central pointing amounts to ~ 8 hr on source. This gives a point source sensitivity of about ~ 7 mJy (~ 16 mJy) in channels of 1.25 MHz width at 3 mm (1 mm). The noise is consistent with a system temperature corresponding to a range of water vapor of 4-10 mm. The GILDAS software packages were used to reduce and map the data (Guilloteau & Lucas 2000). The synthesized beams are $4.7'' \times 3.5''$ at 41° at 3 mm and $2.6'' \times 2.0''$ at 45° at 1 mm.

5.2.2 Mosaic

During winter 2001/2002, a mosaic of NGC 3718 was obtained with the PdBI. Seven mosaic fields of the $\text{CO}(1-0)$ emission were repeatedly observed with six antennae or a subset in C and D configurations. These sample the molecular gas emission along the dust lane, across a region of ~ 12 kpc extent that was previously mapped with the IRAM 30 m by Pott et al. 2004 (Fig. 5.2; see also Hartwich et al. 2002 and Krips et al. 2003). The central field of the mosaic was set to the same position specified in section 5.2.1, and the separation between the pointings was $21''$, corresponding to half the primary beam size. The bandpass was calibrated on 3C84, 3C273, or 0923+392 with an accuracy of about 5%. Together with 1150+498, the latter source was also used as phase and amplitude calibrator. They were observed every 20 minutes. To derive the absolute fluxes of the calibrators and the target source, values for each observing epoch were bootstrapped via a standard IRAM flux monitoring program, yielding an accuracy of $\sim 10\%$ at 3 mm and $\sim 20\%$ at 1 mm. The spectral resolution was set to 1.25 MHz at 114.89 GHz, giving a contiguous bandwidth of 580 MHz. The integration time per field amounted to ~ 2.4 hr. The resulting point-source sensitivity is ~ 17 mJy for a bandwidth of 1.25 MHz and 5 antennae at 3 mm. The noise is consistent with a system temperature corresponding to a range of water vapor of 4-10 mm. Even if the $\text{CO}(2-1)$ line had been

	2000/01		2001/02
	cont@ 3 mm	cont@ 1 mm	cont@ 3 mm
R.A. (hhmmss)	11:32:34.852	11:32:34.878	11:32:34.830
$\Delta\alpha$ (s) ^a	0.003	0.005	0.01
Dec (^o : ['] : ^{''})	53:04:04.51	53:04:04.3	53:04:04.2
$\Delta\delta$ (") ^a	0.06	0.1	0.1
peak flux (mJy beam ⁻¹)	9.4±1.6	9.5±0.7	6.7±0.6

Table 5.1: Interferometric positions and fluxes of the continuum emission at 1 mm and 3 mm from the single field data set (2000/01) and the central field of the mosaic observations from 2001/02 (*right column*). The difference in the 3 mm flux densities between the first epoch and the second is discussed in the text (section 5.3.1.1). ^a errors on derived source position.

simultaneously observed in mosaic mode, the mosaic fields are only usable as single and separate fields since the separations of the mosaic fields are too large at 1 mm (primary beam size at 1 mm: $\sim 21''$). Also the sensitivity is too poor in most of the fields resulting in no detection of the CO(2–1) line except in the central field.

5.3 The data

5.3.1 Central emission

5.3.1.1 Continuum

Before combining the central pointing observation (single-field) with the new central field from the mosaic observations, the continuum for both data sets at 1 mm and 3 mm has been independently determined from the line free channels (3 mm & 1 mm: channels at velocities $< -300 \text{ km s}^{-1}$ and $> 300 \text{ km s}^{-1}$). In both data sets at 3 mm faint continuum emission is detected in the central region of NGC 3718, while at 1 mm only the single-field data set reveals continuum emission due to sensitivity limitations (also concentrated in the center; see Fig.5.3). At 3 mm as well as at 1 mm, the continuum emission is point-like rather than extended in the respective beams (compare Table 5.1). The continuum declines by $\sim 30\%$ between the two observing epochs at 3 mm (see Table 5.1). Assuming an upper limit of $3\sigma = 7.5 \text{ mJy beam}^{-1}$ at 1 mm for the continuum of the central field from the mosaic, a decline of $\geq 20\%$ is obtained relative to the single field data (flux $\sim 10 \text{ mJy beam}^{-1}$) consistent with the 3 mm data. The detected variability can still be partially due to uncertainties in the flux calibration ($\lesssim 10\%$). However, even if this seems to indicate some variability in NGC 3718 ($\sim (30 \pm 10)\%$ accounting for the uncertainties in the flux calibration), there is no evidence for a highly variable source, as is also supported by recent EVN and MERLIN measurements at 18 cm and 6 cm (Krips et al., 2005d, epochs 2001 to 2004) or other cm observations (at 2 cm and 3.6 cm; e.g., Nagar et al. 2002). The derived positions are consistent between the two observing epochs as well as between 1 mm and 3 mm. They also agree with the positions of the nucleus obtained at cm and optical wavelengths within the errors. Accounting for a weak variability, a comparison between our mm fluxes and cm fluxes observed with the VLA in 1997 (Becker et al. 1995), 1998 (Nagar et al. 2001), and 1999 (Nagar et al. 2002) indicates a spectral index of -0.01 depending on which of our two observing epochs is used. This corresponds to a flat to inverted spectrum for the central source in NGC 3718, like those found for many other low-luminosity active nuclei in Seyfert galaxies and LINERs (Wrobel & Heeschen 1991; Slee et al. 1994; Nagar et al. 2000). The flat radio spectra exclude emission from optically thin synchrotron emission, as is often seen from *extended* radio jets, since this produces steep radio spectra. Thus, processes like synchrotron self-absorption or advection

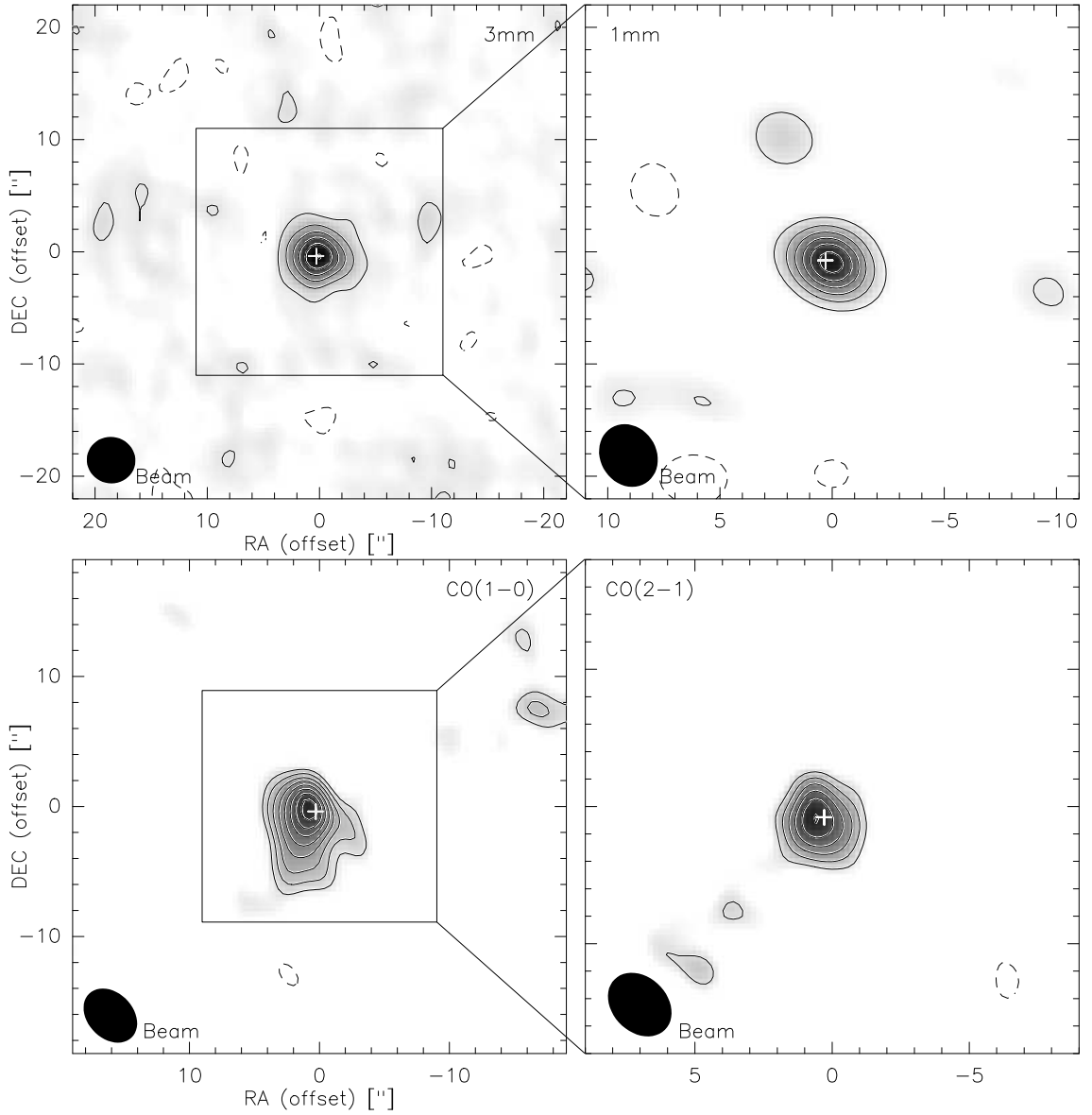


Figure 5.3: *Upper panel:* Continuum emission of the single field observations at 3 mm (*left*) and 1 mm (*right*). The white cross indicates the position at 18 cm with EVN. Contour levels are from 2σ (2σ) = 1.0 (1.6) mJy beam⁻¹ to 9 (9.6) mJy beam⁻¹ in steps of 2σ (2σ) at 3 mm (1 mm). Beam sizes are indicated at lower left. *Lower panel:* PdBI central maps of the integrated CO(1-0) (*left*) and CO(2-1) (*right*) emission in NGC 3718 at same size. The CO(2-1) was smoothed to the beam size of the CO(1-0) map. Contour levels are from 3σ (3σ) = 1.5 (2.7) to 5 (7.2) Jy beam⁻¹ km s⁻¹ in steps of 1σ (1σ) at CO(1-0) (CO(2-1)). The white cross indicates the position at 18 cm with EVN.

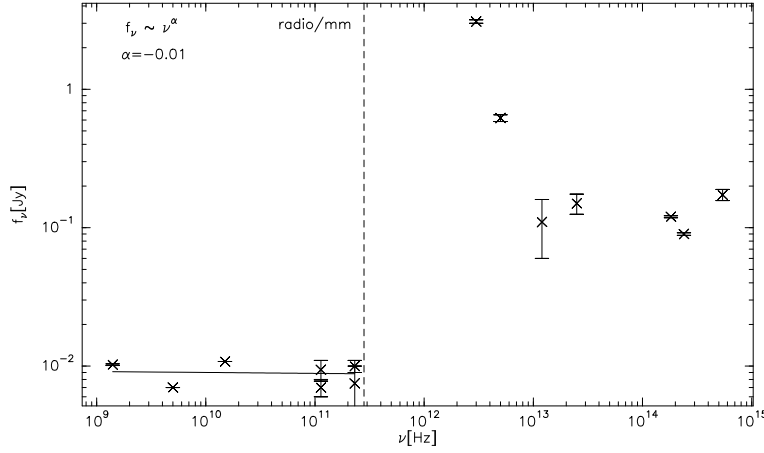


Figure 5.4: The Spectral Energy Distribution (SED) of NGC 3718. IR and optical fluxes are shown for consistency (taken from NED). The cm fluxes were observed with the VLA (FIRST; Nagar et al. 2001, 2002) and thus have an angular resolution comparable to the PdBI maps. The mm fluxes for both observing epochs are plotted (upper limit at 1 mm). The solid line indicates a fit ($f_\nu \propto \nu^\alpha$) with $\alpha = -0.01$.

dominated accretion flows (ADAFs: Narayan, Mahadevan & Quataert 1998; Quataert 2001) have to be considered. A compact jet in combination with an ADAF (Falcke 1996; Falcke & Marloff 2000; Falcke 2001) also cannot be excluded. If a longitudinal pressure gradient were to cause the jet to accelerate rapidly, the integrated compact radio jet emission would also have a slightly inverted radio spectrum.

5.3.1.2 Line

After subtracting the continuum emission in the uv plane from the (continuum+line) channels, CO(1–0) and CO(2–1) line emission is detected in the central $\sim 10''$ ($\equiv 1$ kpc) of NGC 3718. The combined central maps are shown in Fig. 5.3. In both lines the emission is slightly extended. Both the integrated CO(1–0) and CO(2–1) emission are similar to the nuclear position derived from the optical/radio. Also the iso-velocity diagram in Fig.5.6 shows that the dynamical center of the CO emission lies on the radio/optical nucleus. A comparison of the flux observed with the PdBI and the IRAM 30 m single dish reveals that the interferometer recovers less than one third of the peak line flux seen with the 30 m telescope (see Figs. 5.5). This indicates that the emission in NGC 3718 must be much more extended and diffuse than is apparent in the integrated map of Fig. 5.3. Assuming the following equation¹ (for a more detailed review see Krips 2001 (diploma thesis)),

$$M_{\text{gas}} = M(\text{H}_2 + \text{He}) \quad (5.1)$$

$$= 1.36 \times M(\text{H}_2) \quad (5.2)$$

$$= X_{\text{CO}} [M_\odot (\text{K km s}^{-1} \text{pc}^2)^{-1}] \times L_{\text{CO}(1-0)}^l [\text{K km s}^{-1} \text{pc}^2] \quad (5.3)$$

$$= 4.8 \times 3.25 \cdot 10^7 \frac{S_{\text{CO}(1-0)}}{\text{Jy km s}^{-1}} \left(\frac{\nu_{\text{obs}}}{\text{GHz}} \right)^{-2} \left(\frac{D_l}{\text{Mpc}} \right)^2 (1+z)^{-3} M_\odot \quad (5.4)$$

with

¹This method is consistent with the determination of the gas mass via the ratio between the H_2 column density and CO(1-0) line emission measured in Kelvin. Compare Equation 10.7.

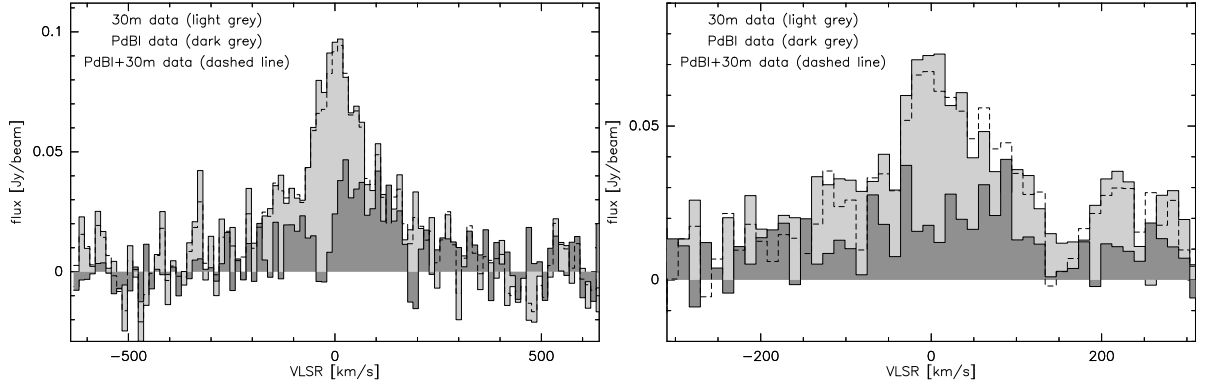


Figure 5.5: *Upper panel*: CO(1–0) spectrum of the central emission in NGC 3718 observed with the PdBI (dark grey; integrated over the emission area) and the IRAM 30 m telescope (light grey; Pott et al. 2004). The rms noise level is here at $\sim 4\text{mJy}$ for the PdBI data ($\Delta v=13\text{ km s}^{-1}$). *Lower panel*: CO(2–1) spectrum of the central emission in NGC 3718 as observed with the PdBI (dark grey; integrated over the 30m beam area) and the IRAM 30 m telescope (light grey; Pott et al. 2004). The short-spaced corrected spectrum is also shown (dashed line; smoothed to the 30m beam). The rms noise level is here at $\sim 6\text{mJy}$ for the PdBI data ($\Delta v=13\text{ km s}^{-1}$). Both spectra are continuum subtracted.

$$\begin{aligned}
 S_\nu &= \text{integrated CO(1–0) line intensity} \\
 \nu_{\text{obs}} &= \text{observed frequency of the CO(1–0) line} \\
 D_l &= \text{luminosity Distance} \\
 z &= \text{redshift} \\
 X_{\text{CO}} &= 4.8\mathcal{M}_\odot(\text{K km s}^{-1}\text{pc}^2)^{-1} \text{ (Solomon \& Barrett 1991),}
 \end{aligned}$$

the central gas mass M_{gas} amounts to $\sim 1 \times 10^7 \mathcal{M}_\odot$ in the PdBI map, in contrast to $3 \times 10^7 \mathcal{M}_\odot$ in the 30 m map (Pott et al. 2004), indicating resolution effects in the PdBI maps. Downes et al. (1993) emphasize, however, that the standard galactic conversion factor X_{CO} between gas mass and CO luminosity might fail for the centers of galaxies where the molecular gas is bound by the total gravitational potential of the galaxy rather than by self-gravity. In such a case, the factor would be up to 5 times lower than the standard galactic one, resulting in gas masses of $\sim 0.2 \times 10^7 \mathcal{M}_\odot$ for the PdBI map and $0.6 \times 10^7 \mathcal{M}_\odot$ for the 30 m map.

By comparing the distributions of the CO(1–0) and CO(2–1) line emission, the CO(1–0) emission is found to show an elongation towards the south, almost perpendicular to the beam. The integrated line ratio $R_{21} = \text{CO(2–1)}/\text{CO(1–0)}$ in temperature (Kelvin) scale is estimated to ~ 0.6 indicating subthermal excitation conditions and cold gas. To obtain this value, the inner uv region of the CO(1–0) data has first been truncated as well as the outer uv region of the CO(2–1) data to get comparable uv coverages and resolutions for the two transitions, integrated both lines over the same velocity range of -350 km s^{-1} to $+350\text{ km s}^{-1}$ and then transformed the flux (Jansky) into temperature (Kelvin). However, due to the limited signal-to-noise and thus the difference of the weighting factors in both transitions, the reliability of this estimate is still questionable and thus the value of ~ 0.75 derived in the center by Pott et al. (2004) might be a better indicator for the physical conditions in NGC 3718.

Fig. 5.6 shows the zero order moment maps of both transitions overlaid with contours from the first order moment maps and the position velocity diagram taken along the axis that follows the apparent velocity gradient of both lines. This axis is coincident with the major axis of the galaxy (indicated in Fig. 5.16; compare also Pott et al. 2004). The CO(2–1) maps are very noisy but are plotted for consistency and comparison purposes, however. Both lines reveal two different velocity systems, one quite extended between $\pm 100\text{ km s}^{-1}$ and a more compact one spread over a higher velocity range of $\pm 200\text{ km s}^{-1}$. Consistent with Pott et al. (2004), the global velocity range of the inner $\sim 15''$ amounts to almost 200 km s^{-1} . However, this “central” feature in the position velocity diagram extends in Pott et al. (2004) out to a radius of $15\text{--}20''$, while in our interferometric data it stops at a radius of

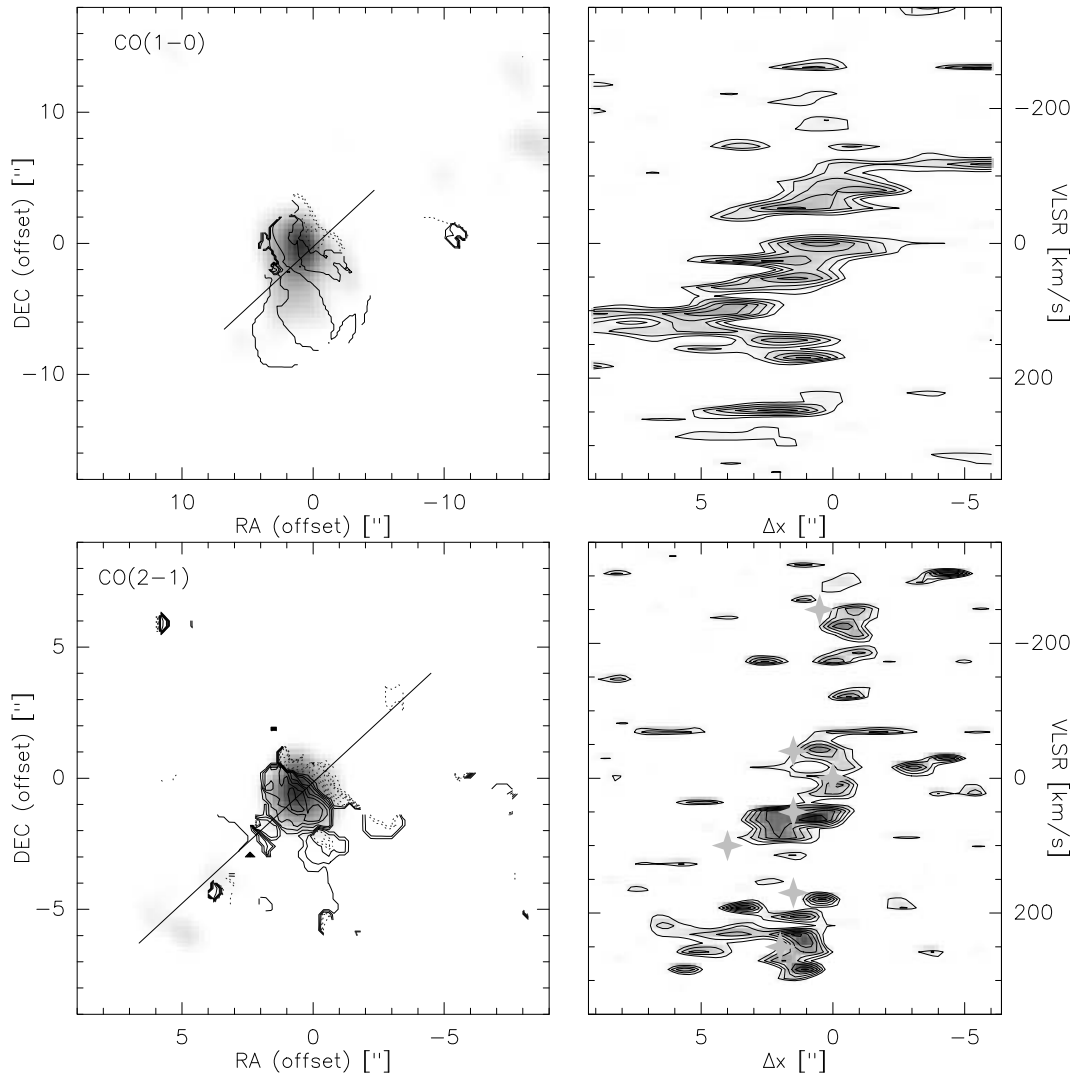


Figure 5.6: Mean iso-velocity fields of the CO(1–0) (*upper left*) and CO(2–1) (*lower left*) lines with their respective position-velocity maps (CO(1–0): *upper right*; CO(2–1): *lower right*) taken along the axis indicated in the left panel (*solid line*: major axis). The grey scale in the images on the right is the velocity integrated line emission of CO(1–0) and CO(2–1) respectively. The light grey stars in the lower right panel illustrate the positions of the CO(1–0) components identified in the upper right panel. Velocity contours are in steps of 25 km s^{-1} for both lines.

almost $10''$, very likely due to missing short spacings. This rapidly rotating nuclear component will be discussed in section 5.4.3. The line emission shows a strong asymmetry in the position velocity diagram with almost no emission towards the blueshifted velocities. As the dynamical center of the CO emission is found to be located on the AGN itself, this asymmetry might be a strong signal of ongoing accretion into the nucleus on these small scales. Section 5.3.4 will show that this asymmetry cannot be traced back to missing short spacings.

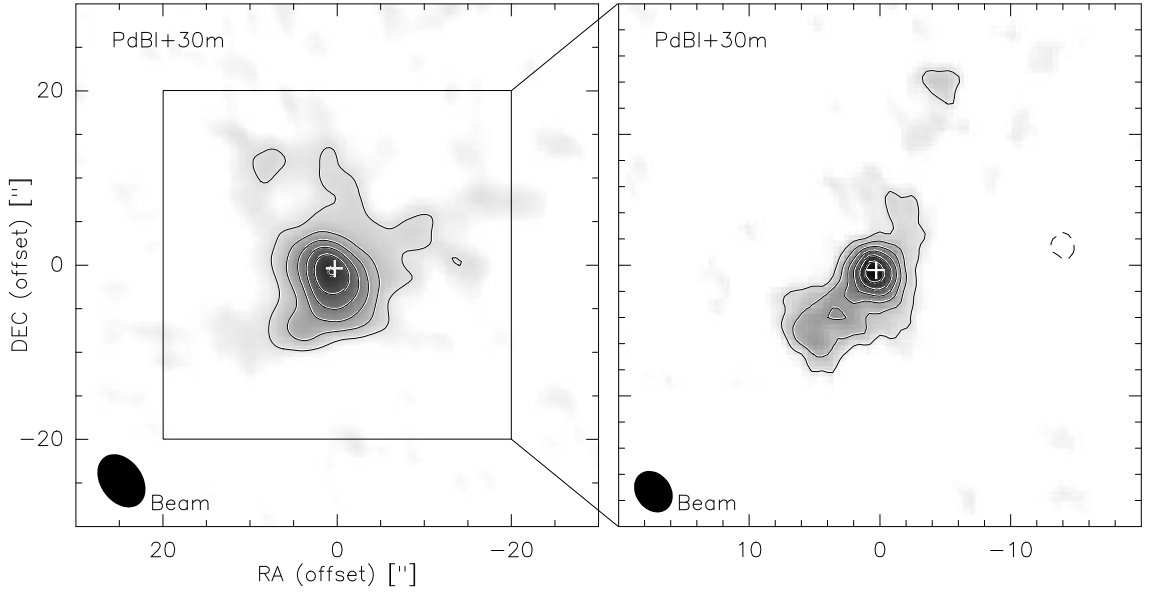


Figure 5.7: PdBI central maps corrected with 30m data for short-spacing effects of the integrated CO(1–0) (*left*) and CO(2–1) (*right*) emission in NGC 3718 at same size. Contour levels are from 5σ (3σ) = 2.0 (2.4) to 8.0 (10.4) $\text{Jy beam}^{-1} \text{ km s}^{-1}$ in steps of 3σ (2σ) at CO(1–0) (CO(2–1)). The white cross indicates the position at 18 cm with EVN.

5.3.2 Overall emission

5.3.3 PdBI-only data

Outside the central mosaic field, there is no evidence of continuum emission in our data. The 30 m map of Pott et al. (2004) has already revealed the existence of two additional maxima in the CO(1–0) emission which are offset by $\sim 30\text{--}40''$ from the nucleus. Further maxima are found in the new PdBI mosaic map which are located farther out at $\sim 60''$ (compare Figs. 5.9 and 5.13). In Fig. 5.9 the eastern components are labeled SE1 and SE2, the western components NW1 and NW2, and the central feature C. There are also indications for further maxima between NW1 and NW2 and also between SE1 and SE2 but they still lack enough sensitivity ($\leq 2\sigma$) in the PdBI-only map to be further substantiated at this point. The brightest line in the spectra turns out to be NW2, located to the northwest in the integrated mosaic map, and the central component C, whereas the other three features appear to be rather weak with a signal-to-noise ratio at line peak of ~ 4 (Fig. 5.9). However, NW2 appears to be quite weak in the integrated map which might be traced back to its weak line width of only $\sim 50 \text{ km s}^{-1}$. The integrated map was produced by averaging the channel maps over a total velocity width of $\sim 600 \text{ km s}^{-1}$. A comparison between the global fluxes derived from the 30 m and the PdBI data again shows that a large part of the - diffuse extended - flux (at least $\sim 70\%$ of the total flux) must be resolved out by the interferometer due to missing short spacings. Adding up all the PdBI spectra leads to a total gas mass of $M_{\text{gas}} \simeq 2.5 \times 10^7 M_{\odot}$. This is a tenth of the total gas mass derived from the 30 m spectra of $\sim 2.4 \times 10^8 M_{\odot}$ (Pott et al. 2004). In general, a special method called short-spacing correction can be used to recover the flux resolved out by an interferometer map by adding data from a single dish telescope.

5.3.4 PdBI+30m data: short spacing correction

To restore missing extended and diffuse emission, the CO(1–0) data from the IRAM 30 m telescope were combined with our interferometric maps. The weights attached to the 30m and PdBI data were varied to find the best com-

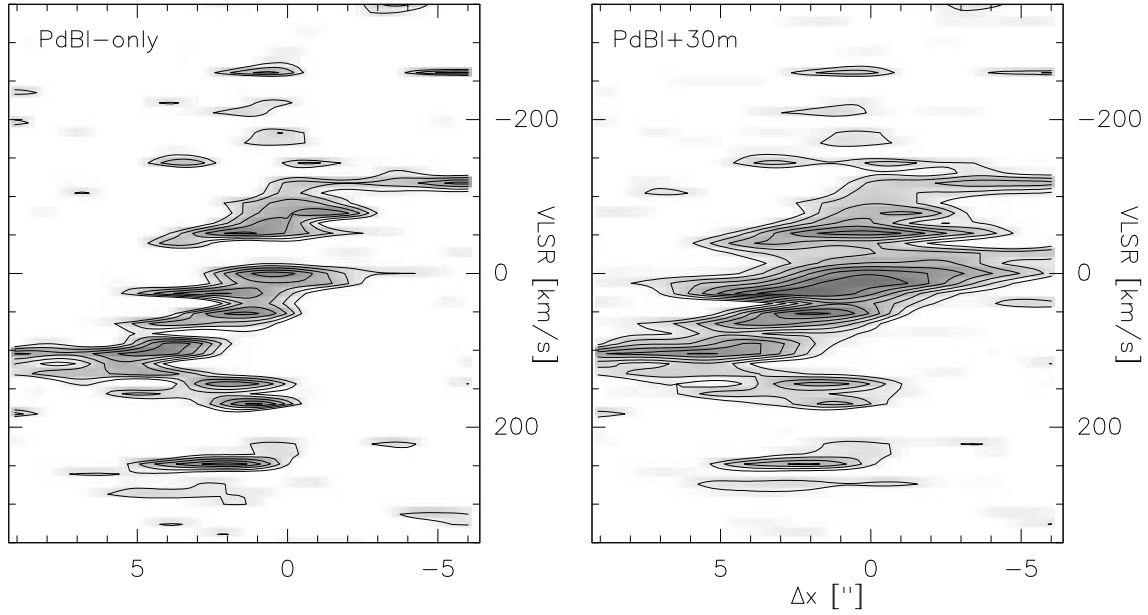


Figure 5.8: Comparison of the pv-diagrams along the axis shown in Fig. 5.6 between PdBI-only data for the single-field pointing (*left*) and PdBI+30 m data for the central mosaic field (*right*). The asymmetry still remains and thus cannot be due to missing short spacings.

promise between good angular resolution and almost complete restoration of the missing extended flux. Finally, a factor of 4 was applied to the weights of the 30m data enabling to recover $\sim 90\%$ of the missing flux (see below) and to still retain a reasonable angular resolution of $7.8 \times 4.5'' @ 20^\circ$. A higher weighting factor would have increased the image restoration to over 90% but at the same time also decreased the angular resolution to $\sim 10''$. The combined maps of 30m and PdBI data have finally been cleaned using standard program packages provided by the GILDAS software for mosaic data. The results are presented in Fig. 5.7 & 5.9 for the single field and mosaic maps. In Fig. 5.8, the position-velocity diagrams along the axis used in Fig. 5.6 for the PdBI-only data are compared with the PdBI+30m data. The asymmetry discussed in Section 5.3.1.2 is still present in the PdBI+30m maps and can hence not be traced back to missing short spacings. This indicates that the asymmetry is an intrinsic property of NGC 3718 and might be an evidence for ongoing accretion onto the nucleus. A first comparison between the PdBI-only and the PdBI+30 m maps shows in the mosaic maps that the short spacing correction strengthens the inner components (NW1, C and SE1) that appear to contain most of the extended and diffuse emission. If we now derive the total gas mass, we obtain $\sim 2.1 \times 10^8 M_\odot$, which is $\sim 90\%$ of the value found for the 30 m-only data. Besides the five main emission peaks seen in Fig. 5.9, further emission between NW1 and NW2 and SE1 and SE2, as already indicated in the PdBI-only map (Fig. 5.9), is substantiated in the PdBI+30m map. Their gas masses are estimated to $\sim 0.2 \times 10^8 M_\odot$, respectively. Also globally seen, the western part of the CO(1–0) emission appear to contain more gas ($M_{\text{gas}} \simeq 10^8 M_\odot$ without C) than the eastern one ($M_{\text{gas}} \simeq 0.5 \times 10^8 M_\odot$ without C). The CO(1–0) emission cannot be associated with a single straight line but rather delineates an “S-like” shape.

The next sections will deal with the modeling of the complex gas distribution in NGC 3718 for a better understanding and a more qualitative interpretation. Also, the effects of missing short spacings are examined in detail on our data by simulating this procedure for the model and comparing the results thus obtained with the observations.

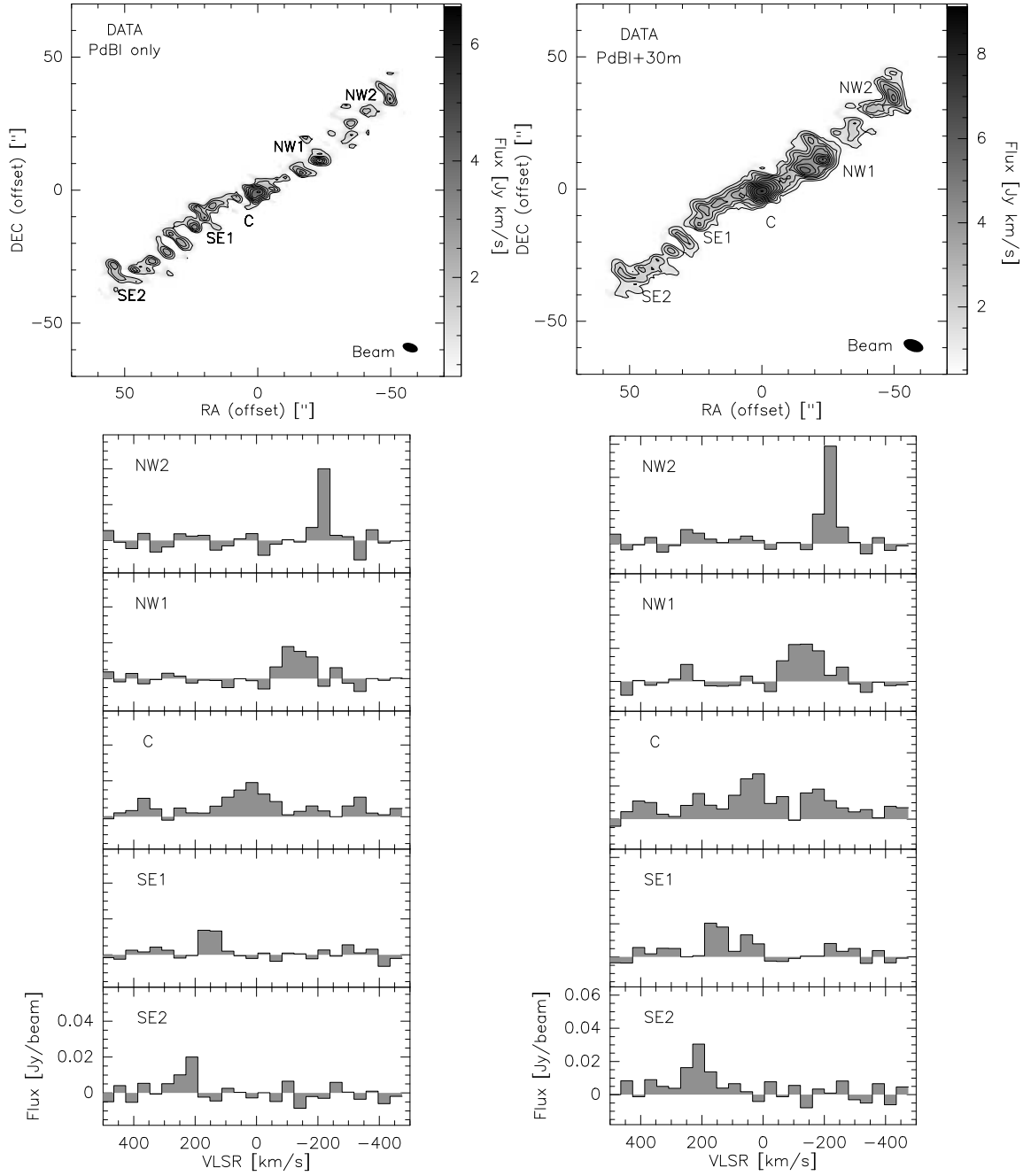


Figure 5.9: PdBI mosaic map of the velocity integrated CO(1–0) emission in NGC3718 for the PdBI-only data (*upper left figure*) and for the PdBI+30m data (*upper right figure*). Spectra are shown in the lower panels. PdBI-only: Contour levels are from $2\sigma = 1.4 \text{ Jy beam}^{-1} \text{ km s}^{-1}$ to $5.6 \text{ Jy beam}^{-1} \text{ km s}^{-1}$ in steps of 1σ . PdBI+30m: Contour levels are from $2\sigma = 1.4 \text{ Jy beam}^{-1} \text{ km s}^{-1}$ to $8.4 \text{ Jy beam}^{-1} \text{ km s}^{-1}$ in steps of 1σ .

Component	R.A. (offset) [$''$]	Dec. (offset) [$''$]	flux Jy km s^{-1}
SE2	$+52 \pm 3$	-34 ± 3	1.2
SE1	$+20 \pm 3$	-8 ± 3	1.3
C	0 ± 1	0 ± 1	3.4
NW1	-19 ± 1	$+9 \pm 1$	2.9
(NW1.5 ^a)	-36 ± 2	$+23 \pm 2$	2.0
NW2	$+49 \pm 1$	$+36 \pm 1$	2.7

Table 5.2: Positions and fluxes for the CO(1–0) components in the PdBI+30m map. Offsets are with respect to $\alpha_{2000}=11\text{h}32\text{m}34.8$ and $\delta_{2000}=53^{\circ}04'04.9''$. ^a This is the apparent “sixth” component between NW1 and NW2.

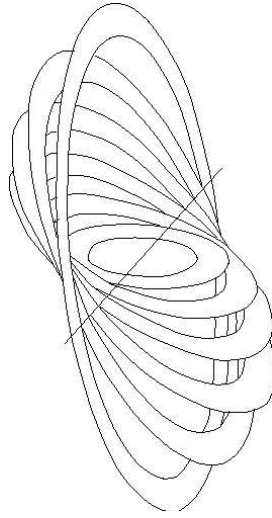


Figure 5.10: Tilted ring to model a warped disk (Schwarz 1985). The variation of the angles of each ring can produce a warping of the disk. For more details see Chapter A in the Appendix.

5.4 Modeling the CO distribution

The special characteristics of the HI data for NGC 3718 led to the conclusion (Schwarz 1985) that the atomic gas is warped at radii $\gtrsim 8$ kpc in a configuration similar to that of the dust lane. IRAM 30 m observations of the molecular gas by Pott et al. (2004) showed such a warp signature of the gas extending down to smaller radii of ~ 1 kpc. Previous modelling based on the Pott et al. CO and the HI data can hence be fine-tuned with the new information gained from our significantly increased spatial resolution of $\sim 4\text{--}7''$ for our PdBI-only map vs. $21''$ for the Pott et al. (2004) 30 m map.

5.4.1 The model

Our simulations of the mosaic maps are based on a tilted ring model (Fig. 5.10) similar to that of Pott et al. (2004); that paper presents more modelling details². Since the Pott et al. (2004) model of NGC 3718 reproduces the 30 m observations with only 3 main maxima, the parameters had to be modified to adapt their model to our PdBI results. The revised best-fit parameters were obtained by starting with the model of Pott et al. (2004), propagating it through the PdBI+30m response function (described in section 5.4.2), comparing the result with the observed

²see also Chapter A in the Appendix

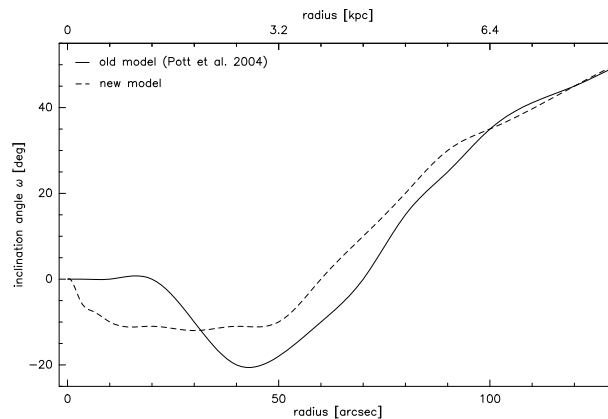


Figure 5.11: Tilt angles $\omega(r)$ of the warp (for definition see Chapter A). The old model of Pott et al. (2004) is given as a solid line, while a dashed line is used for our new model.

data (PdBI+30m), and finally tuning the parameters until the match is optimal. In the new best-fit model, different tilt angles $\omega(r)$ (of a given ring relative to the assumed plane of the innermost reference disk) are mainly used for the inner radii ($\leq 50''$). Our inner rings are less warped, i.e., the tilt angles are smaller for radii from $40''$ to $60''$ than in the previous model, but they remain constant down to radii of $\sim 1''$ (i.e., in our model, the warp continues down to a radius of $\sim 1''$; see Fig. 5.11). Furthermore, a different intensity profile is used compared to Pott et al. (2004). The earlier work assumed an integrated line flux distribution for the rings that is very bright at the center but then decreases rapidly, while the intensities in our model show a slower decrease with radius. A different inclination (70° instead of 60°) and position angle (-60° instead of -85°) is also adopted for the galactic disc in space. The rotation curve, however, remains the same for the new model. The integrated map of our model is shown in Fig. 5.12 (the model has not yet been filtered through the interferometer or single dish response function). While the central (C) and the two outer (SE2, NW2) components are quite compact and bright, the two inner features (SE1, NW1) are rather weak and relatively extended on $\sim 10''$ scales.

5.4.2 Simulating the short-spacing correction

To allow for a direct comparison between the derived model and the CO data (PdBI-only, PdBI+30m, 30m-only), the effect of the different observation methods on the model were simulated. To determine how our model galaxy would look when observed with the interferometer (before and after short-spacing correction), the simulated PdBI map with a program that computes an interferometric image (upper panel of Fig. 5.13) from a given uv coverage (taken here from the observations) and the given three-dimensional intensity distribution (taken here from our best-fit model shown in Fig. 5.12) were first produced. As expected, the two inner maxima are severely weakened, losing around 60% of the original flux. Components SE1 and NW1 are heavily resolved and produce two weak and quite compact features at the corresponding positions in the simulated PdBI map, so that all five maxima appear to be much less extended in this map. The best-fit model was also smoothed to the beam ($\sim 21''$) of the 30 m telescope and the spectra were taken at the same positions as for the observations. Accounting for normalisation, these data were transformed into the 30 m file that would have been produced if such a distribution had been observed with the IRAM 30 m telescope. This file is thus suitable for comparison with the measured 30 m data (see lower panel in Fig. 5.13). Indeed, only three main maxima, a merging of the inner two (SE1, NW1) with the outer two maxima (SE2, NW2), and an indicated S-line shape are found.

As a final test, the simulated 30 m and PdBI maps were combined. All three simulated maps are plotted in Fig. 5.13 (*grey scale*). The loss of flux due to the reduced sensitivity to diffuse extended emission in the interferometer-only data is indeed reproduced by the model. Comparisons of the simulated peak fluxes from the PdBI, the PdBI+30 m, and the 30 m data with each other suggests that the PdBI has lost at least a factor ~ 2 -3 of

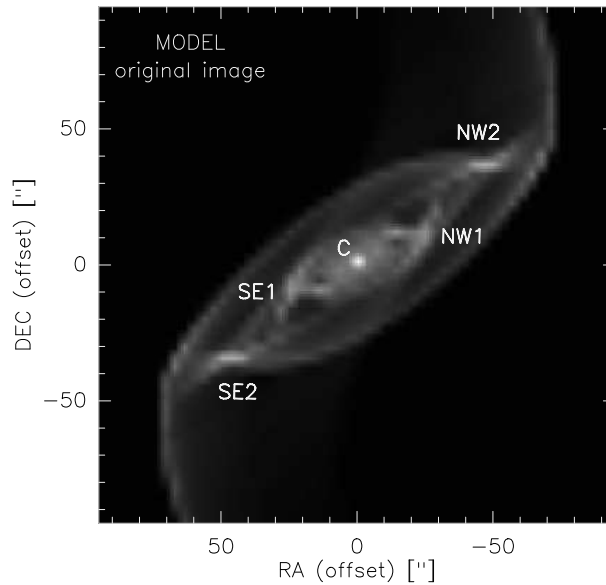


Figure 5.12: The velocity integrated intensity map of our model is plotted here, before spatial filtering to match the response of the interferometer and single dish telescope.

the peak line flux, consistent with what is observed. The short-spacing correction not only reproduces the correct fluxes but also the correct distribution without any artefact or inconsistency in excess of 1% for the model.

5.4.3 Model versus Data

The same steps were carried out to combine the observed PdBI and 30 m data (section 5.3.4). The results are plotted in Fig.5.13 as contours over the simulated maps. A very similar behavior is found in the observed and model maps. Besides the inner two maxima which are more easily visible, the flux level also increases. Thus, a better distinction between signal and noise is possible. As the two eastern components are less dominant (by a factor 2) than the western components in the integrated map over the whole velocity range, plots for each component are separately shown which have been integrated over the respective velocity range (see Fig. 5.14). Such an asymmetry of the gas distribution has already been found in many other galaxies as well (e.g., Richter & Sancisi 1994) and cannot be explained by our symmetric tilted ring model. It might be an indication for a tidal interaction with the companion galaxy which would result in an asymmetric gas distribution. Thus, our warp model could presumably be improved by adding asymmetries to account for interaction mechanisms.

The maps of the data (*left side*) and the model (*right side*) are separately shown in Fig.5.15, along with the good agreement between the model and the data in terms of spectra taken at each of the five components. A somewhat weaker eastern component is also visible in the model. This is due to the asymmetric sampling of the 30 m-spectra with respect to the CO centroid. Simulated and observed line widths are consistent within the noise. Nevertheless, one discrepancy between the model and the data still remains. Due to the slightly higher line widths of the two simulated outer components, they are stronger in the integrated map of the model than the observed data.

In Fig.5.16, first order moment maps were derived with a $\sim 3\sigma$ clipping over a velocity range of -250 km s^{-1} to $+250 \text{ km s}^{-1}$ and taken position-velocity cuts along the major axis of the galaxy for the observed and simulated data. Compared to the pv-diagram of a standard gas disk, a more complex structure is seen in the pv-diagrams of the observations as well as of the simulation due to orbital crowding effects. As might be expected for a rapidly rotating nuclear disk with a size of $\sim 1.5 \text{ kpc}$, a steep linear rise is indicated in the position-velocity diagram. This feature agrees well in orientation and size with the central field velocity component visible in the CO(1-0) map of

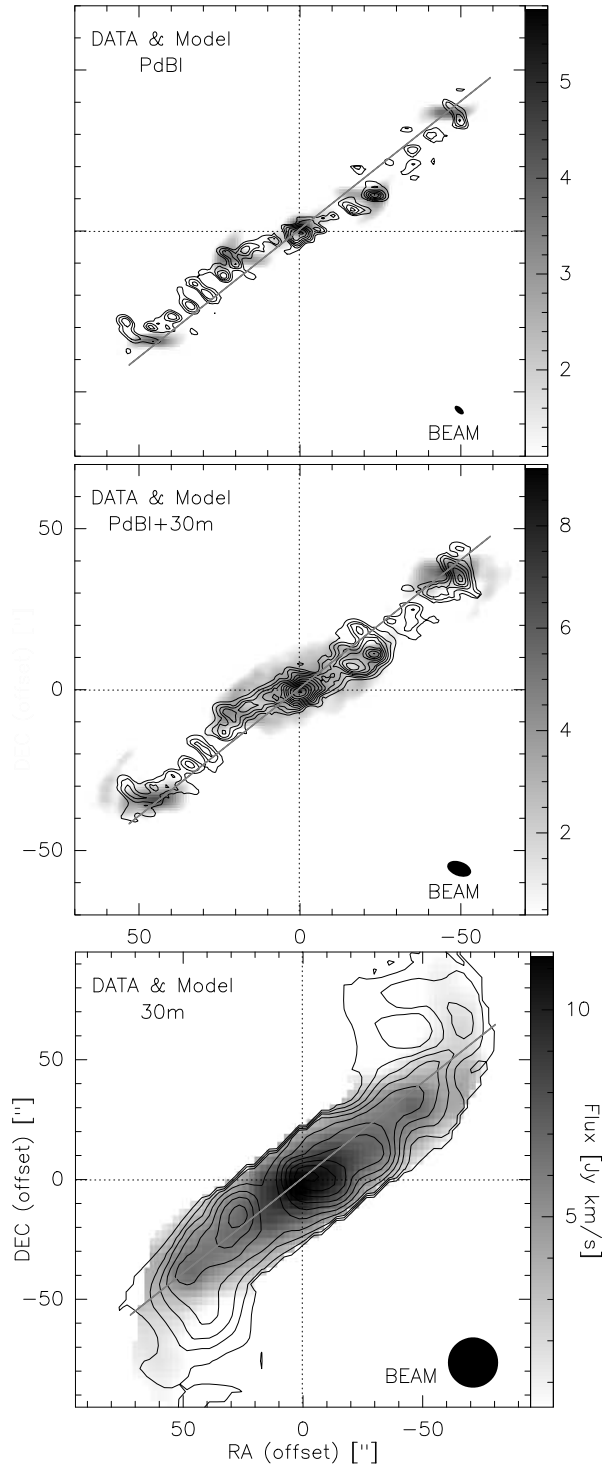


Figure 5.13: Velocity integrated maps of the PdBI data only (*upper panel*), the PdBI+30 m data (*middle panel*) and the 30 m-only data (*lower panel*). The model (grey scale) is overlaid with solid contours of the observed data. Contour levels: *PdBI-only* $2\sigma=1.4$ to $5.6 \text{ Jy beam}^{-1} \text{ km s}^{-1}$ by 1σ ; *PdBI+30m* $2\sigma=1.4$ to $8.4 \text{ Jy beam}^{-1} \text{ km s}^{-1}$ by 1σ *30m-only* $3\sigma = 1.0$ to $10 \text{ Jy beam}^{-1} \text{ km s}^{-1}$ by 3σ .

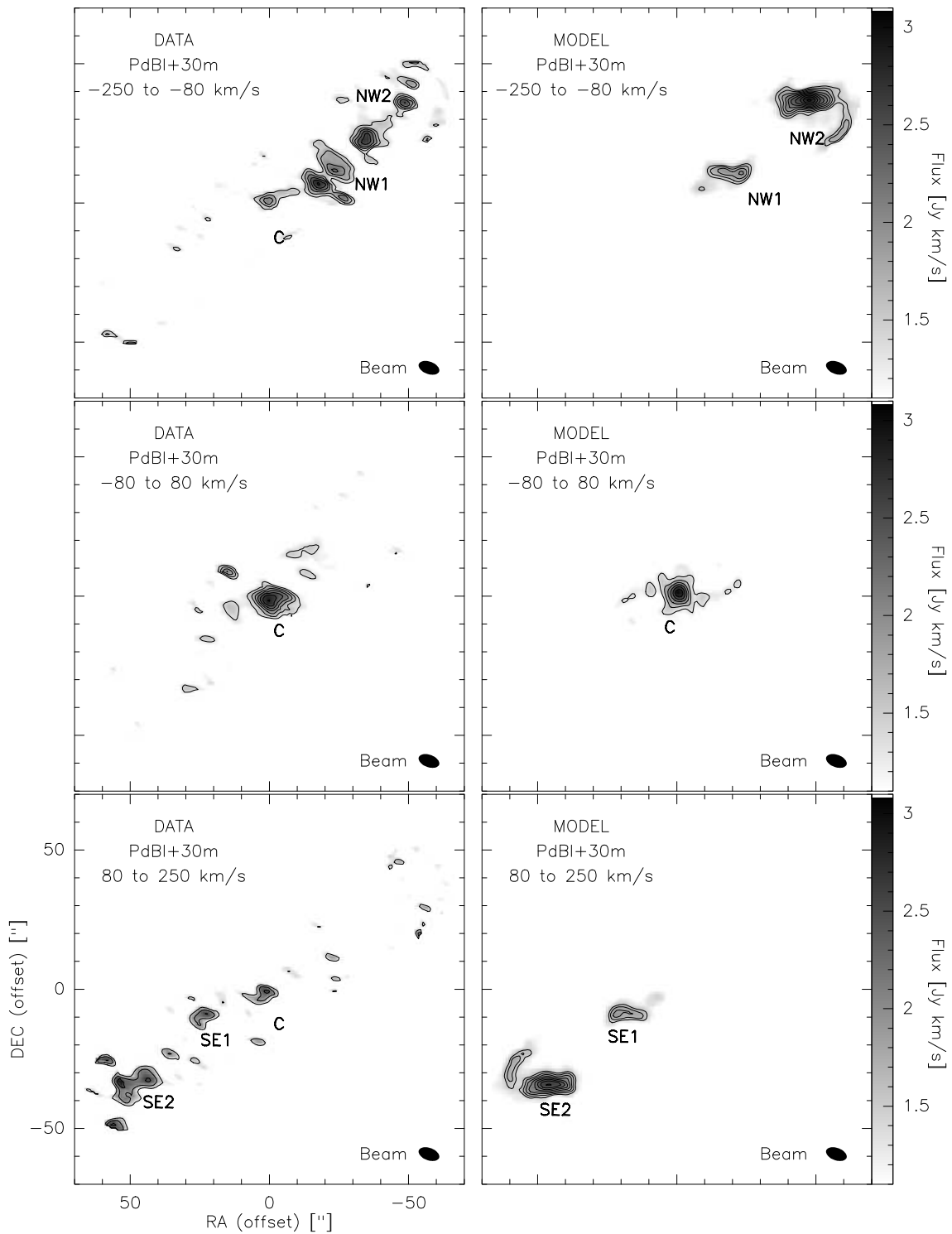


Figure 5.14: Integrated maps of the measured (*left*) and simulated (*right*) PdBI+30m data from: -250 to -80 km s^{-1} (*upper panel*), -80 to 80 km s^{-1} (*middle panel*), and 80 to 225 km s^{-1} (*lower panel*). Contour levels are $3\sigma = 1.2$ in steps of 1σ .

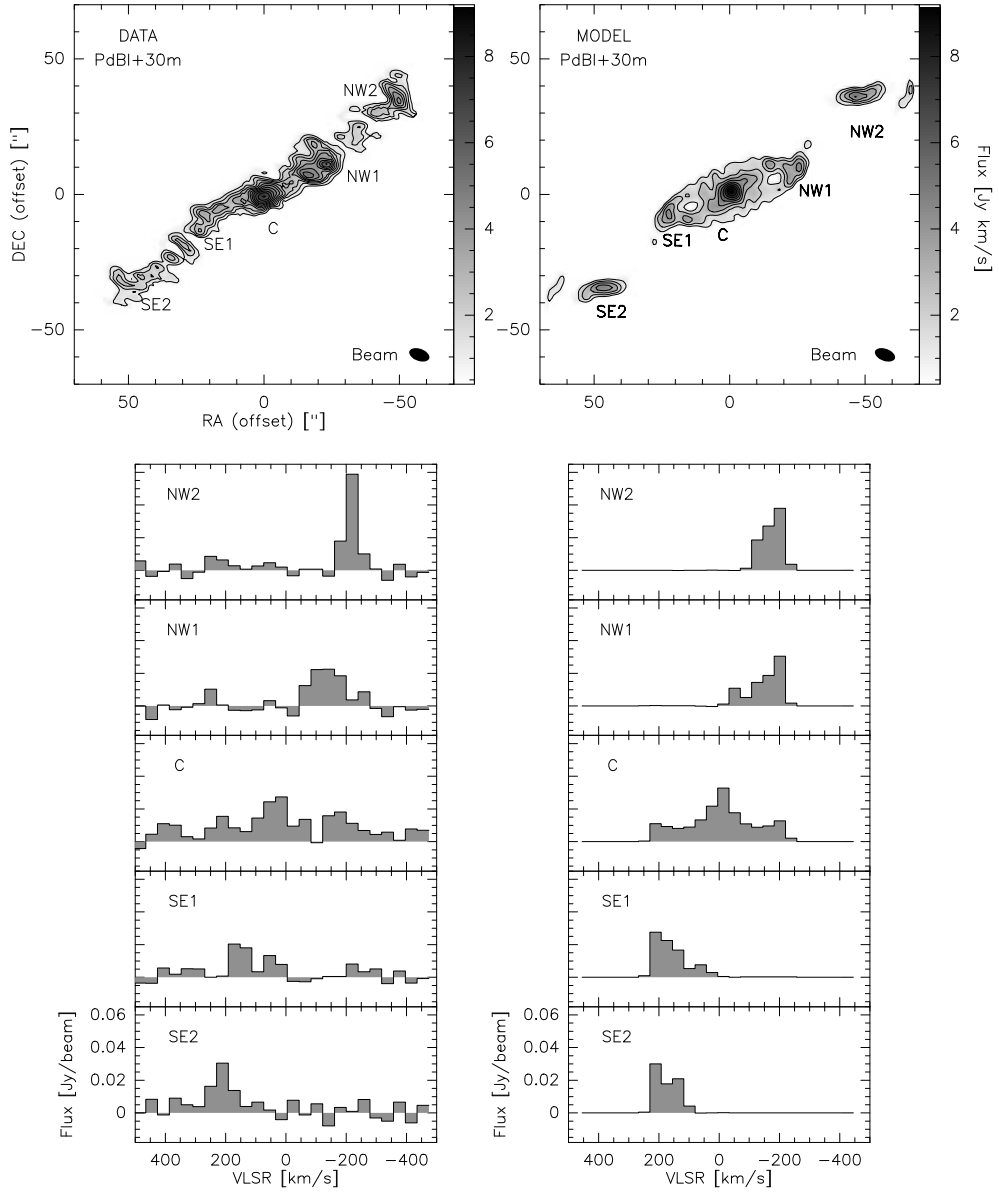


Figure 5.15: Upper panel: the short-spacing corrected images of the observed data (*left*) and of the model (*right*) data. Lower panel: 30m spectra at positions of the CO peaks. Contour levels are from $2\sigma_{1.4}$ to $8.4 \text{ Jy beam}^{-1} \text{ km s}^{-1}$ in steps of 1σ .

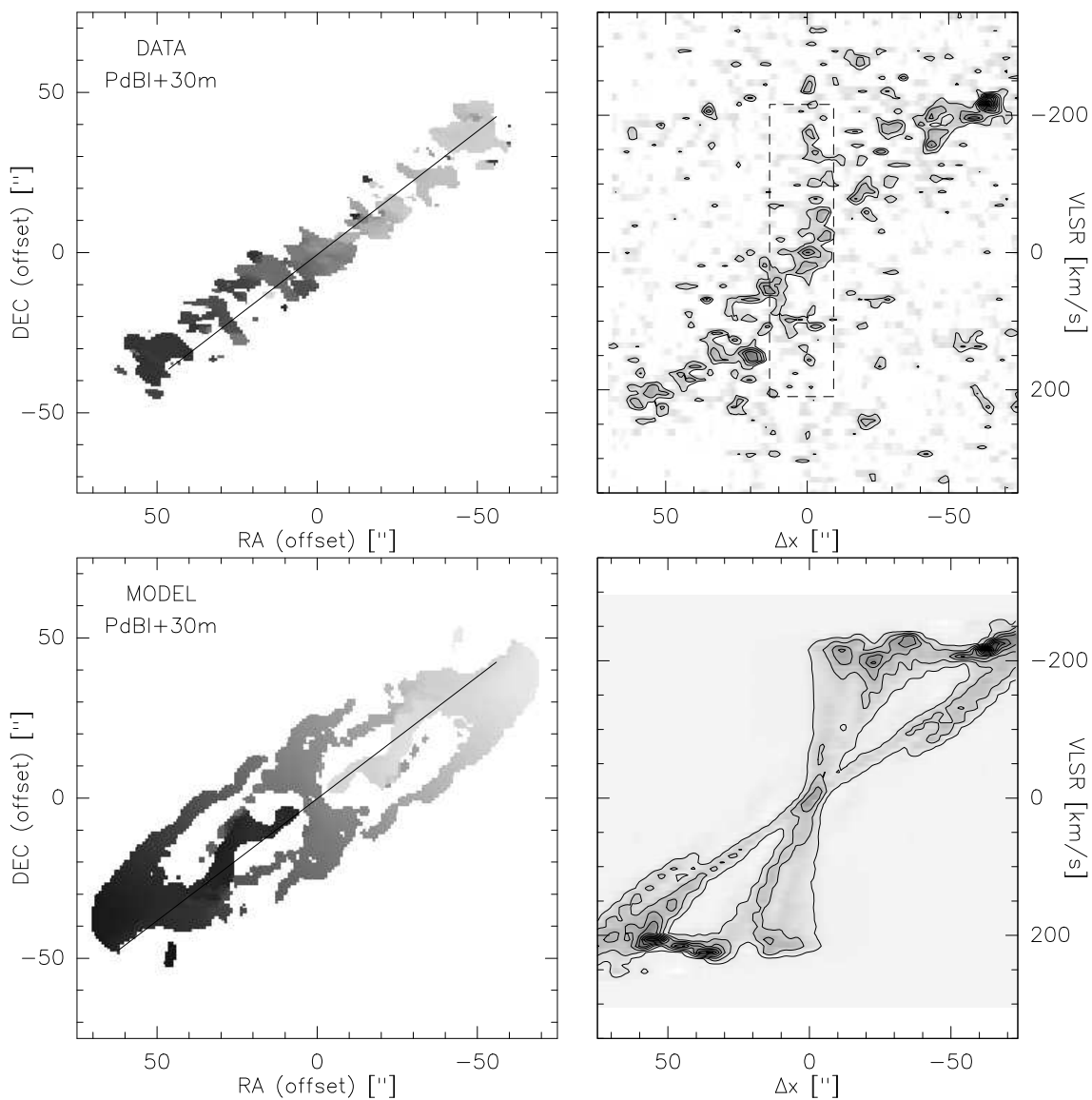


Figure 5.16: Upper panel: observed data, with first order moment maps (*left*) and position velocity cuts (*right*) taken along the axis indicated in the first order moment map (going through the AGN). Lower panel: same as above for the model. The dashed box in the position-velocity diagram for the observed data indicates the location of the central field.

Fig. 5.6. Again, one finds that this central feature in the position-velocity map extends only over a range of $\pm 10''$ in Fig. 5.16, which is smaller than the interval derived by Pott et al. (2004). The difference to position velocity diagram in Pott et al. (2004) has a logical and simple explanation. In their maps, {SE1, SE2} and {NW1, NW2} merged (in the 30 m beam) into single SE and NW features, respectively, and thus all lie on the major axis. In our interferometric map, SE1 and NW1 are no longer aligned with this major axis and thus appear only weakly in the position-velocity diagram of Fig. 5.16. The high velocity gas returns if we rotate the major axis by about 8° . Thus, one has three different velocity regimes. The first ranges from $\pm 10''$ with $\Delta v \sim \pm \sim 150 \text{ km s}^{-1}$ and can be identified with the gas occupying the inner rings. The second region extends to $\pm 30''$ with $\Delta v \sim \pm 200 \text{ km s}^{-1}$ and is caused by intermediate rings. The third extends to $\pm 70''$ with $\Delta v = \pm 220 \text{ km s}^{-1}$ and originates from the outer rings.

5.5 Discussion

This chapter presents an analysis based on arcsec angular resolution PdBI observations of the gas distribution in NGC 3718, complementing previous studies conducted by Pott et al. (2004: CO on $\geq 20''$ scales) and Schwarz (1985: HI on $\geq 30''$ scales). After making a short-spacing correction using the IRAM 30 m data (Pott et al. 2004), the mosaic observations of the total emission as well as single field observations of the central kpc were modelled and interpreted. Three compact and three extended components were found in the mosaic map of the CO(1–0) emission. At the higher angular resolution of the PdBI, the gas structure turns out to be more complex than previously appreciated. To explain the detected molecular gas distribution, the Pott et al. tilted ring model had to be slightly modified. The revised model now not only reproduces well the PdBI+30 m observations, but due to the higher resolution of the observations, also places much tighter constraints on the warp. The disk is most likely already warped on arcsec ($\sim 200 \text{ pc}$) scales and is evident within a radius of $20''$ (the S-like shape between SE1, C, and NW1) even if the warp is less dominant within $50''$ relative to the original Pott et al. model. The five symmetric CO(1–0) peaks (SE2, SE1, C, NW1, and NW2) detected by PdBI can be explained by orbit crowding effects. The two outer maxima merge into one feature on each side of the center in the beam of the IRAM 30 m telescope and thus at this resolution appear as single components. Besides the gas distribution, the gas kinematics can be almost completely explained by the model. The position-velocity diagrams of both data sets - mosaic and central pointing - unveil rapidly rotating nuclear gas within a radius of $\sim 800 \text{ pc}$, as seen in the simulated data. The high velocities in the center are produced by the inner warped rings. Thus, the dynamics of the molecular gas can be traced back to a continuous warped disk with concentric orbits. As in Pott et al. (2004), our model does not require a bar to explain the observed gas properties down to $\sim 200 \text{ pc}$. However, the warp model fails to give an interpretation of the asymmetry between the western and the eastern side in the mosaic maps, and the one found in the central pointing only map. The larger scale asymmetries might be indications for a possible tidal interaction with the companion galaxy, while the asymmetric structure of the gas distribution within the central 100–300 pc might be a prime candidate for driving the fuel into the central engine. A theory of how gas might be transported to the inner parts (here, to 100 pc) of accretion disks has been discussed by Duschl et al. (2000). They proposed a generalization of the α -disk theory through a viscosity prescription where turbulence at the critical effective Reynolds number plays a dominant role. Such viscous disks would evolve on time scales not exceeding the Hubble time and thus enable gas transport to the inner regions. The transport of gas over the remaining 100 pc to the black hole itself still raises many questions and problems. Even in the Milky Way, where a warped circumnuclear molecular torus (Guesten et al. 1987) provides a reservoir for accretion at a distance of only $\sim 1 \text{ pc}$ from the nucleus, the situation is not yet understood. In this context, the mechanisms of gas fueling to the inner few pc/subpc in active nuclei appear even more complex and hard to reveal. Besides the comprehension of our own Galactic center, only detailed studies of further nuclei with the highest angular resolution can provide answers to the wealth of open questions.

Chapter 6

NGC 1068

First results of new IRAM PdBI observations of the $^{13}\text{CO}(1-0)$ and $^{12}\text{CO}(2-1)$ in NGC 1068 are presented in this chapter. Very compact $^{12}\text{CO}(2-1)$ emission is detected at high velocities, supporting a previous finding by Schinnerer et al. (2000) and implying an enclosed mass of a few $10^8 M_{\odot}$. A nuclear ring structure with two peaks is found in the $^{12}\text{CO}(2-1)$ and $^{13}\text{CO}(1-0)$ maps consistent with previous works (Schinnerer et al. 2000; Helfer & Blitz 1995). In the outer regions, the $^{13}\text{CO}(1-0)$ line emission follows the $^{12}\text{CO}(1-0)$ line emission in the two spiral arms while it shows significant differences at the location of the NIR bar. The $^{12}\text{CO}(1-0)$ emission is mostly concentrated in the north-eastern part of the bar whereas $^{13}\text{CO}(1-0)$ line emission is detected at both sides. This implies significant differences and also strong asymmetries in the density of the gas since $^{13}\text{CO}(1-0)$ is known to trace denser gas regions with respect to $^{12}\text{CO}(1-0)$. This is also supported by the line ratios between $^{12}\text{CO}(1-0)$ and $^{13}\text{CO}(1-0)$. While the ratio is around 30-40 at the nuclear ring and the north-eastern part of the bar, it decreases down to ~ 10 at the south-western side of the bar and in the spiral arms. Both, continuum emission at 3 mm and as well at 1 mm is found. Besides a compact component, a jet is detected with $\sim 30\sigma$ at 3 mm and with 6σ at 1 mm. The counterjet is mapped with 6σ at 3 mm. The 3 mm continuum turns out to be in excellent agreement with other radio studies (e.g. Gallimore et al. 2004). The 1 mm continuum indicates a turnover in the non-thermal Spectral Energy Distribution (SED) similar to Sgr A*.

This chapter is outlined as following: a short introduction is given in Section 6.1. The IRAM PdBI observations are presented in Section 6.2. The first and preliminary results are discussed and compared with previous data in Section 6.3. Finally, the chapter finishes with a summary and an outlook for the further analysis of this data in Section 6.6.

6.1 Introduction

NGC 1068, one of the NUGA sources (Section 3.1), is one of the best studied Seyfert galaxies and regarded to be the archetype for unification schemes of this class of active galaxies. Khachikian & Weedman (1974) first classified NGC 1068 as Seyfert 2 due to the detection of unpolarized (direct-path) emission lines with narrow widths originating in the Narrow-Line-Region (NLR). The NLR appears to be extended to the North-East with respect to the nucleus (e.g. Groves et al. 2004). The radio jet (e.g. Gallimore et al. 2004) is found to be located in the same direction (see Fig. 6.1). Also emission from the broad line region (BLR) could be detected through polarized (scattered-path) emission lines with broad line widths (cf. Section 2.2.3; Antonucci & Miller et al. 1985). This strongly suggests that NGC 1068 contains a hidden Seyfert 1 nucleus supporting the unified theory for Seyfert galaxies. The position of the nucleus was narrowed down by radio continuum observations conducted by Gallimore et al. (2004). They report on a compact component with a flat spectrum lying in a maser disk to be most likely the central engine (Fig. 6.2). NGC 1068 is one of the few (i.e. ~ 30) extragalactic systems in which maser emission could be detected (Fig. 6.3). With the aid of H_2O maser emission, Greenhill & Gwinn (1997) achieved determining

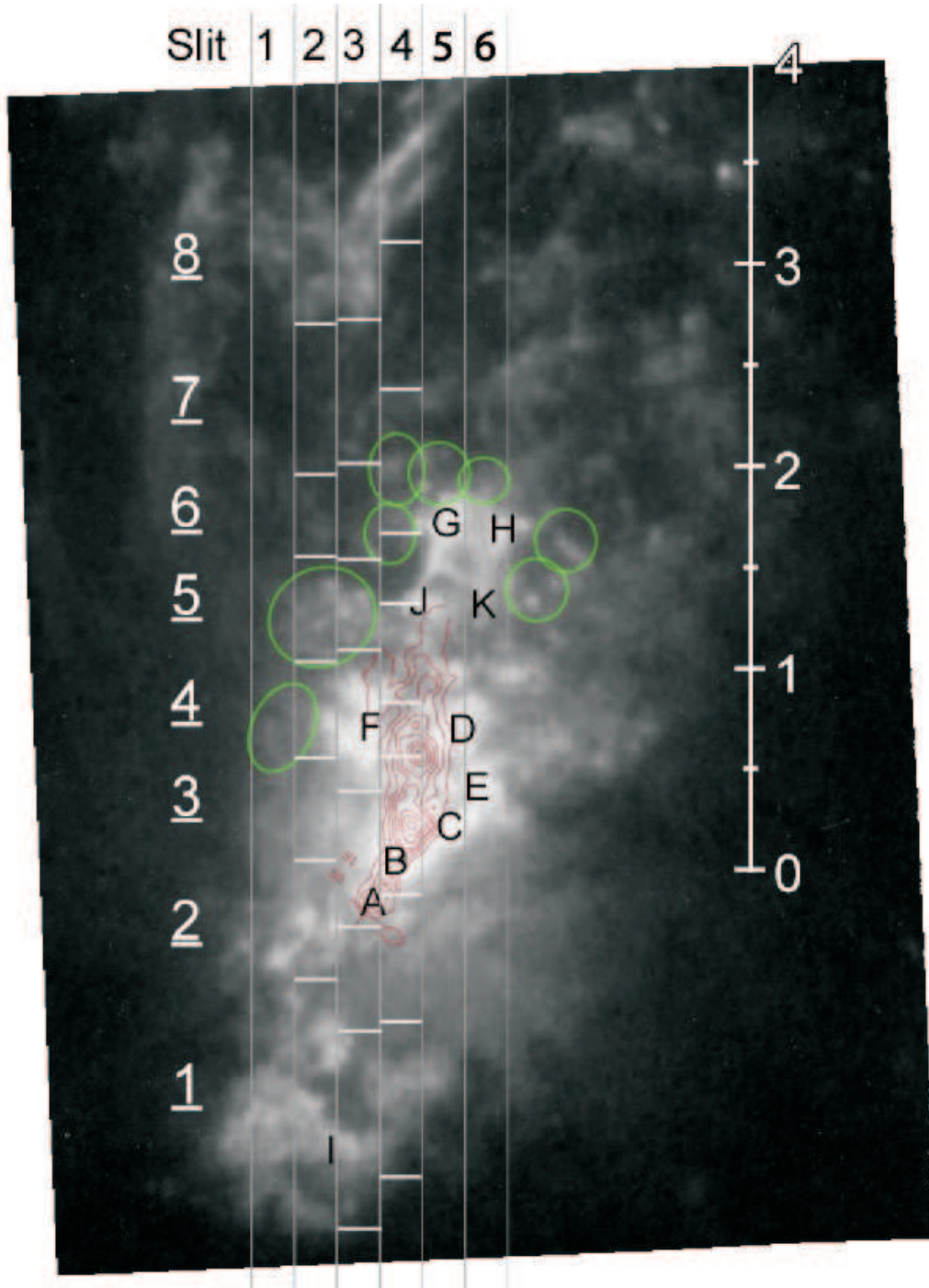


Figure 6.1: [OIII] map of the NLR superimposed with the radio jet (contours). Image was taken from Groves et al. (2004).

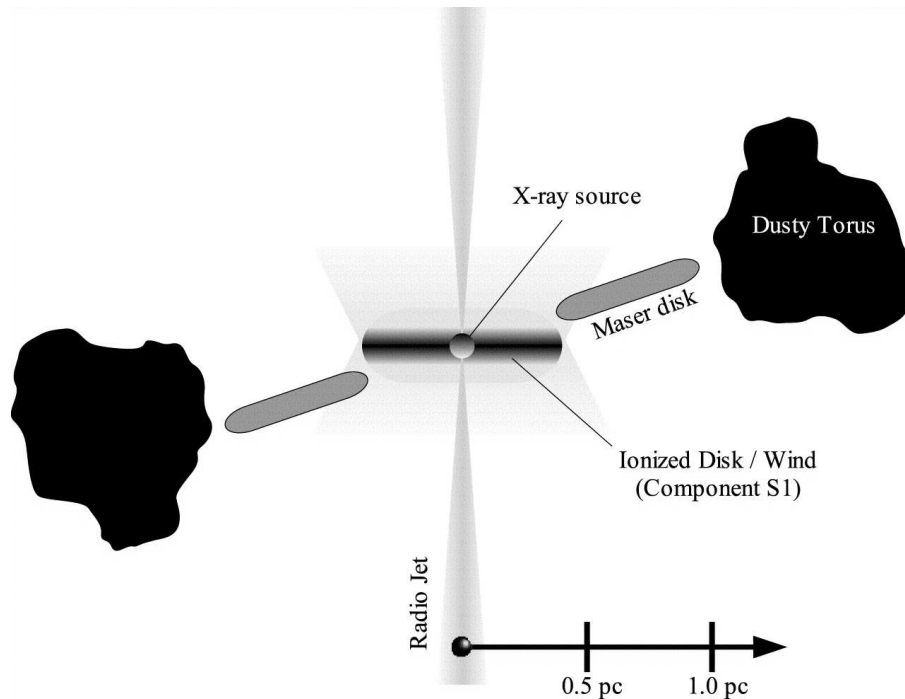


Figure 6.2: Model of the central engine in NGC 1068 proposed by Gallimore et al. (2004).

the mass of the AGN to $1.7 \times 10^7 M_{\odot}$ in the central 2.2 pc. The stellar characteristics of NGC 1068 are found to be also quite complex. A stellar cluster surrounds the nucleus with a diameter of ~ 40 pc (Thatte et al. 1997). Also a stellar bar becomes visible on larger scales extending over 2.3 kpc (Scoville et al. 1988, Thronson et al. 1989). A strong star formation ring was detected around this bar (Telesco et al. 1984; Davies, Sugai & Ward 1998). The bar as well as the starburst ring could also be mapped in molecular gas (Fig. 6.4; Schinnerer et al. 2000 and references therein).

6.2 Observations

Observations of the $^{13}\text{CO}(1-0)$ and $^{12}\text{CO}(2-1)$ emission in NGC 1068 were carried out with the IRAM PdBI in February 2003 using all six antennae in A configuration. The bandpass was calibrated on NRAO150 and 0420-014 while phase and amplitude calibration were performed on 0235+164 and 0238-084. A total bandwidth of 580 MHz with a spectral resolution of 1.25 MHz was used. Applying uniform weighting¹ in the mapping process, beam sizes are derived to $2.1 \times 1.2'' @ 32^\circ$ at 3mm and to $1.0 \times 0.6'' @ 36^\circ$ at 1mm.

6.3 The data - first results

In this section the first results of the new (2003) PdBI observations are presented which were conducted in the framework of this PhD thesis. They will be compared with a previous data set - obtained in 1997 - published by Schinnerer et al. (2000).

¹Actually, when speaking of uniform weighting, it rather corresponds to robust weighting which is a compromise between natural and pure uniform weighting. This is a convention in the IRAM GILDAS Packages.

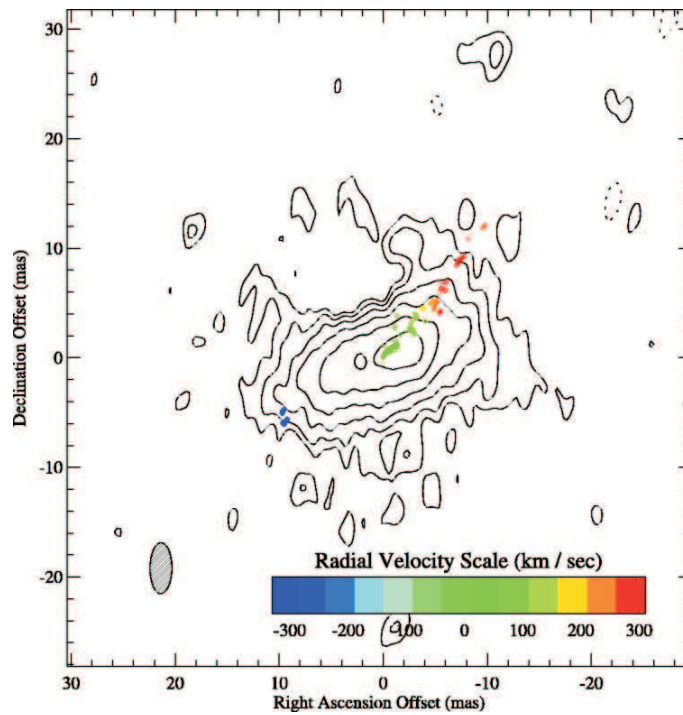


Figure 6.3: Map of the maser disc in NGC 1068 (Gallimore et al. 2004).

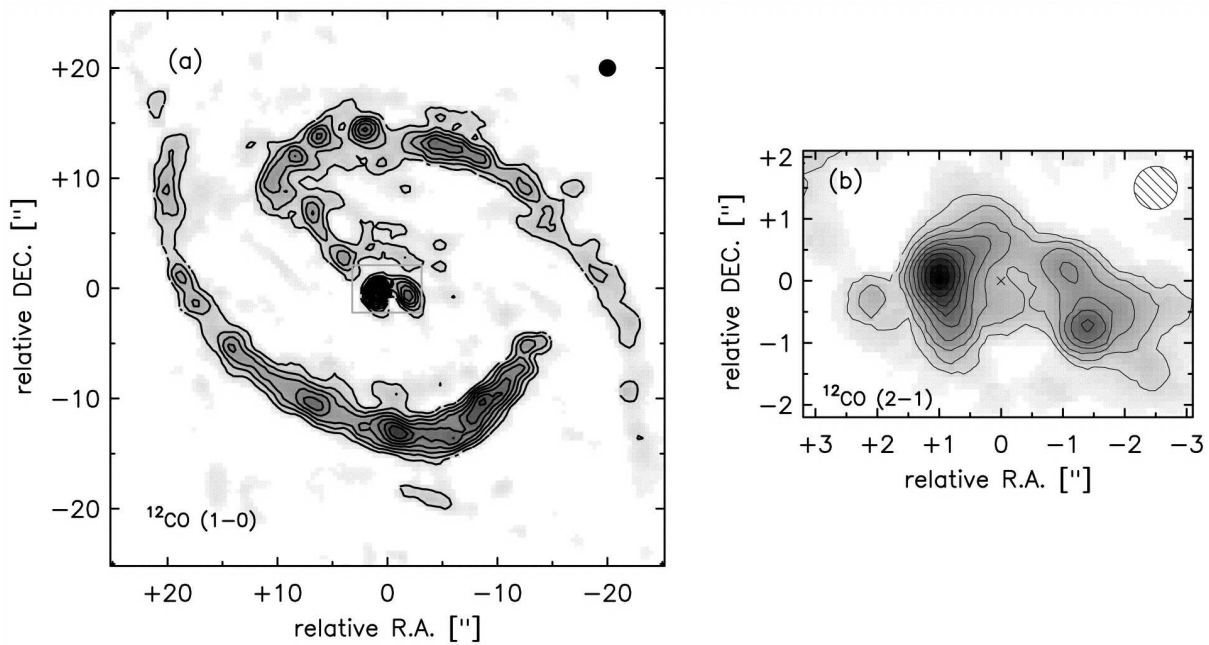


Figure 6.4: Velocity integrated $^{12}\text{CO}(1-0)$ and $^{12}\text{CO}(2-1)$ line emission map of NGC 1068 (Schinnerer et al. 2000).

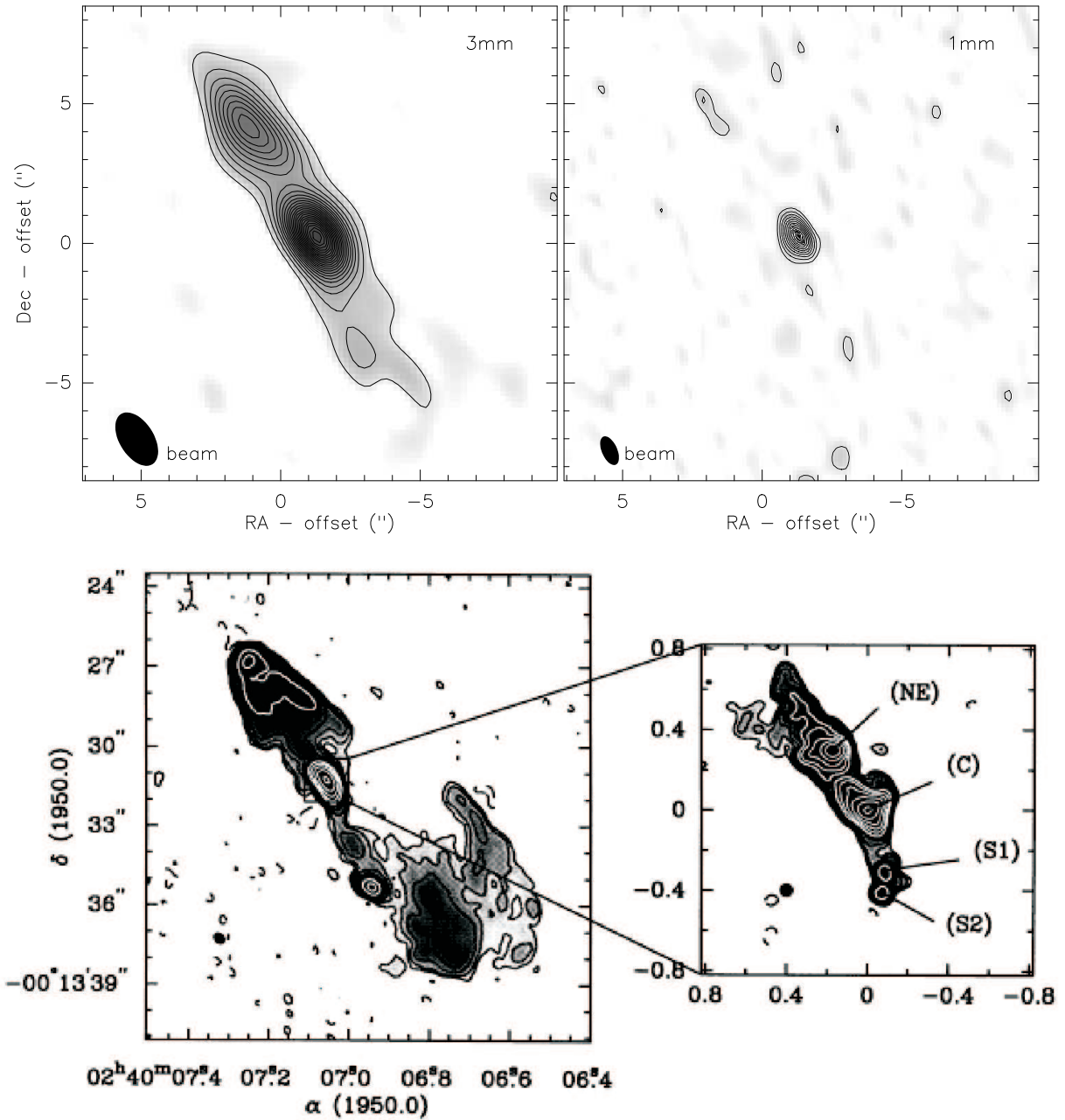


Figure 6.5: Continuum maps of NGC 1068 at 1 mm (*upper right panel*), 3mm (*upper left panel*) and 6cm (*lower panel*, Gallimore et al.). Contour levels are from $3\sigma=1.1$ to 25.3 mJy/beam in steps of 3σ at 3 mm and from $3\sigma=2.1$ mJy/beam in steps of 2σ . The beam size at both wavelengths is indicated as filled black ellipse in the lower left corner of the upper maps. The VLA (*lower left*) and MERLIN (*lower right*) 6cm maps are taken from Gallimore et al. (1996). The core is labeled here S1.

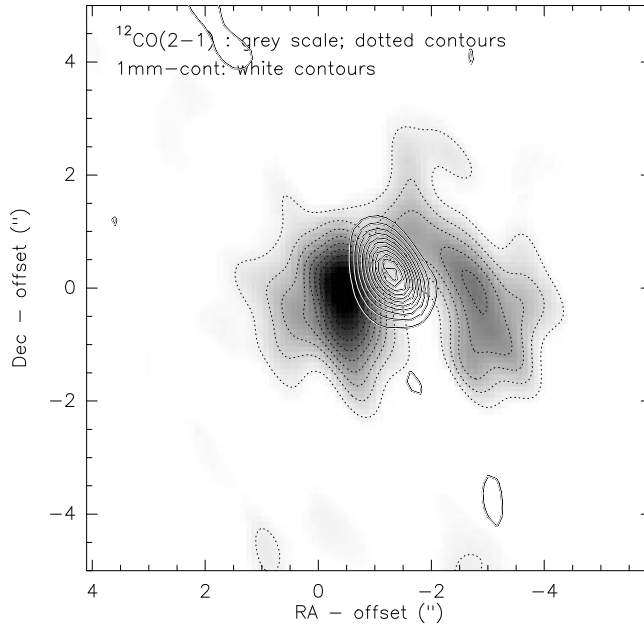


Figure 6.6: Overlay of the velocity integrated $^{12}\text{CO}(2-1)$ line emission with the 1.2 mm continuum. Contours are as in Fig. 6.5 and Fig. 6.8

Component	RA (offset) ^a [$''$]	Dec (offset) ^a [$''$]	flux [mJy/beam]	Size [$'' \times '' @^\circ$]
core-3mm	-1.27 ± 0.01	0.24 ± 0.01	30.0 ± 0.6	$(0.83 \pm 0.06) \times (0.6 \pm 0.07) @ (70 \pm 10)$
core-1mm	-1.29 ± 0.02	0.23 ± 0.02	22 ± 1	$(0.6 \pm 0.1) \times (0.47 \pm 0.04) @ (40 \pm 20)$
jet-3mm	1.08 ± 0.03	4.10 ± 0.03	24.0 ± 0.8	$(2.6 \pm 0.1) \times (1.22 \pm 0.05) @ (39 \pm 2)$
(jet-1mm) ^b	~ 2	~ 5	6 ± 2	-
counterjet-3mm	-2.8 ± 0.2	-3.8 ± 0.2	14 ± 2	$(5.5 \pm 0.7) \times (2.7 \pm 0.3) @ (56 \pm 5)$

Table 6.1: Continuum parameters for the 3 mm and 1 mm continuum. Parameters were determined by fitting Gaussian profiles to the respective components. ^a offsets with respect to $\alpha_{J2000} = 02^{\text{h}}42^{\text{m}}40.8^{\text{s}}$ and $\delta_{J2000} = -00^{\circ}00'47.94''$.

6.3.1 Continuum emission

The continuum maps at 3 mm and 1 mm were computed from the respective opposite side bands (Upper Side Band (USB) at 3 mm and Lower Side Band (LSB) at 1 mm) in which no line emission is expected. Continuum emission was detected at 3 mm ($\equiv 109.8$ GHz) and as well at 1 mm ($\equiv 231.1$ GHz) in contrast to Schinnerer et al. (2000).

6.3.1.1 3 mm

The 3 mm continuum map is shown in Fig. 6.5 revealing three different components, one associated with the nucleus, one with the jet and one with the counterjet. The jet component is elongated in North-East direction, agreeing with results found at cm wavelengths (lower panel of Fig. 6.5). Also a 6σ feature is detected on the opposite side of the nucleus indicating the counter jet. In contrast to Schinnerer et al. (2002) who confirmed the jet only within 3σ at a slightly higher frequency (115 GHz) and missed the counter jet, the new continuum data constitute a real improvement. Three elliptical Gaussian profiles were fitted to the data. The results are listed in

Table 6.1. The position of the core is determined at $\alpha_{J2000}=02^{\text{h}}42^{\text{m}}40.71^{\text{s}}$ and $\delta_{J2000}=-00^{\circ}00'47.7''$ consistent with the core position derived at 6 cm (Gallimore et al. 2004). Taking the fluxes of the core at 5 GHz of 12 ± 1 mJy (MERLIN; Gallimore et al. 2004), at 22 GHz of 19.1 ± 0.6 mJy (VLA, Gallimore et al. 1996) and at 109.8 GHz of 30 ± 0.6 mJy (PdBI), the spectral index of the core can be estimated to $\alpha \simeq 0.3$ ($f_{\nu} \propto \nu^{\alpha}$; Fig.6.7), i.e. the core spectrum is inverted consistent with Gallimore et al. (1996). Such a behaviour is expected for the compact core emission that might be produced by optically thick synchrotron emission (see Chapter B.1). Also, the jet fluxes are plotted at different frequencies showing a steep spectral index of ~ -1 which is consistent with optically thin synchrotron emission. The estimate of the spectral index of the core is biased by the fact, that the core component (S1, see Fig. 6.5) at 3 mm still includes contributions from other radio jet components (NE,C,S2) within $\sim 2''$, which are already visible on MERLIN scales (Gallimore et al. 1996). In contrast to the MERLIN maps in which these components could be separated from each other (Fig. 6.5), the new 3 mm map cannot distinguish between the central $2''$ features and thus also contains more extended emission than the MERLIN maps due to the lower angular resolution of the PdBI. The contribution of the NE,C and S2 components to the 3 mm flux can be estimated to $\sim 25\%$ from the MERLIN fluxes at 22 GHz assuming a steep jet spectrum with $f_{\nu} \propto \nu^{-1}$ for these features. Subtracting this from the 3 mm flux, the spectral index is lowered slightly down to 0.2 instead of 0.3 (Fig. 6.7).

6.3.1.2 1 mm

We detect clear ($>20\sigma \equiv 22$ mJy/beam) continuum emission at 1 mm in our new data set (Fig. 6.5) while Schinnerer et al. (2000) report on an upper limit of the 1 mm continuum of 6 mJy. To understand the discrepancy to Schinnerer et al. (2000), the velocity channel maps of the 1997 data set were also reanalysed parallel to our new data. While the continuum emission remains hidden in the individual velocity channel maps of this old (1997) data set because its flux of ~ 22 mJy (Table 6.1) is of the order of the noise level (3σ), it is, however, clearly visible in the integrated map by taking velocities $> +250$ km s $^{-1}$ and < -250 km s $^{-1}$ contrary to what is reported in Schinnerer et al. (2000). The flux and position of this 1 mm component is in agreement within 10% with what one finds in the new data by either integrating over the line free channel maps, similar to what was done with the Schinnerer data, or by taking the opposite side band in which no line emission should occur. The position of the core derived from the new (2003) data is consistent with the position derived at 3 mm. However, the flux of the 1 mm core component does not follow the power law fitted to the lower frequencies in Fig.6.7 but indicates a turnover in the synchrotron spectrum (see Chapter B.1), similar to what is found for Sgr A*. One has again to keep in mind on the one hand, that also the core emission at 1 mm might still be biased by the different components (NE,C and S2; compare Fig.6.5) within the central $2''$ detected with MERLIN or VLBA. Assuming a steep spectral index of $\alpha = -1$ and taking the (MERLIN) fluxes at 8.4 GHz (Gallimore et al. 1997), the fraction of these further components (NE,C, S2) to the pure core (S1) emission at 1 mm can be estimated to $\sim 20\%$. Thus, the 1 mm continuum should most likely be mainly dominated by S1 alone and only slightly lower than observed (Fig. 6.5). On the other hand, resolving effects might cause an artificially lower flux since the beam at 1 mm is smaller than the one at 3 mm. If the turnover is not real but an artefact of resolving extended emission, the 1 mm flux of S1 can be extrapolated to ~ 40 mJy from the 3 mm emission accounting also for the contribution of NE, C and S2, i.e. twice as much as what is detected. This is rather unlikely since S1 appears to be quite compact. Thus, resolving effects are supposed to be negligible so that the turnover is most likely real. Besides the core emission, a further weak ($\sim 5\sigma$) continuum peak is detected at (roughly) the position of the radio jet. The flux is compatible with a steep jet spectrum ($f_{\nu} \propto \nu^{-1}$) extrapolated from lower frequencies.

6.3.2 $^{13}\text{CO}(1-0)$ line emission

The 3 mm continuum was first subtracted from all (continuum+line) channels. The integrated $^{13}\text{CO}(1-0)$ line emission is plotted together with the integrated $^{12}\text{CO}(2-1)$ line emission in Fig. 6.8. The $^{13}\text{CO}(1-0)$ emission is located in two spiral arms of diameter $\sim 40''$ agreeing with the $^{12}\text{CO}(1-0)$ emission (Fig. 6.10; Schinnerer et

²No continuum data from the LSB is available for the 1997 data set.

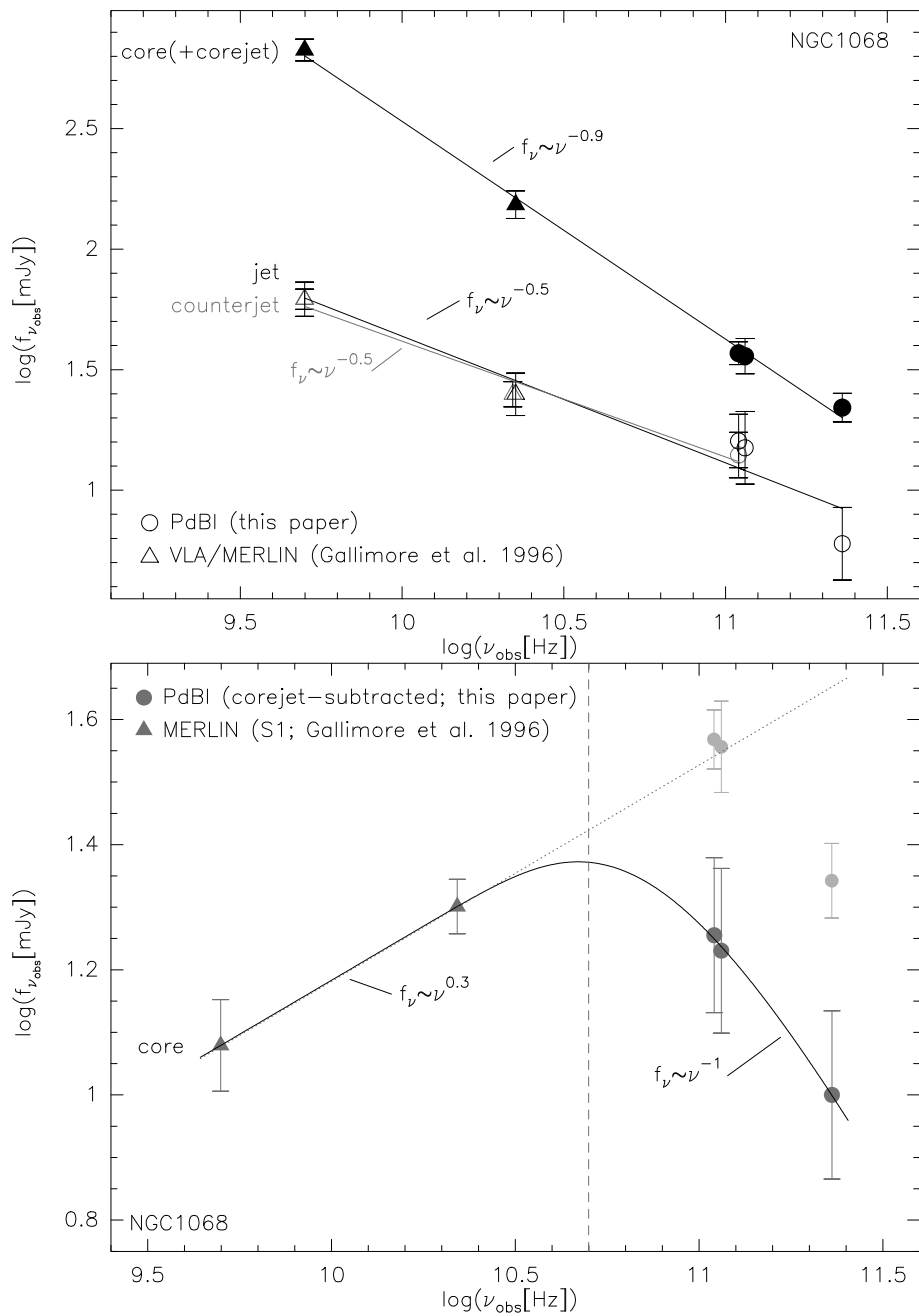


Figure 6.7: Spectral energy distribution of the continuum emission in NGC 1068 from cm to mm wavelengths. *Upper panel:* The 230 GHz and 110 GHz fluxes of the core (*filled black circles*), the jet (*open black circles*) and of the counter-jet (*open grey circles*) are compared to 22 GHz and 5 GHz VLA observations (*triangles*; Gallimore et al. 1996). The filled black triangles correspond to fluxes still including contributions from the corejet components visible on MERLIN scales ($\leq 1''$; Gallimore et al. 1996), i.e. they do not represent the pure core flux. *Lower panel:* Pure core spectrum. The filled grey triangles show the cm flux obtained with higher angular resolution MERLIN observations (Gallimore et al. 1996; their S1 component). The filled grey circles represent the (estimated) pure core flux at mm wavelengths for which the corejet flux was subtracted (see text for more details). The light grey circles indicate the uncorrected PdBI fluxes.

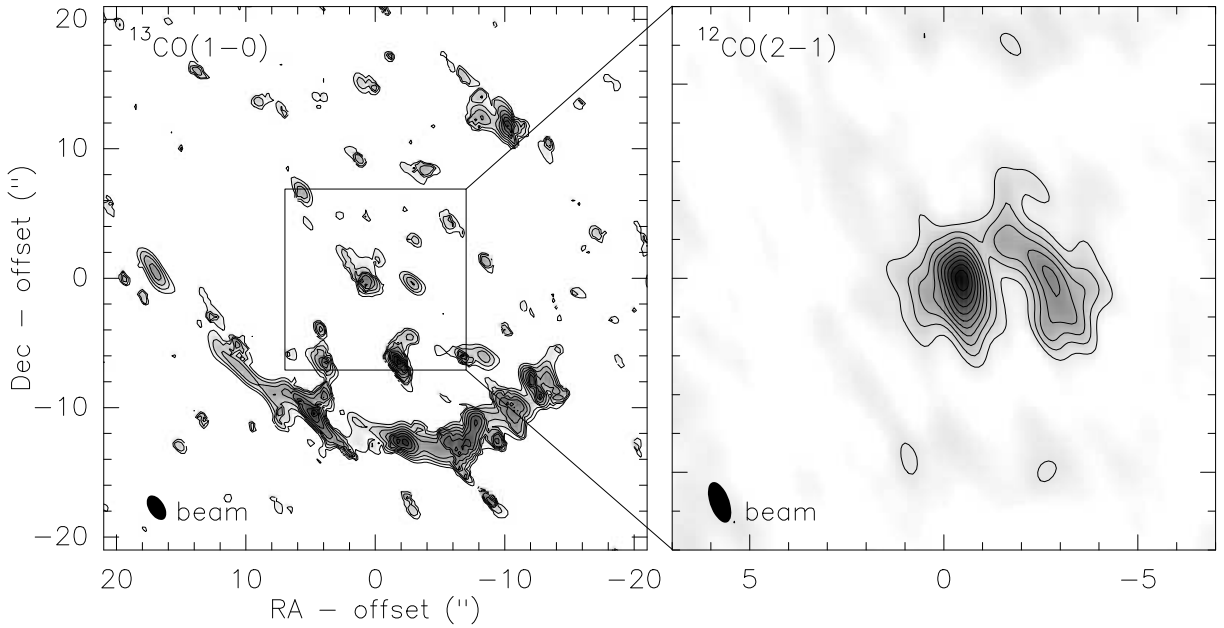


Figure 6.8: Velocity integrated $^{13}\text{CO}(1-0)$ (*left*) and $^{12}\text{CO}(2-1)$ (*right*) line emission of NGC 1068 from the new data. Contours are from $3\sigma=0.5\text{mJy/beam km s}^{-1}$ in steps of 1σ for the $^{13}\text{CO}(1-0)$ line and from $5\sigma=7\text{Jy/beam km s}^{-1}$ in steps of 5σ for the $^{12}\text{CO}(2-1)$.

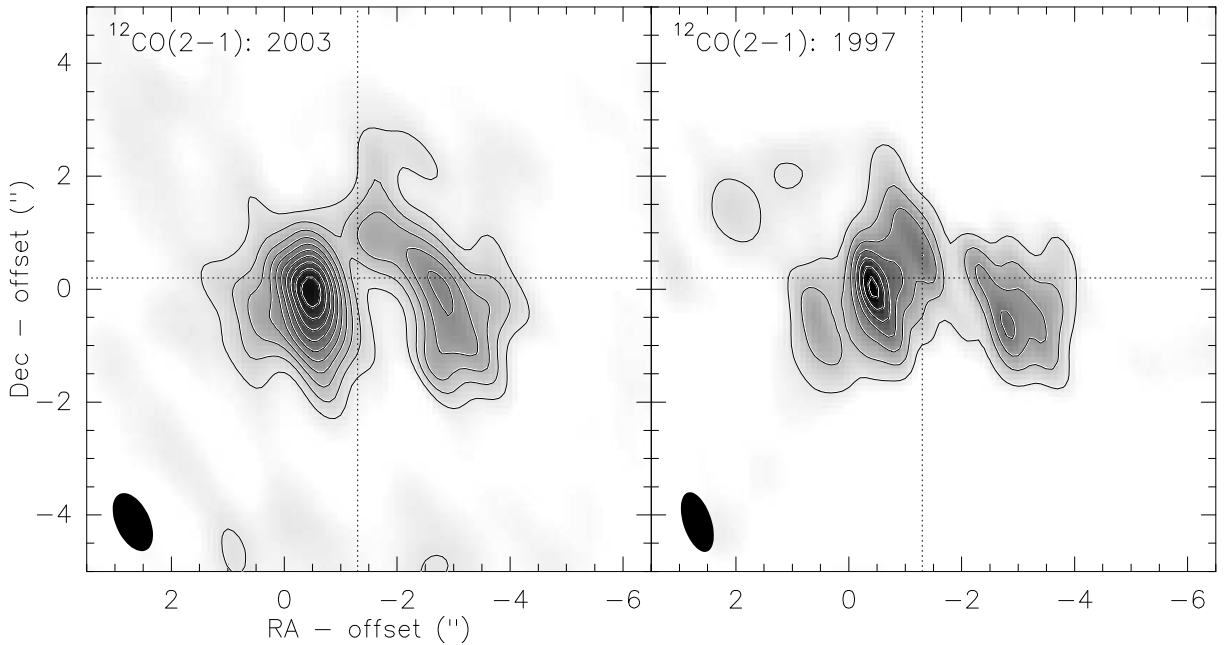


Figure 6.9: Velocity integrated $^{12}\text{CO}(2-1)$ line emission of NGC 1068 for the new (*left*) and old (*right*) data. Contours are from $5\sigma=7\text{Jy/beam km s}^{-1}$ in steps of 5σ for both data sets.

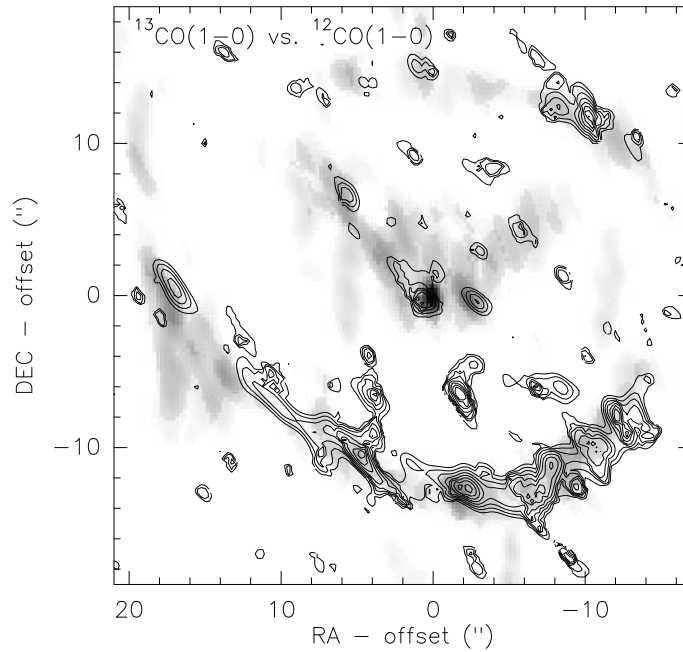


Figure 6.10: Velocity integrated $^{12}\text{CO}(1-0)$ (grey scale) and $^{13}\text{CO}(1-0)$ (contours) line emission of NGC 1068. Contours are identical to Fig.6.8. $^{13}\text{CO}(1-0)$ data are from our new observations while $^{12}\text{CO}(1-0)$ data are taken from Schinnerer et al. (2000).

al. 2000 and references therein). The southern arm is more luminous than the northern arm. While the $^{13}\text{CO}(1-0)$ emission follows nicely the spiral structure of the $^{12}\text{CO}(1-0)$ emission, the situation on the NIR bar is quite different. The $^{12}\text{CO}(1-0)$ emission is concentrated on the north-eastern part of the bar whereas the $^{13}\text{CO}(1-0)$ emission is found at both sides of the bar (Fig.6.10). A further peak at roughly $(2'', -7'')$ is also detected. It has no counterpart at $^{12}\text{CO}(1-0)$. Going down to radii of $\sim 4''$, two emission knots are visible in the $^{13}\text{CO}(1-0)$ emission consistent with $^{12}\text{CO}(1-0)$. The line ratios between $^{12}\text{CO}(1-0)$ and $^{13}\text{CO}(1-0)$ are estimated to ~ 30 at the eastern knot of the ring, to ~ 25 at the western knot, to ~ 40 at the north-eastern part of the bar, to ~ 6 at the south-western part of the bar, and to ~ 10 along the spiral arms. The latter value is consistent with the one published by Helfer & Blitz (1995) for NGC 1068 and with other nearby galaxies (e.g., Sage & Isabell 1991). This might indicate that at least in the spiral arms the physical conditions can be regarded as “normal” while the bar shows a strong asymmetry in its gas density. For both the $^{12}\text{CO}(1-0)$ and $^{13}\text{CO}(1-0)$ line, the spectra, which were integrated over the spiral arms, the bar and the inner ring, are plotted in Fig. 6.11. The line width of $^{13}\text{CO}(1-0)$ is slightly narrower than of $^{12}\text{CO}(1-0)$ but accounting also for the errors this difference is still within 10% and thus rather negligible.

6.3.3 $^{12}\text{CO}(2-1)$ line emission

The 1 mm continuum was first subtracted from all (continuum+line) channel maps for both data sets although having only a small influence on the final results since the continuum is of the order of the noise level in the channel maps. The new data were not combined with the data set of Schinnerer et al. (2000) due to several reasons which will be explained in the following. As already indicated in the $^{13}\text{CO}(1-0)$ and $^{12}\text{CO}(1-0)$ line emission, also the $^{12}\text{CO}(2-1)$ line emission reveals a strong double-peak structure in our new data (Fig. 6.8). The third peak at $^{12}\text{CO}(2-1)$ mentioned in Schinnerer et al. (2000; cf. Fig. 6.4) cannot be confirmed. This feature is most likely an artefact of the deconvolution process. Also, the positions of the two peaks with respect to each other are not identical (see Fig.6.9). While the map of Schinnerer et al. (2000) shows two peaks which lie on a line with a PA

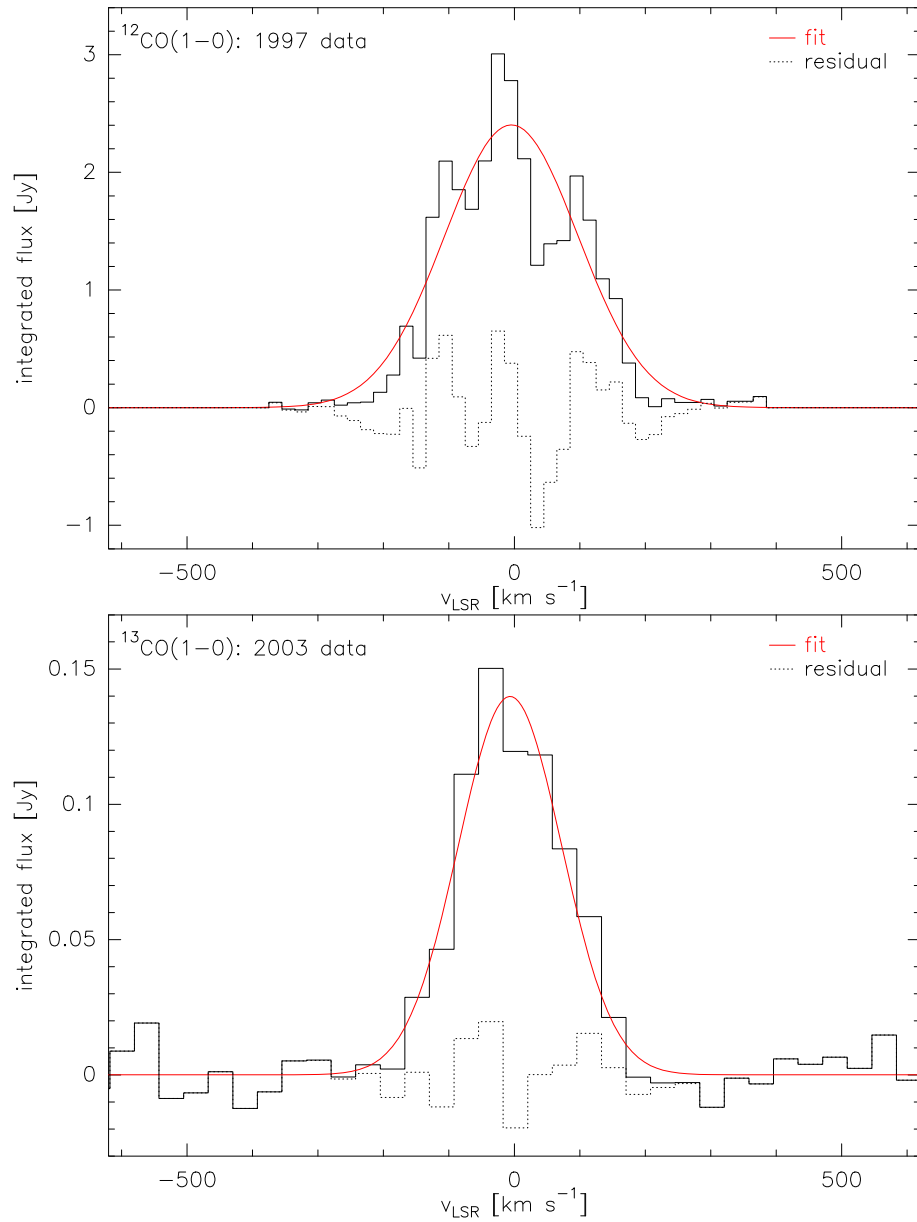


Figure 6.11: Spatially (over spirals, bar and nuclear ring) integrated $^{12}\text{CO}(1-1)$ and $^{13}\text{CO}(1-1)$ spectrum of NGC 1068 derived from the new 2003 data (*upper panel*) and from the old 1997 data (*lower panel*). A Gaussian fit with one component has been applied to the 2003 and 1997 data, which is marked with a solid red line. The dotted line indicates the residuum between the fit and the data.

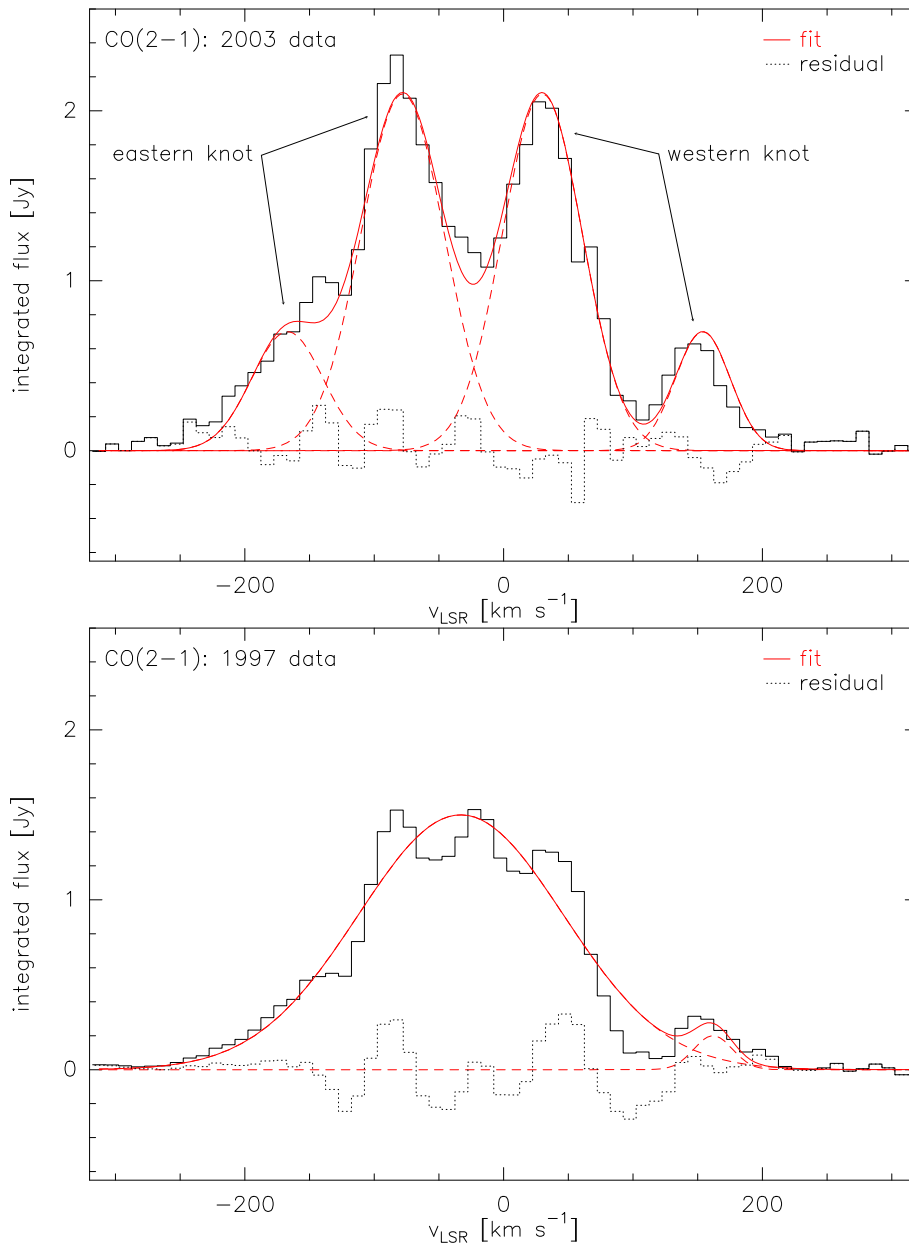


Figure 6.12: Spatially (over the ring) integrated $^{12}\text{CO}(2-1)$ spectrum of NGC 1068 derived from the new 2003 data (*upper panel*) and from the old 1997 data (*lower panel*). A Gaussian fit with four (2) components has been applied to the 2003 (1997) data, which is marked with a dashed red line for each of the four (two) components and with a solid red line of the composite fit. The dotted line indicates the residuum between the fit and the data.

Line	data set	component	S_ν [Jy km s ⁻¹] ^a	M_{gas} [10 ⁸ M_\odot]	velocity width [km s ⁻¹]	M_{dyn} [10 ⁸ M_\odot]
¹² CO(1-0)	1997	total	640±40	16	240±20	90
		ring	100±10	2.5	180±7	6
¹³ CO(1-0)	2003	total	28±1	-	190±8	60
¹² CO(2-1)	2003	eastern knot	223±6	1.4 ^b	-	-
		western knot	201±6	0.8 ^c	-	-
		ring	424±10	2.4 ^d	228±10	12
¹² CO(2-1)	1997	ring	300±10	1.8 ^e	190±10	8

Table 6.2: CO line parameters and gas/dynamical masses for NGC 1068. ^a obtained by spatially integrating over the respective region and fitting Gaussian profiles to the spectrum. ^b assuming a line ratio of $R_{21/10} = ^{12}\text{CO}(2-1)/^{12}\text{CO}(1-0) \simeq 1$ (Usero et al. 2004). ^c $R_{21/10} \simeq 1.5$ (Usero et al. 2004). ^d adding the eastern and western knot. ^e assuming an “average” $R_{21/10} \simeq 1$ (Usero et al. 2004).

of roughly 60°, the two peaks in our new data are rather located on a horizontal line (PA=90°). Furthermore, the integrated fluxes are not consistent. The fluxes given in Schinnerer et al. (2000) are too low (by a factor of 20, cf. Fig. 6.12). Also, by re-estimating the integrated ¹²CO(2-1) line emission from the old (1997) data set directly, only 70-80% of the integrated peak flux derived in our new data set is found towards the western and eastern knot. This difference can be explained with the improved uv-coverage of the new 2003 observations. As a further consequence, the iso-velocity map of the new 2003 data reveals much clearer a ring structure than the old 1997 data (Fig. 6.13). Looking at the position-velocity (pv) diagrams taken along cuts every 20° starting with 10° and with all going through the radio core position (see grey lines in Fig. 6.13), a very complex kinematic structure becomes visible in our new data (Fig. 6.14). Parts of it could already be modelled by Schinnerer et al. (2000) by using a warp and a bar model while other parts remained either questionable or unexplainable. Unfortunately, the pv-diagrams of the new data alone are not in all respects identical with the one published by Schinnerer et al. (2000) which might be a sign for a different image processing of the ¹²CO(2-1) data and also sensitivity effects. While the diagram at PA=110° of the combined data is very similar to the pv diagram published by Schinnerer et al. (2000), the maps at PA=10° and 150° are significantly different in some details. At PA=10°, the feature visible in the Schinnerer et al. (2000) maps at velocity $\sim 50 \text{ km s}^{-1}$ and $-0.5''$ has disappeared in the combined data set. At PA=150°, the strongest peak in the Schinnerer et al. (2000) maps is located at 20 km s^{-1} and $+0.5''$ while in the new data the strongest peak is at 100 km s^{-1} and $+1''$. These differences were quite suspicious and cannot ad hoc be explained. Thus, the old (1997) data were separately re-mapped using the uniform beam sizes and new pv diagrams were derived identical to the new data to allow for a better comparison. Although the global morphology is comparable, some of the discrepancies still remain above all for pv-maps with $\text{PA} \geq 130^\circ$. Also, the lower flux level in the 1997 data is again visible. The differences are most likely due to sensitivity limitations in the old 1997 data. This might explain the observed differences. Thus, a combination of both data sets, which have such a big discrepancy between their data quality, is not the best choice here although generally increasing the sensitivity.

One of the open points is the reliability of a very compact ($\leq 1''$), strongly rotating nuclear component at the position of the radio core that Schinnerer et al. (2000) detected with 3σ in their data. The new data alone also independently indicate such a nuclear component although it is shifted by about $\sim 0.4''$ more to the East but this is still within the position uncertainties. The new data result in a slightly better detection of $4 - 5\sigma$ supporting the finding of Schinnerer et al. (2000).

Another open point lies in redshifted gas (see PA=10,30 in Fig. 6.14 at a radius of $\sim 1.5''$) that Schinnerer et al. (2000) failed at explaining with their simulations and that was again found in the new data as well. Based on the new data, new simulations will be carried out in the framework of a diploma thesis starting in January 2005.

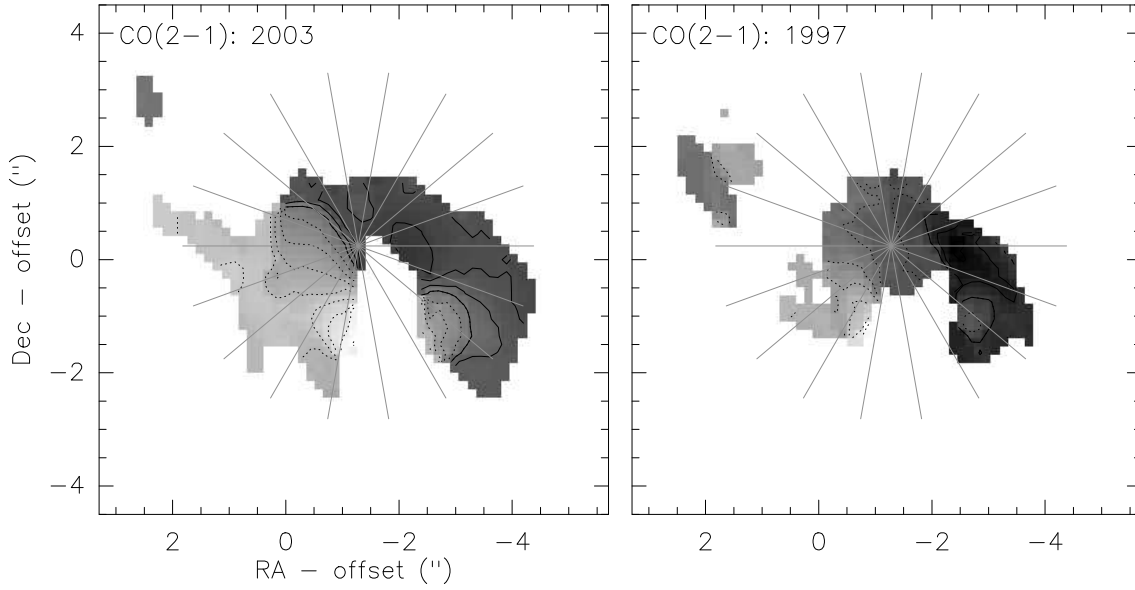


Figure 6.13: Iso-velocity diagrams of the nuclear $^{12}\text{CO}(2-1)$ line emission for the new 2003 data (*left*) and the old 1997 data (*right*). Contour levels are from -160 km s^{-1} to 120 km s^{-1} in steps of 20 km s^{-1} . The grey solid lines mark the cuts along which the position velocity diagrams were taken.

6.4 Gas and dynamical masses

The higher integrated $^{12}\text{CO}(2-1)$ line intensity derived from our new data (see Figure 6.12) imply a much higher gas mass of $\sim 2.4 \times 10^8 M_{\odot}$ (Equation 5.4) for the inner ring assuming a line ratio of 1-1.5 between $^{12}\text{CO}(2-1)$ and $^{12}\text{CO}(1-0)$ along the ring (Usero et al. 2004; Table 6.2). This is consistent with the gas mass derived from the $^{12}\text{CO}(1-0)$ line of $\sim 2.5 \times 10^8 M_{\odot}$. The total gas mass can be estimated from the old $^{12}\text{CO}(1-0)$ data yielding a value of $\sim 1.6 \times 10^9 M_{\odot}$, which is a factor of 2 as much as the value calculated by Schinnerer et al. (2000) who used the H_2 column densities to integrated temperatures conversion factor of $2 \times 10^{20} \text{ cm}^{-2} (\text{K km s}^{-1})^{-1}$ (Strong et al. 1987). We based our estimate on the standard $M_{\text{gas-to-}L'_{\text{CO}}}$ conversion factor of $4.8 M_{\odot} / (\text{K km s}^{-1} \text{ pc}^2)$ (Solomon & Barrett 1991)³. Both conversion factors agree with each other and the differences in the two calculation might thus rather be due to a too low source area in Schinnerer et al. (2000).

Where possible, the dynamical masses were determined via the following equation (based on the Virial theorem: $E_{\text{kin}} = -\frac{1}{2}E_{\text{pot}}$):

$$M_{\text{dyn}}(r) = v(r)^2 \cdot r \cdot \frac{1}{G} \cdot \sin^{-2} i \quad (6.1)$$

$$= 2.3 \cdot 10^5 \cdot \left(\frac{v(r)}{\text{km s}^{-1}} \right)^2 \cdot \frac{r}{\text{kpc}} \cdot \sin^{-2} i M_{\odot} \quad (6.2)$$

Actually, this equation is true a spherical gas distribution (Combes et al. 1995). For a a gas disk, one has to multiply this equation with $2/\pi=0.64$, i.e.

$$M_{\text{dyn}}(r) = 1.5 \cdot 10^5 \cdot \left(\frac{v(r)}{\text{km s}^{-1}} \right)^2 \cdot \frac{r}{\text{kpc}} \cdot \sin^{-2} i M_{\odot} \quad (6.3)$$

In the central $r=2''$ ($\equiv 0.16 \text{ kpc}$), i.e. for the inner ring, the dynamical mass is derived to $\sim 2 \times 10^9 M_{\odot}$ and for a radius of $\sim 18''$ (or 1.4 kpc equivalently), the dynamical mass results in a value of $\sim 1 \times 10^{10} M_{\odot}$. Accounting also

³see Equation 5.4

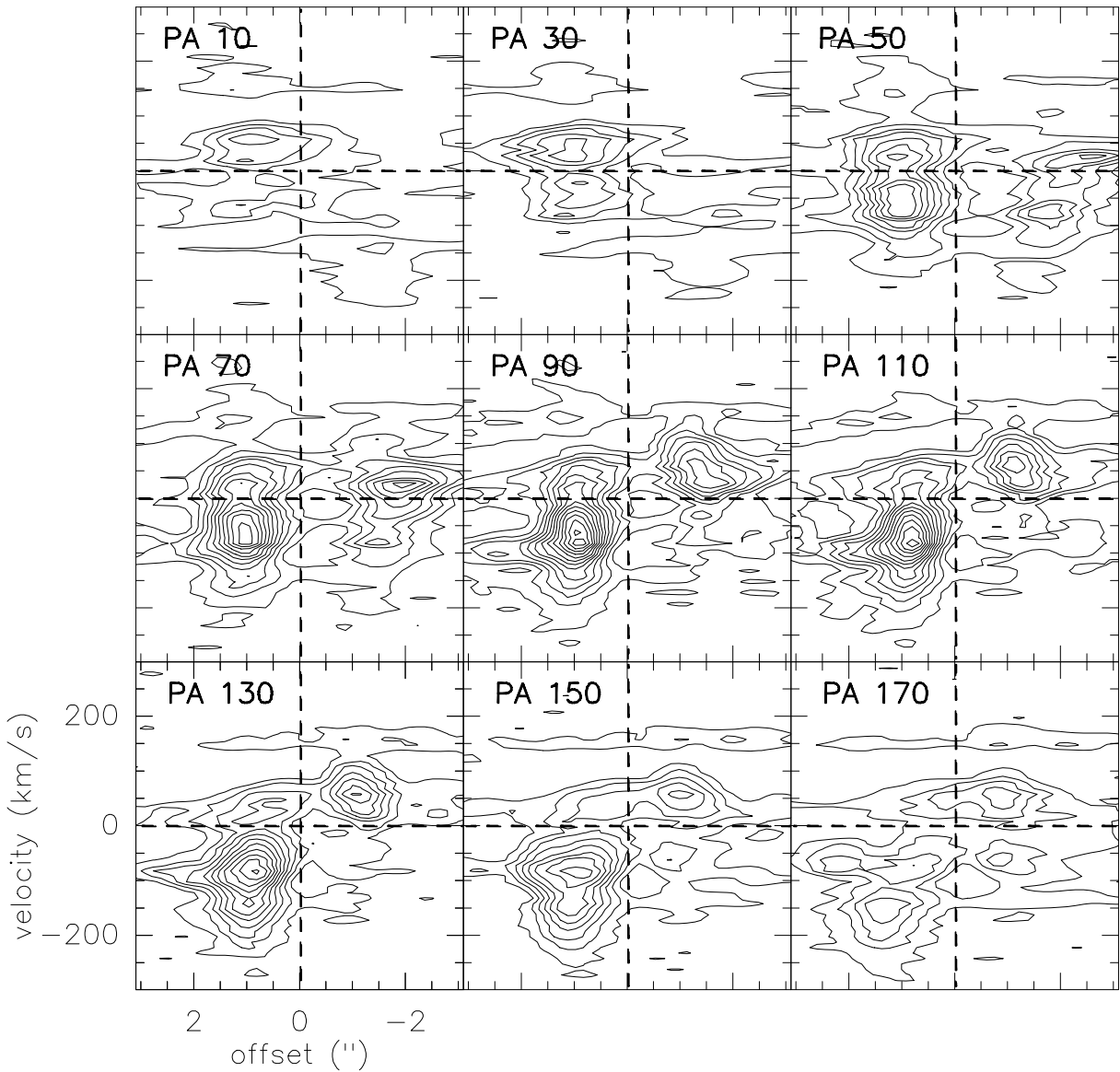


Figure 6.14: Position velocity diagrams of the nuclear $^{12}\text{CO}(2-1)$ line emission along different position angles for our new data alone (cuts indicated in Fig. 6.13). Contour levels are from $3\sigma=18\text{mJy/beam}$ in steps of 6σ .

for the highly nuclear component found in the $^{12}\text{CO}(2-1)$ line, the enclosed mass within the inner $0.7''$ amounts to $\sim 5 \times 10^8 M_{\odot}$ which is one order of magnitude more than the estimate for the black hole (inner 2 pc) via maser emission (Greenhill & Gwinn 1997). As already pointed out by Schinnerer et al. (2000), the enclosed mass via the $^{12}\text{CO}(2-1)$ emission is most likely still dominated by the central compact part of the stellar cluster in a radius of $0.7''$ ($\equiv 50$ pc) detected by Thatte et al. (1997).

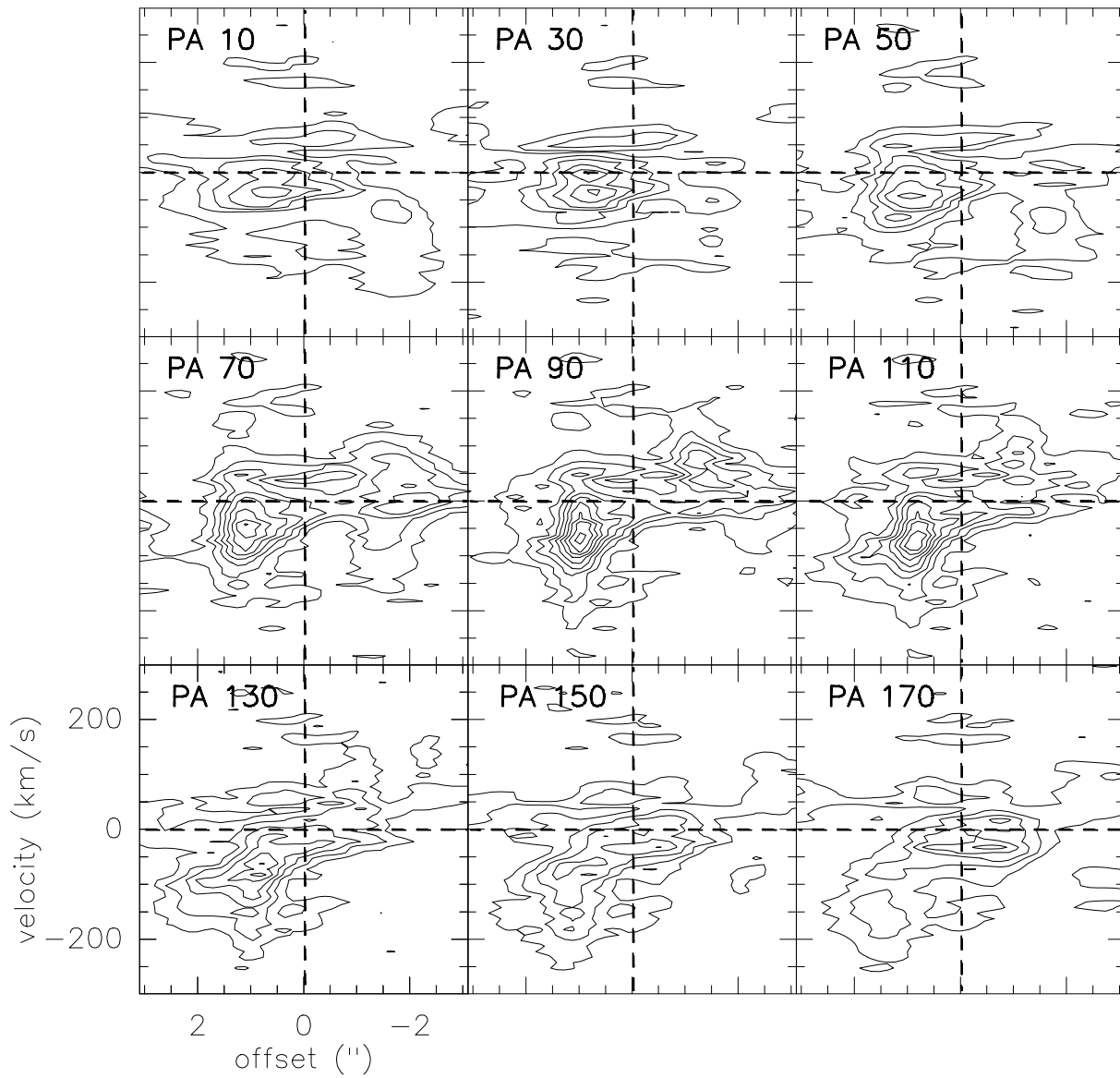


Figure 6.15: Position velocity diagrams of the nuclear $^{12}\text{CO}(2-1)$ line emission along different position angles (cuts indicated in Fig. 6.13). for the old data set alone (Schinnerer et al. 2000). Contour levels are from $3\sigma=18\text{mJy/beam}$ in steps of 6σ .

6.5 Estimating the magnetic flux density around the black hole

Kellermann & Pauliny-Toth (1981) provide the following equation that allows to calculate the maximum or frequency ν_m of the synchrotron emission (compare Section B.1)

$$\nu_m[\text{GHz}] = f(\gamma) \cdot B^{\frac{1}{5}}[\text{Gau\ss}] \cdot S_m^{\frac{2}{5}}[\text{Jy}] \cdot \theta^{-\frac{4}{5}}[\text{mas}] \cdot (1+z)^{\frac{1}{5}} \quad (6.4)$$

with $f(\gamma)$ (with $f(\gamma=2)=8$; γ is the Lorentzfactor) being the distribution of relativistic electrons⁴, B as magnetic flux density, S_m the flux at ν_m , θ the angular source size and z the redshift of the source. ν_m is also called the synchrotron self absorption frequency since it denotes the frequency below which the emission becomes optically thick. Resolving the equation after B , one gets

$$B[\text{Gau\ss}] = 3 \cdot 10^{-5} \cdot (\nu_m[\text{GHz}])^5 \cdot (S_m[\text{Jy}])^{-2} \cdot (\theta[\text{mas}])^4 \cdot (1+z)^{-1} \quad (6.5)$$

where $\text{mas} \equiv$ milli-arcsecond. Assuming $z = 0.004$, $\nu_m=50$ GHz, $S_m=0.026$ Jy and $\theta \simeq 0.02$ mas⁵, B is determined to a few Gau\ss. This value is of the order of the estimated magnetic flux density in SgrA* (Quataert & Gruzinov 2000)⁶. However, one has to keep in mind that this determination is very sensitive to the assumed angular size θ . By taking an angular size which differs by a factor of 2 from the value taken above, the magnetic flux density must already be corrected by a factor of 16, i.e. by roughly one order of magnitude.

6.6 Summary and Outlook

In this chapter, some first and preliminary results of new IRAM PdBI observations of the ¹³CO(1–0) and ¹²CO(2–1) line emission were presented. Also, new information was gained on the 3 mm and 1 mm continuum. Besides the 27σ detection of the jet at 3 mm, the counterjet can also be confirmed with 6σ . Positions, fluxes, and position angles of the jet components are in excellent agreement with other radio continuum studies (e.g., Gallimore et al. 2004). Furthermore, 1 mm continuum emission was also detected at the position of the core with $\sim 20\sigma$ and at the position of the jet with $\sim 6\sigma$. The core emission at 1 mm indicates a turnover in the SED similar to what is reported for Sgr A* (for a review see Eckart et al. 2004) although resolution effects which could also provoke an artificial decrease of the flux between 3 mm and 1 mm, cannot totally be disregarded. The CO emission is also quite consistent with previous publications but differences are found, too. The distribution of the ¹³CO(1–0) emission follows the one of the ¹²CO(1–0) at the outer spiral rings while the distribution along the bar is quite different. The ¹²CO(1–0) is detected to be concentrated at the north-eastern part of the bar (Schinnerer et al. 2000) while ¹³CO(1–0) can be mapped at both sides. However, lower angular resolution observations of NGC 1068 conducted with the BIMA/NRAO array by Helfer & Blitz reveal also ¹²CO(1–0) emission at the south-western part of the bar. This difference between Helfer & Blitz (1996) and Schinnerer et al. (2000) might be explainable by the lower angular resolution of the BIMA observation and resolution effects in the PdBI maps but it cannot, however, explain the differences between the ¹²CO(1–0) and ¹³CO(1–0) distribution since the latter line has been mapped at similar angular resolution compared to the ¹²CO(1–0) line. Thus, resolution effects should play a comparable role at both lines. This indicates that the difference between ¹³CO(1–0) and ¹²CO(1–0) along the bar might rather be an intrinsic property of NGC 1068 revealing the dominance of denser gas in the bar and an asymmetry of less dense gas traced by the ¹²CO(1–0) line. The new data of ¹²CO(2–1) agrees in its global morphology with Schinnerer et al. (2000), although some significant difference between the old 1997 data set and our new one are also discovered. The strongly rotating nuclear component indicated at 3σ in the data by Schinnerer et al. (2000)

⁴ $N_e = N_0 \cdot E^{-\gamma}$

⁵ The assumed angular size corresponds to a radius of ~ 100 Schwarzschild radii which is roughly the size of the accretion and maser disc (see Fig. 6.2 and Gallimore et al. 2004). The Schwarzschild radius is defined as $R_S = 2 \cdot G \cdot M_{\text{BH}} \cdot c^{-2} = 3 \times M_{\text{BH}}[M_{\odot}]$ km.

⁶ Assuming accretion rates beyond the Bondi value

can now be independently supported with a $4 - 5\sigma$ detection in our new data set. This nuclear component implies an enclosed mass of a few times $10^8 M_{\odot}$ within the central ~ 15 pc. Another open question that was not solved in Schinnerer et al. (2000) and neither with the new data is the origin of a redshifted part of the gas in the pv-diagrams which could not be modelled with previous simulations. These redshifted components were also redetected in the new data but they still lack an explanation. The differences between both data sets can be mostly referred to a significantly reduced data quality of the 1997 observations compared to our new data. The total gas mass is now estimated to $\sim 2.5 \times 10^8 M_{\odot}$ for the ring and to $\sim 1.6 \times 10^9 M_{\odot}$. The dynamical mass, enclosed in the inner radius of $0.4''$, is found to be $\sim 5 \times 10^8 M_{\odot}$.

The results of the new data set presented here have to be still regarded as a first step of the analysis. In the future, simulations will be carried out and observations to correct for short-spacings are also planned. Some of these points will probably be part of a diploma thesis starting in January 2005.

Chapter 7

HE1029-1831

In this chapter, new observations of the CO(1–0) and CO(2–1) line emission of the barred QSO HE1029-1831 are presented. The CO emission is well associated with the optical bar and extended along it. The position-velocity diagrams show a strong velocity gradient across the bar indicating a bar-driven inflow of the gas. The redshift can now be exactly derived to $z=0.0389\pm 0.0001$ which is slightly different to the redshift of $z=0.0403\pm 0.0001$ that was published before (Kaldare et al. 2003). The gas mass is derived to $\sim 7.6 \times 10^9 M_{\odot}$. The difference between gas and dynamical mass ($\sim 1 \times 10^9 M_{\odot}$) sets an upper limit on the inclination of $\sim 30^{\circ}$. The molecular gas appears to be subthermally excited and cold being consistent to what is expected for gas from a disk.

7.1 Introduction

HE 1029-1831 belongs to the Cologne Nearby QSO Sample. The sources of this sample were selected from the Hamburg/ESO survey for bright QSOs and the Véron-Cetty and Véron quasar catalogue via their low redshifts of $z < 0.06$ providing the possibility of observations on the smallest available angular scales and the accessibility of several important diagnostic lines in the NIR (e.g. the CO(2-0) rotation vibrational band head absorption line). We aim at determining the distribution and dynamics of molecular gas in the inner 1kpc of these objects. This will add - as a final goal - to a systematic study of the different mechanisms of gas fueling into active galactic nuclei (AGN). Together with the NUGA PdBI survey containing Seyfert and LINER galaxies (García-Burillo et al. 2003a,b, Combes et al. 2004, Krips et al. 2005a) this study will span the whole activity sequence of AGN. Especially we are interested in nuclear embedded bars, rings, spirals as well as mini-spirals, warps and micro-warps - supposed to be the driving force in the fueling process - in order to investigate a possible link between different nuclear disk morphologies and activity types.

HE 1029-1832 is so far an almost white sheet of paper. Only an optical strong bar¹ ($PA \simeq 30^{\circ}$), its approximate redshift ($z = 0.04$, angular size distance $D_A = 150$ Mpc) and some diverging classifications of its active nucleus, ranging from an HII region over extreme starburst to an AGN (Kewley et al. 2001), are known.

7.2 Observations

The CO(1–0) and CO(2–1) observations of HE1029-1831 were conducted in February 2002 with 6 antennae in B and C configurations of the IRAM PdBI and again in March 2003 with 6 antennae in A configuration. The bandpass calibrator was set to 3C273 and Amplitude and Phase calibrators were 1045-188 and 1055+018. The

¹A bar can be described as (quasistationary) density waves. They can be formed by a successive reflection of short trailing waves which move into the centre and then leave as short leading waves, if amplification is sufficiently strong and no Inner Lindblad resonances exist (see Combes et al. 1995).

Line	line flux [mJy/beam]	line width [km s ⁻¹]	integr. intensity [Jy/beam km s ⁻¹]	centr. v_{LSR} [km s ⁻¹]	corr. centr. frequency [GHz]	z
CO(1-0)	65	121±3	8.4±0.2	-248±1	110.79	0.0389
CO(2-1)	89	131±7	12.4±0.6	-107±3	221.58	0.0389

Table 7.1: Line parameters for CO(1-0) and CO(2-1) in HE 1029-1831.

latter were observed every twenty minutes. The receiver at 3.5mm was tuned on 110.7 GHz (redshifted ¹²CO(1-0); $z=0.040$), and the receiver at 1.2 mm on 221.5 GHz (redshifted ¹³CO(2-1)). The water vapor was derived to ≤ 6 mm for both observations thus providing ideal weather conditions. At both frequencies a total bandwidth of 580MHz was used with a frequency resolution of 1.25MHz. The central position was set to $\alpha_{J2000} = 10^{\text{h}}31^{\text{m}}57.3^{\text{s}}$ and $\delta_{J2000} = -18^{\circ}46'34.0''$, taken from NED. The total integration time on source amounted to ~ 5 hours for the 2002 data and to ~ 3 hours for the 2003 data.

7.3 The data - results

Both, the CO(1-0) and CO(2-1) lines are clearly detected, while no continuum emission was found at 3 mm (upper limit: $3\sigma=1.2$ mJy) and 1 mm (upper limit: $3\sigma=4$ mJy).

7.3.1 CO emission

The emission is already clearly detected with $\geq 5\sigma$ in the channel maps of both transitions (Fig. C.1 and C.2). Apparently, both lines do not peak at zero velocities indicating that the assumed redshift might not be correct. This is better visible in the spectrum taken at the respective centroids of both lines presented in Fig. 7.1. While the CO(1-0) roughly extends from velocities of -350 km s⁻¹ to -40 km s⁻¹, the CO(2-1) line appears at velocities from -220 km s⁻¹ to 40 km s⁻¹. Correcting the actual redshift can explain this difference for both lines. Based on the central velocities for the CO(2-1) ($v_0=-110$ km s⁻¹) and CO(1-0) line ($v_0=-250$ km s⁻¹), the actual redshift is identically determined to $z=0.0389\pm 0.0001$ for both transitions instead of the previously assumed $z=0.0403\pm 0.0001$. The corrected redshift is indicated in Fig. 7.1. A Gaussian profile has been fitted to both lines. The derived line parameters are given in Table 7.1. The integrated maps are plotted in Fig. 7.3. Both CO lines are centered at the same position of $\alpha_{J2000} = 10:31:57.3$ $\delta_{J2000} = -18:46:33.2$. The CO emission is clearly extended in both transitions and reveals elongations in North/North-East and South/South-West directions which agree with the optical bar (Fig. 7.5). Thus, two further spectra, which were integrated over the respective emission area, are additionally shown in Fig. 7.2. Again, a Gaussian profile was fitted to both lines. Table 7.2 lists the fit parameters. The integrated CO(1-0) intensity (Table 7.2) results in a gas mass of $7.6 \times 10^9 M_{\odot}$ assuming the standard M_{gas} to L'_{CO} conversion factor of $4.8 M_{\odot} (\text{K km s}^{-1} \text{pc}^2)^{-1}$ (Solomon & Barret 1991, Equation 5.4). As the angular resolutions of both transitions are roughly comparable by using uniform weighting for CO(1-0) and natural weighting for CO(2-1), the line ratio $R_{21}=\text{CO}(2-1)/\text{CO}(1-0)$ of both lines can be estimated to ~ 0.7 . However, one has to keep in mind that this estimate might still be biased by artefacts due to the uv -coverage which has to be interpreted differently for both lines. Although the baselines are the same at the two frequencies, they correspond to different angular resolutions. One can reduce such a bias by apodising and truncating the respective uv -coverages to the overlapping region of both frequencies. However, the role of the weighting factors used for mapping is still important and remains critical. Thus, the line ratio must be regarded critically and taken as a rough estimate.

The position velocity diagrams have been taken along a cut in direction of the CO extension (i.e., at a Position Angle (PA) of 0°) and perpendicular to it (PA= 90°). They are presented in Fig. 7.6. The position velocity map at PA= 90° show a velocity gradient which extends over a radius of $\sim 0.5''$ perpendicular to the bar. Again both lines agree well with each other. Assuming a radius of $\sim 0.5''$ or 350 pc equivalently and a velocity of ~ 100 km s⁻¹,

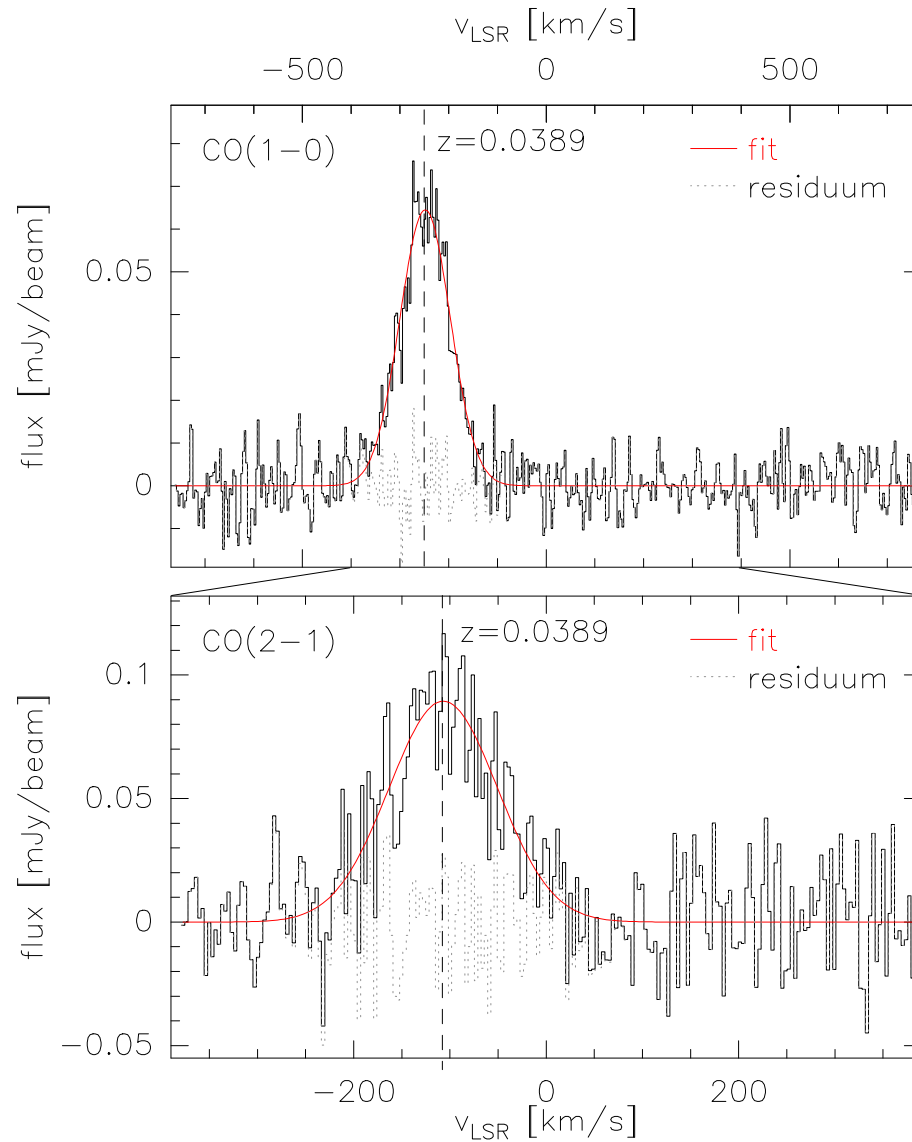


Figure 7.1: CO(1-0) (*upper panel*) and CO(2-1) (*lower panel*) spectrum. The shift in velocity between the CO(1-0) and CO(2-1) line shows that the assumed redshift of $z=0.040$ for the observations which was taken from NED turned out to be too high. Thus, both lines peak physically at the same velocity but due to the different redshift they are shifted with respect to each other.

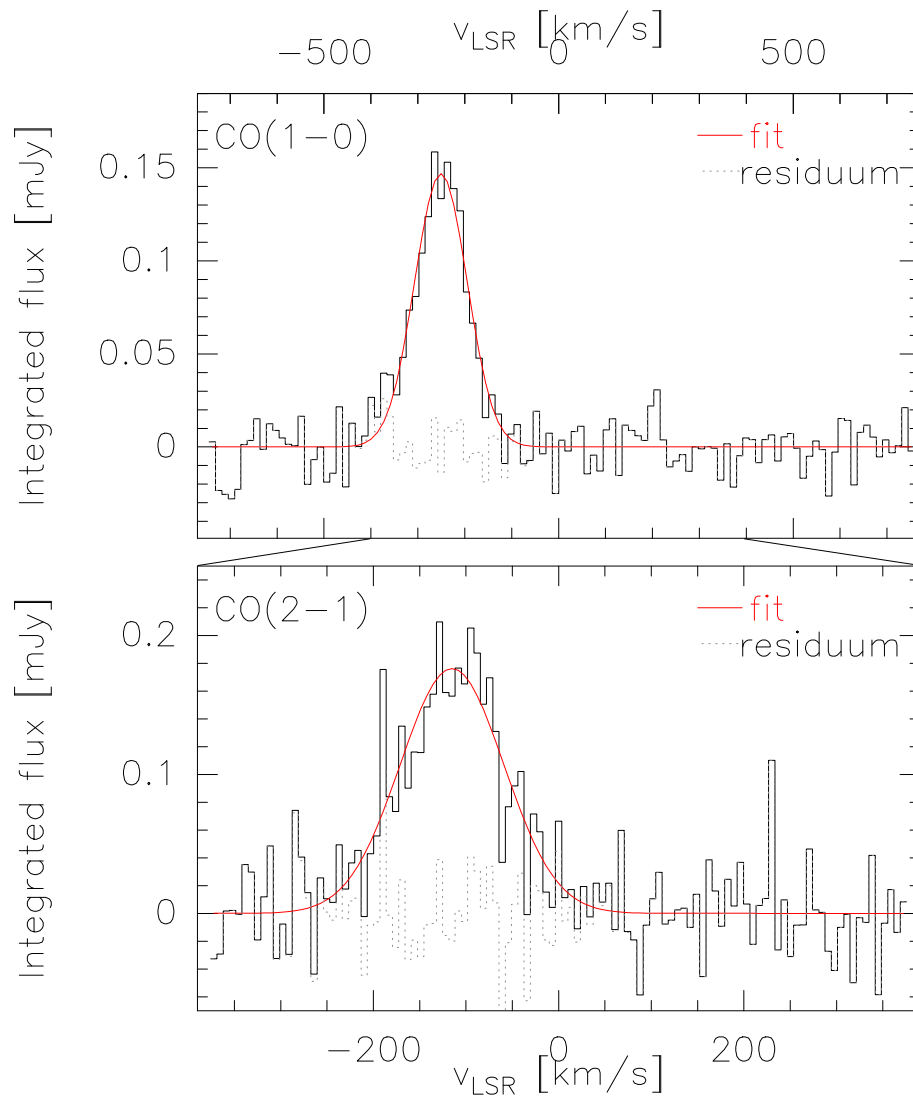


Figure 7.2: Spatially (over the bar) integrated CO(1-0) (*upper panel*) and CO(2-1) (*lower panel*) spectrum.

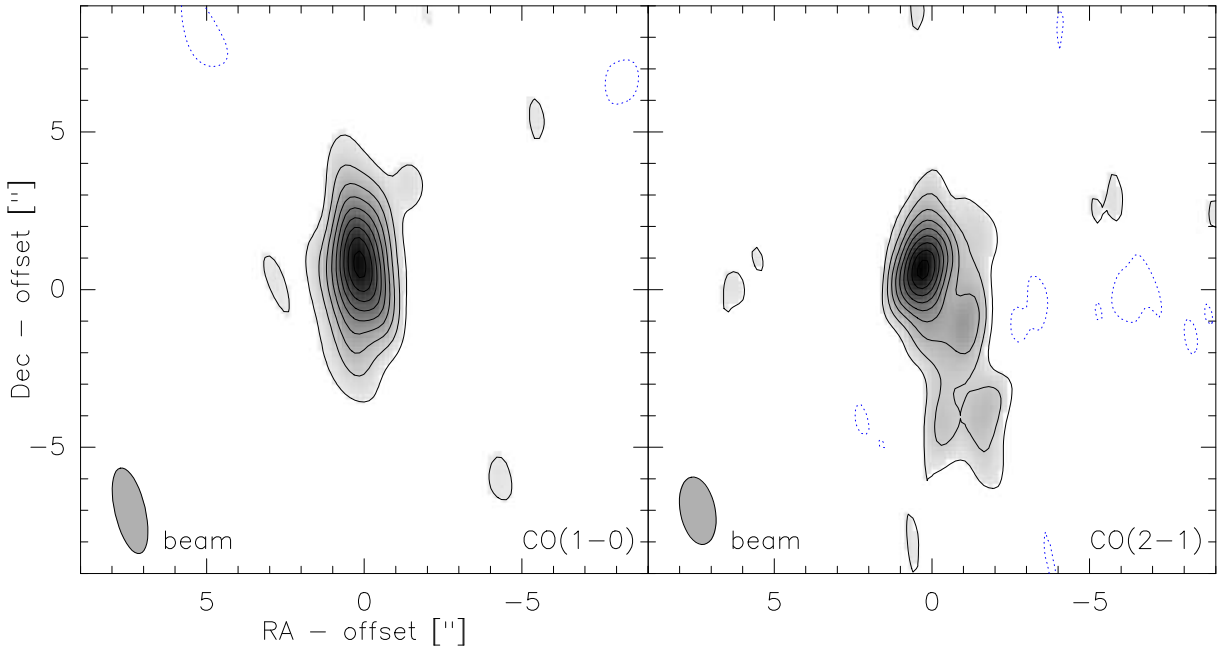


Figure 7.3: Velocity integrated CO(1-0) (*left*) and CO(2-1) (*right*) emission in HE 1029-1831. Contours are in steps of $3\sigma = 3.6$ mJy (9 mJy) for CO(1-0) (CO(2-1)). $1''$ corresponds to 0.7kpc.

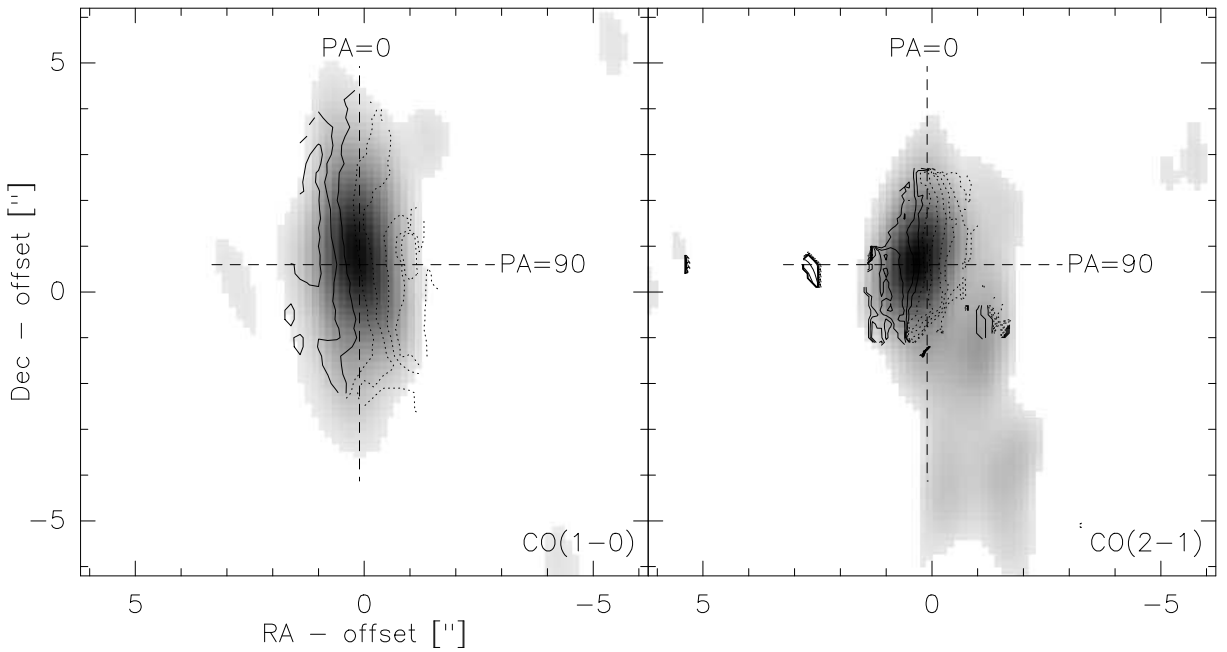


Figure 7.4: Iso-velocity map of the CO(1-0) and CO(2-1) emission CO(1-0) (*left*) and CO(2-1) (*right*) emission in HE 1029-1831. Contours are around the dynamic center (i.e. $v_{\text{LSR}} = -248$ km s $^{-1}$ for CO(1-0) and $v_{\text{LSR}} = -107$ km s $^{-1}$ for CO(2-1)) in steps of 10 km s $^{-1}$.

Line	integr. intensity [Jy km s ⁻¹]	velocity width [km s ⁻¹]	M _{gas} [10 ⁹ M _⊙]
CO(1-0)	21±1	131±6	7.6
CO(2-1)	25±1	131±9	-

Table 7.2: Fit parameters and gas mass of HE 1029-1831 derived from the CO(1-0) and CO(2-1) line spectrum. The latter shows the over the bar integrated line emission (Fig.7.2).

the total dynamical mass within the central 350 pc - not corrected for inclination effects - can be derived to $\sim 1 \times 10^9 M_{\odot}$ (Equation 6.3). Probably, the gas disk is seen closer to face-on than to edge-on so that this value must be regarded as lower limit explaining why the dynamical mass is lower than the gas mass. Assuming that the enclosed dynamical mass must at least be of the order of the gas mass, we can give an upper limit for the inclination ϑ of the galaxy which can be estimated via Equation 6.3:

$$\vartheta[^{\circ}] \leq \arcsin \left(\sqrt{150 \times \frac{r}{pc} \times \left(\frac{v(r)}{\text{km s}^{-1}} \right)^2 \times \frac{M_{\odot}}{M_{\text{gas}}(r)}} \right) \quad (7.1)$$

$$\simeq 30^{\circ} \quad (7.2)$$

assuming $M_{\text{gas}}(r = 1'') \simeq 5 \cdot 10^9 M_{\odot}$. However, one has to keep in mind, that also the molecular gas mass is quite uncertain due to the conversion factor as detailed by Downes et al. (1993) for instance.

As already indicated, the CO distribution is well correlated with the optical bar (see Fig. 7.5). Roberts et al. (1979) present a bar model for NGC 1300 and NGC 5383 whose (optical) morphologies are quite similar to HE 1029-1831. Their simulations are based on a steady-state gas flow description (in a thin disk) assuming standard hydrodynamic equations. All three galaxies show a strong bar with a velocity gradient across the bar. This striking velocity gradient can be nicely reproduced by the model of Roberts et al. (1979; see lower right panel of Fig. 7.5) which appears to hold also for HE 1029-1831. The velocity gradient can then be explained by highly oval gas circulation caused by the barlike potential in the inner parts. This is consistent with a bar-driven gas inflow.

7.3.2 Continuum emission

The continuum emission at 3 mm and 1 mm could not be detected. The upper limits were determined in the line free channels (i.e. at velocities $\gtrsim -50 \text{ km s}^{-1}$ and $\lesssim -500 \text{ km s}^{-1}$ at 3mm and at velocities $\gtrsim 150 \text{ km s}^{-1}$ and $\lesssim -300 \text{ km s}^{-1}$ at 1mm) to $3\sigma = 1.2 \text{ mJy}$ at 3mm and to $3\sigma = 4 \text{ mJy}$ at 1mm.

7.4 Summary and Conclusions

Strong CO(1-0) and CO(2-1) emission is detected in the barred QSO HE 1029-1831 with the IRAM PdBI interferometer while no continuum emission was found. Both lines agree well with each other in distribution and position. The optical redshift of $z=0.040$ had to be corrected by about $\sim -3\%$. The redshift of the CO emission is determined to $z=0.0389 \pm 0.0001$. The CO(1-0) and CO(2-1) emission are extended along the optical bar. Also, a striking velocity gradient is found at a position angle of 90° , i.e. across the bar, extending over $\sim 1''$ approximately. Adopting the model from Roberts et al. (1979), this can be interpreted as bar-driven inflow of the gas. In the direction of the bar (PA= 0°), almost no velocity gradient is seen anymore most likely indicating the velocity dispersion of $\Delta V = \pm 70 \text{ km s}^{-1}$. The line ratio between CO(2-1) and CO(1-0) is estimated to ~ 0.7 although probably still biased by resolution effects. This indicates subthermally excited and cold gas which is typical for

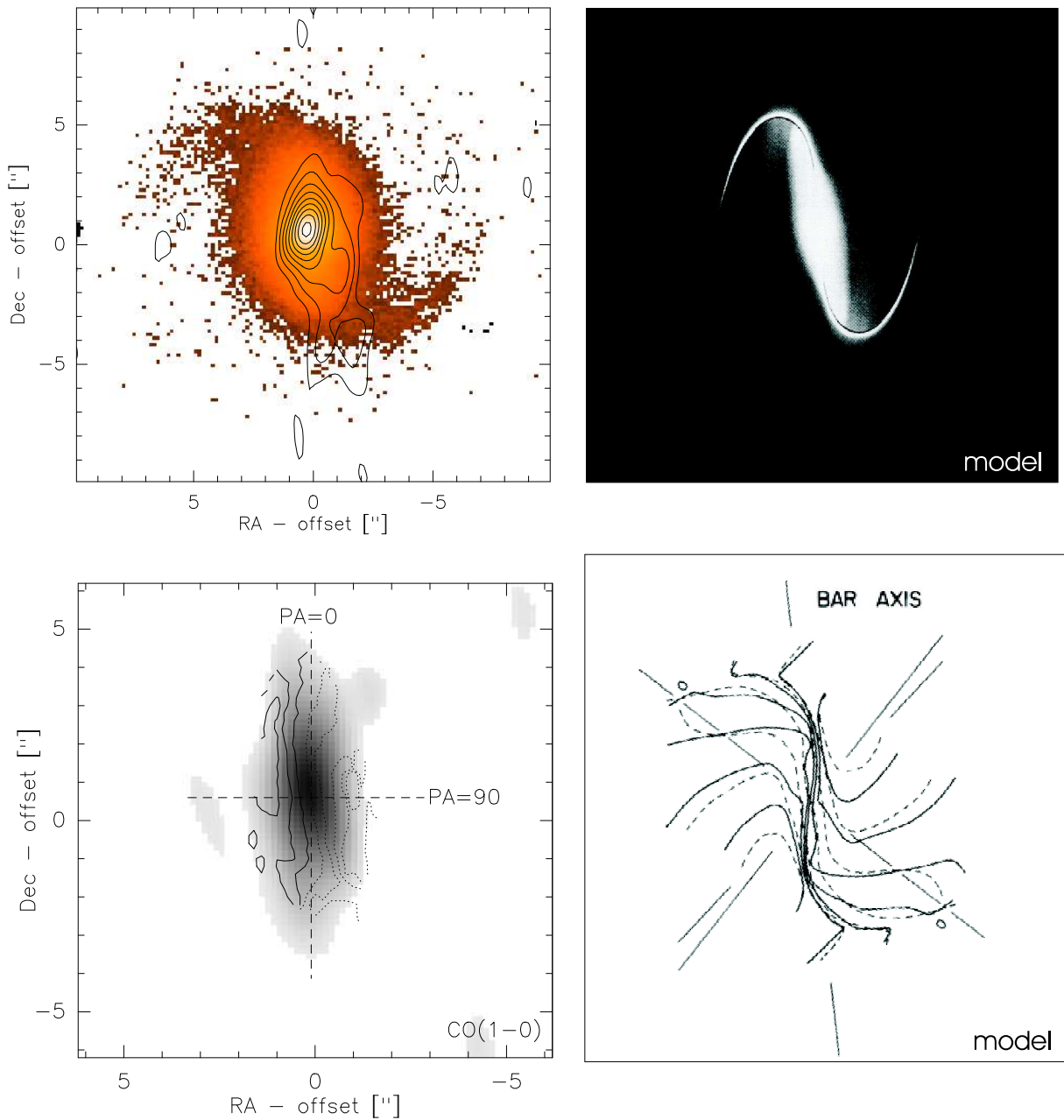


Figure 7.5: *Upper panel:* H-band image of HE1029-1831 superimposed with contours of the CO(2–1) line emission (*left*) and of a bar model *right* that was developed for NGC 5383 (Roberts et al. 1979). The model was tilted by an angle of approximately 50° (from North to East) for a better comparison with HE 1029-1831. Increments of left image as in Fig.7.3. *Lower panel:* Iso-velocity diagrams of HE 1029-1831 (*left*) and of a simulated bar potential (*right*) from Roberts et al. (1979). The dashed lines in the lower right map correspond to the model shown in the upper right panel (solid line refer to another model).

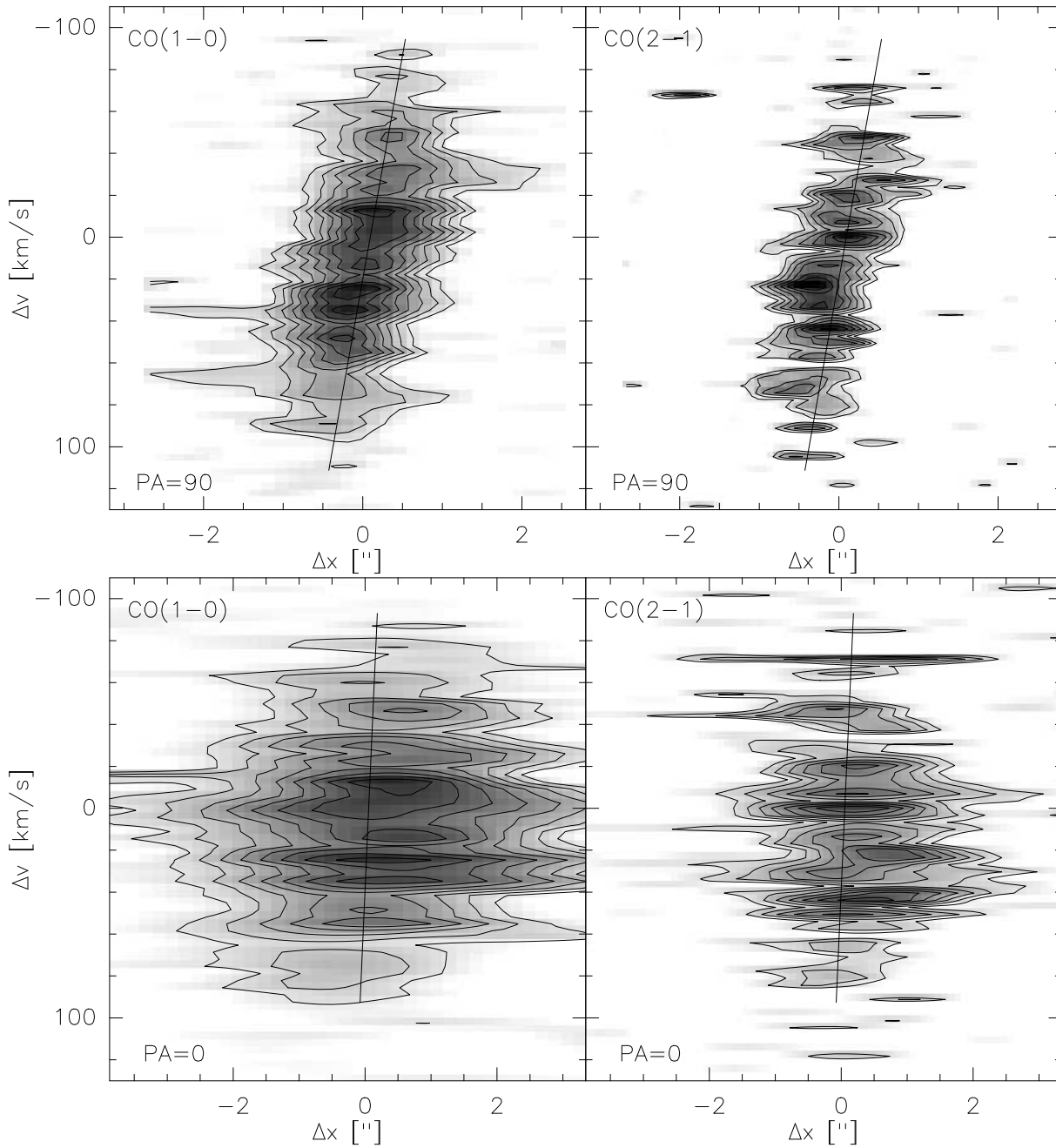


Figure 7.6: Position velocity diagram of the CO(1–0) (*left*) and CO(2–1) (*right*) emission. The upper panels show the position velocity diagrams taken across the bar (PA=90°), and the lower panel those of a cut perpendicular to it, i.e. along the bar (PA=0°).

gas in a disk. The gas mass amounts to $\sim 8 \times 10^9 \mathcal{M}_\odot$ while the dynamical mass is roughly estimated to only $\sim 1 \times 10^9 \mathcal{M}_\odot$ indicating that the galaxy is seen almost face on (i.e., with an inclination of $\leq 30^\circ$).

Chapter 8

3C48

New interferometric observations have been analysed of the CO(1-0) line and mm continuum emission in the bright host galaxy around 3C48 - one of the prime candidates for a nearby merger event (Krips et al., 2005b). The new results of the CO(1-0) line emission give substantial evidence for a velocity gradient ($\sim \pm 70 \text{ km s}^{-1}$) of the gas centered between the QSO and an apparent second nucleus, 3C48A, about $\sim 1''$ to the North-East recently detected also in the NIR (Zuther et al. 2004). This implies an extended rotating gas disk. Moreover, the new data indicate a second gas reservoir on the position of the QSO itself. At 1.2 mm, the emission is elongated towards 3C48A and in direction of the radio jet. Thus, 3 different sources in 3C48 are suggested powering the 1.2 mm continuum - the QSO, 3C48A and a jet.¹

This chapter is outlined in the following manner: Section 8.2 gives information on the new PdBI observations. In Section 8.1, the results of the combined data sets for the mm continuum and the CO emission are presented. In section 8.4, the quality of the estimate for the molecular gas mass is discussed. In Section 8.5, 3C48 is compared with two other merger candidates, the “Antennae” galaxies and Arp220. Finally, Section 8.6 finishes the Chapter with a summary and some conclusions.

8.1 Introduction

Merger events between galaxies are regarded as one of the key issues to understand the enormous activity found in Active Galactic Nuclei (AGN). One of the first candidates associated with this phenomenon was 3C48 classified as QSO after its first detection in the optical (Matthews et al. 1961). It was also directly connected to a surrounding host galaxy which turned out to be unusually large and bright. This, the existence of a second bright compact component labeled 3C48A about $1''$ North-East to the QSO (Stockton & Ridgway 1991, Zuther et al. 2004), a tail-like extension to the North-West (Canalizo & Stockton 2000), and its richness in molecular gas (Scoville et al. 1993; Wink et al. 1997 (in the following W97)) are the main arguments leading to the idea that 3C48 is experiencing a recent merger event. During a major merger, two tidal tails are usually expected and the absence of the second counter tidal tail has been an unsettled question raising doubts about the merger hypothesis. However, Scharwächter et al. (2004) recently proposed a simple solution for the missing counter tidal tail. While previous works misleadingly associated the counter tidal tail with a background galaxy (Boyce et al. 1999; Canalizo & Stockton 2000) or suggested it to extend from the south-east to the south-west (Canalizo & Stockton 2000) but lacked observational evidence for such a hypothesis, Scharwächter et al. (2004) alternatively locate the counter tidal tail in front of the main body of the 3C48 host from the south-west to the north-east based on multi-particle simulations. Similar to Canalizo & Stockton (2000), they assume a configuration that is generally used for the Antennae galaxies but seen from a different viewing angle (e.g., Toomre & Toomre 1972). This scenario is also in

¹Luminosity Distance of 3C48: 1.581 Mpc. $1''$ corresponds to $\sim 4.1 \text{ kpc}$.

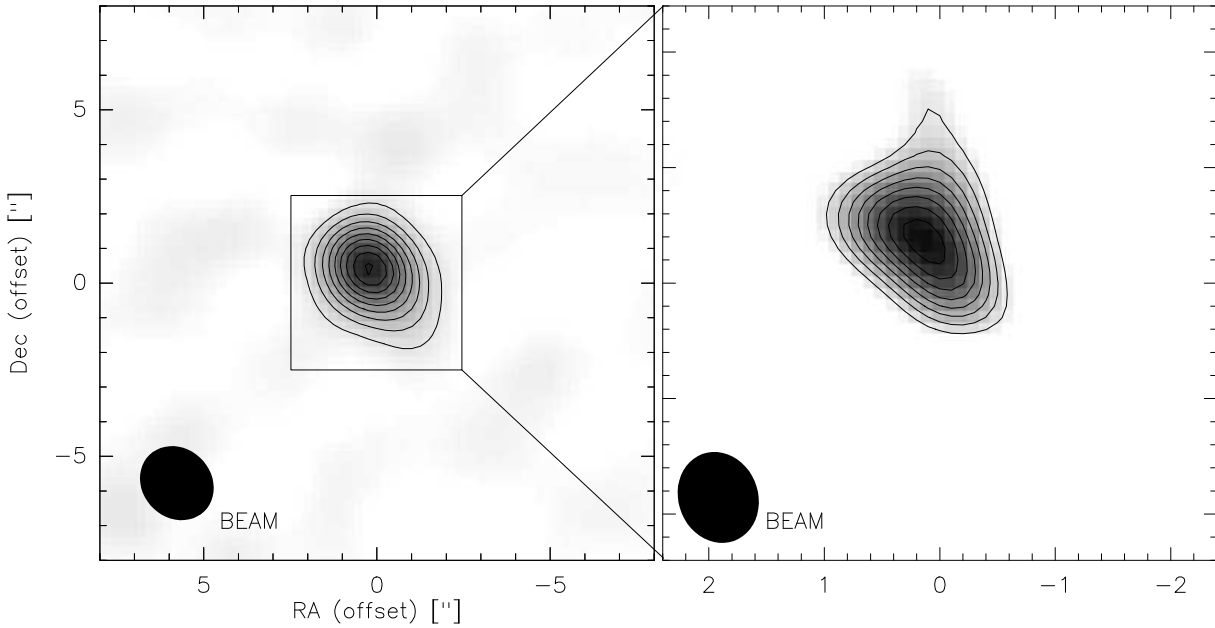


Figure 8.1: Continuum maps at 3.5 mm (*left*) and 1.2 mm (*right*) of 3C48 obtained with the IRAM PdBI (epoch 2003). Contour levels at 3.5 mm: $20\sigma = 0.025$ to 0.23 Jy/beam by 20σ . Contour levels at 1.2 mm: $5\sigma = 0.01 \text{ Jy/beam}$ to 0.044 Jy/beam by 2σ . Both maps were produced by using uniform weighting.

better agreement with information about the stellar dynamics than the previous suggestions. A second vulnerability of the interpretation of 3C48 as a merger is constituted in the unknown nature of the apparent second nucleus 3C48A. Although Zuther et al. (2004) recently succeeded in detecting 3C48A also in the NIR, they could, however, neither resolve doubts about 3C48A being the result of the interaction of the radio jet with the surrounding interstellar medium (see also Chatzichristou et al. 1999).

Scoville et al. (1993) were the first to detect CO(1–0) emission (4σ) in 3C48 with the Owens Valley Millimeter Array (OVRO). A few years later, Wink et al. (1997) confirmed Scoville et al.’s results with new observations of the CO emission carried out with the IRAM Plateau de Bure interferometer (PdBI). Both groups find a large molecular gas mass of a few times $10^{10} M_{\odot}$. The analysis of the molecular gas content in a system like 3C48 can help to understand the initial steps leading to the enormous nuclear activity. Regardless of the question whether starbursts or accretion onto a supermassive black hole cause the huge release of energies, molecular gas plays a major role in forming new stars and fueling a black hole.

In this chapter, new successful interferometric observations are presented of the $^{12}\text{CO}(1-0)$ line and 3.5 mm plus 1.2 mm continuum emission in 3C48 carried out with the IRAM PdBI. To still increase sensitivity, the data were also combined with previous measurements by Wink et al. (1997) resulting in new and important information about the molecular gas properties in the host galaxy. The combined data set is by almost a factor 2 more sensitive than those from W97 alone.

8.2 Observations

Two different observations of the $^{12}\text{CO}(1-0)$ emission in 3C48 were conducted with the IRAM PdBI. The first data set was obtained by Wink et al. (1997) between November 1994 and February 1995 in BC configuration with 3 antennae. For more details of this measurement we refer to their publication. The second one was observed between December 2002 and March 2003 in AC configuration with 6 antennae. Amplitude and phase calibrators were

Epoch	RA	Dec.	Cont. flux density 3.5mm/1.2mm (mJy)
	($''$)	($''$)	
1992 ^a	not publ.	not publ.	266/n.a.
W97 ^b (1995)	not publ.	not publ.	307 \pm 2/n.a.
1995 ^c	01:37:41.3	33:09:35.4	303 \pm 2/n.a.
2003 ^d	01:37:41.3	33:09:35.5	270 \pm 1/82 \pm 2 ^e
“QSO” ^f			-/36 \pm 8
“Jet” ^f			-/15 \pm 4
“3C48A” ^f			-/25 \pm 7

Table 8.1: Continuum data at 3.5 mm and 1.2 mm of 3C48 from all available epochs. Values were determined by fitting a Gaussian to the data. ^a taken from Scoville et al. 1993. ^b $4 \times 2'' @ 34^\circ$. ^c Position of the 3.5 mm continuum centroid from the new reduction of W97’s data; beam: $4 \times 2'' @ 38^\circ$. ^d position at 3.5 mm; beam at 3.5 mm: $2.3 \times 2.0'' @ 44^\circ$. ^e total flux of the whole component, beam at 1.2 mm: $0.9 \times 0.7'' @ 15^\circ$. ^f fluxes derived by fitting 3 Gaussian components to the sky plane at 1.2 mm (see Fig.8.4).

3C84 and 3C111 being observed every 20 minutes. The receiver at 3.5 mm was tuned on 84.17GHz (redshifted $^{12}\text{CO}(1-0)$; $z=0.367$), and the receiver at 1.2 mm on 241.39GHz (redshifted $^{13}\text{CO}(3-2)$). At both frequencies a total bandwidth of 580MHz at 3.5 mm and of $2 \times 580\text{MHz}$ (DSB) at 1.2 mm was used with a frequency resolution of 1.25MHz. The central position was set to $\alpha_{2000} = 01^{\text{h}}37^{\text{m}}41.3^{\text{s}}$ and $\delta_{2000} = 33^\circ 09' 35.0''$ coincident with the one used by Wink et al. (1997). The total integration time on source amounted to ~ 6.5 hours.

The data by W97 have been re-reduced together with our new data and merged afterwards.

8.3 The data

8.3.1 Continuum

The strong mm continuum emission by itself can already be interpreted as a consequence of the large nuclear activity in 3C48. Both, thermal as well as non-thermal processes have to be equally regarded as possible sources for this emission.

8.3.1.1 3.5 mm

The continuum fluxes from both observations (new reduction of data from 1995; new data from 2003) have been independently determined at 3.5 mm by averaging channels greater than $+380 \text{ km s}^{-1}$ and lower than -380 km s^{-1} . The values for the reduction of the 1995 data and those of W97 agree well with each other while the value of the 2003 data differs slightly by about 10% from the W97 data which might be partially due to resolving effects (cf. beam sizes of different epochs in caption of Table 8.1). The continuum emission appears to be slightly extended in the beamsize of $2.3 \times 2.0'' @ 44^\circ$ (see Fig. 8.1). The position obtained from our mm-observations differs by about $0.4''$ from that known from 13cm and 3.5cm VLBI measurements (Ma et al. 1998). A comparison with the recently detected NIR images of 3C48-QSO and 3C48A shows that the mm continuum is located between both features (Fig. 8.2). This might explain the difference in position with respect to the cm /IR observations. In the beam of the PdBI at 3.5 mm, the two nuclear components are not resolved but a difference is found between the peak flux ($\sim 230 \text{ mJy/beam}$) and the integrated flux density ($\sim 270 \text{ mJy}$) indicating that the continuum component cannot only be a single point source. This implies that there might also be some emission originating in the second North-East component labeled 3C48A and/or the radio jet. The continuum flux at 3.5 mm nicely follows the

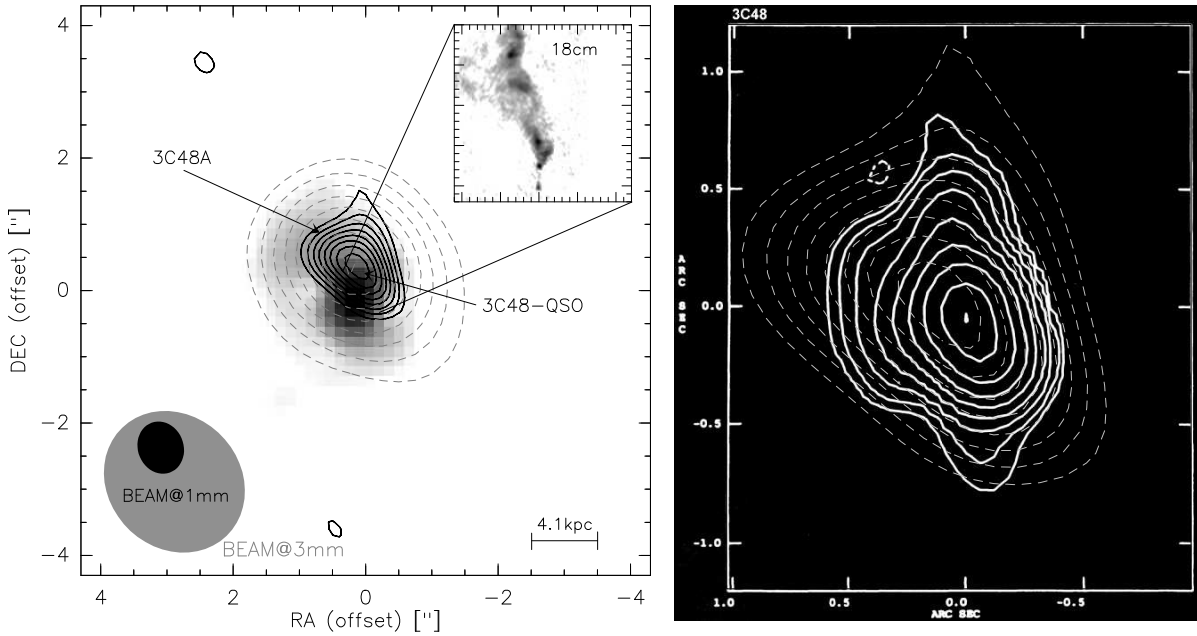


Figure 8.2: *Left panel:* NIR-image (Zuther et al. 2004; the nucleus was already subtracted) overlaid with contours from the 3.5 mm (grey dashed lines) and 1.2 mm (black solid lines) continuum (mapped with uniform weighting; epoch 2003). The radio jet at 18cm is plotted in the small box (upper right) taken from NED (data are originally from Wilkinson et al. 1991). Contours are the same as in Fig.8.1. *Right panel:* 18cm MERLIN image (solid contours; Akujor et al. 1994) superimposed with dashed contours of the 1.2 mm continuum.

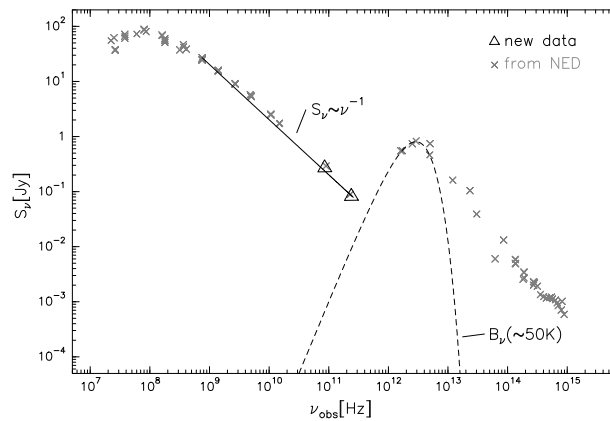


Figure 8.3: SED plot of 3C48. Grey points are taken from NED. Triangles (total flux at 3.5 mm and 1.2 mm) are from our new PdBI data (total flux of all components). The solid line is a power law fit to the radio data indicating non-thermal synchrotron emission while the dashed curve shows a simple black body fit (temperature with respect to restframe) for the IR data ($\nu \sim 2\text{-}10\text{THz}$).

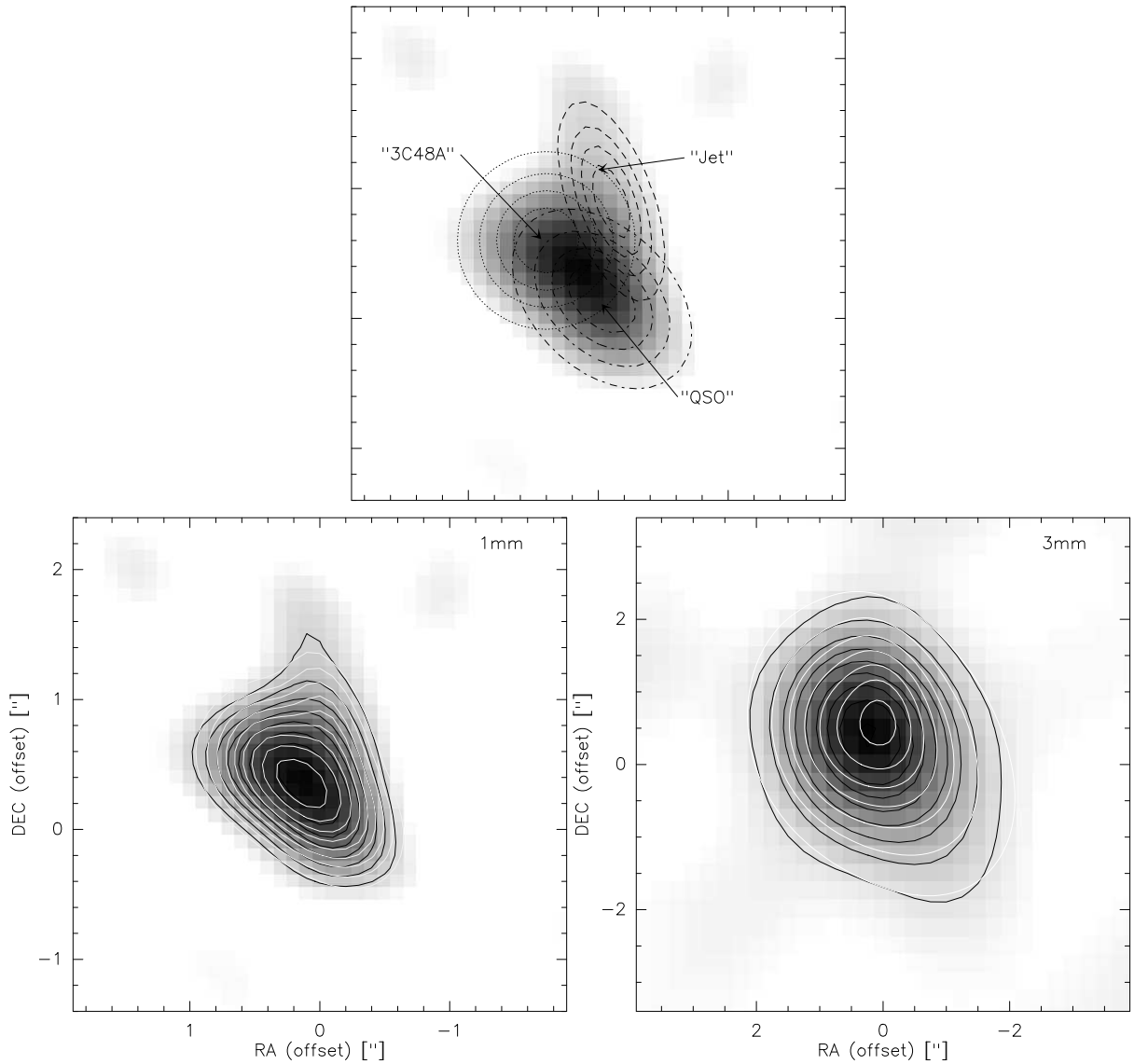


Figure 8.4: Continuum emission at 1.2 mm (grey scale & black solid contours, scale as in lower left panel) overlaid with contours of a three Gaussian component model: QSO (upper panel: dotted/dashed lines; epoch 2003), “jet” (upper panel: dashed lines), “3C48A” (upper panel: dotted lines) and total (lower left panel: white solid lines). Contours are from 20% to 100% in steps of 20% of the respective peak flux for each component (upper panel). Contours of solid lines (lower left panel) for model and data as in Fig.8.2. Lower right panel: Continuum emission at 3.5 mm (grey scale & black solid contours) overlaid with contours of a three Gaussian component model taken from 1mm with corrected fluxes (white solid lines). Contours of solid lines (lower panel) for model and data as in Fig.8.2.

steep spectrum (with $S_\nu \propto \nu^{-1}$) obtained at cm wavelengths (see Fig.8.3 & Meisenheimer et al. 2001). Thus, the continuum emission at 3.5 mm is still mainly dominated by synchrotron processes.

8.3.1.2 1.2 mm

The 1.2 mm continuum has only been observed in the second epoch (Fig.8.1). Since no line emission was found at 1.2 mm (see section 8.3.5), the continuum was averaged over the whole bandwidth of 2×580 MHz (DSB). It is detected with a SNR of ~ 25 and well centered on the position derived at 3.5 mm. Furthermore, the emission appears clearly extended towards 3C48A (North-East) and also to the North of the radio jet (Fig.8.2) being very similar to the 18cm MERLIN map (Akujor et al. 1994). This motivated to fit a profile with three Gaussian components (QSO, 3C48A & jet) to the data at 1.2 mm (Fig.8.4) to explain the unusual shape allowing at least to estimate flux values for each component with $\sim 4\sigma$ (see Table 8.1). Extrapolating the cm continuum fluxes with the steep spectral index of $\alpha = -1$ ($S_\nu \propto \nu^\alpha$; Fig.8.3) towards 1.2 mm results in a value that is similar to the flux of the QSO and jet component, i.e. the estimated flux of 3C48A is not needed to satisfy the synchrotron spectrum. Thus, the continuum emission of the QSO itself might still be affected by synchrotron emission produced by the jet. Indeed, a significant part of the radio jet is still present towards the southern component on smaller scales $\leq 1''$ (Wilkinson et al. 1991; see also Fig.8.2). The estimate of the continuum flux emission at 1.2 mm of 3C48A lies closer to the black body part of the continuum thus being probably dominated by the long-wavelength tail of the dust emission rather than synchrotron processes. This would also support the result of Zuther et al. (2004) who found that 3C48A is very reddened. However, non-thermal processes can neither be discarded for 3C48A since the 18cm map also indicates emission towards 3C48A. Additionally, the 3.5 mm continuum emission might be also produced by more than one source alone, i.e. besides the QSO component also 3C48A and the jet as possible candidates. Unfortunately, the angular resolution of the 3.5 mm data does not allow to support either 3C48A or the jet alone as source of emission. However, it seems quite likely that both contribute to the continuum at 3.5 mm. Assuming a spectral index of -1 between the 1.3mm and 3.5 mm continuum flux and taking also into account the higher beam size at 3.5 mm, the 1.3mm model can also be naively adopted for the 3.5 mm data. Fig.8.4 shows that our 1.3mm model also holds for the 3.5 mm data. However, to substantiate the 3 continuum components proposed in this paper for 3C48, further observations with a higher angular resolution at 3.5 mm and 1.3mm are still necessary.

8.3.2 Line emission

8.3.3 $^{12}\text{CO}(1-0)$

The continuum was separately subtracted before merging for both observation epochs (1995, 2003) from the channel maps directly in the uv-plane. The line peak fluxes between the W97 data and our new data are compatible within the errors with each other and agree also with the value found by Scoville et al. (1993). The line widths are also consistent with each other taken the errors into account. The positions (where determined) agree with each other within the errors between the different epochs.

Fig.8.5 shows the cleaned velocity channel maps (resampled to 11 MHz) of the CO(1-0) emission in 3C48 being here already detected with a SNR of $\sim 4-5$ in the individual channel maps from $\sim -200 \text{ km s}^{-1}$ to $\sim +120 \text{ km s}^{-1}$. A decrease in intensity can be observed at velocities $+80 \text{ km s}^{-1}$ and -160 km s^{-1} indicating a complex kinematic system in 3C48. The spectrum (Fig.8.6) taken at the centroid of the CO(1-0) emission (velocity resolution of $\sim 13 \text{ km s}^{-1}$) indicates three different lines but the data still lacks enough sensitivity to totally exclude possible noise effects here. We thus fitted only a single Gaussian profile to the line and subtracted it from it to compare it with the rms estimated to $\sim 0.9 \text{ mJy}$ at a position where no CO emission is expected. This value is consistent with a theoretical estimate of the noise based on the visibilities of the combined data. The residual spectrum is found to have a significant higher (i.e. by a factor of ~ 2) rms of $\sim 1.9 \text{ mJy}$ implying that a single Gaussian profile is most likely too simple to explain the observed line shape. The line parameters are given in Table 8.2. The integrated emission over the whole velocity range (from -220 to 160 km s^{-1}) is plotted in Fig.8.7. The centroid of the total CO(1-0) emission is located in between the QSO and 3C48A. The emission nicely covers the QSO and 3C48A and two extensions are found, one to the North and one to the South-West, which are both not aligned with the position angle of the synthesized beam. The position velocity diagrams taken along the two cuts shown in Fig.8.7 & 8.9 reveal three different velocity components. A velocity gradient is visible between velocities from

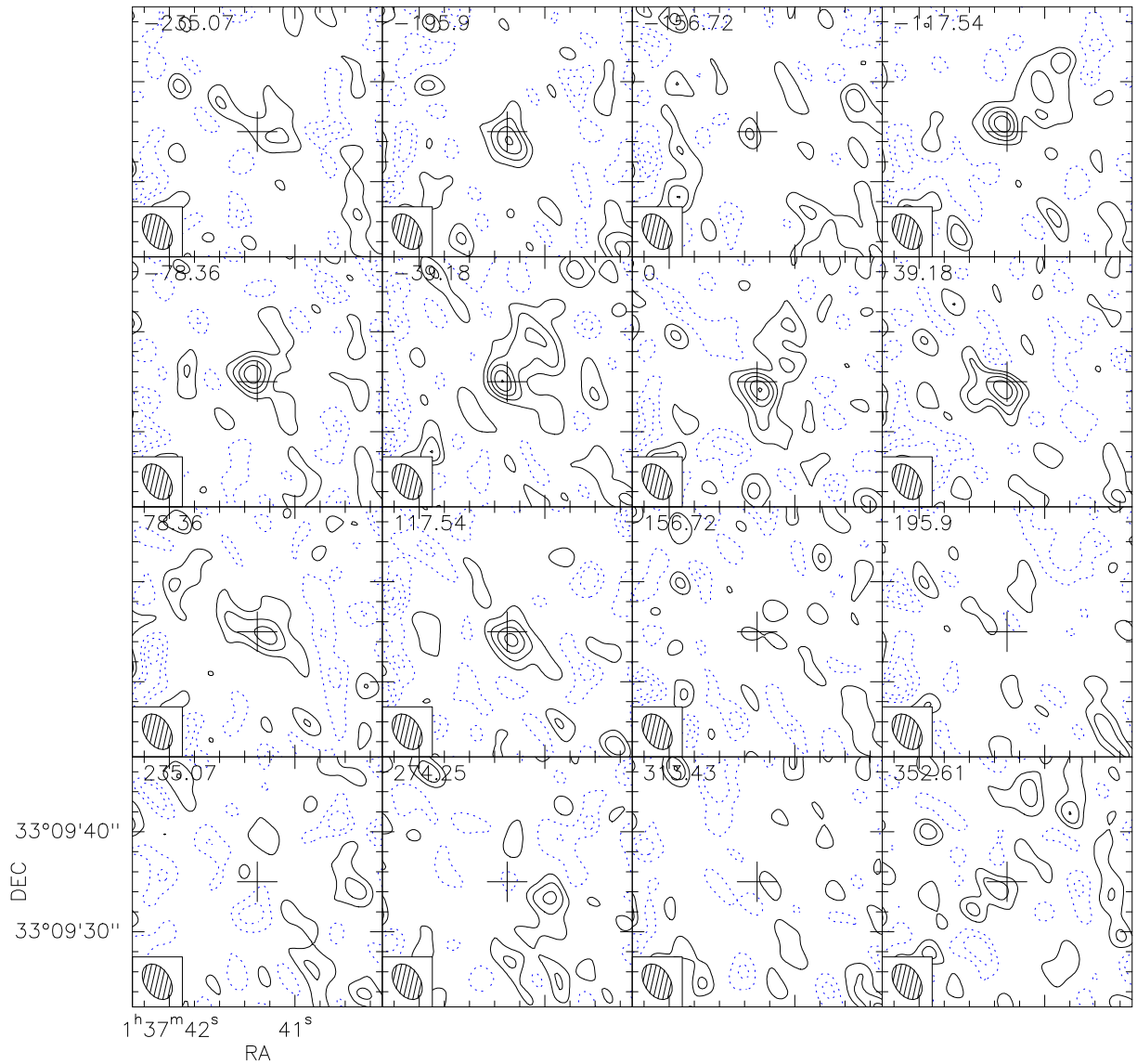


Figure 8.5: Channel maps of the CO(1-0) emission. Contour levels: $1\sigma=1.2$ to 6.0mJy/beam by 1σ .

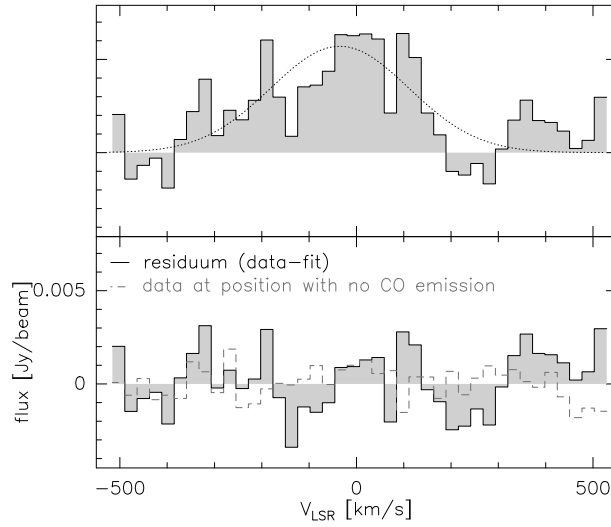


Figure 8.6: Spectrum at the position of the CO(1–0) centroid in 3C48 (*solid histogram; upper panel*) and residual spectrum where the fit has been subtracted from the data (*lower panel*). The *dotted* line is a Gaussian fit to the data. The *dashed, grey* histogram is a spectrum taken at a position at which no CO(1–0) emission is expected from 3C48 to indicate the noise level of 0.9 mJy. Velocity resolution: $\sim 26 \text{ km s}^{-1}$.

Epoch	RA offset ^b (")	Dec. offset ^b (")	Flux ¹² CO(1–0) (mJy/beam)	Width FWHP (km s^{-1})
1992 ^a	n.p.	n.p.	~ 7	~ 250
W97 ^d	n.p.	n.p.	9 ± 1	270 ± 20
1995 ^c	-0.5 ± 0.6	0 ± 0.6	8.6 ± 1	240 ± 40
2003	0.5 ± 0.4	0 ± 0.4	5.6 ± 2	330 ± 50
combined	0.3 ± 0.3	0 ± 0.3	6.0 ± 1	320 ± 30

Table 8.2: CO(1–0) data. ^a taken from Scoville et al. (1993). ^b with respect to: $\alpha_{2000}=01^{\text{h}}37^{\text{m}}41.300^{\text{s}}$, $\delta_{2000}=33^{\circ}09'35.00''$. ^c From the new reduction of W97’s data. ^d epoch 1995.

roughly -120 km s^{-1} to 80 km s^{-1} . Two further components appear at -200 km s^{-1} and $+120 \text{ km s}^{-1}$ which seem to be unrelated to the “inner” velocity gradient. Motivated by these findings, three different integrated intensities maps were generated over the respective velocity range (see Fig. 8.9). The positions of the CO components compared to the infrared components led to label the feature that corresponds to velocities between -120 km s^{-1} to $+80 \text{ km s}^{-1}$ as 3C48A and the other two as QSO-red ($+120 \text{ km s}^{-1}$) and QSO-blue (-200 km s^{-1}). 3C48A is centered close to 3C48A while QSO-red and QSO-blue are roughly on the QSO. All three components appear to be slightly extended in the synthesized beam of the PdBI.

8.3.3.1 3C48A

At velocities corresponding to 3C48A (from $\sim -120 \text{ km s}^{-1}$ to $\sim +80 \text{ km s}^{-1}$), the position of the CO component moves from the South-West (positive velocities) to the North-East (negative velocities) in Fig. 8.5. Such a variation in position is already reported in W97 but they lack enough sensitivity so that any conclusions from their data alone remain speculative (compare W97 and the Appendix). This shift is seen as a significant feature in our new data (epoch 2003). Therefore, this positional change can be independently confirmed by the new data. The variation of

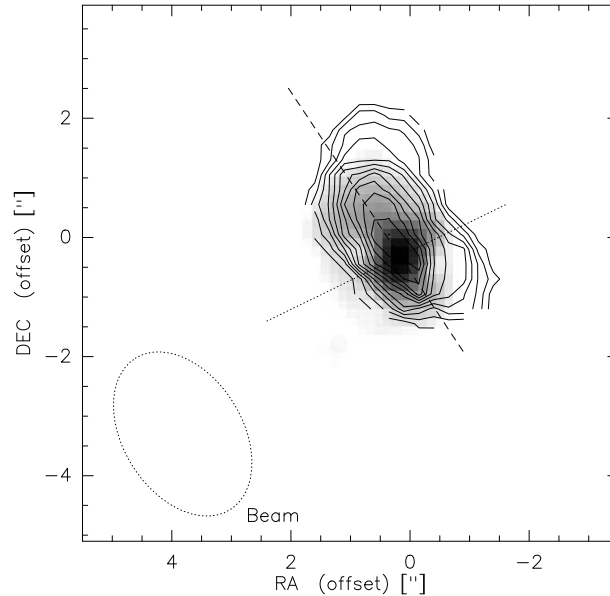


Figure 8.7: Integrated CO(1–0) emission of 3C48 (from -220 km s^{-1} to 160 km s^{-1}). The synthesized beam is indicated in the lower left (*dotted ellipse*). The *dashed* and *dotted* lines show the cuts along which the position-velocity diagrams were taken.

the position with velocity is clearly visible in the iso-velocity map shown in Fig.8.10 (*right*) and also apparent in the pv-diagram (Fig.8.8).

8.3.3.2 QSO-red/QSO-blue

In Fig.8.5, 8.8 & 8.9, two further compact peaks (at -200 km s^{-1} and $+120 \text{ km s}^{-1}$) are identified as QSO-red with 6σ and QSO-blue with 5σ . In the integrated intensity map (Fig.8.9) and also in the position-velocity diagram (Fig.8.8) taken along the cut indicated in the upper and lower panel of Fig.8.9, one finds that the centroids of these two components differ by about $\sim 0.5''$. According to the positional uncertainties of about $\sim 0.3''$ induced by the signal-to-noise ratio, the two features are roughly at the same position and almost coincident with the one of the QSO component. Thus, both components might be connected with each other and arise from the same gas reservoir. However, it remains speculative whether this gas reservoir is a (strongly rotating) disk associated with the QSO.

8.3.4 Earlier vs new data set

In Fig.8.11 & 8.12, the channel maps of the CO(1–0) emission from the earlier data set (epoch 1995; new reduction) and from our new data set (epoch 2003) are separately presented. Contours are the same as in Fig.8.5. Different to W97, Fig.8.12 has been mapped using natural instead of uniform weighting ($\text{robust}=1$) such as in Fig.8.5&8.11. In both channel maps, we independently find the high velocity features (QSO-red, QSO-blue) at $+118 \text{ km s}^{-1}$ and -196 km s^{-1} (compare Section 8.3.3) and a velocity gradient along the same direction. However, while the positions of the QSO-blue component between both epochs agree well with each other, QSO-red seems to be located more to the North in the earlier data set but this can be still due to position uncertainties induced by the signal to noise ratio. Another remarkable difference is the stronger peak in the earlier data set compared to the new one as it was already mentioned in Section 8.3.3. This might be explicable by the better sensitivity in our new data compared to W97 (factor of ~ 1.4 between both data sets), thus producing an increased certainty in the

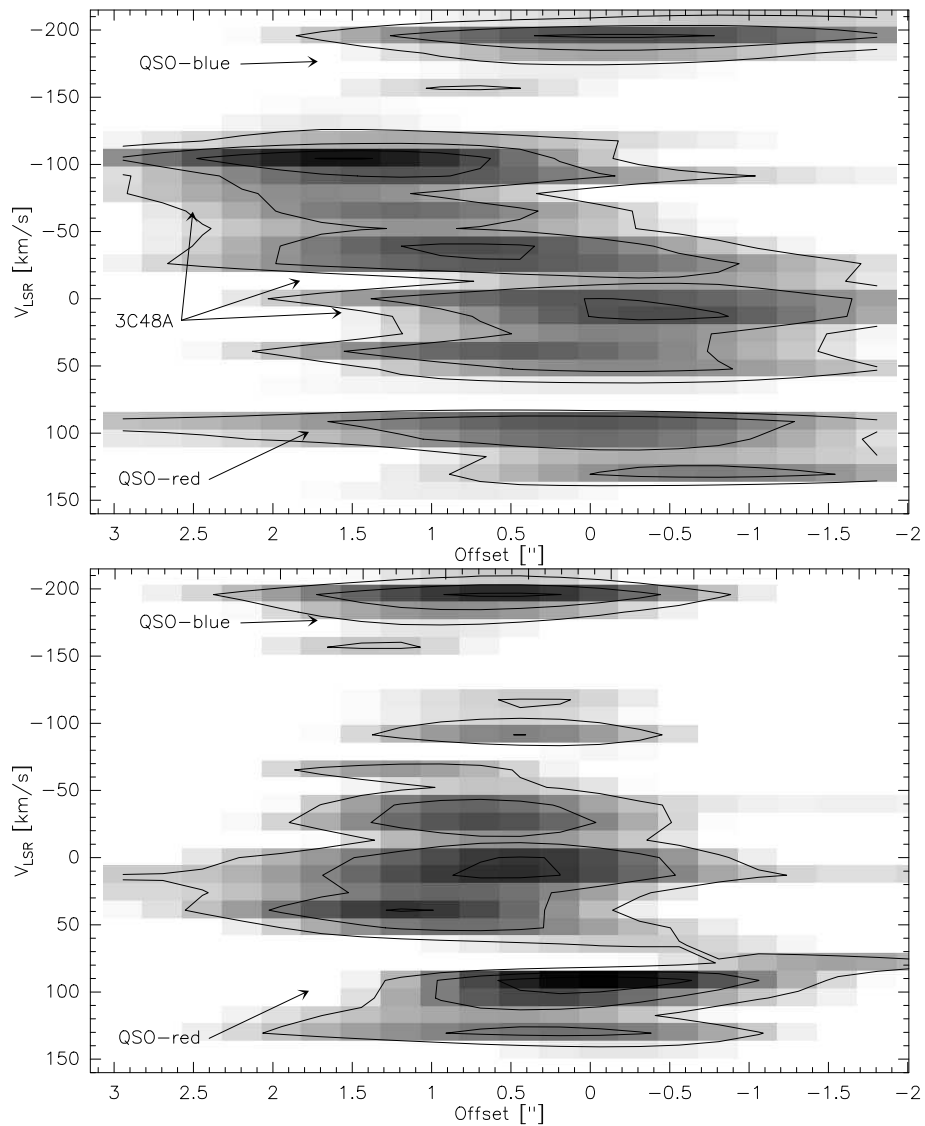


Figure 8.8: Position velocity diagram of the CO(1–0) emission in 3C48 along the two velocity gradients (dashed lines in Fig.8.7&8.9): *Upper panel*: from the South-West to the North-West (see Fig. 8.7 and middle panel in Fig.8.9). *Lower panel*: from South-East to the North-West (see Fig. 8.7 and upper and lower panel in Fig.8.9). Offset with respect to the position of QSO-red.

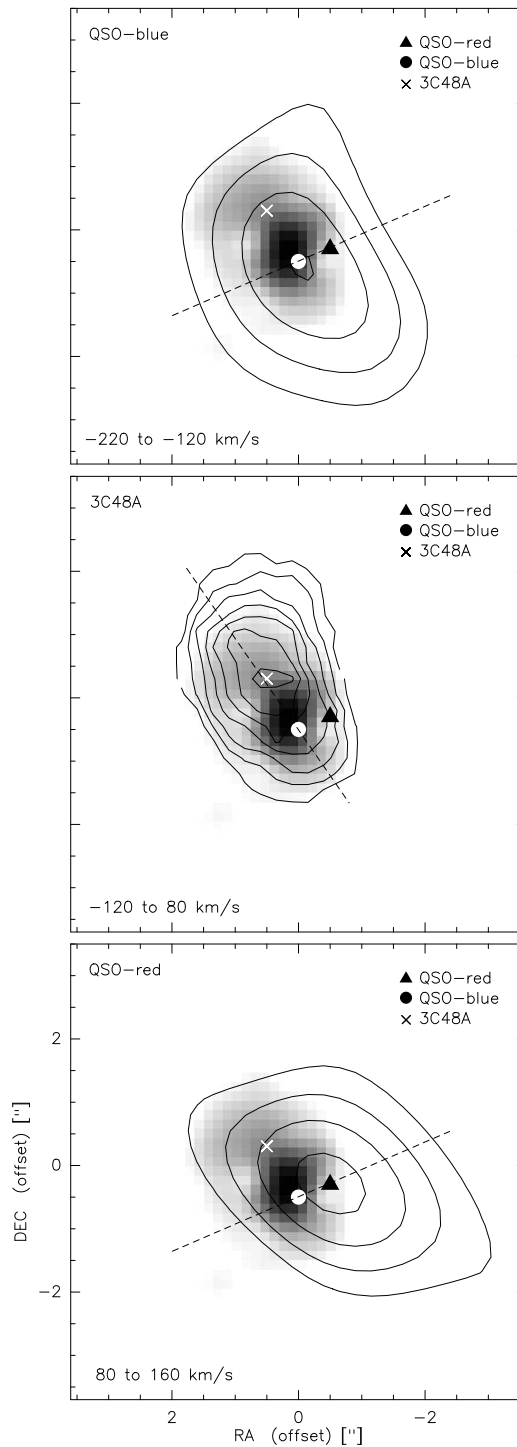


Figure 8.9: NIR image (Zuther et al. 2004; *grey scale*) overlaid with the integrated CO intensities of: QSO-blue (*upper image*: from -220 to -120 km s^{-1} ; $2\sigma=0.08$ to 0.2 Jy km s^{-1} by 1σ), 3C48A (*middle panel*: from -120 to 80 km s^{-1} ; $2\sigma=0.2$ to 0.8 Jy km s^{-1} by 1σ), QSO-red (*lower panel*: from 80 to 160 km s^{-1} ; $3\sigma=0.15$ to 0.3 Jy km s^{-1} by 1σ). Dashed lines indicate the cuts along which the pv-diagrams were taken.

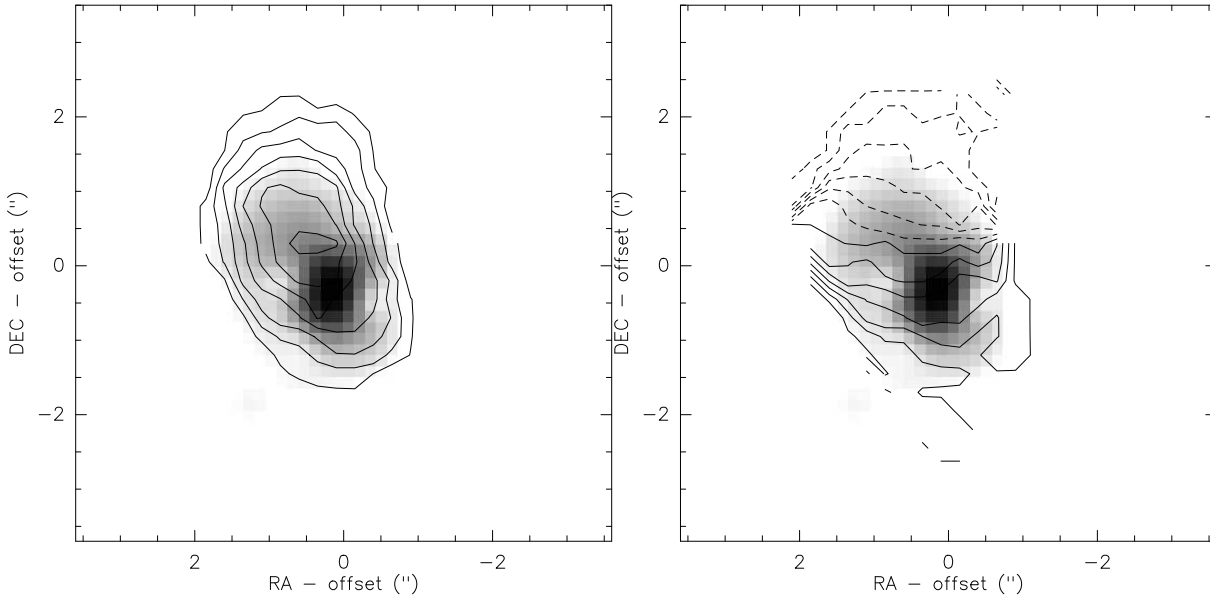


Figure 8.10: IR map of Zuther et al. 2004 (*grey scale*) overlaid with integrated CO(1-0) emission (*left*; from -95 to $+35$ km s^{-1}) and position-velocity (*right*) map of 3C48. Contours: 0.2 to 0.8 Jy km s^{-1} by 0.1 Jy km s^{-1} (*left*); -95 to -45 km s^{-1} (*dashed contours*) and -35 to 25 km s^{-1} (*solid contours*) in steps of 10 km s^{-1} (*right*). Beam: $3 \times 2 @ 32^\circ$ (uniform weighting).

continuum calibration and as a consequence in the continuum subtraction as well. Indeed, the peak flux derived with our new data is in better agreement with Scoville et al. (1993) than the W97 experiment. If uniform weighting is used for the earlier data set (W97), QSO-red appears to be weaker consistent with the channel maps published in W97 while the velocity gradient becomes more apparent due to the increased resolution. Thus, both data sets show independently the same morphology and kinematics indicating not only that the velocity gradient is indeed real but they also show the QSO-red and QSO-blue components.

8.3.5 $^{13}\text{CO}(3-2)$

At the given sensitivity, $^{13}\text{CO}(3-2)$ line emission remains undetected in 3C48. However, after subtracting the 1.2 mm continuum from the channel maps, a 1σ peak of $\sim 3 \text{ mJy}$ remains in the integrated map (from 200 km s^{-1} to $+200 \text{ km s}^{-1}$) at the position of the $^{12}\text{CO}(1-0)$ emission. Setting an upper limit of about $3\sigma \simeq 9 \text{ mJy}$ on the integrated line emission and integrating the CO(1-0) line in the same velocity range, $R_{32/12} = ^{13}\text{CO}(3-2)/^{12}\text{CO}(1-0) \leq 1.5$ is found which is very high. A ratio of $R_{32/12} = 0.1$ would have been expected if assuming similar conditions as in M82.

8.4 Gas and dynamical mass in 3C48

Even if the CO(1-0) line is in general a good tracer of the molecular gas content of a galaxy, an estimate of the molecular gas mass in 3C48 remains difficult and uncertain since this galaxy shows strong signs of a merger event. Thus, the standard CO-to- H_2 conversion factor², based on a determination in Galactic giant molecular clouds having undoubtedly very different properties and conditions, will not result in a correct value. Downes et al. (1993) emphasized that, in a case of molecular gas bound by the total gravitational potential of the galaxy

²see Equation 5.4

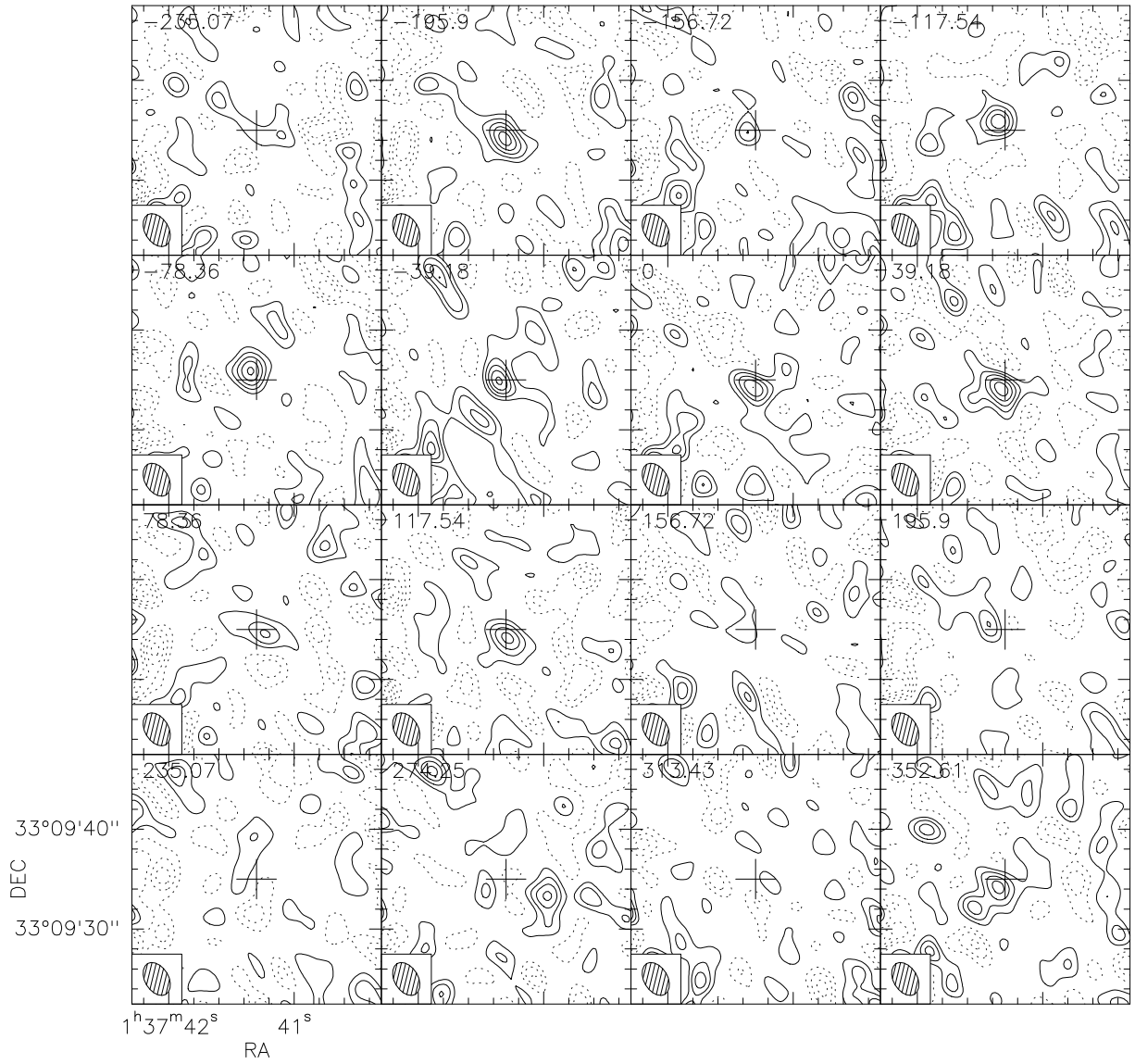


Figure 8.11: Channel maps of the CO(1-0) emission in 3C48 from the new data set alone (epoch 2003). Contours as in Fig.8.5. Noise: $1\sigma=1.5\text{mJy}$.

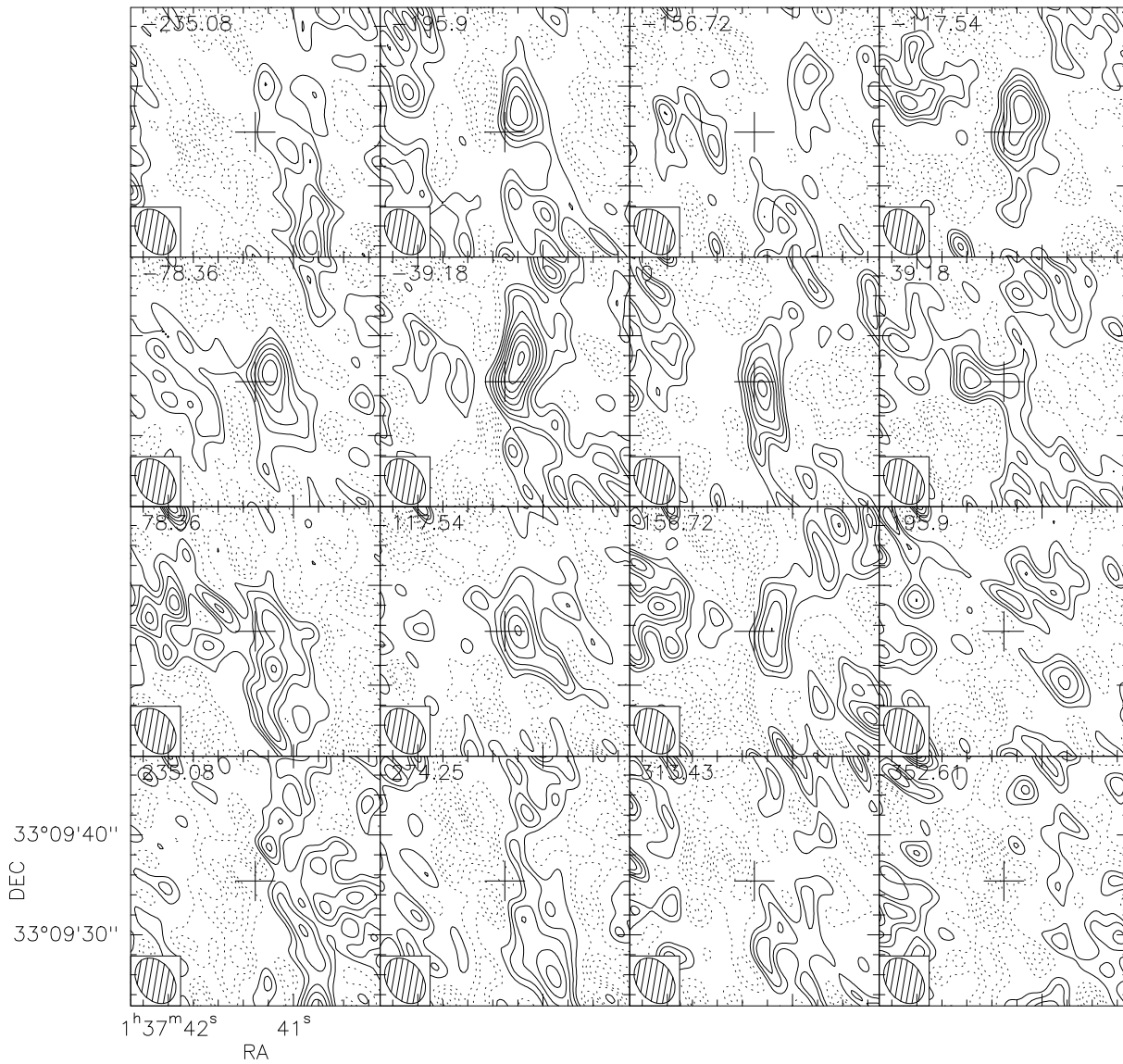


Figure 8.12: Channel maps of the CO(1–0) emission in 3C48 from the earlier data set alone (epoch 1995; new reduction). Contours as in Fig.8.5. Noise: $1\sigma=2.0\text{mJy}$.

(gas *and* stars) instead by self-gravity like in an ensemble of individual clouds (for instance in the *circumnuclear* regions of galaxies), the standard *galactic* CO-to-H₂ conversion factor could in fact be five times lower. Thus, the standard M_{gas} to L'_{CO} conversion factor of $4.8 M_{\odot} (\text{K km s}^{-1} \text{pc}^2)^{-1}$ (Solomon & Barret 1991) may yield at least an upper limit of $M_{\text{gas}} \sim 4 \times 10^{10} M_{\odot}$ ($M_{\text{gas}} = M(\text{H}_2 + \text{He})$) for 3C48 as well, taking the flux density of 1.9 Jy km s^{-1} integrated over the velocity range of -220 km s^{-1} to $+160 \text{ km/s}$. This splits up into $\sim 9 \times 10^9 M_{\odot}$ for QSO-red, $\sim 5 \times 10^9 M_{\odot}$ for QSO-blue or into $\sim 1.4 \times 10^{10} M_{\odot}$ for (QSO-red+QSO-blue) and $\sim 2.8 \times 10^{10} M_{\odot}$ for the extended disk located close to 3C48A. An independent control of the gas mass can be achieved via the dust mass. Taking the flux density (optically thin) of 0.55 Jy at $\nu_{\text{obs}} = 1620 \text{ GHz}$ (Meisenheimer et al. 2001) and $T_d = 53 \text{ K}$ (Fig.8.3), a dust mass of $M_{\text{dust}} \simeq 8 \times 10^7 M_{\odot}$ is obtained. Assuming a standard (*galactic*) gas to dust mass ratio of ~ 150 , the gas mass can be estimated to $M_{\text{gas}} \sim 1 \times 10^{10} M_{\odot}$ agreeing with the lower limit of the CO based estimate. However, also here a *galactic* value is assumed. Solomon et al. (1997) determined dust-to-gas mass ratios for ULIRGs between ~ 100 - 1000 while for QSOs Yun et al. 2004 found a ratio which is tendentially ~ 10 times lower. 3C48 is considered as transition object between ULIRGs and QSOs. Thus, the gas mass derived via the dust emission must also be regarded rather as a *lower* limit. Nevertheless, both estimates show that the true gas mass is probably indeed in the range of $1 - 4 \times 10^{10} M_{\odot}$. Another approach to find a *lower* limit for the gas mass, is to assume that the CO is optically thin (Solomon et al. 1997). This method results in a limit of the gas mass of $\sim 4 \times 10^9 M_{\odot}$ which is by a factor 2 lower than the gas mass obtained via dust.

The total dynamical mass³ - not corrected for inclination - amounts to $\sim 2 \times 10^{11} M_{\odot}$ assuming $\Delta v = 320 \pm 30 \text{ km s}^{-1}$ (Table 8.2) and a source radius of $\sim 4 \text{ kpc}$ (source diameter estimated to $2'' \equiv 8 \text{ kpc}$; Fig.8.7). This value is a factor of 6 higher than the one derived by Wink et al. (1997) but this is due to the fact that we used the “merger” equation from Genzel et al. (2003b) instead of the “standard” one. We thus get a gas-to-dynamical mass ratio of $\sim 20\%$ adopting the upper limit for the CO based estimate of the gas mass. In fact, this range could also be lower since inclination effects were not taken into account. However, this ratio is in good agreement with other estimates based on a sample of ULIRGs with double nuclei done by Evans et al. (2002) for instance. Scharwächter et al. (2004) pointed out that the morphology of 3C48 can indeed be explained through the merging process of two spiral galaxies. The standard gas-to-dynamical mass ratio of 10% known from spiral galaxies is also still compatible with the our estimate.

8.5 3C48 versus the Antennae galaxies and Arp220

In terms of a unification of active nuclei (Sanders et al. 1988), QSOs are supposed to evolve from Ultra-Luminous InfraRed Galaxies (ULIRGs). This evolution is assumed to be triggered by preceding galaxy interaction and mergers. Arp220 and the “Antennae” galaxies (NGC 4038/39) belong to the class of ULIRGS and show both strong signs for a merger event (Whitmore et al. 1999, Graham et al. 1990). Scharwächter et al. (2004) recently succeeded in simulating 3C48 with a multi-particle model by using the setup of the “Antennae” galaxies but seen from a different viewing angle. Due to its optical morphology (e.g. Whitmore et al. 1999), the “Antennae” galaxies are regarded to be an archetypical early-stage merging system of two gas-rich spiral galaxies at a distance of only 18 Mpc . Gao et al. (2001) report on a huge reservoir of molecular gas in the whole system ($\sim 1.5 \times 10^{10} M_{\odot}$). Also in the overlapping region of the two merging galaxies, an unusually large amount of molecular gas of $\sim 4 \times 10^9 M_{\odot}$ has been observed (Zhu et al. 2003). Not only the CO emission, but also the MIR (mid-infrared), FIR (far-infrared) as well as submillimeter and radio continuum emission peak at the intermediate region between the two colliding disks. The large infrared luminosity of $\sim 10^{11} L_{\odot}$ classified the “Antennae” galaxies as ULIRGs (Sanders & Mirabel 1996). Based on long-wavelength studies (e.g. Hummel & van der Hulst 1986, Mirabel et al. 1998, Haas et al. 2000, Neff & Ulvestad 2000), the enormous activity of the “Antennae” galaxies is triggered by a system-wide starburst rather than by an AGN. The two nuclei are separated by about $\sim 7 \text{ kpc}$ (projected separation), almost twice as far as in the case of 3C48 (projected separation of the two components $\sim 4 \text{ kpc}$).

³Since 3C48 is supposed to be merger, Equation 6.3 was not taken. Genzel et al. (2003b) proposed the following equation in the case of mergers: $M_{\text{dyn}} \sin^2(i) = 2.1 \cdot 10^6 \Delta v_{\text{FWHM}}^2 \times r [']$, with i the inclination.

Arp220 has a high molecular gas content of $\sim 10^{10} \mathcal{M}_{\odot}$ within the central kiloparsec (Scoville et al. 1986). It also contains two nuclear components with a projected separation of ~ 300 pc, interpreted as two nuclei, and an extended tidal tail leading thus to the hypothesis of an ongoing merging process (Norris 1985; Graham et al. 1990). The detected huge infrared luminosities ($L_{8-1000\mu\text{m}} = 1.4 \times 10^{12} L_{\odot}$) established the classification as a ULIRG (Soifer et al. 1987). Similar to Zuther et al. (2004), Scoville et al. (1998) report on a high dust obscuration of one of the two nuclei (3C48A is found to be reddened as well). Besides a large molecular gas disk ($r \sim 1$ kpc) rotating around the dynamical center of the system, high resolution ($\sim 0.5''$) observations of the CO emission unveil nuclear disks ($r \sim 100$ pc) around both nuclei (Sakamoto et al. 1999). These two nuclear disks appear to counterrotate with respect to each other and have gas masses of $\sim 10^9 \mathcal{M}_{\odot}$ and dynamical masses of $\gtrsim 2 \times 10^9 \mathcal{M}_{\odot}$. The situation in 3C48 is reminiscent of that in Arp220. Two rotating gas rich disks are also found in 3C48. However, while Eckart & Downes (2001) have shown, that the results for Arp220 can also be interpreted in the framework of a warped disk, such an interpretation is unlikely for 3C48 since one of the two nuclear components indeed contains the active nucleus in contrast to Arp220.

8.6 Summary and Conclusions

New PdBI observations of the CO(1–0) as well as 1.2 mm and 3.5 mm continuum emission in 3C48 combined with a previous data set from Wink et al. (1997) were presented. The 1.2 mm continuum was observed and mapped for the first time at such a high resolution of $\sim 0.8''$. The continuum images at both wavelengths unveil extended emission. At 1.2 mm, the continuum is clearly elongated towards the second NIR nuclear component 3C48A. Also, an extension co-aligned with the VLBI radio jet (Wilkinson et al. 1991) is found. While the QSO component and the radio jet appear to be dominated by synchrotron emission, the situation for 3C48A is not that clear. Indications for both are found, synchrotron and thermal processes. The latter one seems maybe a little bit more likely since thermal emission caused by dust would be supported by the finding of Zuther et al. (2004) that 3C48A is reddened. On the other hand, the shape of the 3.5 mm continuum rather points towards synchrotron emission. Higher resolution observations at 3.5 mm and 1.3mm, enabling to distinguish between the respective components, are thus needed for clarification.

The presence of strong CO(1–0) line emission is confirmed and its line parameters are consistent with both Scoville et al. (1993) and W97. It appears to be slightly extended in the synthesized beam towards the North and the South-West. The higher sensitivity allows to confirm a velocity gradient seen across 3C48A and the IR-QSO indicating rotation of a gas disk located close 3C48A, and a second steep velocity gradient almost perpendicular to it across the IR-QSO probably implying a more compact nuclear gas reservoir if not even a disk (~ 2 kpc) on the QSO itself (South-Western component). The total gas mass of a few times $10^{10} \mathcal{M}_{\odot}$ is not unusual for merger galaxies but an exact estimate is still tentative since the physical properties might differ significantly from those assumed for the mass determination.

However, what can be concluded from the new data? What is the nature of 3C48A? Two different hypotheses can be mainly imagined: 1) 3C48A is a second nucleus leftover from a merger process. 2) 3C48A unveil an interaction between the jet and the interstellar medium. Unfortunately, none of these scenarios can be totally discarded but at least the second one appears to be rather unlikely with respect to the new information based on the 1.2 mm continuum and the CO(1–0) emission. A detailed analysis of the 1.2 mm continuum component suggests three distinct features: one at the position of the IR-QSO to the South-West, one in elongation of the VLBI jet to the North and a third one at the position of 3C48A to the North-East. Also the continuum data at 3.5 mm indicate extended but unresolved emission towards 3C48A. 3C48A already lies in another direction with respect to the VLBI jet. If the third “jet-like” 1.2 mm continuum component represents indeed the jet emission, 3C48A cannot at the same time be caused by an interaction of the jet and the ISM since it is located in a quite different direction. Therefore, this would rather exclude the second hypothesis even if a bending of the jet can neither be totally disregarded. Another argument supporting the hypothesis of 3C48A as a second nucleus can be found in the different CO(1–0) velocity components. The data clearly indicate two different dynamical systems of the molecular gas: one extended disk centered between both nuclear features and another compact and stronger

rotating gas reservoir almost centered on the QSO itself (South-Western component). Thus, we favour 3C48A being a second nucleus.

Compared to Arp220 and the “Antennae” galaxies, 3C48 shows quite similar properties. All three objects have high gas masses of a few times $10^{10} \mathcal{M}_{\odot}$, they all show high infrared luminosities and have two nuclear components with different projected separations interpreted as two nuclei. Also the higher concentration of dust in one of the nuclei appears to be comparable. Hence, 3C48 seems to be indeed in a stage similar to the “Antennae” galaxies and Arp220 in terms of an evolutionary sequence.

Chapter 9

Q0957+561

New interferometric observations of the CO(2–1) and 3.1 mm continuum emission in the high-redshifted ($z=1.4141$) quasar Q0957+561 (Krips et al. 2004a,b) will be presented in this chapter. In combination with a previous data set obtained by Planesas et al. (1999, in the following P99), a reanalysis of the data was carried out based on precedent work by Krips 2001 (diploma thesis). The emission in the CO(2-1) lines reveals a gas-rich host galaxy with a peculiar double-peaked profile at one of the two lensed images. Our new interferometric CO maps agree well with HST images of the host galaxy around Q0957+561 obtained by Keeton et al. (2000). Thus, the two velocity components are associated with one and the same system, a rotating molecular gas disk in the host galaxy. In the following sections, further arguments will be presented to substantiate the rotating disk hypothesis. New model calculations of the gravitational lensing effect in this system will also be discussed¹.

The chapter is structured as following: A brief introduction of the lensed quasar will be given in section 9.1. The observations will be presented in section 9.2. Section 9.3 contains the observational results. The modelling will be outlined in section 9.4 and the chapter will be finished with a discussion.

9.1 Introduction

Since the discovery of Q0957+561, the first confirmed gravitationally lensed quasar (Walsh et al. 1979) at a redshift of $z = 1.4141$, several models have been developed to understand the lensing potential of the intervening galaxies: a giant elliptical galaxy (G1) at a redshift of $z = 0.355$ with a surrounding cluster and probably another group of background galaxies at $z = 0.5$ (Angonin-Willaime et al. 1994; Chartas et al. 1998). Besides flux amplification, gravitational lensing helps also to improve on spatial resolution as detailed by Kneib et al. (1998). Differential lensing effects, which are detectable through the comparison of lensed images at different wavelengths, indeed provide a powerful tool to probe the structure of a galaxy at a much higher resolution than possible with current millimeter interferometers.

In the optical and radio domain, the gravitational lensing effect in Q0957+561 produces two observable images of the quasar (*compact* source) and one to two images of the radio jet (*extended* source) depending on the part of the jet (Fig.9.1; Harvanek et al. 1997, Keeton et al. 2000). Keeton et al. (2000) have recently also detected the stellar component of the host galaxy. According to simulations carried out by Keeton et al. (2000), the host galaxy is lensed up to five times. P99 have succeeded in detecting the molecular gas in the host galaxy traced by the CO(2–1) line. They report on mainly three gas components, one, labeled CO-A, associated with the northern image of the quasar, a second one (CO-B) at the position of the southern image and an apparent third one (CO-F) which was interpreted as an arc extending over $\sim 6 - 8''$ from CO-B to the East. Towards CO-A, the authors

¹In contrast to the other chapters in this PhD thesis, a Hubble constant of $H_0=65 \text{ km s}^{-1} \text{ Mpc}^{-1}$ instead of $75 \text{ km s}^{-1} \text{ Mpc}^{-1}$ was used to be consistent with my diploma thesis. Distances have thus to be multiplied with a factor $h_0^{-1} = 75/65$ and masses with h_0^{-2} to convert them into a cosmology with $H_0=75 \text{ km s}^{-1} \text{ Mpc}^{-1}$.

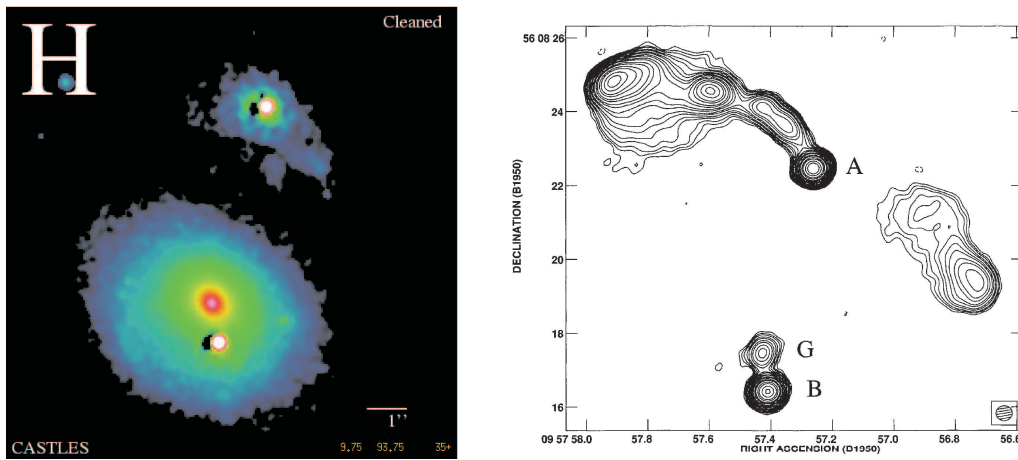


Figure 9.1: *On the left*: optical image (H-band) of Q0957+561 obtained by Keeton et al. 2000. The northern object corresponds to image A, the southern to image B and the intermediate is the main lensing galaxy labeled as G. Besides the bright quasar, also the host galaxy is visible towards the northern image A. *On the right*: radio map (6cm) of Q0957+561 observed by Harvanek et al. (1997). The two images A and B of the quasar appear here plus the jet and counterjet with their lobes. The main lensing galaxy G is also visible.

found a double-peaked line profile with an unusually large linewidth of $\sim 1000 \text{ km s}^{-1}$. The attempt to connect all different CO components to one system, like a rotating gas disk, located in the host galaxy around Q0957+561, led to contradictions based on predictions from gravitational lensing theory. P99 hence interpreted the blueshifted part in CO-A, CO-B and CO-F as a rotating gas disk while the redshifted line emission at CO-A was suggested to originate from a close companion towards Q0957+561 so far undetected at other wavelengths. To scrutinise and further improve on P99's interpretation, a numerical code was developed which incorporates existing lensing models of Q0957+561 (Krips 2001; diploma thesis). New model calculations done with this code excluded arcs with a size greater than $4''$ based on constraints for the lens potential from mainly radio and also other wavelengths. Thus, the genuineness of CO-F was strongly doubted. Furthermore, the significant inconsistencies between the gas properties and the stellar distribution published by Keeton et al. (2000) gave reasons for strong caveats against the interpretation of the double-peaked CO(2-1) line profile given by P99. A reanalysis of P99's data also revealed an overestimate by a factor of ~ 1.5 of the linewidth derived towards CO-A by P99 (see Krips 2001 (diploma thesis) and section 9.2.1). Due to all these reasons and to gain in sensitivity to allow for a more qualitative interpretation, new observations with the IRAM interferometer have been carried out which were finally also combined with the previous data set of P99.

9.2 Observations

CO(2-1) and (5-4) observations of Q0957+561 were made simultaneously in 1998 and again in 2003 with the IRAM interferometer. The first observation run is discussed in P99. Only additional details are given on the refined reduction of this data set.

9.2.1 Data taken in 1998

The observations were carried out in the B, C and D configurations. The bandwidth of the cross-correlator was set up to cover 420 MHz at both frequencies with a spectral resolution of 2.5 MHz, equivalent to 7.8 km s^{-1} at 95.5 GHz (redshifted CO(2-1)) and 3.1 km s^{-1} at 238.7 GHz (CO(5-4)). The bandpass was calibrated on 3C273,

Position	A('') ^a	B('')	reference
<i>Optical</i>			
RA	0	1.229±0.005	Keeton et al. 2000
DEC	0	-6.048±0.004	
<i>Radio</i>			
RA	0	1.229±0.005	Harvanek et al. 1997
DEC	0	-6.046±0.004	
redshift	1.4141		Walsh et al. 1979
Luminosity Distance	~ 11 Gpc		^b
Angular-size Distance	~ 1.9 Gpc		^b
Scaling factor	1''≡9 kpc		
Flux	A	A/B	reference
<i>Optical (H-band)</i>			
quasar	15.6±0.03 mag	1.1	Keeton et al. 2000
host galaxy	~ 18.4 mag	1.0	
<i>Radio (6 cm)</i>			
quasar	38 mJy	1.3	Harvanek et al. 1997

Table 9.1: Some basic properties of Q0957+561. ^a centered on $\alpha_{J2000}=10^{\text{h}}01^{\text{m}}20.71^{\text{s}}$ $\delta_{J2000}=+55^{\circ}53'55.6''$. ^b assuming a flat cosmology with $H_0=65 \text{ km s}^{-1}\text{Mpc}^{-1}$ and $q_0=0.5$ ($\Omega_M=0.3$).

3C345 or 0923+392 while phase and amplitude calibrations were performed on 0917+624. Unlike P99, data from an entire observing run had to be discarded that were substantially reducing the quality of the maps. The velocity scale was also corrected which was wrong by a factor of 1.5 in P99 due to a data header error.

9.2.2 Data taken in 2003

The observations were carried out in the C and D configurations. The bandwidth of the cross-correlator was set up to cover 580 MHz with a spectral resolution of 1.25 MHz corresponding to 3.9 km s^{-1} at 95.5 GHz and 1.6 km s^{-1} at 238.7 GHz. The two data sets were resampled to a spectral resolution of 7.8 km s^{-1} (2.5 MHz) over the 420 MHz band covered by the first observations to ensure uniform noise in the merged velocity channels. 3C273, 0851+202 and 0420-014 were used as bandpass calibrators while 0804+499 and 1044+719 were taken as phase and amplitude calibrators. Relative to P99, the sensitivity of the combined data sets is now higher by a factor of ~ 2 .

9.3 The data

9.3.1 Continuum emission

9.3.1.1 3.1 mm

The radio continuum was computed separately for the two data sets by averaging channels with a velocity lower than -510 km s^{-1} and higher than $+540 \text{ km s}^{-1}$. Two lensed images of the quasar, labeled A and B, and a radio jet C appear at this wavelength (Fig.9.2), in agreement with VLA observations (Harvanek et al. 1997). The positions coincide with the optical ones within the errors (Tab. 9.1 and 9.2). Also in agreement with previous work, the A and B components are pointlike whereas the radio jet C component is slightly elongated ($\sim 2.7''$) in the beam of the interferometer. Finally, there is no evidence for variability above 10% between May 1998 and April 2003 in all three components. This coincides with results obtained at 3.6 cm with the VLA by Harvanek et al. (1997).

	CO(2→1)		
	A-blue	A-red	B-blue
Rel. positions (")	(-1.9,+3.8)	(-1.6,+6.1)	(+0.2,-1.1)
Position errors (") ^a	(+0.2,+0.2)	(+0.3,+0.3)	(+0.2,+0.2)
Peak flux ^c (mJy/beam)	0.9±0.2	2.1±0.2	2.2±0.2
	(1.1±0.3)	(1.7±0.3)	(2.3±0.3)
FWHM (km s ⁻¹)	280±60	160±20	280±50
Vel. at line peak ^d (km s ⁻¹)	-140±30	340±15	-140±23
Integr. line flux (Jy km s ⁻¹)	0.25±0.06	0.34±0.06	0.61±0.06
	Continuum at 3.1 mm ^b		
	A	B	C
Rel. positions (")	(-1.45,+5.00)	(-0.24,-1.0)	(3.23,7.13)
Position errors (") ^a	(+0.06,+0.08)	(+0.08,+0.10)	(+0.07,+0.08)
Flux density (mJy)	4.7 ± 0.2	3.4 ± 0.2	6.2 ± 0.2
Peak flux ^c (mJy/beam)	4.6±0.2	3.3±0.2	5.1±0.2
	(4.2±0.3)	(2.5±0.3)	(5.5±0.3)

Table 9.2: Flux densities, velocities and positions of individual image components. Values have been determined by fitting Gaussian profiles to the visibilities. Offset position (0,0) is at the lens position specified in the caption of Fig.9.2. ^a Relative position uncertainties are based on statistical noise and do not include astrometric errors. ^b Values taken from the second observation campaign in 2003. ^c Values in brackets are from the reanalysis of the P99 data, and do not include data from 2003. ^d Velocities are relative to the redshift at $z = 1.4141$. The CO(2-1) line parameters for the two A components were not derived from the spectrum shown in Fig.9.14 that was taken between A-red and A-blue, but are based on spectra determined at the respective positions of A-blue and A-red.

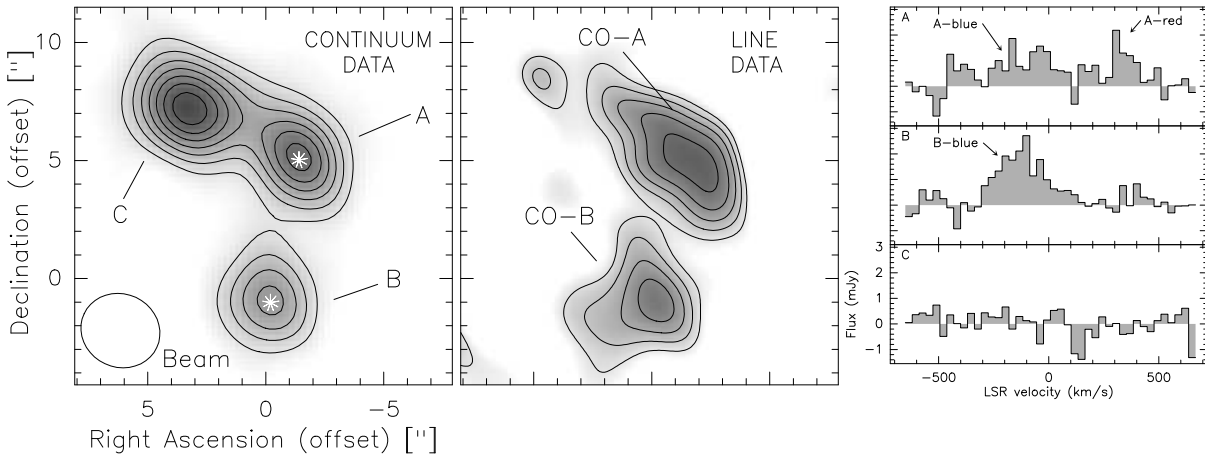


Figure 9.2: *On the left*: 3.1 mm continuum emission observed with the PdBI. The synthesized beam is indicated in the lower left corner. Contour levels are from $5\sigma=1.0$ to 4.7 mJy beam⁻¹ in steps of 0.6 mJy beam⁻¹. Offset position (0,0) is at the position of the lens, i.e. at $\alpha_{J2000} = 10:01:21.0$, $\delta_{J2000} = +55:53:50.5$. The white stars indicate the optical positions of the A and B image. *In the middle*: Integrated CO(2-1) emission. Contour levels are: $3\sigma=0.33$ to 0.77 Jy beam⁻¹ km s⁻¹ in steps of 0.11 mJy beam⁻¹ km s⁻¹. *On the right*: Spectra of the CO(2-1) line emission taken at the position of CO-A (*upper panel*), CO-B (*middle panel*) and the jet C (*lower panel*). The rms noise per 10 MHz channel is ~ 0.65 mJy. The spectrum at the position of the jet is indicative of the noise level. Velocities are relative to the redshift at $z = 1.4141$.

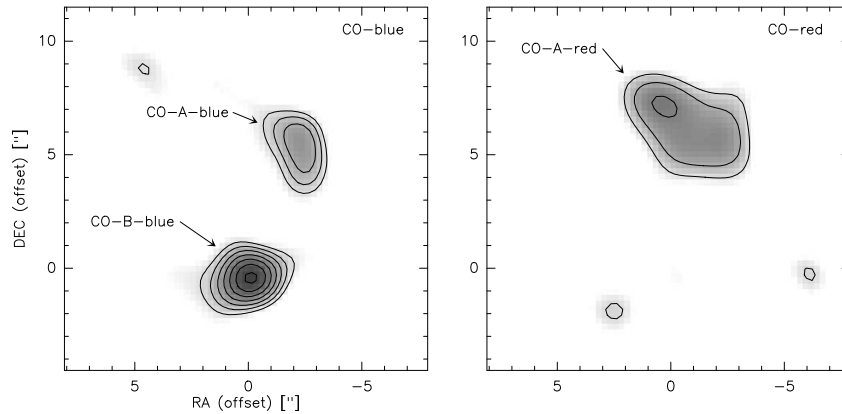


Figure 9.3: *On the left:* Integrated emission of the blueshifted CO(2–1) line (from -350 km s^{-1} to $+150 \text{ km s}^{-1}$). Contours are from $3\sigma=0.2$ to $0.62 \text{ Jy beam}^{-1} \text{ km s}^{-1}$ in steps of $0.07 \text{ Jy beam}^{-1} \text{ km s}^{-1}$. *On the right:* Integrated emission of the redshifted CO(2–1) line (from $+150 \text{ km s}^{-1}$ to $+450 \text{ km s}^{-1}$). Contours are from $3\sigma=0.17$ to $0.3 \text{ Jy beam}^{-1} \text{ km s}^{-1}$ in steps of $0.06 \text{ Jy beam}^{-1} \text{ km s}^{-1}$.

9.3.1.2 1.3 mm

A noise level of $\sigma = 0.6 \text{ mJy}$ was obtained in the 2003 data by averaging over the entire bandwidth available at 1.3 mm (-360 km s^{-1} to $+360 \text{ km s}^{-1}$). A 3.5σ peak is found at the 3 mm position of the A-continuum component, a 2σ peak at the position of the B component and a 4σ peak at the position of C. The steep drop in flux density at 1.3 mm is consistent with the weakness of the synchrotron emission expected if one extrapolates to this short wavelength the spectral index of $\simeq -0.6$ measured in the 20 cm (Harvanek et al 1997) to 3 mm (P99, and this work) range. Any dust emission is either too weak or too extended (say $> 3''$) to be detected at this frequency. Data from the 1998 run were not taken into consideration as they were significantly less sensitive.

9.3.2 Line emission

9.3.2.1 CO(2-1)

To estimate flux densities in the CO(2-1) line (Tab. 9.2), the 3.1 mm continuum was first removed separately from each data set to account for possible low level continuum variability. Then, all data sets were combined to a single uv-table, and velocity channels in the -510 km s^{-1} to $+540 \text{ km s}^{-1}$ range was summed to produce an integrated line map (Fig. 9.2). The resulting map shows two lensed images labeled CO-A and CO-B (P99). The emission centroids of the two images are separated by $\simeq 7''$, about $1''$ more than in the optical, radio and millimeter continuum (Tab. 9.2). The spectral profiles (Fig. 9.3) taken towards positions CO-A and CO-B are different. While a double-peaked profile is visible towards the northern image CO-A, a single blueshifted velocity component is detected towards CO-B. The shape of the blue components measured towards CO-A and CO-B is similar. The integrated emission of the red- and blueshifted line are separately shown in Fig. 9.3. The CO-A-red component is located more to the North-East than the CO-A-blue feature. The CO-F image reported by P99 could not be confirmed with the new observations.

9.3.2.2 CO(5-4)

No significant line emission was found at the position of CO-A and CO-B, the two line components at 3mm. A $\sim 1.9 \text{ mJy}$ ($= 3\sigma$) peak is only tentatively detected in the velocity integrated map (-350 km s^{-1} to $+150 \text{ km s}^{-1}$) at the position of CO-B. The intensity of the CO-B component at 3mm over the same velocity range is estimated to be 1.8 mJy . Although uncertain because of the low signal to noise ratio of the (5-4) line, and possibly because of

some residual continuum emission, an upper limit of ≤ 1 is set on the velocity averaged intensity ratio $R_{54} = \text{CO}(5-4)/\text{CO}(2-1)$ toward CO-B, the strongest of the two line components.

9.4 Modelling Q0957+561

A numerical code² was developed based on the standard gravitational lens equation (Schneider et al. 1992) to explain the absence of the double-peaked line profile toward CO-B and to investigate the distribution and kinematics of the molecular gas around Q0957+561.

The code has been applied on 6 different models of Q0957+561 (Tab. 2), all based on previous work by Barkana et al. (1999) and Chae et al. (1999). The mass distributions of the three models are based on King profiles, as proposed by Falco et al. (1985— models: FGS, FGSE, FGSE+CL), the remaining three on a softened power-law distribution, as suggested by Grogin et al. (1996—models: SPLS, SPEMD, SPEMD+CL). FGS and SPLS are spherical models where the effects of the surrounding cluster at $z = 0.355$ are approximated by an external shear, FGSE and SPEMD models take into account the ellipticity in the lens galaxy, the remaining models use a single isothermal sphere (SIS) to model the lens properties of the cluster (SPEMD+CL, FGSE+CL). A point mass was added to the King profiles to account for a black hole in the center of the lens galaxy (Mediavilla et al. 2000; Barkana et al. 1999), except for the softened power law models which implicitly cover this case. The group of background galaxies at $z = 0.5$ has not been considered, however. The composite pseudo-Jaffe models used by Keeton et al. (2000) have not been taken into account as they would not have provided further details for our analysis.

To find the set of parameters for each model reproducing our observations with the lowest χ_r^2 , the parameter space was first restricted with simple assumptions based on the number of lensed images, separations among them etc. and with comparisons to previous work done by other groups (e.g. Keeton et al. 2000, Barkana et al. 1999 and Chae et al. 1999). The parameter space was then scanned for each model to get the lowest χ_r^2 and included the following constraints: relative positions of the A and B continuum components at 3.1mm with respect to the lens (4 constraints; (Tab.8.1)), relative positions of the CO-A-blue and CO-B-blue features, the intensity ratio between the two lensed images for the CO(2–1) line and 3.1mm continuum emission and the optical/radio time delay of 400-420 days taken from Kundic et al. (1997) and Haarsma et al. (1999). This results in a total of 11 constraints (cf. Tab.9.3). For simplicity, compact fixed-size Gaussians were used to approximate the respective components. The so found best-fit models turned out to be in excellent agreement with simulations based on VLA and optical data (e.g. Barkana et al. 1999, Chae et al. 1999 and Keeton et al. 2000).

The SPEMD+CL, FGSE+CL and the FGS models reproduce the observed constraints with the lowest χ_r^2 (≤ 3 ; Tab. 9.3). Although the FGS model yields one of the best results, the spherical mass distributions are not favoured because of the ellipticity of the lens (Bernstein et al. 1997). The contribution of the cluster is also important: The models that best explain these observations all require an SIS cluster (FGSE+CL and SPEMD+CL, the latter has a lower χ^2)³. The time delay derived from the same models are in rather good agreement with recent optical and radio measurements ($\sim 400 - 420$ days; Kundic et al. 1997; Haarsma et al. 1999).

9.4.1 Line emission

In the following two subsections, different approaches for modelling the blueshifted line emission based on the best-fit FGSE+CL potential are discussed and then the difference seen in the profiles toward CO-A and CO-B is explained.

²A detailed description of the code can be found in Krips 2001 (diploma thesis)

³For the following discussion, the best-fit FGSE+CL model will be mainly used since it is closer to already published results, e.g. Keeton et al. (2000). However, both models are fully equivalent for argumentation purposes.

	SPLS ^e	SPEMD ^e	SPEMD +CL ^f	FGS ^e	FGSE ^e	FGSE +CL ^e
SOURCE POS. (SOURCE PLANE)						
<i>Radio continuum</i>						
$(\Delta\alpha_s, \Delta\delta_s)$ ($''$) ^a	(-0.02,0.90)	(-0.14,1.02)	(2.20,2.49)	(-0.15,1.06)	(-0.18,1.10)	(1.80,2.58)
<i>Line emission</i>						
$(\Delta\alpha_s, \Delta\delta_s)$ ($''$) ^a	(-0.23,0.95)	(-0.32,1.00)	(1.93,2.39)	(-0.38,1.05)	(-0.40,1.05)	(1.54,2.47)
LENS PROPERTIES						
<i>Galaxy:</i>						
σ_v (km s ⁻¹)	400	400	360	300	340	320
ξ_c ($''$)	0.12	0.12	0.02	1.2	0.6	1.1
ε	—	0.1	0.2	—	0.1	0.3
Φ_{PA} ($^\circ$) ^b	—	64	64	—	64	64
η	1.1	1.0	1.1	—	—	—
<i>Cluster:</i>						
γ' ^d	0.3	0.2	—	0.4	0.3	—
$\Phi_{\gamma'}$ ($^\circ$) ^b	60	60	—	60	60	—
σ_{cl} (km s ⁻¹)	—	—	375	—	—	350
$(\Delta\alpha_{\text{cl}}, \Delta\delta_{\text{cl}})$ ($''$) ^b	—	—	(13.7,6.9)	—	—	(13.7,6.9)
<i>Black hole:</i>						
M_{bh} ($10^{12} M_\odot$)	—	—	—	0.5	0.3	0.2
$\Delta\tau_{\text{cont}}$ [days]	411	420	417	417	421	416
$\Delta\tau_{\text{line}}$ [days] ^g	421	450	412	423	454	414
$m_{\text{RC}}^{\text{total}}$	5	4	4	3	3	3
$m_{\text{CO}}^{\text{total}}$	6	7	9	5	6	6
N_{dof} ^c	3	2	2	3	2	2
χ_r^2 ^c	3.0 (3.4)	5.5 (40)	1.5 (1.5)	1.3 (1.2)	5 (40)	2.0 (2.5)

Table 9.3: Best fit parameters for Q0975+561. Parameters are: $\Delta\alpha \equiv$ right ascension, $\Delta\delta \equiv$ declination, $\sigma \equiv$ velocity dispersion, $\xi_c \equiv$ core radius, $\varepsilon \equiv$ ellipticity, $\Phi_{\text{PA}} \equiv$ position angle, $\eta \equiv$ power law index, $\gamma^{(\prime)} \equiv$ shear term, $\Phi_{\gamma'} \equiv$ shear angle, $M_{\text{bh}} \equiv$ mass of the black hole, $\Delta\tau \equiv$ time delay, $m \equiv$ magnification factor. ^a Offset from lens position. ^b Fixed parameters. ^c Values in brackets are χ_r^2 -tests with time delay. The reduced χ_r^2 is defined as: $\chi_r^2 = \chi^2/N_{\text{dof}}$ where N_{dof} is the degrees of freedom. ^d γ' is only taken for the elliptical potentials ($\gamma' = \gamma/(1 - \kappa)$) where $\kappa = \Sigma_{\text{clus}}/\Sigma_{\text{crit}}$ is defined as the surface mass density of the cluster in units of the critical surface density (Barkana et al. 1999). For the spherical models, $\kappa = 0$ and for the elliptical ones it can be approximated by $\kappa \simeq \gamma$, i.e. $\gamma' = \gamma/(1 - \gamma)$. ^e based on Barkana et al. (1999). ^f based on Chae et al. (1999). ^g determined for the blue component.

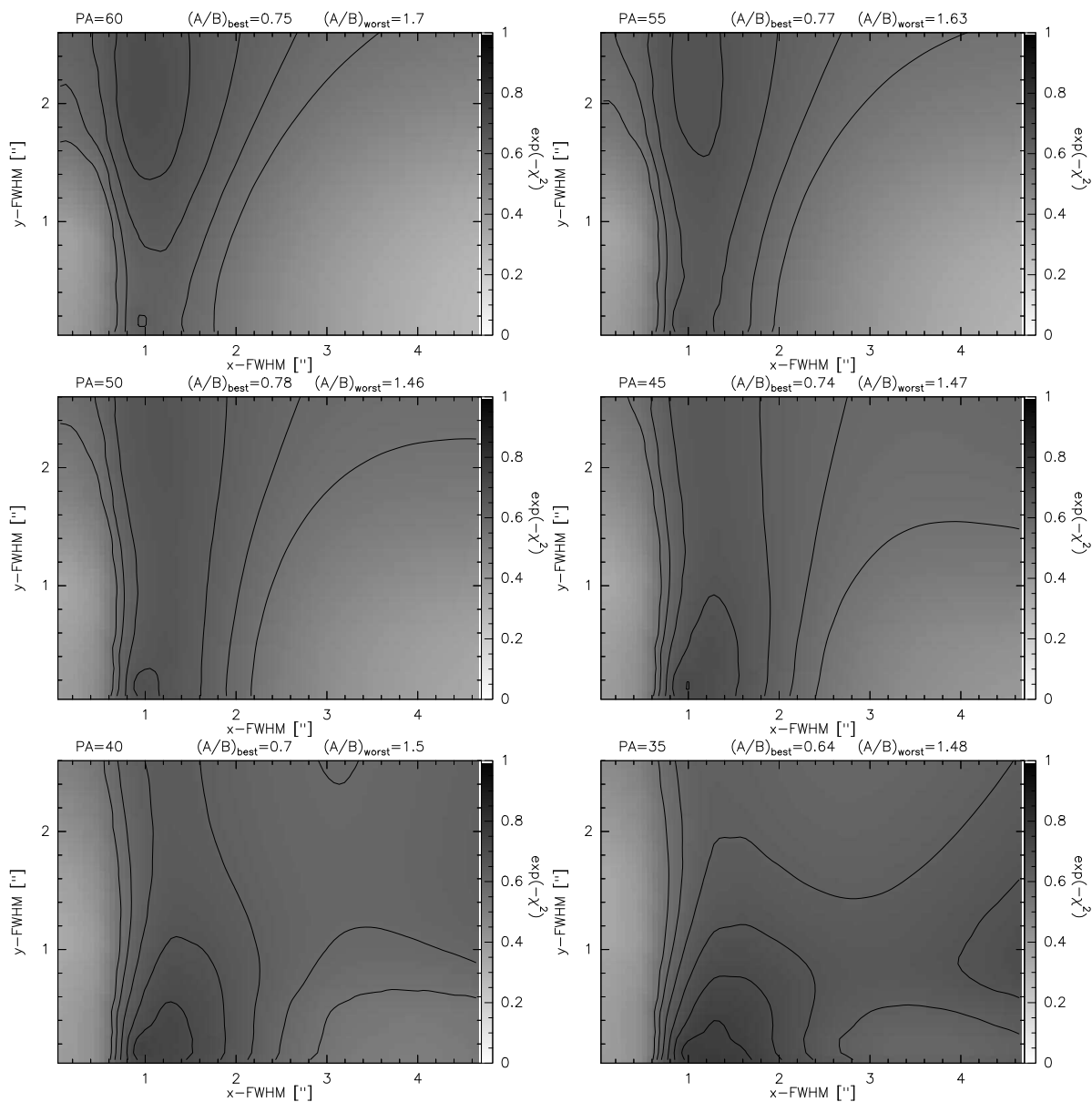


Figure 9.4: χ^2 -test to constrain the size parameters (elliptical Gaussian) of the molecular gas emission in dependency on the ratio $A\text{-blue}/B\text{-blue}=0.4\pm 0.1$. Plotted are the FWHM for different PAs with the respective ratios. The FGSE+CL best-fit model is used. The position of the Gaussian model source was fixed to the quasar centre.

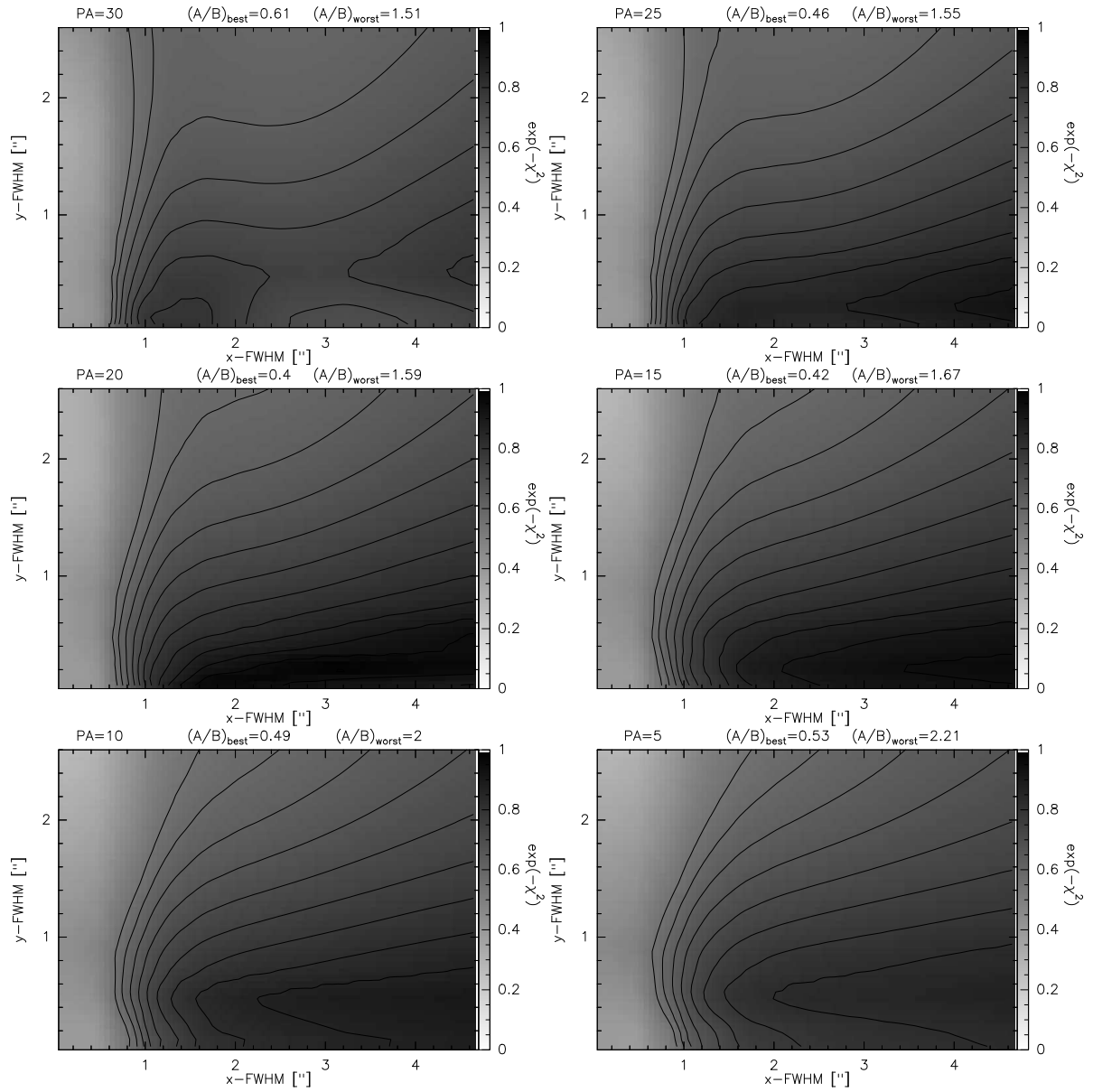


Figure 9.5: Continuation of Fig. 9.4.

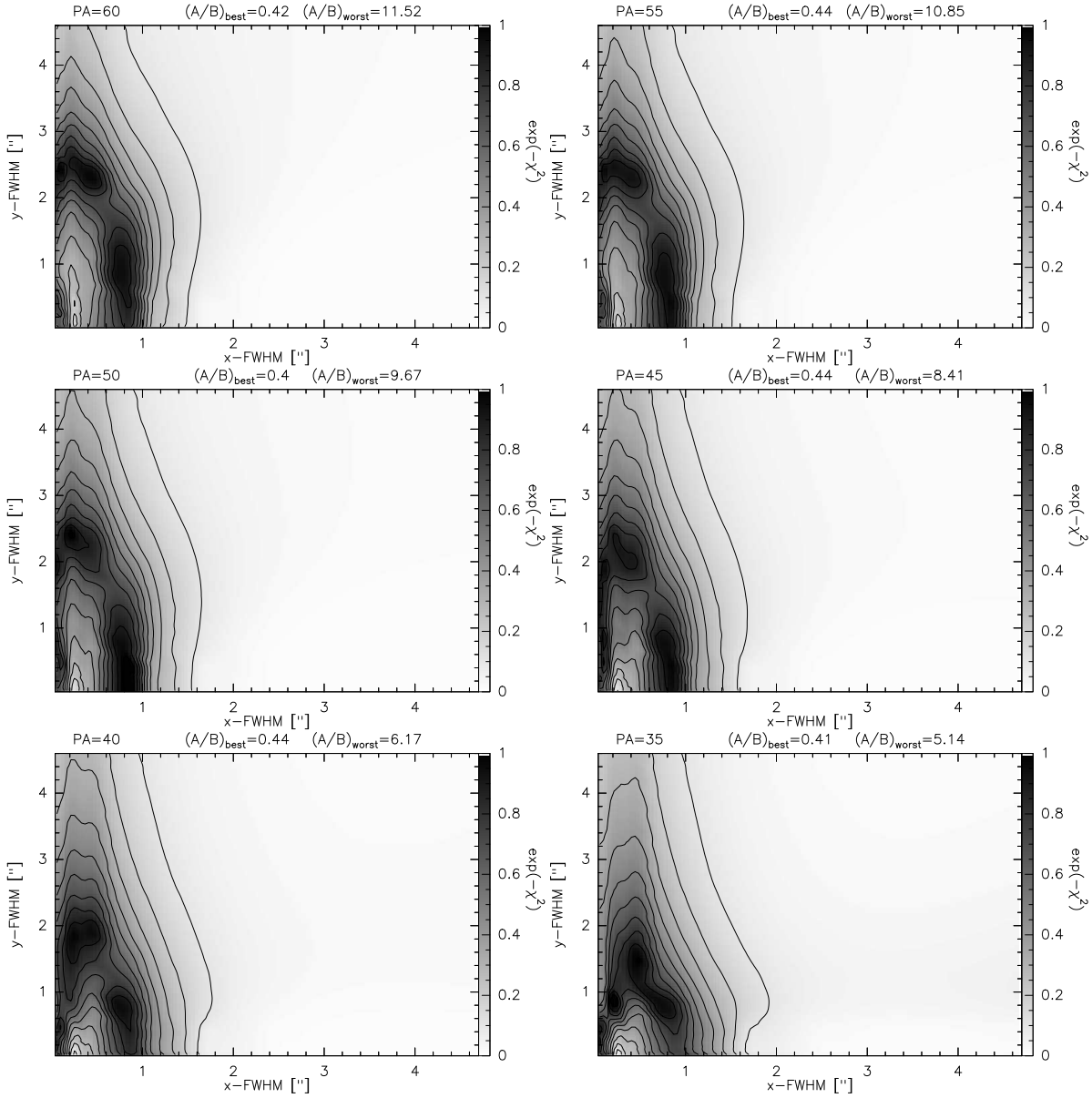


Figure 9.6: χ^2 -test to constrain the size parameters (elliptical Gaussian) of the molecular gas emission in dependency on the ratio $A\text{-blue}/B\text{-blue}=0.4\pm 0.1$. Plotted are the FWHM for different PAs with the respective ratios. The FGSE+CL best-fit model is used. The position of the Gaussian model source was fixed to an off-nuclear position closer to the inner tangential caustics with respect to the position of the quasar.

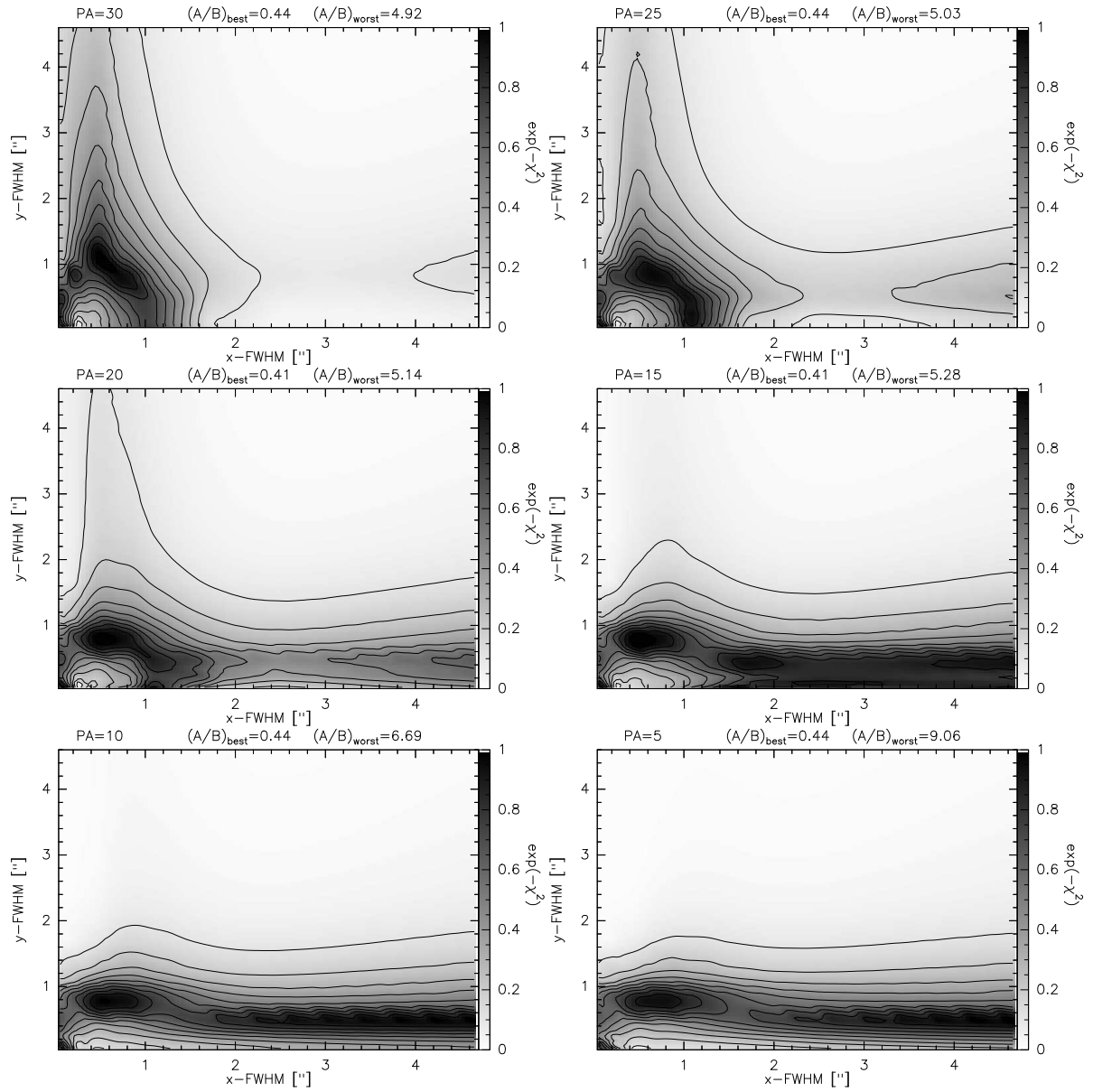


Figure 9.7: Continuation of Fig. 9.6.

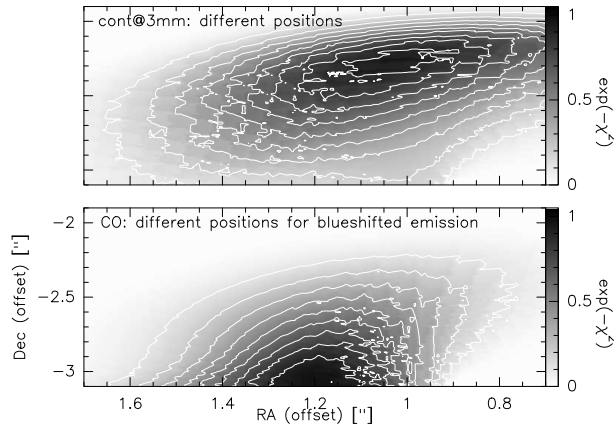


Figure 9.8: χ^2 results for the continuum (*upper panel*) and blueshifted line fits (*lower panel*) based on the FGSE+CL model. Assumed values for the 3mm continuum: $A/B = 1.5$, blueshifted line: $CO-A-blue/CO-B-blue = 0.4$ and their respective positions.

9.4.1.1 The blueshifted line

Let us first concentrate on the blueshifted line. Two different scenarios can be proposed for the origin of blueshifted line emission:

- an either compact or extended region centered on the nucleus
- an either compact or extended region spatially not coincident with the nucleus.

The small line ratio $CO-A-blue/CO-B-blue$ of ~ 0.4 already rules out a compact region in the first scenario, since it disagrees with the measured 3mm continuum ratio A/B of 1.5 ± 0.1 (Fig.9.8). Even if one accounts for a contribution of the jet in the A component and assumes a lower ratio for the core emission at 3mm, the ratio A/B at the core, known from VLBI observations, is close to 1.3 (Garret et al. 1994). Thus, the continuum at 3mm and the blueshifted CO emission cannot originate from the same compact region but have at the same time different ratios between the lensed images A and B.

On the other hand, an extended line emitting region centered on the nucleus can indeed result in an $CO-A-blue/CO-B-blue$ of 0.4. To derive the best-fit parameters for an extended source fulfilling the line ratio criterium, an elliptical Gaussian profile is assumed with a fixed position on the nucleus and varied the position angle (PA) and the size in x - and y -direction. Constraints for the maximum size were given by the H-band images of the host galaxy (Keeton et al. 2000). The line ratios were then calculated for each combination between the two lensed images and conducted a χ^2 -test. Fig. 9.4 and 9.5 shows the results of the χ^2 -test. A best-fit is obtained for a disk-like region extended in the direction of the nuclear jet ($PA=20^\circ$, $\sim 3 - 4''$) but tiny in the direction perpendicular to the jet ($\sim 0.2''$; Fig. 9.9). The south-western part of the disk crosses the inner tangential caustic⁴ of the lens producing multiple images (up to 5). This results in a stronger CO-B image and thus a low $CO-A-blue/CO-B-blue$ ratio.

Alternatively to the extended region centered on the nucleus, blueshifted emission from a rather compact region close to the inner tangential caustic and slightly off ($\sim 0.5''$ to the south-west) the nuclear position is also consistent with a line ratio of ~ 0.4 (Fig. 9.8). Similar to Fig. 9.4 and 9.5, Fig. 9.6 and 9.7 show the χ^2 -test obtained by fitting the size of the emitting region which is centered at an off-nuclear position closer to the inner tangential caustics with respect to the quasar centre. A compact and rather circular region with size $< 2''$ appears to be clearly favoured to

⁴Caustics separate the source plane into regions of different image multiplicity (Schneider et al. 1992). The corresponding lines in the lens plane are called critical lines.

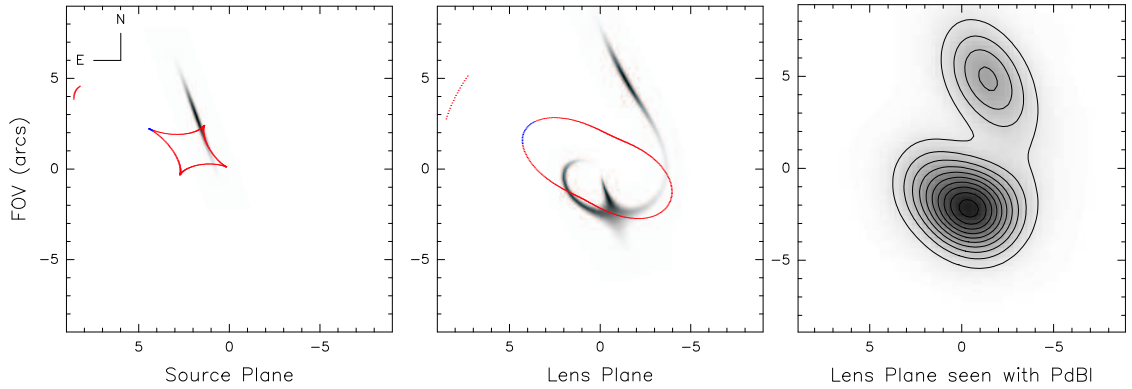


Figure 9.9: Best-fit model for an extended blueshifted line emission region centered on the nucleus. *Left panel:* Unlensed source in the source plane. *Middle panel:* Lensed images in the lens plane. *Right panel:* Lensed images after propagating it through the PdBI response function.

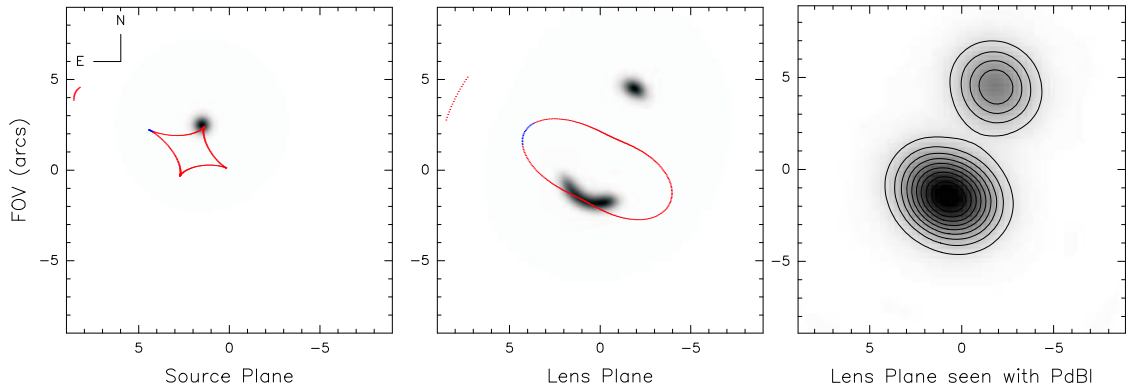


Figure 9.10: Best-fit model for a rather compact blueshifted line emission region centered at an off-nuclear position. *Left panel:* Unlensed source in the source plane. *Middle panel:* Lensed images in the lens plane. *Right panel:* Lensed images after propagating it through the PdBI response function.

produce the searched low line ratio between the two lensed images (Fig.9.10). A *symmetric* and *extended* region at an off-nuclear position does not produce such a low A-blue/B-blue of 0.4.

Thus, an independent blueshifted emission must either originate in an extended region centered on the nucleus or in a compact region with a position closer to the tangential caustic.

9.4.1.2 The redshifted line

The difference in the line profiles observed toward CO-A and CO-B can be explained by the location of the redshifted gas component relative to the lens caustic. The best-fit simulation for the SPEMD+CL model produces a configuration of two caustics, very close together (see also Fig. 9.11). While blueshifted emission is found between the caustics (to the south-west of the outer caustic but to the north-east of the inner caustic), redshifted emission must originate from above (north) the outer caustic. This explanation is also valid for the best-fit FGSE+CL model, even if here the radial caustic is at infinity. While the continuum and blueshifted line components remain close to the tangential caustic and are thus deflected into two distinct images, the redshifted component is already located too far off the caustic to produce two lensed images (Fig. 9.11). Thus, it appears that both blue- and redshifted gas become visible toward CO-A while blueshifted gas only can be detected toward CO-B. The unlensed separation

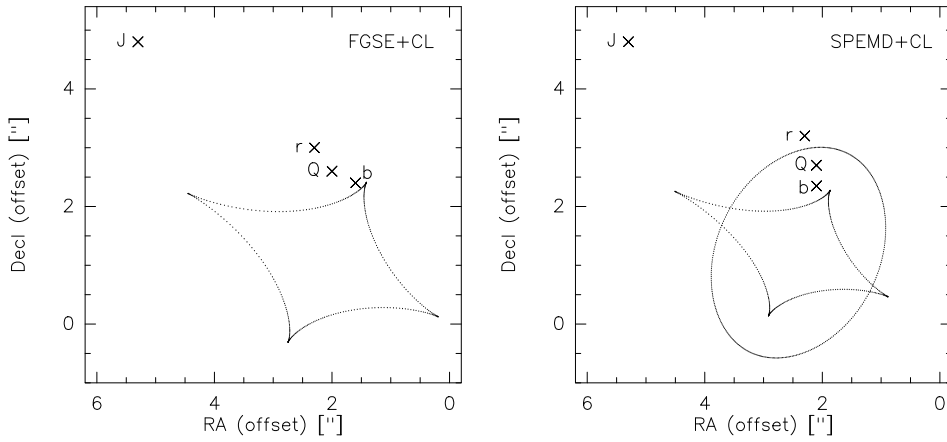


Figure 9.11: Unlensed positions of the respective components from the line emission ($r \equiv \text{CO-A-red}$, $b \equiv \text{CO-B-blue} \equiv \text{CO-A-blue}$) and radio continuum ($J \equiv \text{jet}$, $Q \equiv \text{quasar}$). The lensing galaxy (G) is at $(-0.5'', -5.5'')$. The radial and tangential caustics are also shown. *Right panel:* used best-fit model is FGSE+CL *Right panel:* used best-fit model is SPEMD+CL (Table 9.3). Both models are shown for better comparison and explanation.

between the centroids of the blue- and the redshifted components, corrected for magnification, are estimated to $\sim 1''$, or equivalently ~ 9 kpc at the distance of Q0957+561.

Likewise, an extended region centered on the nucleus where the north-eastern part corresponds to the redshifted component and the south-western part to the blueshifted one produces equivalent results. To obtain the derived line ratio $(A\text{-blue}+A\text{-red})/B\text{-Blue} \sim 1.0$, the size of the region has to be extended by about $\sim 2 - 4.5''$ in x -direction and by $\sim 0.5 - 2.5''$ in y -direction (Fig.9.12) restricted to the position angle of the host galaxy estimated from the H-band images detected by Keeton et al. (2000). The best-fit region is plotted in Fig. 9.13 and 9.14 (*lower right panel*). This value seems to be independent of the used lens potential even if the SPEMD+CL model appears to favour slightly more elliptical profiles for the emission than the FGSE+CL model (cf. also Keeton et al. 2000). If the lensed CO-A is divided into a red- and blueshifted part and derive then the ratio between A-blued and B-blue, again a value of $\sim 0.4^5$.

The sensitivity is not sufficiently high to establish the absolute genuineness of the CO-A-blue component from the observations alone, but our best-fit FGSE+CL model of the host galaxy not only agrees with the Barkana model of Keeton et al. (2000), but a priori corroborates the detection of blueshifted CO gas in the direction of component A.

9.4.2 Radio continuum

The morphology and the intensity ratios of the radio continuum can easily be modelled. As already noted by Schneider et al. (1992), the radio jet J is lensed only once due to its location out of the two caustics. Fig. 9.14 compares the simulated data with the observed ones for the radio continuum and the CO(2-1) line emission demonstrating a good agreement.

⁵In contrast to Subsection 9.4.1.1, where an extended blueshifted emission region would not result in an A-blue/B-blue ratio of 0.4 if *symmetrically* centered on a position closer to the tangential caustic, the extended emission region for the blueshifted part is not *symmetric* with respect to the position used there. This might explain why nevertheless such a low ratio is obtained for the blueshifted part alone.

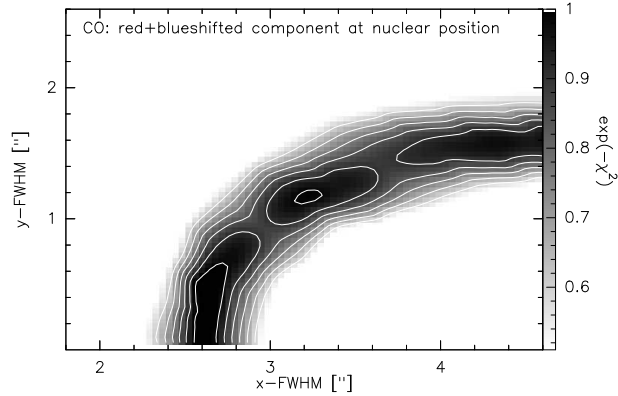


Figure 9.12: χ^2 -test for the red+blueshifted emission region. For this fit the PA angle was constrained to $\sim 50 \pm 10^\circ$ due to the PA estimated from the host galaxy detected by Keeton et al. 2000.

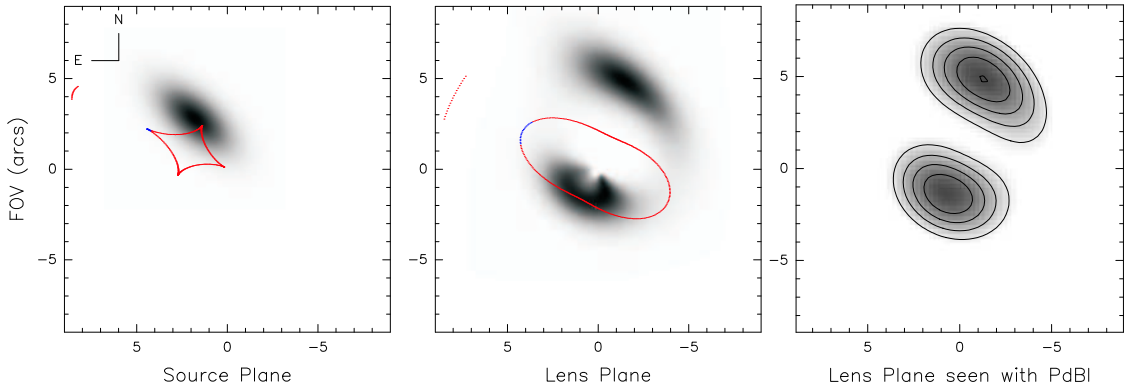


Figure 9.13: Best-fit model for an extended emission region for the red- and blueshifted line centered on the position of the quasar. *Left panel:* Unlensed source in the source plane. *Middle panel:* Lensed images in the lens plane. *Right panel:* Lensed images after propagating it through the PdBI response function.

9.5 Discussion

The 3mm continuum observations of the redshifted double quasar Q0957+561 are in good agreement with observations at other wavelengths. While the 3mm continuum emission from the quasar is unresolved, emission from the radio lobes is extended along the direction of the jet. The CO(2-1) line, however, does not originate in the quasar. The difference in position, and therefore in the deflection, explains also the difference between the flux density ratios in the 3mm continuum ($A/B = 1.5$ i.e. like in the radio continuum) and in the line (CO-A-blue/CO-B-blue = 0.4 for the blue component), and accounts for different time delays for the CO(2-1) and the radio images. However, the time delay difference is only marginally significant (at most 5–20 light days, according to the models).

What can be concluded about the origin of the redshifted CO(2-1) velocity component? P99 suggested that it was originating from a companion galaxy, very close to Q0957+561 (see also Papadopoulos et al. 2001) and rather excluded the alternative that it was tracing the presence of molecular gas in the rotating disk of the host galaxy since this led to contradictions within their argumentation. Our models discard the first hypothesis, however. First, there has been no detection of such a companion galaxy at other wavelengths, but the host galaxy, which has already been revealed in HST observations by Keeton et al. (2000), is oriented in the direction of the two line

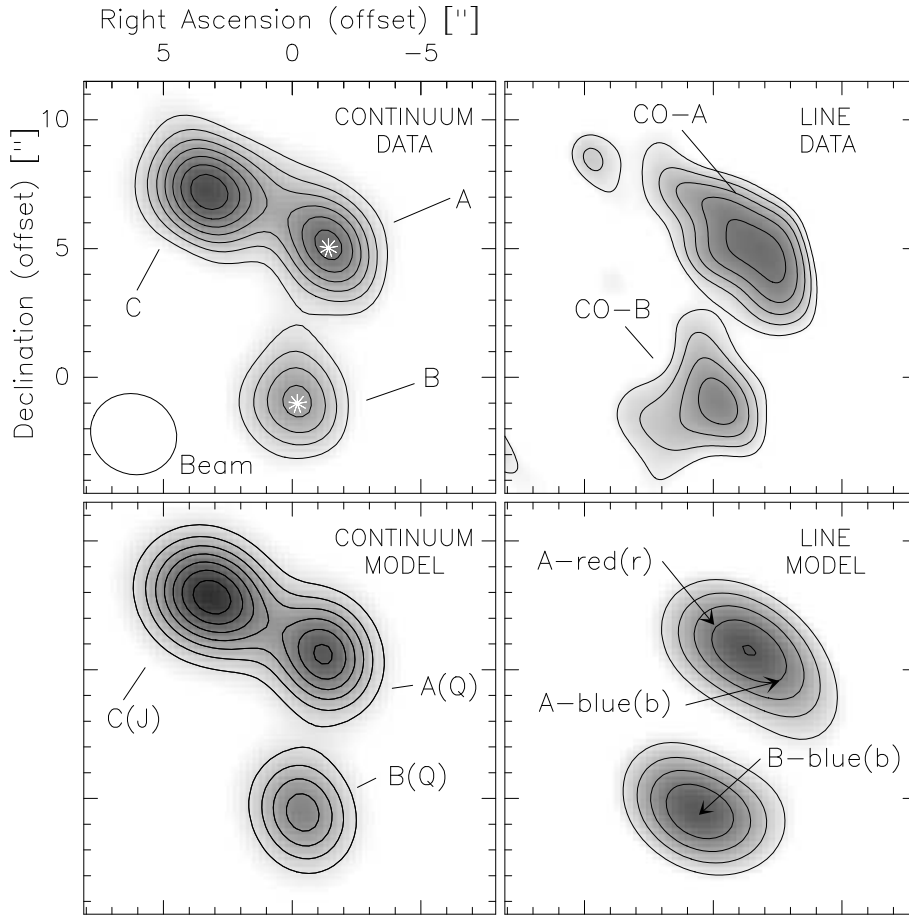


Figure 9.14: The line-free continuum at 95 GHz (*upper left panel*) and the $^{12}\text{CO}(2\rightarrow 1)$ line emission (*upper middle panel*) as observed with the IRAM interferometer from both data sets. The offset position (0,0) of each map corresponds to the position of the lensing galaxy. The white stars indicate the optical positions of the A and B image. Contour levels are from $5\sigma = 1.1$ to $4.7 \text{ mJy beam}^{-1}$ in steps of $0.6 \text{ mJy beam}^{-1}$ for the 3.1 mm continuum and $3\sigma = 0.33$ to $0.77 \text{ Jy km s}^{-1}$ in steps of $0.11 \text{ Jy km s}^{-1}$ for the line. The same contour levels were used for the simulated maps. The synthesized beam of $3.2'' \times 3.0''$ at p.a. 87° is shown in the lower left corner ($1''$ corresponds to 9 kpc at an angular-size distance $D_A = 1.87 \text{ Gpc}$). The lower panels show the *simulated* radio continuum (*left*) and line emission (*middle*) convolved with the synthesized beam. The letters in the brackets correspond to Fig. 9.11. Used model is (FGSE+CL).

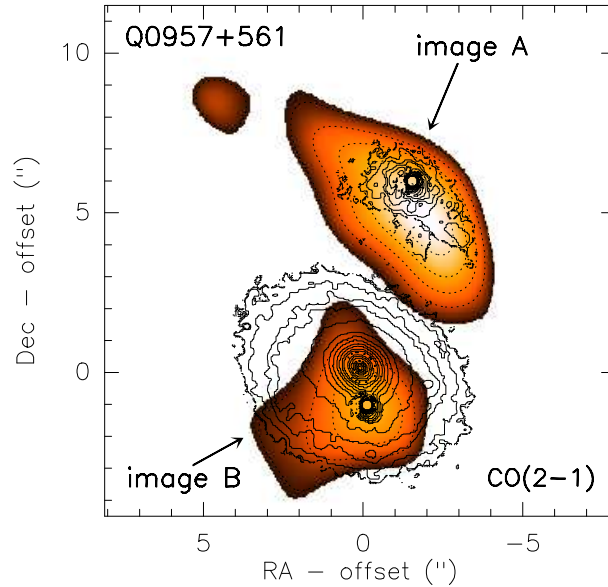


Figure 9.15: HST image in the H-band of the host galaxy in Q0957+561 (Keeton et al. 2000) with contour levels from Fig.9.14 of the velocity integrated CO(2–1) emission. Besides the bright optical quasar also the host galaxy can be seen. At image B, only the bright quasar is visible while the host galaxy is outshone by the lens galaxy.

components in CO-A and appears to be extended by $\sim 3''$ (Fig. 9.15). Furthermore, models for the gas emission in the host galaxy that take the velocity profiles observed toward CO–A and CO–B into account, are very similar in size and shape (see Fig.9.14) to those used by Keeton et al. (2000). The blue- and redshifted CO(2–1) emission appear to be very likely connected to the stellar distribution of the host galaxy and thus corroborates the results of Keeton et al. (2000), whereas models based on a single blueshifted component favour a very thin, elongated disk or a compact CO(2–1) emitting region slightly off the nuclear region, and as such are in contrast with images of the host galaxy. Moreover, the integrated line ratio of (CO–A-red+CO–A-blue)/CO–B ~ 1.0 is consistent with the one for the stellar components derived by Keeton et al. (2000). This is what one would expect if the profile of the gas distribution is very similar to the stellar one. Also the integrated line ratio of (CO–A-red+CO–A-blue)/CO–B ~ 1.0 is consistent with Keeton et al.’s (2000) optical data. Furthermore, lens models that take the velocity profiles observed toward A and B into account, all corroborate Keeton et al.’s (2000) host galaxy models, whereas models based on a single blueshifted component favour a very thin, elongated disk or a compact CO(2–1) emitting region slightly off the nuclear region, and as such are in contrast with images of the host galaxy. Also, the double-peaked line profile at CO-A, which appears to be symmetric and centered within the errors at $z = 1.4141$, is a classical signature for rotation, and therefore provides further support that the CO emission is associated with the host galaxy. By the same arguments, also a recent galaxy merger in Q0957+561 ca most likely be excluded, though this possibility cannot be ruled out completely.

Based on these arguments, P99’s second hypothesis is favoured which has been previously discarded by them: the presence of an important reservoir of molecular gas in the disk of the host galaxy surrounding Q0957+561 producing the double-peaked line profile toward CO-A and due to lensing effects only a single, blueshifted line toward CO-B.

According to the models the continuum is less magnified by a factor of 2–3 relative to the strongly lensed optical images (~ 10) while the total magnification factor derived in the CO line varies between $m_{\text{CO}}^{\text{total}} \simeq 6$ (FGSE+CL) and $m_{\text{CO}}^{\text{total}} \simeq 8$ (SPEMD+CL). Based on the lower magnification, an upper limit to the gas mass was estimated for the integrated blue- and redshifted velocity profile in CO-A and CO-B. The FGSE+CL model

	CO–A-red	CO–A-blue	CO–B-blue
$mL'_{\text{CO}}{}^a$ ($10^{10} \text{ K km s}^{-1} \text{ pc}^2$)	0.8 ± 0.3	0.8 ± 0.2	1.8 ± 0.2
$m_{\text{FGSE+CL}}{}^b$	1.5	1.7	4.3
M_{gas} ($10^{10} M_{\odot}$)	2.7 ± 1.0	2.4 ± 0.6	2.3 ± 0.6
total gas mass	$M_{\text{gas}}^{\text{tot}} \equiv M_{\text{gas}}^{\text{red}} + M_{\text{gas}}^{\text{blue}} \simeq 5 \times 10^{10} M_{\odot}$		

Table 9.4: Apparent CO luminosity L' and molecular gas mass M_{gas} of Q0957+561. ^a $m \equiv$ magnification factor. ^b determined with the FGSE+CL model.

corresponds to the higher CO–luminosity case and provides therefore a slightly higher gas mass. Under the assumption that the brightness temperature of the (1–0) and (2–1) lines is the same, we adopt a CO to H_2 conversion factor of $\simeq 4.8 M_{\odot} (\text{K km s}^{-1} \text{ pc}^2)^{-1}$ based on a determination for the Milky Way (Solomon & Barret 1991)⁶. Clearly, the Milky Way and the Q0957+561 host galaxy are in different evolutionary stages and show different properties, so the adopted conversion factor is likely to be an overestimate (cf. Downes et al. 1993), and an upper limit for the gas mass will be obtained. Based on the FGSE+CL magnification factor, $M_{\text{gas}} = M(\text{H}_2 + \text{He}) \simeq 2.4 \times 10^{10} M_{\odot}$ can be estimated for the blue profile and to $\sim 2.7 \times 10^{10} M_{\odot}$ for the reddened profile ($\simeq 9 \times 10^9 M_{\odot}$ for SPEMD+CL), giving an upper limit for the total gas mass of $\simeq 5.1 \times 10^{10} M_{\odot}$. Also, a lower limit can be given for the gas mass of $M_{\text{gas}} \sim 8 \times 10^9 M_{\odot}$ assuming that the CO(1–0) line is optically thin (Solomon et al. 1997). This relatively small difference of only a factor of 4 indicates that the standard conversion factor might nevertheless already give a reliable estimate of the gas mass in the host galaxy around Q0957+561. Assuming a radius of $\sim 10 \text{ kpc}$ and a velocity separation between both line profiles of $\sim 400 \text{ km s}^{-1}$, a dynamical mass of $\sim 4 \times 10^{11} M_{\odot}$ is found (not including inclination effects). This is about ten times higher than the derived gas mass consistent with what is found for other active galaxies (e.g. Evans et al. 2002, Sakamoto et al. 1999). The low upper limit on the velocity-averaged line intensity ratio, $R_{54} \simeq 1$, favours the hypothesis of low excitation CO emitted mainly from the disk of the host galaxy. The agreement between gas masses, obtained with the integrated CO luminosities and individual magnification factors, each tracing line emission from half of the quasar host, is further support for the rotating disk hypothesis. If our assumptions are correct, the molecular gas in the disk cannot be very hot, but to our knowledge no sensitive observations in the ground and higher rotational CO transitions have been carried out yet to confirm this conclusion.

9.6 Conclusions

Recent sensitive observations were combined with earlier data by P99 to corroborate their original discovery of CO(2–1) line emission from Q0957+561. A numerical program was developed to analyse the properties of the lensed system, the results of which can be summarized as follows: While the region of blueshifted line emission is found to lie in between the two caustics, and is therefore deflected into two images, redshifted emission is found outside the caustics, and therefore results in a single lensed image. Both, redshifted and blueshifted line emission, are supposed to originate from the same system: a disk with a molecular gas mass of $\simeq 1 - 5 \times 10^{10} M_{\odot}$ in the host galaxy in Q0957+561. Our results for the host galaxy are in excellent agreement with previous optical work by Keeton et al. (2000). So far, HR10 (Andreani et al. 2000) and Q0957+561 are the only systems at redshifts of $1 < z < 2$ in which CO emission was clearly detected, but in contrast to Q0957+561, where no dust emission was yet detected, HR10 is rich in dust and molecular gas. Although both systems are significantly different, they both independently give crucial insights into an epoch during which the bulk of stars of the present day Universe formed, and thus mark an important phase in galaxy evolution.

⁶see Equation 5.4

Part IV

Observations II: Molecular gas traced by HCN

Chapter 10

NUGA: IRAM 30m observations of HCN

This chapter presents first results obtained with IRAM 30m observations of the $^{12}\text{CO}(1-0)$, $^{12}\text{CO}(2-1)$ and $\text{HCN}(1-0)$ line emission of the core NUGA sample but it will mainly concentrate on the analysis of HCN. The ^{12}CO was observed to correct for short-spacings in the PdBI maps and thus to reduce possible effects due to missing extended, diffuse emission (cf. Chapter 5). $\text{HCN}(1-0)$ emission was detected in 7 of the 12 core sources. The $\text{HCN}(1-0)$ to $^{12}\text{CO}(1-0)$ ratio emission of 0.2 is similar to what is reported for active galaxies by other groups (0.17, Curran et al. 2000 & 2001). A comparison of our data also indicates a strong correlation between the dense gas and star formation as it is expected. This is again in excellent agreement with other (active) galaxy samples (Solomon et al. 1992, Curran et al. 2001). Furthermore, the amount of dense gas derived via the HCN line is of the order of the one of less dense gas traced by CO in the centre of the NUGA galaxies.

The chapter is structured as following: A brief introduction is given in Section 10.1. The observations are described in 10.2. Section 10.3 presents the results. The chapter finishes with a summary of the results and an outlook.

10.1 Introduction

The NUClei of GALaxies survey (García-Burillo et al. 2003a) has increased significantly the number of high-resolution/high-sensitivity maps of the gas in the direct vicinity of the AGN and aims at establishing on a more statistical basis which gas dynamical processes determine the activity level (Section 3.1). Thereby, the NUGA project mainly concentrates on analysing the distribution and kinematics of the molecular gas traced by ^{12}CO . The PdBI maps of the 12 NUGA sources reveal a fascinating and large variety of different structures and complex dynamics (García-Burillo et al. 2003b, Combes et al. 2003, Krips et al. 2004c, 2005b) certainly improving our knowledge about active galaxies. However, as the complexity of the ^{12}CO prove as well, the question of why some galactic nuclei are active and other are quiescent will not be easily solved with the ^{12}CO data alone. Kohno et al. (1999 & 2003) have recently demonstrated that additional information gained by HCN observations are indispensable to interpret the properties of the gas and to assemble them with the stellar characteristics of the galaxy into a more global context. Moreover, Tacconi et al. (1996) and Helfer & Blitz (1997) showed in high resolution observations that HCN is not only more centralised than ^{12}CO in all galaxies but also tends to measure gas in the *nuclear* regions of active galaxies in particular. The ^{12}CO emission is known to trace regions with a rather low density ($n(\text{H}_2) \geq 200 \text{cm}^{-3}$), whereas molecules like HCN and ^{13}CO are associated with denser gas regions ($n(\text{H}_2) \sim 10^5 \text{cm}^{-3}$) in which active high mass star formation (SF) typically occurs. Kohno et al. (1999 & 2003) and Tacconi et al. (1994) find in the cases of NGC 6951, NGC 1097 and NGC 1068 that the HCN emission unveils a different gas structure compared to what is obtained via the ^{12}CO lines. In NGC 1097 and NGC 1068 (Fig. 10.1), HCN emission is enhanced toward the nucleus with respect to the ^{12}CO emission. Looking at the spiral arms in NGC 1097 and NGC 6951, the HCN line peaks at different spatial positions than the ^{12}CO line. While the ^{12}CO

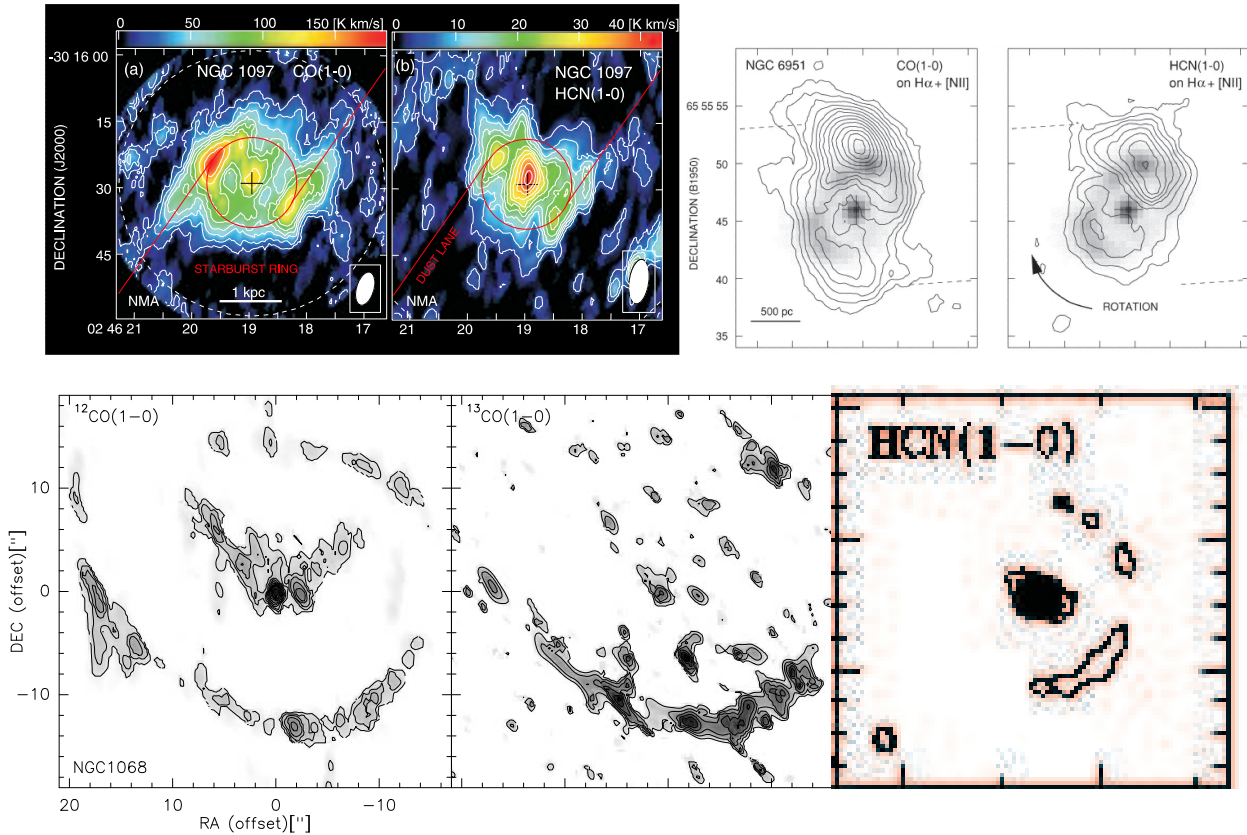


Figure 10.1: CO(1–0) and HCN(1–0) images of NGC 1097 observed by Kohno et al. 2003 with the NMA (*upper left* panel), of NGC 6951 (*upper right* panel; Kohno et al. 1999) and of NGC1068 (*lower* panel; Schinnerer et al. 2000, this thesis (*left*) and Tacconi et al. 1997 (*right*; tickmarks: 5’’)).

morphology can be connected to the two spiral arms and the dust lane, the HCN emission is strongly correlated with the circumnuclear ring and the vigorous star formation in it. Kohno et al. (1999 & 2003) also report on a spatial variation of the HCN to CO integrated intensity ratio. The averaged value lies around 0.16 for NGC 1097 and NGC 6951 at the radius of the ring/spiral arms consistent with what is found with the 30m telescope (Table10.3). For NGC 1097, it even increases to 0.34 at the centre agreeing with results obtained for NGC 1068 while it decreases to 0.086 in the central 120pc of NGC 6951 but this might still be dominated by the starburst ring. Kohno et al. 2002 find in further 2 galaxies an enhancement of HCN in the centre which cannot be explained by nuclear starburst alone. They argue that this is produced by “X-ray irradiated dense obscuring tori” providing a *new* diagnostic tool to separate “pure” AGNs without composite nuclear starburst (NGC 1068) from those with associated starburst (NGC 6951). Thus, ^{12}CO emission cannot initially give a complete picture about the gas properties of a galaxy and teach us something about the denser gas regions. To understand the nature of these objects, not only information gained through multi-wavelength approaches is crucial, but also the comparability between the different properties, such as the link between gas and stars. The analysis of the distribution and kinematics of one molecule is certainly a first and very important step but cannot be enough. According to these arguments, IRAM 30m observations (Subsection10.2) were conducted, as an initial step, to search for HCN emission in 11¹ of the core NUGA galaxies. Significant HCN emission is detected in 7 galaxies. These observations will be presented in the next subsections. Follow-up interferometric observations are in preparation.

¹NGC 3718 was already observed before by Pott et al. 2004

	$^{12}\text{CO}(1-0)$	$^{12}\text{CO}(2-1)$	HCN(1-0)
at rest (GHz)	115.271202	230.538000	88.6304157
Beam size (")	21.0	10.5	27.5
Forward efficiency ^a	0.97	0.91	0.95
Beam efficiency ^a	0.75	0.52	0.78

Table 10.1: Basic observing parameters. ^a taken from the IRAM 30m homepage.

10.2 Observations

Observations of the $^{12}\text{CO}(1-0)$, $^{12}\text{CO}(2-1)$ and HCN(1-0) line emission in the core NUGA sample (Section 3.1) were conducted with the IRAM 30m telescope near Granada, Spain in July 2002 and June 2004. A filter bank of $512 \times 1\text{MHz}$ channels was mainly used at 3mm, while the auto correlator (VESPA) with a frequency resolution of 1.25MHz and a resulting bandwidth of 640MHz was taken at 1mm. Additionally, a second filter bank with $512 \times 4\text{MHz}$ channels was also applied at both wavelengths to ensure for a backup in case of technical problems with the other two backends. The receivers were tuned to the respective redshifted lines (cf. Table 3.1). The following HPBW² were obtained: $27.5''$ at 88GHz, $21''$ at 115GHz and $10.5''$ at 230GHz. During observations, the pointing and the focus of the antenna were regularly verified as well as a chopper wheel calibration on a load at ambient and cold temperatures. Temperatures were measured in T_a^* scale and then converted into main beam brightness temperatures considering parameters given in Table 10.1. The so derived temperatures were also corrected for the (estimated) filling factor (Table 10.2). The continuum was subtracted from all spectra by fitting a linear polynom to the data (excluding velocities within which line emission is visible).

For all 12 NUGA sources, at least 3×3 point maps were observed with a separation of $7''$. Due to technical problems and bad weather, only 5×5 point maps have so far been finished for 10 galaxies in the $^{12}\text{CO}(1-0)$ and $^{12}\text{CO}(2-1)$ lines. Complementing observations for the remaining 2 galaxies are repropesed.

10.3 Results

The respective temperatures, luminosities and the ratios of the CO(1-0), CO(2-1) and HCN(1-0) line transitions are summarized in Table 10.2 and 10.3. Luminosities were calculated via the following equation

$$L_{\text{line}} = I_{\text{line}} D^2 \Omega \quad (10.1)$$

with

$$I_{\text{line}} = \int T_{\text{line}} \times dv \quad (10.2)$$

D is the luminosity distance to the source, I_{line} the integrated line temperature, i.e. T_{line} the main beam brightness temperature and dv the line width, and Ω corresponds to the solid angle of the beam convolved with the source. Additionally, also the Far-Infra-Red (FIR) luminosities are given in Table 10.3 determined via fluxes at $100\mu\text{m}$ taken from NED. The ratio between the HCN(1-0) and CO(1-0) luminosities result in a value of ~ 0.2 on average that is consistent with the average value of ~ 0.17 found for other LINER and Seyfert galaxies (Curran et al. 2000; Curran et al. 2001; Solomon et al. 1992). Fig. 10.3 shows the relation between HCN and FIR luminosities and between the ratio of FIR to CO luminosities and the one of HCN to CO luminosities. Our data are in excellent agreement with data obtained for other active galaxies including Luminous InfraRed Galaxies (LIRGs; Solomon et al. 1992) and Seyfert and LINERs (Curran et al. 2001). The HCN luminosities are strongly correlated with the FIR luminosities which is expected since FIR luminosities probe star formation while HCN luminosities measures

²Half Power Beam Widths

the amount of dense gas. The comparison between the star formation efficiency, i.e. the efficiency of the transformation of molecular gas into OB stars (Solomon et al. 1992), and the fraction of dense gas also results in a strong correlation. Only one galaxy, NGC 3718, falls significantly below the obtained correlation. Either the upper limit is still too high, or the dense gas and dust is less heated by hot stars than in the rest of our survey.

The molecular gas masses were estimated via the CO(1–0) line and also via HCN(1–0) using the following equations. Assuming the standard conversion factor of $X'_{\text{CO}}=2.3 \times 10^{20} \text{ cm}^{-2}/(\text{K km s}^{-1})$ (Strong et al. 1989) between H_2 column density and integrated line temperature I_{CO} , and assuming optically thin emission, one gets

$$N_{\text{H}_2}^{\text{CO}} [\text{cm}^{-2}] = \frac{X'_{\text{CO}}}{\text{cm}^2/\text{K km s}^{-1}} \times \frac{I_{\text{CO}}}{\text{K km s}^{-1}} \quad (10.3)$$

Defining the assumed source area as A and the proton mass as $m_{\text{proton}} (= 1.6725 \cdot 10^{-27} \text{ kg} = 8.4 \cdot 10^{-58} \mathcal{M}_{\odot})$, one can calculate the mass via

$$M_{\text{H}_2}^{\text{CO}} [\mathcal{M}_{\odot}] = N_{\text{H}_2}^{\text{CO}} [\text{cm}^{-2}] \times A [\text{pc}^2] \times 2 \cdot m_{\text{proton}} [\mathcal{M}_{\odot}] \quad (10.4)$$

$$= 3.5 \times \frac{I_{\text{CO}}}{\text{K km s}^{-1}} \times \frac{A}{\text{pc}^2} \mathcal{M}_{\odot} \quad (10.5)$$

$$M_{\text{gas}}^{\text{CO}} = M_{\text{H}_2+\text{He}}^{\text{CO}} \quad (10.6)$$

$$= 1.36 \times M_{\text{H}_2}^{\text{CO}} \quad (10.7)$$

For the HCN luminosity, Solomon et al. (1992) found the following relation

$$M_{\text{H}_2}^{\text{HCN}} [\mathcal{M}_{\odot}] = 20_{-10}^{+30} \times \frac{L_{\text{HCN}}}{\text{K km s}^{-1} \text{pc}^2} \mathcal{M}_{\odot} \quad (10.8)$$

$$M_{\text{gas}}^{\text{HCN}} = M_{\text{H}_2+\text{He}}^{\text{HCN}} \quad (10.9)$$

$$= 1.36 \times M_{\text{H}_2}^{\text{HCN}} \quad (10.10)$$

where L_{HCN} is the HCN luminosity. The latter equation holds for kinetic temperatures of 20 to 60K. A distinction between the global, i.e. for the whole galaxy, H_2 masses and the central, i.e. in the central beam, H_2 masses was made (Table 10.4). Comparable masses imply that the size of the galaxy is of the order or smaller than the beam size of the IRAM 30m telescope. Table 10.5 compares the masses obtained via the CO(1–0) line with the denser gas masses derived via the HCN(1–0) line at the centre. The masses estimated via HCN and CO are roughly of the same order at the centre of the NUGA galaxies indicating that the amount of dense gas traced by HCN is as important as the one of less dense gas traced by CO.

10.4 Summary and Outlook

Besides CO emission, also HCN emission has been observed in all 12 NUGA core galaxies. An analysis of the HCN information comprising also a comparison to the FIR luminosities of these galaxies, provide results which are in excellent agreement with previous work. The average HCN to CO luminosity ratio of ~ 0.2 is consistent with values found by other groups (e.g. Curran et al. 2001). The strong correlation obtained between HCN luminosities, tracing the amount of dense gas, to the FIR luminosities, probing star formation, implies that the dense gas is probably not negligible with respect to the less dense gas traced by CO. This is emphasized by the fact that the masses of dense gas are comparable to those of less dense gas in our sample. Thus, dense gas is an important piece of puzzle for a better understanding of the nature of active galaxies. The apparent role as outsider of NGC 3718 might imply that the activity mechanisms in this object are different from those of the other galaxies. However, a

Name	$T_{\text{CO}(1-0)}$ (mK)	$T_{\text{CO}(2-1)}$ (mK)	$T_{\text{HCN}(1-0)}$ (mK)	$L_{\text{CO}(1-0)}$ ($10^8 \text{K km s}^{-1} \text{pc}^2$)	$L_{\text{CO}(2-1)}$ ($10^8 \text{K km s}^{-1} \text{pc}^2$)	$L_{\text{HCN}(1-0)}$ ($10^8 \text{K km s}^{-1} \text{pc}^2$)
NGC 1961	171	280	11	15 ± 0.1	5.7 ± 0.1	1.5 ± 0.2
NGC 2782	77	121	$\leq 9^a$	2 ± 0.1	0.9 ± 0.02	≤ 0.5
NGC 3147	51	≤ 60	$\leq 9^a$	2 ± 0.1	≤ 0.7	≤ 0.7
NGC 3627	317	543	33	0.6 ± 0.01	0.2 ± 0.003	0.1 ± 0.01
NGC 3718	13	12	$\leq 2^b$	0.5 ± 0.01	0.01 ± 0.001	≤ 0.03
NGC 4569	380	525	63	6 ± 0.04	2.0 ± 0.02	1.5 ± 0.2
NGC 4579	76	105	31	0.6 ± 0.04	0.2 ± 0.01	0.2 ± 0.03
NGC 4826	380	508	52	0.2 ± 0.001	0.04 ± 0.001	0.07 ± 0.006
NGC 5953	165	298	$\leq 9^a$	2 ± 0.03	0.7 ± 0.01	≤ 0.2
NGC 6574	152	210	25	3 ± 0.07	0.5 ± 0.01	0.4 ± 0.05
NGC 6951	190	368	53	2 ± 0.03	0.8 ± 0.01	0.3 ± 0.05
NGC 7217	48	39	$\leq 9^a$	0.2 ± 0.01	0.02 ± 0.001	≤ 0.03

Table 10.2: Central CO and HCN line temperatures of the NUGA sources measured with the IRAM 30m telescope and corrected with filling factor. The respective luminosities are also given derived via $L_{\text{line}} = I_{\text{line}} D^2 \Omega$, $I_{\text{line}} = \int T_{\text{line}} \times dv$ with D luminosity distance to the source, I_{line} the integrated line temperature and Ω the solid angle of the beam convolved with the source. Errors are roughly of the order of 3-5% for CO(1-0) and CO(2-1) and of ~ 10 -20% for HCN(1-0). ^a for a velocity resolution of 30 km s^{-1} .

Name	L_{FIR} [$10^{10} L_{\odot}$]	$T_{\text{CO}21}/T_{\text{CO}10}$	$L_{\text{HCN}10}/L_{\text{CO}10}$	$L_{\text{CO}21}/L_{\text{CO}10}$	$L_{\text{FIR}}/L_{\text{CO}10}$
NGC 1961	5.6 ± 0.3	1.2 ± 0.07	0.1 ± 0.01	0.56 ± 0.02	37 ± 2
NGC 2782	1.7 ± 0.1	1.2 ± 0.07	≤ 0.3	0.45 ± 0.07	85 ± 7
NGC 3147	4.1 ± 0.03	≤ 1.0	≤ 0.3	≤ 0.35	210 ± 10
NGC 3627	1.4 ± 0.4	1.3 ± 0.08	0.2 ± 0.02	0.33 ± 0.03	230 ± 60
NGC 3718	0.03 ± 0.001	0.7 ± 0.04	≤ 0.07	0.02 ± 0.07	6 ± 0.2
NGC 4569	2.1 ± 0.1	1.0 ± 0.06	0.25 ± 0.03	0.33 ± 0.2	35 ± 1
NGC 4579	0.7 ± 0.04	0.8 ± 0.05	0.12 ± 0.02	0.33 ± 0.07	120 ± 10
NGC 4826	0.2 ± 0.03	1.0 ± 0.06	0.35 ± 0.03	0.20 ± 0.03	100 ± 10
NGC 5953	1.3 ± 0.01	1.4 ± 0.08	≤ 0.08	0.35 ± 0.03	65 ± 1
NGC 6574	2.4 ± 0.1	1.0 ± 0.06	0.1 ± 0.01	0.17 ± 0.03	80 ± 3
NGC 6951	1.3 ± 0.1	1.2 ± 0.07	0.15 ± 0.03	0.40 ± 0.02	65 ± 4
NGC 7217	0.3 ± 0.02	0.6 ± 0.03	≤ 0.15	0.10 ± 0.04	150 ± 10

Table 10.3: FIR luminosities and luminosity ratios for the NUGA sample. The FIR luminosities are calculated from $\lambda = 100 \mu\text{m}$ fluxes taken from NED.

Name	$I_{\text{CO}(1-0),\text{centre}}$ (K km s ⁻¹)	$M_{\text{gas,centre}}^{\text{CO}}$ (10 ⁸ \mathcal{M}_{\odot})	$A_{\text{CO,centre}}$ (kpc ²)	$I_{\text{CO}(1-0),\text{av}}$ (K km s ⁻¹)	$M_{\text{gas,global}}^{\text{CO}}$ (10 ⁸ \mathcal{M}_{\odot})	$A_{\text{CO,global}}$ (kpc ²)
NGC 1961	87.9±0.6	90	21.7	67±3	140	44
NGC 2782	28.6±0.7	12.6	9.3	17.4±0.1	16	19
NGC 3147	22±1.0	11.7	11.2	26.4±0.1	51	41
NGC 3627	74.8±0.7	3.2	0.8	72.7±0.4	5	1.6
NGC 3718	4.5 ^a	0.3	1.4	1.1 ^a	3	47
NGC 4569	130±2.0	43	7.1	130±0.6	43	7.1
NGC 4579	30±2.0	4.5	3.0	42.0±0.2	6	3
NGC 4826	114±1.0	1.3	0.2	110±0.6	2	0.5
NGC 5953	39.9±0.6	1.0	5.5	29.7±0.4	16	11
NGC 6574	43±1.0	15.1	7.4	38.0±0.3	27	15
NGC 6951	101±2.0	14	2.9	101±0.6	13	3
NGC 7217	17.7±0.9	1.1	1.3	20.1±0.4	3	2.6

Table 10.4: Integrated CO(1–0) intensities in the centre and averaged over the whole map (14'' × 14'') and the gas masses in the respective beams. ^a taken from Pott et al. 2004

more detailed interpretation is in need of more detailed information about the distribution of the HCN emission. Thus, interferometric observations with the IRAM PdBI are in preparation to map the HCN emission, allowing to compare more qualitatively and quantitatively the distribution of dense and less dense gas with each other and to search for spatial variations in the HCN-to-CO luminosity ratios as reported by Kohno et al. (1999 & 2003).

Name	$M_{\text{gas,centre}}^{\text{CO}}$ ($10^8 M_{\odot}$)	$M_{\text{gas,centre}}^{\text{HCN}}$ ($10^8 M_{\odot}$)
NGC 1961	90	40 ± 30
NGC 2782	13	≤ 14
NGC 3147	12	≤ 20
NGC 3627	3	3 ± 4
NGC 3718	0.3	≤ 0.8
NGC 4569	43	40 ± 30
NGC 4579	4.5	5 ± 3
NGC 4826	1.3	2 ± 1
NGC 5953	1.0	≤ 5
NGC 6574	15	11 ± 5
NGC 6951	14	8 ± 4
NGC 7217	1.1	≤ 0.8

Table 10.5: Gas masses determined with the central CO(1–0) and HCN(1–0) luminosity assuming $M_{\text{H}_2,\text{centre}}^{\text{HCN}} = 20_{-10}^{+30} \times L_{\text{HCN}} M_{\odot} (\text{K km s}^{-1} \text{pc}^2)$ (Solomon et al. 1992). Errors were estimated via the errors of the given equation.

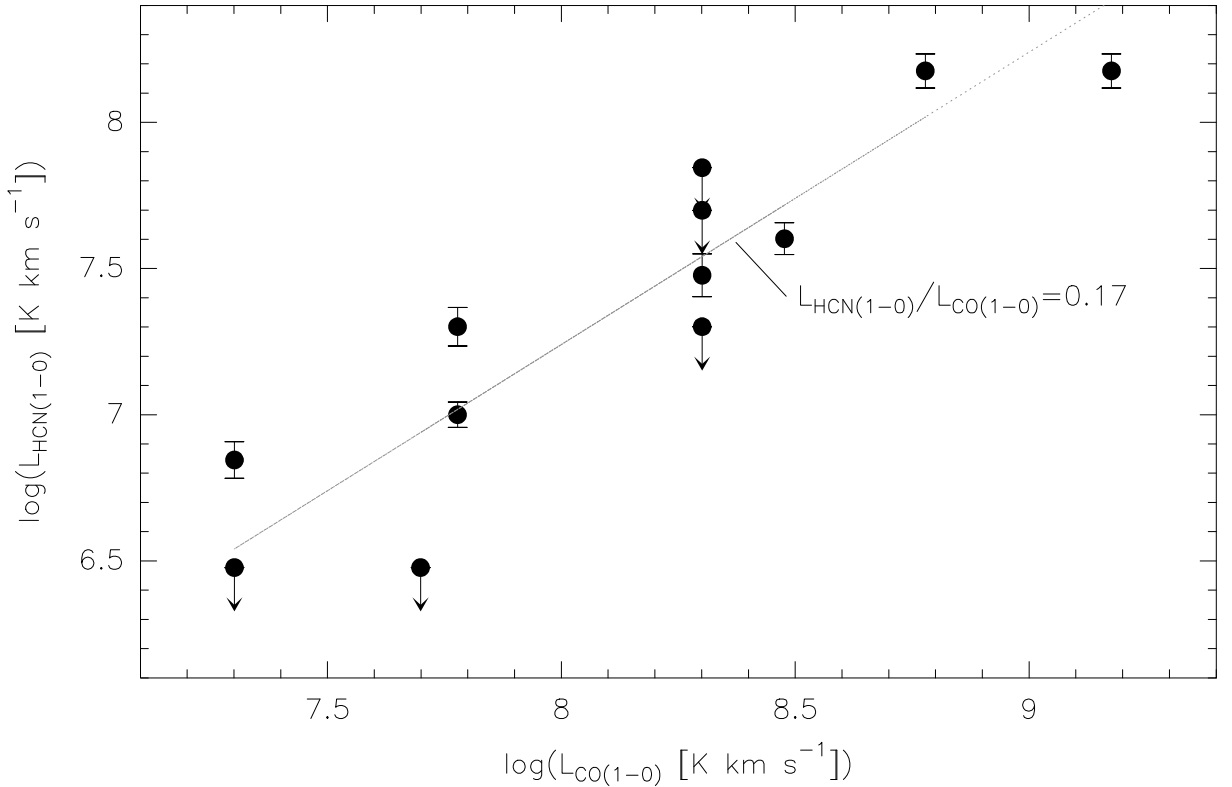


Figure 10.2: Comparison of the measured HCN(1–0) and CO(1–0) luminosities. Errors of CO(1–0) are of the order of the symbol size.

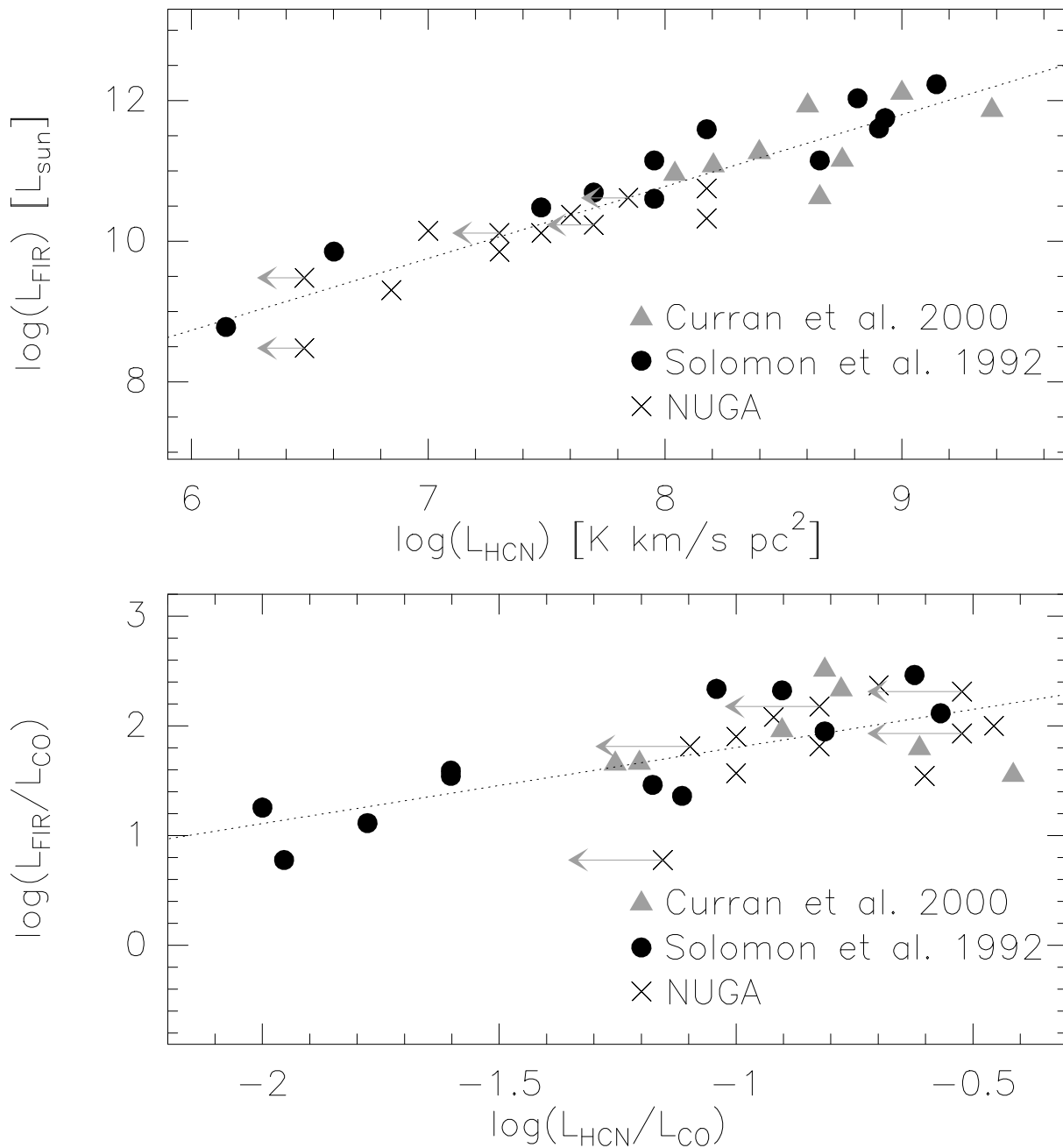


Figure 10.3: Comparison of the measured HCN(1–0) and CO(1–0) luminosities with the FIR luminosities of the NUGA sample (crosses; errors are roughly of the order of the symbol sizes). Upper limits are indicated with an arrow. Values marked by filled circle are taken from Luminous InfraRed Galaxies (LIRGs; Solomon et al. 1992). The lower panel implies the relation between star formation and fraction of dense gas.

Part V

Observations III: Radio emission

Chapter 11

NUGA sources

In this chapter, high angular resolution radio snap-shot observations of seven nearby active galaxies taken from the NU(clei of) GA(laxy) survey are presented (Krips et al. 2004d, 2005c). The observations were conducted with MERLIN and VLBI at 18 cm and 6 cm. On MERLIN scales, jets are clearly detected in two sources. Extended emission is revealed in three further objects. On EVN scales, most of the seven nuclei appear pointlike at both frequencies with three exceptions where also extended emission becomes visible. The fluxes are found to decrease with increasing angular resolution at the respective frequency implying further extended and diffuse emission. The EVN radio fluxes at 6cm correlate excellently with the X-Ray luminosities published by Roberts & Warwick 2000 and their black holes masses estimated via the respective velocity dispersion (McElroy 1995). All seven NUGA sources fall in the range of sub-Eddington systems so that their compact nuclear radio emission may be related to ADAFs. The derived tight correlations between radio and X-ray luminosities on the one hand, and radio luminosity and black hole mass on the other hand agree well with predictions from ADAF theory. This further implies that the weak radio emission is more likely to be associated with an AGN, i.e. accretion mechanisms onto a central black hole, rather than individual SuperNova Remnants (SNR).

This chapter is outlined in the following way: A short Introduction will be given in Section 11.1. Section 11.2 describes the conducted observations with MERLIN and EVN. The observational results are presented in Section 11.3. The correlation between radio and X-ray luminosities on the one hand and radio luminosity and black hole mass on the other are discussed in Section 11.5. The Chapter finishes with a Summary and Conclusions in Section 11.6.

11.1 Introduction

The nature of Low-Luminosity Active Galactic Nuclei (LLAGN) and their differences from quasars are still pending questions. While highly active galaxies, like quasars, are supposed to be powered by the accretion of matter onto a supermassive nuclear black hole, the processes responsible for the increased nuclear activity in LLAGN is much less clear. Besides fueling of a monstrous central black hole, also enhanced star formation could be made responsible for the observed properties in this type of objects. One approach to disentangle the differences between low and high luminosity AGN (HLAGN) is to study emission that is associated with processes in the direct vicinity of the central black hole. HLAGN often show strong continuum radiation at radio frequencies with different structures, such as extended radio jets or compact (sub-parsec) sources, but all originating in the nucleus (Irwin & Seaquist 1988; Duric & Seaquist 1986; (Hummel et al. 1983). Recent studies (e.g. Ulvestad & Wilson 1984, Pedlar et al. 1993, Falcke et al. 2000) have demonstrated that LLAGN might also produce non-thermal radio emission in form of jets and/or compact sources even if much less powerful than observed in HLAGN. Jets are highly correlated with accretion processes onto compact objects (e.g. Pringle 1993, Blandford 1993) and are thus regarded to be a clear signature for accretion-powered AGN. Therefore, the idea of LLAGN being only scaled

down HLAGN seems to be reasonable. In such a case, the low luminosity would be explained by either low or inefficient accretion.

To understand the nature of the very weak radio emission in LLAGN (of the order of a few mJy or below) and to search for differences from or similarities to HLAGN, seven nearby active galaxies from the NUGA survey were observed with MERLIN and EVN at 18 cm and 6 cm. So far, only lower angular resolution samples of LLAGN (e.g., VLA, REF) or samples with higher angular resolution (e.g., VLBA, Ulvestad & Ho 2001) but consisting of not more than 3 objects or limited to only one frequency (e.g., Nagar et al. 2002), were analysed. These studies also often contain LLAGN with much brighter radio fluxes than in our sample. Thus, the study presented here is so far the most sensitive analysis ($1\sigma=0.1$ mJy) with the highest currently available angular resolution (a few milli-arcseconds) for such radio-weak AGN.

11.2 Observations

Radio snap-shot observations of seven NUGA sources listed in Table 11.1 were conducted in 6 different epochs. In 2001/2002, we started with 18cm observations of six objects¹ using MERLIN followed by higher angular resolution observations at 18cm for the two brightest galaxies (NGC 3147 and NGC 3718) with EVN in February 2002. Before switching to another wavelength to obtain information on the spectral index, we tried to finish 18cm EVN observations for the remaining five galaxies in November 2002 which was not successful due to technical problems with the antennae so that we repeated this observing run in November 2003. We then begun with 6cm MERLIN observations of all seven objects and again looked first in the two strongest sources at the 6cm continuum emission with EVN. Finally, we decided to complement the 6cm observations for five galaxies² by using global VLBI (EVN plus antennae spread over the USA) to increase further sensitivity. At both, MERLIN and EVN/VLBI, we took advantage of the phase-reference technique (Beasley & Conway 1995) by observing alternately the target and a phase calibrator located within a few arcminutes of the respective galaxy so that the time need to switch between calibrator and target is still smaller than the coherence time enabling phase referencing experiments. The amplitudes were calibrated assuming a priori gain values and system temperatures measured during the respective observations providing typical accuracies within 5-10%. Approximate beamwidths span the range of 0.05 to 0.5'' at MERLIN and of 0.001 to 0.04'' at EVN. RMS noise in the images ranges from $\sim 1\mu\text{Jy}$ to $\sim 1\text{mJy}$. At MERLIN, also polarisation measurements were carried out but without any significant detection.

Gaussian profiles were fitted to all of the radio maps to get estimates of the source sizes (by setting as upper limit half the beamwidths) and to derive the respective fluxes. The results are given in Table 11.2 & 11.3 and will be discussed in the next section.

11.3 Observational results

First, some general results of the whole sample will be presented in Section 11.3.1 and then each galaxy will be individually discussed in Section 11.3.2.

11.3.1 General results

Tables 11.2 and 11.3 list the derived positions, fluxes and sizes of the respective sources. The positions of each galaxy are in excellent agreement between both frequencies and both instruments. Fig. 11.1 to 11.3 show the continuum maps of the seven sources for each frequency and instrument. Extended emission can be found in several maps on all angular scales. This is confirmed by comparing the peak intensities and integral intensities

¹NGC 4579 was already observed with MERLIN.

²Actually, all seven galaxies were planned to be observed with global VLBI at 6 cm since the first EVN 6cm run for NGC 3147 and NGC 3718 did not provide the long baselines due to technical problems with the telescopes in Shanghai and Urumqi. NGC 3147 (again) and NGC 4579 were then, however, excluded because they were already mapped by Ulvestad & Ho (2001) so that the observing list was finally reduced to five targets.

Instrument	Wavelength	month - year	sources
MERLIN	18cm	2001/2002	all except NGC 4579 ^a
EVN	18cm	February - 2002	NGC 3147, NGC 3718
EVN	18 cm	November - (2002) 2003 ^c	NGC 1961, NGC 2782, NGC 4579, NGC 5953, NGC 7217
MERLIN	6cm	2002/2003	all
EVN	6cm	dune - 2003	NGC 3147, NGC 3718
global VLBI	6cm	may - 2004	NGC 1961, NGC 2782, NGC 3718, NGC 5953, NGC 7217 ^b

Table 11.1: The respective parts of our radio observations for seven NUGA sources. ^a NGC4579 was excluded since MERLIN observations were already carried out before. ^b NGC 3147 and NGC 4579 were not observed because VLBA data were already accessible in Ulvestad & Ho (2001). ^c The first observations in 2002 were not successful due to immense technical problems and were thus reconducted in 2003.

with each other. For several galaxies they differ from each other indicating resolved emission. In at least four objects, there are clear signs for a jet on MERLIN scales (NGC 2782, NGC 3718, NGC 5953 and NGC 7217). Another strong indication of extended and also diffuse emission is the decrease of flux with increasing angular resolution (e.g. in NGC 1961 and NGC 7217), comparable to an “onionskin-behaviour”. Unfortunately, this fact complicates at the same time the comparison of the 18 cm with the 6 cm fluxes since resolution effects could cause a bias in the form of an artificial flux decrease due to different angular resolutions at 18 cm and 6 cm. Thus, spectral indices could be systematically too low³ but this will be taken into account in the discussion of each object.

Interestingly, most of the sources (within their errors and accounting also for the caveat mentioned above) have flat to inverted spectra (i.e., $\alpha \gtrsim -0.3$ roughly with $S_\nu \propto \nu^\alpha$; see Fig. 11.4 and Table 11.4) with only one exception (NGC 5953) which will be discussed in Subsection 11.3.2.6. Where detected, continuum fluxes at 3 mm and 1 mm obtained with the IRAM PdBI are additionally listed in Table 11.3.

11.3.2 Results for individual galaxies

11.3.2.1 NGC 1961

NGC 1961 contains a LINER type 2 nucleus in an SAB(rs)c host galaxy at a distance of 52 Mpc. It is therefore the most distant source of our survey. The mass of its black hole can be estimated via the tight $M_{\text{bh}}-\sigma_s$ correlation with σ_s being the velocity dispersion of the galaxy (see Section 2.5). Assuming $\sigma_s=255 \text{ km s}^{-1}$ (McElroy 1995), M_{bh} is derived to $3.0 \times 10^8 M_\odot$ (Table 11.5). Ulvestad & Ho (2000) propose an empirical equation to estimate the bolometric luminosity in active galaxies. Based on a limited sample of 10 objects, they found $L_{\text{bol}} = 6.7 \times L_x (2-10 \text{ keV})$. Assuming this equation and taking $L_x \simeq 4 \times 10^{40} \text{ erg s}^{-1}$, the bolometric luminosity of NGC 1961 can be determined in a simple way to $\sim 2 \times 10^{41} \text{ erg s}^{-1}$ (Ho et al. 1999) implying a sub-Eddington⁴ system with $L_{\text{bol}}/L_{\text{ed}} \simeq 2 \times 10^{-5}$ (Table 11.5). NGC 1961 thus falls within the definition for ADAFs.

The MERLIN 18cm map clearly shows extended emission supported by the difference between the peak and the integral intensity (see Fig. 11.1 and Table 11.3). However, the deconvolved size is of the order of the beam size. A two component Gaussian fit assuming a core and a “jet-like” feature results in a 10σ value for the core flux but only in a $\sim 2\sigma$ estimate for the flux of the potential jet. The MERLIN 6cm maps also indicates extended emission and besides a rather compact core also three further components. The North-Eastern and the (South-)Eastern feature lie in the direction of the extensions seen in the MERLIN 18cm map. However, accounting also for the South-Western feature which appears to be symmetrically positioned on the other side of the core with respect to the North-Eastern component, sidelobe effects cannot be totally excluded. Also the signal-to-noise ratios of all

³ assuming $S_\nu \propto \nu^\alpha$; spectral indices (α) will only be determined from fluxes which were measured with the same instrument.

⁴ $L_{\text{ed}}/L_\odot = 3.22 \times 10^4 M/M_\odot$; L_{ed} is the Eddington luminosity at which gravity pressure counterbalance radiation pressure.

Name	MERLIN				EVN			
	18cm		6cm		18cm		6cm	
	RA [h:m:s] Dec [°:':"]	$\Delta\alpha$ [s] $\Delta\delta$ ["]						
NGC1961-core	05:42:04.648	± 0.001	05:42:04.657	± 0.005	05:42:04.650	± 0.001	05:42:04.6477	± 0.0002
	69:22:42.384	± 0.005	69:22:42.37	± 0.04	69:22:42.380	± 0.003	69:22:42.3749	± 0.0001
NGC1961-jet	05:42:04.67	± 0.01	-	-	-	-	-	-
	69:22:42.4	± 0.2	-	-	-	-	-	-
NGC2782-core	09:14:05.11	± 0.01	09:14:05.101	± 0.001	09:14:05.1001	± 0.0001	09:14:05.1124	± 0.0001
	40:06:48.8	± 0.1	40:06:49.15	± 0.01	40:06:49.200	± 0.003	40:06:49.316	± 0.002
NGC2782-jet	09:14:05.105	± 0.001	09:14:05.104	± 0.001	-	-	-	-
	40:06:49.27	± 0.01	40:06:49.34	± 0.01	-	-	-	-
NGC3147-core	10:16:53.650	± 0.001	10:16:53.651	± 0.001	10:16:53.6507	± 0.0001	10:16:53.6500	± 0.0001
	73:24:02.701	± 0.001	73:24:02.698	± 0.001	73:24:02.685	± 0.001	73:24:02.6800	± 0.0001
NGC3718-core	11:32:34.846	± 0.001	11:32:34.8519	± 0.0001	11:32:34.8560	± 0.0001	11:32:34.85300	± 0.00001
	53:04:04.57	± 0.02	53:04:04.530	± 0.001	53:04:04.499	± 0.001	53:04:04.5180	± 0.0001
NGC3718-jet	11:32:34.854	± 0.001	-	-	-	-	-	-
	53:04:04.523	± 0.002	-	-	-	-	-	-
NGC4579-core	12:37:43.511 ^a	-	12:37:43.522	± 0.001	12:37:43.4001	± 0.0001	12:37:43.522 ^b	-
	11:49:05.420 ^a	-	11:49:05.498	± 0.001	11:49:05.0001	± 0.0004	11:49:05.488 ^b	-
NGC5953-core	15:34:32.383	± 0.002	15:34:32.51	± 0.01	not detected	-	not detected	-
	15:11:37.59	± 0.02	15:11:38.0	± 0.1	not detected	-	15:11:37.574 ^c	-
NGC5953-jet	15:34:32.390	± 0.003	-	-	-	-	-	-
	15:11:38.03	± 0.02	-	-	-	-	-	-
NGC7217-core	22:07:52.395	± 0.001	22:07:52.3901	± 0.0001	22:07:52.3932	± 0.0001	22:07:52.39333	± 0.00003
	31:21:33.64	± 0.01	31:21:33.702	± 0.002	31:21:33.642	± 0.002	31:21:33.6462	± 0.0002

Table 11.2: Radio positions of the seven NUGA sources derived from the respective observations. ^a Taken from the MERLIN archive (PI: N.Nagar). The given positional errors are only statistical errors and do not include uncertainties of the respective phase calibrator positions. ^b taken from VLBA observations carried out by Ulvestadt & Ho 2001. ^c derived from a 4σ continuum peak.

three “off-core” components are still marginal and thus their reality remains questionable and to be verified by further observations. Again, indications of extended emission are found in the EVN 18cm data by comparing the peak with the integral intensity. Also, this distribution appears to be slightly resolved and shows an elongation to the North-East but with a different PA than found in the MERLIN maps. The extensions are also in direction of the beam and one has to deal with sidelobe effects, which are visible in the two artificial components to the West and to the East. The 6cm EVN component is finally only marginally resolved and the deconvolved size is of the order of the beam size. Both EVN and MERLIN data result in a spectral index of -0.3 indicating the decrease of flux with decreasing wavelength. Resolution effects cannot totally be discarded so that the spectral index might be higher and the so the spectrum even flatter. The upper limit of the spectral index derived from the PdBI fluxes is similar to the cm-values and also suggests a flat spectrum.

11.3.2.2 NGC 2782

The SAB(rs)pec host galaxy of NGC 2782 harbours a dominant nuclear HII region at a distance of 35Mpc. Its central black hole mass can be estimated to $4 \times 10^7 M_{\odot}$ assuming $\sigma_s = 146 \text{ km s}^{-1}$ (McElroy 1995). The bolometric luminosity amounts to $\sim 9 \times 10^{40} \text{ erg s}^{-1}$ (Table 11.5). A comparison with the Eddington luminosity indicates that NGC 2782 also radiates at a sub-Eddington rate at $L_{\text{bol}}/L_{\text{ed}} \simeq 6 \times 10^{-4}$ and fulfills the criterion for ADAFs.

A core and an extended jet are visible in both the MERLIN 18 cm and 6 cm maps (see Fig. 11.1 and Table 11.3). The jet is elongated towards the South/South-West and has a length of $\sim 0.3''$. Also, the core seems to be slightly resolved. Going to 6 cm and thus to a higher angular resolution, the core and the jet become more resolved, consistent with the lower fluxes measured. The positions at both wavelengths for the respective components are in excellent agreement. Also, the EVN 18cm map shows an extended component ($\sim 4\sigma$), which is supported again by the different peak to integral intensity. The extension is not in the direction of the beam. However, the PA of the extended emission is slightly different compared to the MERLIN maps producing doubts about the reliability of this extension. At EVN 6cm, there is only a marginal detection of a $\sim 3\sigma$ peak at the position of the nucleus.

The spectral index derived from the MERLIN data differs significantly from the one obtained from the EVN data but this can be explained by the extended emission at the EVN 18cm map while the 6cm EVN continuum emission is only marginally detected and heavily resolved producing an artificially lower spectral index. Parts of the jets might also affect the core emission in the MERLIN maps since core and jet emission cannot be easily separated from each other in the 18cm MERLIN map. Thus, the optically thin synchrotron emission from the jet might manipulate the optically thin synchrotron emission in the core yielding hence also an artificially lower index. This might explain why the spectral index of the jet is lower than the one of the core.

No continuum emission was detected at 3 mm nor 1 mm with the IRAM PdBI.

11.3.2.3 NGC 3147

NGC 3147 is classified as SA(rs)bc galaxy with a Seyfert type 2 nucleus at a distance of 38Mpc. The central black hole mass can be derived to $\sim 4 \times 10^8 M_{\odot}$ with $\sigma_s = 268 \text{ km s}^{-1}$ and the bolometric luminosity lies at $\sim 2 \times 10^{42} \text{ erg s}^{-1}$ resulting in $L_{\text{bol}}/L_{\text{ed}} \simeq 5 \times 10^{-5}$. Therefore, NGC 3147 radiates at a sub-Eddington rate and can thus also be associated with an ADAF.

NGC 3147 belongs to the strongest radio sources within our survey (see Fig. 11.1 and Table 11.3). In all maps, it appears to be pointlike including the mm-data. Also, the almost continuous fluxes determined at both wavelengths and instruments are a further sign for very compact emission in this object. The flat to inverted spectral index, i.e. the increase of flux towards shorter wavelengths, derived from the EVN/MERLIN-fluxes indicates that probably no extended jet is at play here. The pointlike structure and the spectral indices (at cm-wavelengths) are consistent with what Ulvestad & Ho (2002) found with the VLBA. Our two observing epochs for the EVN 18cm data have given no evidence for any variability of this source. Similar to NGC 1068, one finds a turnover between the cm- and the mm-fluxes (Fig. 11.4 and 11.5) expressed also in the different spectral indices at mm- and cm-wavelengths (Table 11.4). As NGC 3147 appears to be rather compact, resolution effects should play only a minor role. Even if, the decrease of flux from the 6cm EVN flux of $10.1 \pm 0.3 \text{ mJy}$ (angular resolution of a few milli-arcseconds) to

MERLIN						
Name	18cm			6cm		
	Peak Intensity [mJy/b] ^c	Integral Intensity [mJy]	Deconv. Size " × " @°	Peak Intensity [mJy/b] ^c	Integral Intensity [mJy]	Deconv. Size " × " @°
NGC1961-core	2.3±0.2	2.4±0.3	0.06×0.08@150	1.2±0.3	1.8±0.6	0.3×0.3@170
NGC1961-jet	0.4±0.2	2.3±1.0	0.9×0.1@11	-	-	-
NGC2782-core	1.4±0.1	4.6±0.6	0.3×0.1@20	0.7±0.2	2.5±0.7	0.1×0.06@153
NGC2782-jet	0.3±0.1	1.8±1.0	0.7×0.2@74	0.6±0.2	1.4±0.5	0.08×0.06@145
NGC3147-core	7.4±0.3	8.0±0.3	0.06×0.04@150	10.2±0.1	10.0±0.1	0.02×0.01@18
NGC3718-core	1.2±0.1	4.0±0.6	0.4×0.1@150	5.3±0.1	6.1±0.3	0.05×0.01@139
NGC3718-jet	4.7±0.2	4.5±0.3	0.05×0.03@70	-	-	-
NGC4579-core	5.0 ^a	-	-	15.2±0.2	17.2±0.3	0.09×0.02@146
NGC5953-core	1.6±0.2	1.5±0.3	0.03×0.3@176	0.5±0.1	0.4±0.2	0.05×0.03@67
NGC5953-jet	1.2±0.2	1.2±0.3	0.3×0.2@85	-	-	-
NGC7217-core	1.5±0.1	2.6±0.3	0.2×0.1@157	5.0±0.5	5.0±0.5	0.04×0.02@13
EVN						
Name	18cm			6cm		
	Peak Intensity [mJy/b] ^c	Integral Intensity [mJy]	Deconv. Size " × " @°	Peak Intensity [mJy/b] ^c	Integral Intensity [mJy]	Deconv. Size " × " @°
NGC1961-core	0.50±0.07	1.2±0.2	0.05×0.01@21	0.73±0.05	0.9±0.1	0.002×0.001@55
NGC2782-core	0.40±0.06	1.2±0.2	0.05×0.01@170	0.4±0.1	0.3±0.2	0.01×0.01
NGC3147-core	6.1±0.1	6.0±0.2	0.004×0.004	10.1±0.3	9.3±0.5	0.006×0.006
NGC3718-core	4.8±0.1	4.7±0.3	0.005×0.004@173	5.6±0.1	7.1±0.2	0.004×0.001@115
NGC4579-core	17.8±0.6	20.7±1.0	0.02×0.01@4	-	-	-
Ulv01 ^b	-	18.3	-	-	22.8	-
NGC5953-core	≤0.3	-	-	≤0.4	-	-
NGC7217-core	0.5±0.1	0.5±0.1	0.01×0.02@71	0.41±0.06	1.2±0.2	0.005×0.003@106
PdBI						
Name	3mm			1mm		
	Peak Intensity [mJy/beam]	Integral Intensity [mJy]	Size " × " @°	Peak Intensity [mJy/beam]	Integral Intensity [mJy]	Size " × " @°
NGC 1961	2.6±0.4	3	3.5×1.8@57	≤2 (3σ)	-	-
NGC 2782	≤1.0 (3σ)	-	-	≤3 (3σ)	-	-
NGC 3147	5.3±0.3	5.0	1×1	2.8±0.5	3.0	1×1
NGC 3718	9±2	10	2×2	9.5±0.7	10	1×1
NGC 4579	11.3±0.5	11	0.5×0.5	12±2	11	0.5×0.5
NGC 5953	≤2 (3σ)	-	-	≤4 (3σ)	-	-
NGC 7217	≤1.5 (3σ)	-	-	≤4 (3σ)	-	-

Table 11.3: Results of the radio observations. ^a from the MERLIN archive (PI: N.Nagar). ^b taken from VLBA observation carried out by Ulvestad & Ho (2001; Ulv01). ^c mJy/b≡mJy/beam.

Name	$\alpha_{113}^{230}(\text{PdBI})$	$\alpha_{1.7}^5(\text{MERLIN})$	$\alpha_{1.6}^5(\text{EVN})$	$\alpha_{1.7}^5(\text{VLBA})^a$
NGC 1961	≤ -0.4	-0.3 ± 0.3	-0.3 ± 0.2	-
NGC 2782	-	-0.6 ± 0.3	≤ -1.0	-
jet	-	-0.2 ± 0.6	-	-
NGC 3147	-0.7 ± 0.3	0.14 ± 0.03	0.39 ± 0.06	0.2 ± 0.1
NGC 3718	0.0 ± 0.2	0.4 ± 0.1	0.37 ± 0.06	-
NGC 4579	0.1 ± 0.2	$\sim 1^b$	0.09 ± 0.04	0.2 ± 0.1
NGC 5953	-	-1.2 ± 0.5	-	-
NGC 7217	-	0.6 ± 0.1	0.8 ± 0.2	-

Table 11.4: Spectral indices of the respective sources. $S_\nu \propto \nu^\alpha$. ^a taken from Ulvestad & Ho 2001. ^b This value is most likely not reliable since, on the one hand, the 18cm MERLIN flux was taken from an archive map and thus nothing can be said about its reliability. NGC 4579 is also known to be variable (see Text for more details).

the 3mm PdBI flux of 5.3 ± 0.3 mJy (angular resolution of a few arcseconds) cannot not be produced by resolution effect since then one should find an increase of the fluxes between 6 cm and 3 mm and not a decrease. The flux calibration of the mm-data could, however, present a weak point. While the cm fluxes are in excellent agreement within the observed epochs and also compared to other published values, the situation for the mm fluxes is not that clear and has to be further clarified. A wrongly assumed calibrator flux, that is induced, for instance, by a variability of the calibrator source which was not taken into account, could cause an artificial decrease (or increase) of the target flux. However, the calibrator fluxes are regularly monitored at the IRAM PdBI thus accounting for effects such as variability. One of the flux calibrators used for NGC 3147 was MWC349 which has a constant (over the last 4 years) and well known flux of $\sim 1\text{-}1.2$ Jy at 115 GHz with an accuracy of $\sim 15\%$. Taking these uncertainties into consideration, the error of the 3 mm flux of NGC 3147 would increase to ~ 1 mJy. Therefore, the turn-over seen in the synchrotron spectrum might indeed be an intrinsic property of NGC 3147. Assuming now Equation 6.5 to determine the magnetic flux density, a turnover frequency of $\nu_m \simeq 12$ GHz, the corresponding frequency of $S_m = 0.012$ Jy, a source size of ~ 100 Schwarzschild radii similar to NGC 1068, the magnetic flux density around the black hole can be estimated to ~ 1 Gauß. This value is of the order of that one derived for NGC 1068.

11.3.2.4 NGC 3718

The galaxy NGC 3718 hosts a LINER type 1.9 nucleus and shows a very peculiar morphology. A black hole mass of $\sim 5 \times 10^7 M_\odot$ is found with $\sigma_s = 157 \text{ km s}^{-1}$ (Ho et al. 1997) and a bolometric luminosity of $\sim 3 \times 10^{41} \text{ erg s}^{-1}$ implying again a sub-Eddington system with $L_{\text{bol}}/L_{\text{ed}} \simeq 4 \times 10^{-5}$. The central core in NGC 3718 can thus also be connected to an ADAF.

Similar to NGC 3147, NGC 3718 belongs to the strongest radio sources in our survey (Table 11.3). It shows on MERLIN 18cm scales extended emission and signs for a quite compact 4σ jet in North-West direction (Fig. 11.2). There are some weak indications for extended emission in the 6cm maps at MERLIN and EVN as well, by looking at the peak and integral intensities. A pointlike source would suggest identical values but here, they are significantly different. Moreover, the EVN 6cm map reveals also an extension but in contrast to the MERLIN 18cm image, in West-direction. Comparing the fluxes from MERLIN with those obtained with EVN, the fluxes remain again quite constant indicating that there might be no diffuse and very extended emission in NGC 3718 besides the jet. The spectral indices for the MERLIN, and EVN data are also consistent and derived to 0.4 expressing an inverted spectrum. This agrees still with index calculated from the PdBI data within the errors.

11.3.2.5 NGC 4579

NGC 4579 is a SAB(rs)b galaxy with a Seyfert 1.9 and/or LINER type 1.9 nucleus at a distance of 20 Mpc. The black hole estimate provides a value of $\sim 10^8 M_\odot$ assuming $\sigma_s = 185 \text{ km s}^{-1}$ (McElroy 1995). Ho et al. (1999)

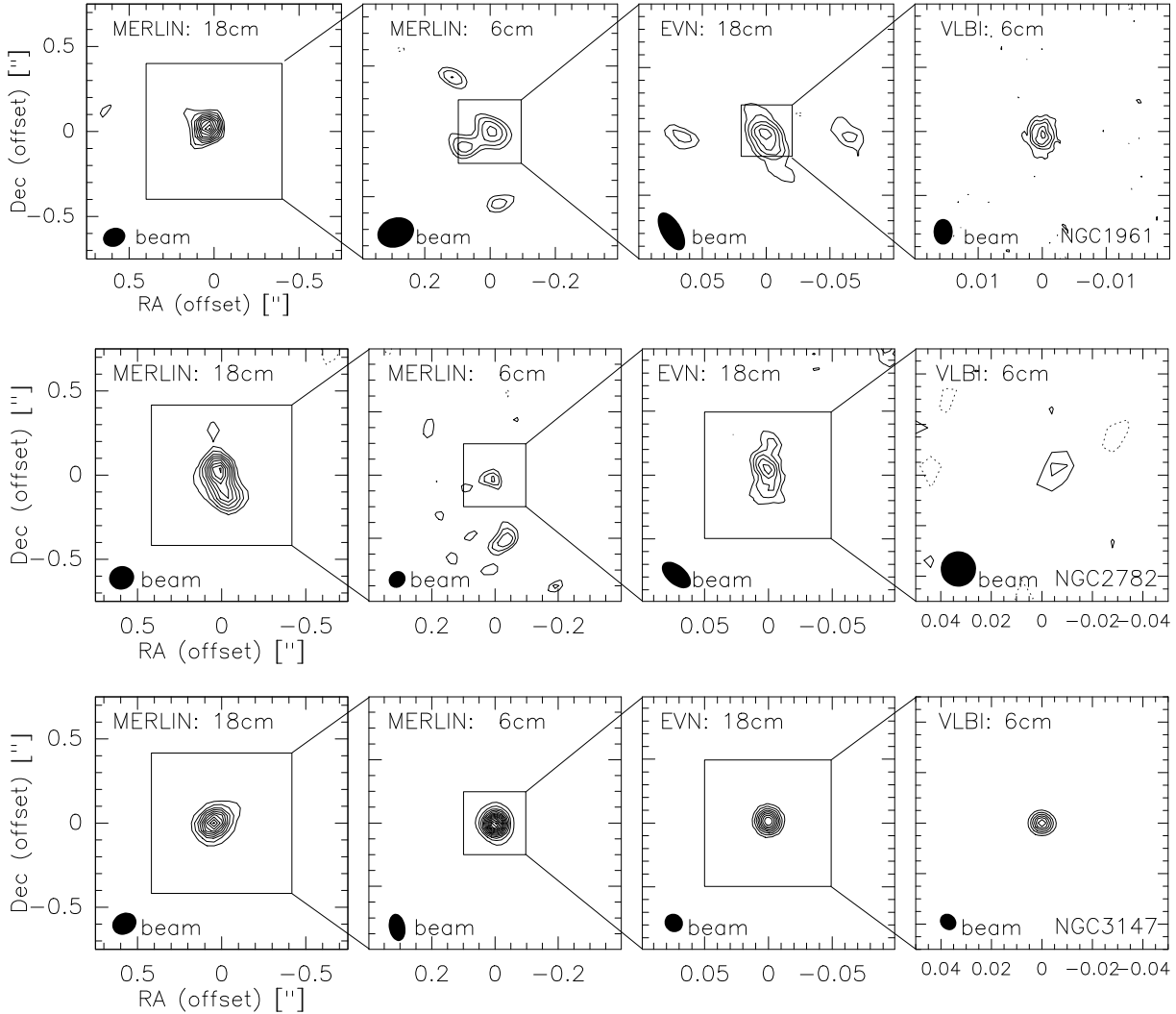


Figure 11.1: MERLIN (2 images on the *left*) and EVN/VLBI (two images on the *right* panel) of the 18cm and 6cm continuum emission in NGC1961 (*upper panels*), NGC2782 (*middle panels*) and NGC3147 (*lower panels*). The respective synthesized beams are shown in the lower middle part of each map. Contour levels for MERLIN-18cm (NGC 1961; *upper left*): (3σ)=0.57 to 2.28 mJy/beam in steps of 1σ ; for MERLIN-6cm (*upper left middle*): (3σ)=0.39 to 0.78 mJy/beam in steps of 1σ ; EVN-18cm (*upper right middle*): (3σ)=0.21 to 0.49 mJy/beam in steps of 1σ ; EVN-6cm (*upper right*): (3σ)=0.14 to 0.61 mJy/beam in steps of 1σ ; MERLIN-18cm (NGC2782; *middle left*): (3σ)=0.45 to 1.7 mJy/beam in steps of 1σ , for MERLIN-6cm (*middle left middle*): (3σ)=0.39 to 0.78 mJy/beam in steps of 1σ , for EVN-18cm (*middle right middle*): (3σ)=0.18 to 0.36 mJy/beam in steps of 1σ ; for EVN-6cm (*middle left*): (3σ)=0.18 to 0.54 mJy/beam in steps of 1σ . MERLIN-18cm (NGC3147; *lower left*): (5σ)=0.75 to 7.5 mJy/beam in steps of 5σ , for MERLIN-6cm (*lower left middle*): (3σ)=0.72 to 10.1 mJy/beam in steps of 5σ , for EVN-18cm (*lower right middle*): (3σ)=0.65 to 5.2 mJy/beam in steps of 5σ ; for EVN-6cm (*lower left*): (5σ)=1.4 to 8.3 mJy/beam in steps of 5σ . Negative contours (marked by dotted lines), if visible, correspond to 3σ .

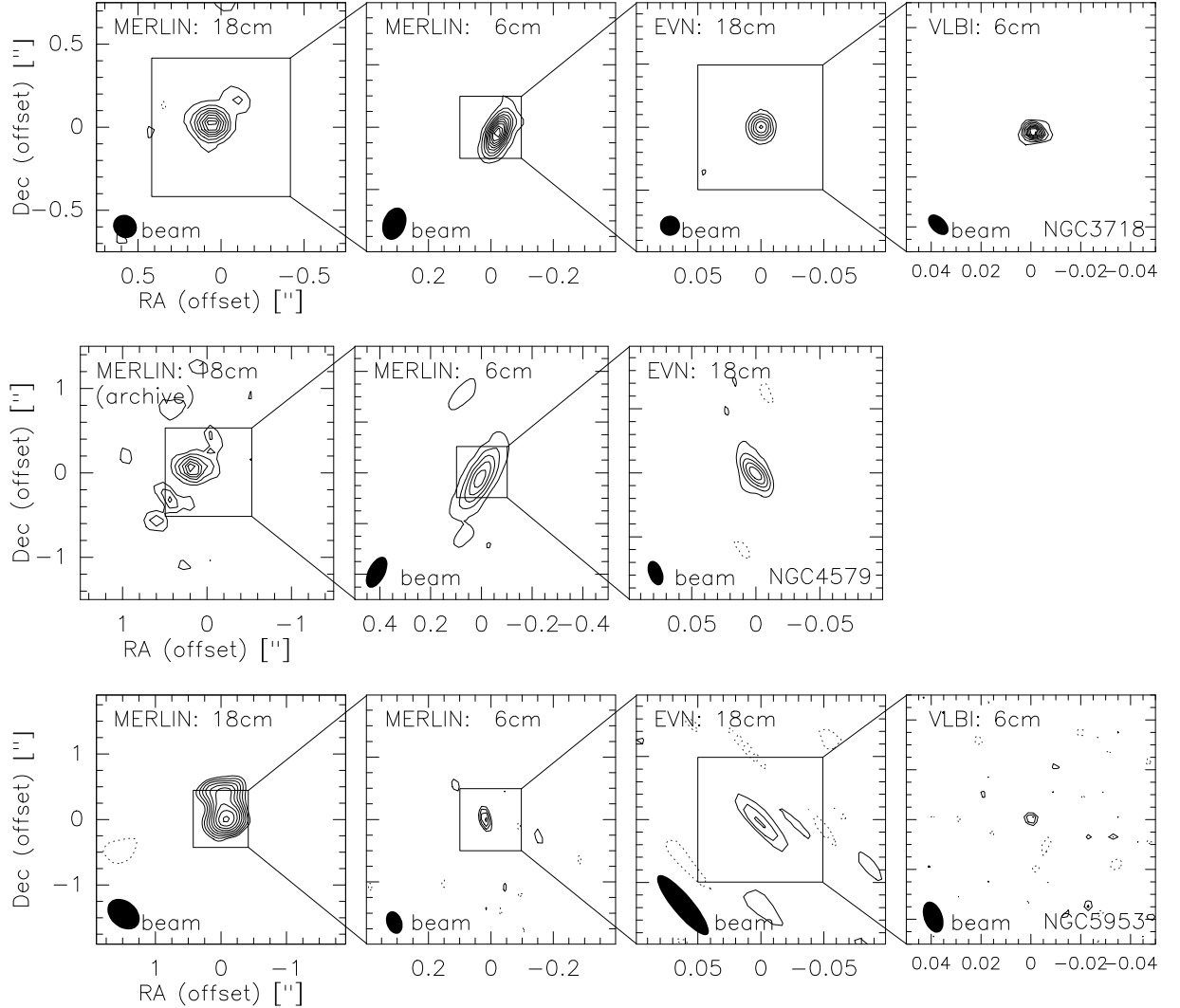


Figure 11.2: MERLIN (2 images on the *left* respectively) and EVN (2 images on the *right* respectively) of the 18cm and 6cm continuum emission in NGC3718 (*upper panel*), NGC4579 (*middle panel*) and NGC5953 (*lower panel*). The respective synthesized beams are shown in the lower middle part of each map. MERLIN-18cm (NGC 3718; *upper left*): (5σ)=0.64 to 5.1 mJy/beam in steps of 5σ , for MERLIN-6cm (*upper left middle*): (5σ)=0.5 to 5.0 mJy/beam in steps of 5σ , for EVN-18cm (*upper right middle*): (5σ)=0.75 to 4.5 mJy/beam in steps of 5σ ; for EVN-6cm (*upper right*): (5σ)=0.55 to 5.0 mJy/beam in steps of 5σ ; MERLIN-18cm (NGC4579; *middle left middle*): 0.7 to 4.9 mJy/beam in steps of 0.7 mJy/beam; MERLIN-6cm (5σ)=1.0 to 15.0 mJy/beam in steps of 10σ , for EVN-18cm (*middle right middle*): (3σ)=3.3 to 16.5 mJy/beam in steps of 3σ ; MERLIN-18cm (NGC5953; *lower left*): (3σ)=0.48 to 1.5 mJy/beam in steps of 1σ , for MERLIN-6cm (*lower left middle*): (3σ)=0.74 to 1.7 mJy/beam in steps of 1σ , for EVN-18cm (*lower right middle*): (3σ)=0.13 to 0.29 mJy/beam in steps of 1σ ; for EVN-6cm (*lower right*): (3σ)=0.24 to 0.4 mJy/beam in steps of 1σ . Negative contours, if visible, correspond to 5σ .

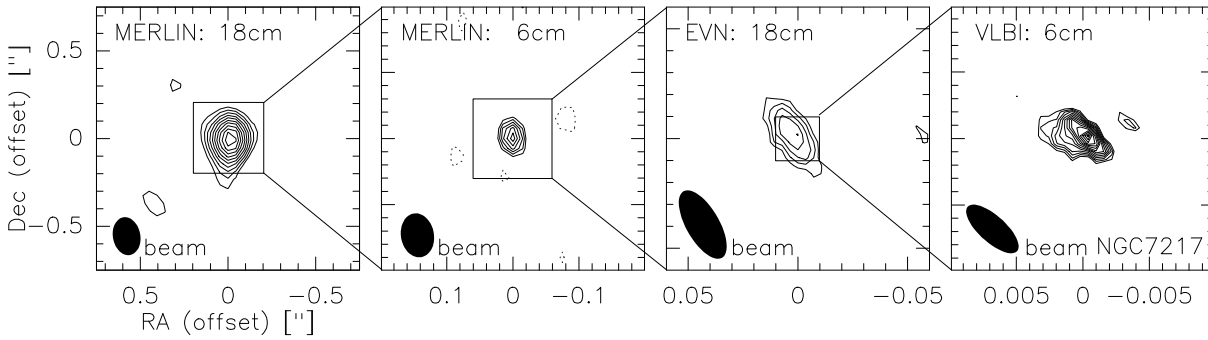


Figure 11.3: MERLIN (2 images on the *left*) and EVN (2 images on the *right*) of the 18cm and 6cm continuum emission in NGC7217. The respective synthesized beams are shown in the lower middle part of each map. Contour levels for MERLIN-18cm (*left*): (3σ)=0.36 to 1.4 mJy/beam in steps of 1σ , for MERLIN-6cm (*left middle*): (3σ)=1.5 to 4.0 mJy/beam in steps of 1σ , for EVN-18cm (*right middle*): (3σ)=0.21 to 0.5 mJy/beam in steps of 1σ ; for EVN-6cm (*lower right*): (3σ)=0.2 to 0.6 mJy/beam in steps of 1σ . Negative contours, if visible, correspond to 3σ .

determines the bolometric luminosity to $\sim 10^{42} \text{erg s}^{-1}$. This gives a value of $\sim 10^{-4}$ for $L_{\text{bol}}/L_{\text{ed}}$ indicating a sub-Eddington system and thus an ADAF.

NGC 4579 was already observed with MERLIN at 18cm (PI: N.Nagar, from MERLIN archive) and with VLBA at 6cm (Ulvestad & Ho 2001). Thus, only complementary observations were conducted with MERLIN at 6cm and EVN at 18cm (Fig.11.2 and Table11.3). Falcke et al. (2001) report on a variability of the radio flux at 15 GHz on timescales of 1-3 years. One also finds a difference of $\sim 10\%$ between the flux derived with EVN and the one obtained with the VLBA at 18cm. Thus, the determination of the spectral index must be made and interpreted with caution since all fluxes were not instantaneously derived but in different epochs. This might explain the outstanding discrepancy between the MERLIN 18 cm flux of 5 mJy and the higher angular resolution EVN 18 cm flux of 17.8 mJy^5 , reflected in the differing spectral indices.

11.3.2.6 NGC 5953

NGC 5953 is characterised as SAa pec galaxy hosting a Seyfert type 2 nucleus at a distance of 26 Mpc. The black hole mass of $\sim 7 \times 10^6 M_{\odot}$ ($\sigma_8=94 \text{ km s}^{-1}$; McElroy 1995) is the smallest one in our sample. However, Wo et al. 2002 find a surprisingly high bolometric luminosity of $\sim 10^{44} \text{erg s}^{-1}$. The $L_{\text{bol}}/L_{\text{ed}}$ ratio of 0.1 implies that NGC 5953 is radiating close to the Eddington rate and is probably already at the edge for ADAFs. Unfortunately, no X-ray luminosity has been published so far.

Although showing such a bolometric luminosity NGC 5953, turns out to be the weakest radio source in our sample (Table 11.3). It is clearly detected in the MERLIN 18 cm and 6 cm maps while it remains hidden in the EVN maps (Fig. 11.1). A 4σ peak is found in the latter at the position of the nucleus. The MERLIN 18 cm also shows a strong jet to the North which is slightly resolved in the MERLIN beam. The low spectral index of ~ -1.2 for the core derived from the MERLIN data indicate that the MERLIN 6cm observations have most likely missed a significant amount of extended flux thus explaining the unexpected low core intensity measured here and thus the low spectral index.

11.3.2.7 NGC 7217

NGC 7217 contains a LINER type 2 nucleus in an (R)SAB(rs)a host galaxy at a distance of 13 Mpc. It has a black hole mass of $\sim 3 \times 10^7 M_{\odot}$ and an estimated bolometric luminosity of $\sim 4 \times 10^{40} \text{erg s}^{-1}$. Both values result in

⁵hence excluding resolution effects

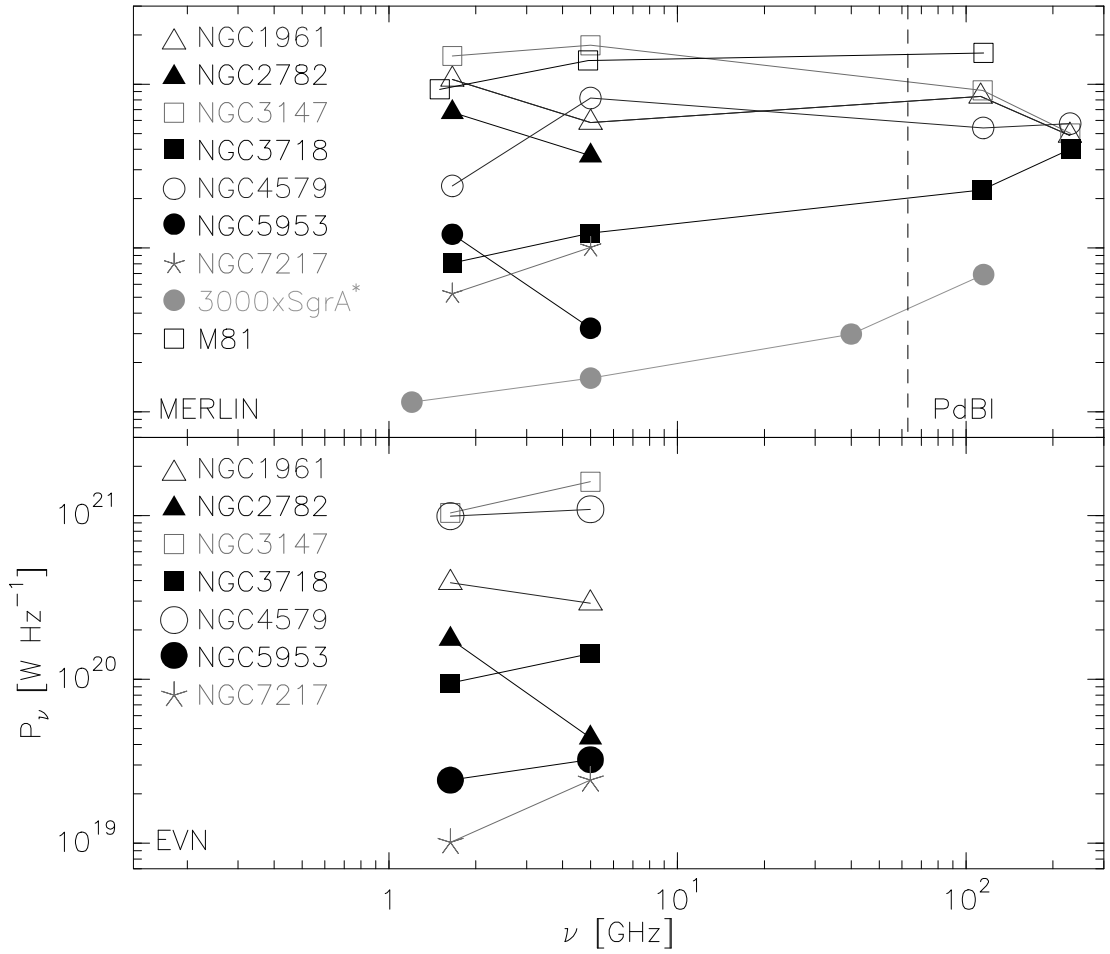


Figure 11.4: Spectral energy distribution from the MERLIN/PdBI (*upper panel*) and EVN data (*lower panel*). Value for SgrA* were taken from Falcke et al. 1998 and Zhao et al. 2001. Errors are not plotted due to presentation purposes. $P_\nu = 4\pi D^2 \cdot S_\nu$.

$L_{\text{bol}}/L_{\text{ed}} \simeq 10^{-5}$. Thus, NGC 7217 is also a sub-Eddington system and contains an ADAF.

The MERLIN 18cm map (Fig.11.3 and Table11.3) clearly shows an extended component with an elongation to the South. The MERLIN 6cm and EVN 18cm sources, however, remain pointlike while the EVN 6cm maps reveal again an extended component but in East direction. The two spectral indices, derived from the MERLIN and EVN data, are strongly inverted and indicate the strongest increase of flux with decreasing wavelength within our sample. However, nothing can be said about variability in this source so that this high spectral index has to be taken with caution.

11.4 Spectral Energy Distribution

The spectral energy distributions (SEDs) of all seven NUGA galaxies are plotted almost over the entire electromagnetic spectrum in Fig. 11.5. Besides the radio fluxes, also infrared, optical and X-ray fluxes are included (Table 11.6). The morphology of the individual SEDs are comparable. The spectra of the radio core emission is mostly flat to inverted, consistent with optically thick synchrotron radiation. The infrared fluxes, which measures

Name	D [Mpc]	M_{bh} [$10^8 M_{\odot}$]	$\log(L_{5.0}^{\text{obs}})^j$ [erg s^{-1}]	$\log(L_{\text{x}})$ [erg s^{-1}]	$\log(L_{\text{bol}})$ [erg s^{-1}]	$\log(L_{\text{ed}})^i$ [erg s^{-1}]
NGC 1961	52	3.0 ^a	37.16	40.56 ^c	41.39 ^g	46.57
NGC 2782	35	0.4 ^a	36.34	40.11 ^c	40.94 ^g	45.70
NGC 3147	38	3.6 ^a	37.91	41.53 ^d	42.35 ^g	46.65
NGC 3718	13	0.5 ^{a,b}	36.86	40.59 ^e	41.42 ^g	45.79
NGC 4579	20	1.0 ^a	37.74	40.95 ^d	41.99 ⁱ	46.09
NGC 5953	26	0.07 ^a	≤ 36.21	-	44.05 ^h	44.94
NGC 7217	13	0.3 ^a	36.08	39.81 ^f	40.64 ^g	45.57
NGC 1068	14	0.2 ^m	37.17 ⁿ	41.94 ^o	42.77	46.15
Name	$\log(L_{\text{bol}}/L_{\text{ed}})$	$\log(L_{5.0}^{\text{obs}}/L_{\text{x}})$	$\log(L_{5.0}^{\text{obs}}/L_{5.0}^{\text{pre}})^k$			
NGC 1961	-5.18	-4.23	0.38			
NGC 2782	-4.76	-3.77	0.58			
NGC 3147	-4.30	-3.62	-0.35			
NGC 3718	-4.37	-4.56	0.39			
NGC 4579	-4.10	-4.04	0.61			
NGC 5953	-0.89	≤ -7.01	-			
NGC 7217	-4.93	-4.56	0.62			
NGC 1068	-3.38	-4.77	1.57			

Table 11.5: Black hole masses, bolometric and Eddington luminosities for the seven observed galaxies and NGC 1068. ^a assuming $M_{\text{bh}} = 1.2 \times 10^8 M_{\odot} \times (\sigma_s/200[\text{km s}^{-1}])^{3.75}$ from Gebhardt et al. 2000 with σ_s taken from McElroy et al. 1995. ^b σ_s taken from Ho et al. (1997) and assuming $\text{FWHM}([\text{O III}])=\text{FWHM}([\text{N II}])$. ^c taken from Roberts & Warwick 2000. ^d taken from Ulvestad & Ho 2001. ^e taken from Fabbiano et al. 1992. ^f taken from Terashima et al. 2002. ^g assuming $L_{\text{bol}}=6.7 \times L_{\text{x}}(2\text{-}10\text{keV})$ from Ulvestad & Ho 2001. ^h taken from Wo et al. 2002. ⁱ taking the standard Eddington equation. ^j assuming $L_{5.0} = \nu_{5.0} \times 4\pi D^2 S_{\nu}$ where S_{ν} is the integral intensity from Table 11.3. ^k $L_{5.0}^{\text{pre}}$ has been estimated via L_{x} assuming equation (2.10) from Yi & Boughn et al. 1998. ^l Ho et al. 1999. ^m from Greenhill & Gwinn (1997). ⁿ from Gallimore et al. (2004). ^o from Brinkmann et al. (1994).

Name	S_{x}^a [10^{-7} Jy]	S_{BAND}^b [Jy]	S_{FIR}^b [Jy]	$S_{230\text{GHz}}^c$ [mJy]	$S_{5.0\text{GHz}}^d$ [mJy]
NGC 1961	0.356	0.5	21.6	≤ 1.5	0.9
NGC 2782	0.279	0.2	14.6	≤ 3.0	≤ 0.4
NGC 3147	6.226	0.7	30.0	2.8	9.3
NGC 3718	6.108	0.55	31.0	9.5	7.1
NGC 4579	5.912	1.8	18.1	12	22.8
NGC 5953	-	0.14	19.5	≤ 4	≤ 0.4
NGC 7217	1.01	1.3	18.5	≤ 4	1.2
NGC 1068	0.7	2	280	17	12

Table 11.6: Some representative fluxes from radio, Far-Infra-Red (FIR) and optical frequencies to X-rays of the seven NUGA sources are given. ^a see caption of Table 11.5 for the references. ^b taken from NED. ^c taken from our IRAM PdBI observations. ^d taken from the EVN observations.

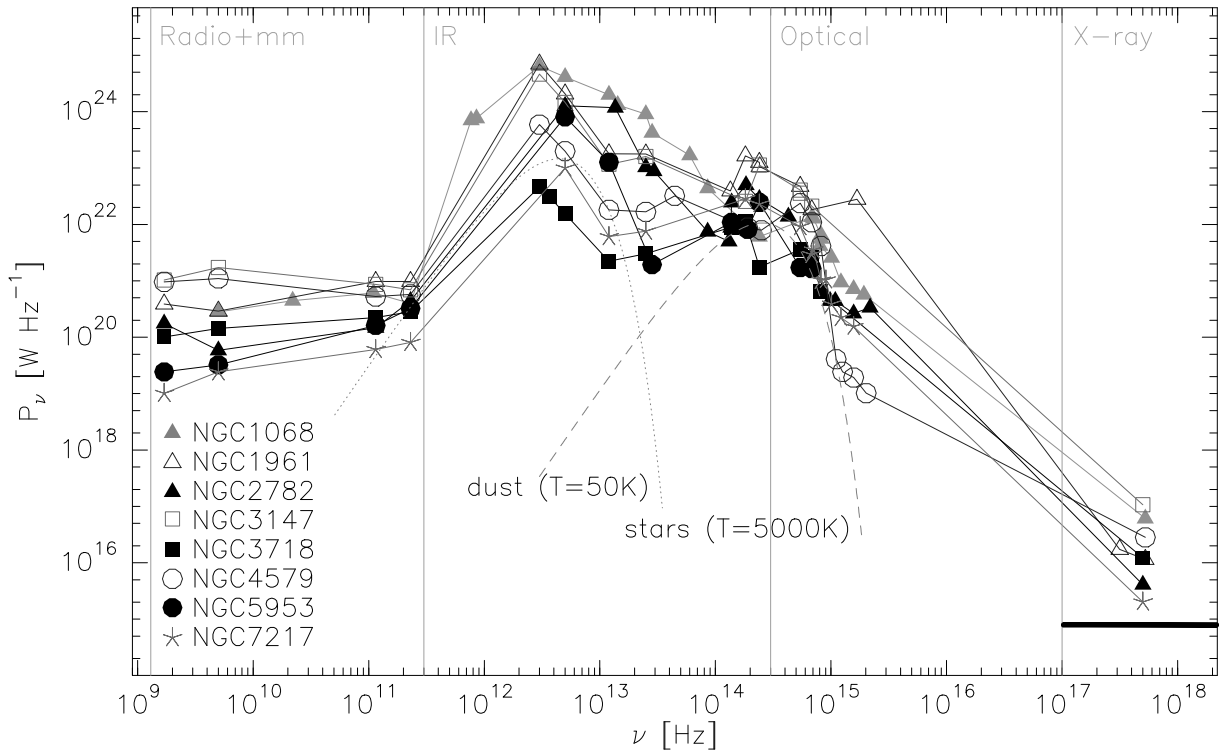


Figure 11.5: Spectral Energy Distribution for the 7 NUGA galaxies and NGC 1068. Plotted are the observed EVN/VLBI radio and IRAM PdBI mm fluxes (Table 11.3) together with IR, optical and X-ray data taken from NED. Errors are smaller than or roughly of the order of the symbol size. $P_\nu = 4\pi D^2 \cdot S_\nu$. Assuming a turnover below 100 GHz, one can extrapolate the optically thin synchrotron emission from cm-/mm-wavelengths towards higher frequencies. At the higher frequencies, the photons are inverse Compton scattered towards the X-rays. The thick black line at X-ray frequencies indicates the bandwidth over which the X-ray fluxes were derived.

the dust emission, obey a thermal black body spectrum at a (mean) temperature of ~ 50 K indicated in Fig. 11.5. Also, the stellar emission follows a thermal black body spectrum but at a much higher (mean) temperature of ~ 5000 K⁶. These temperatures are consistent with what one would expect. The X-ray flux can be extrapolated from the radio fluxes assuming a turnover between roughly 100 and 400 GHz of the synchrotron spectrum and a following inverse Compton scattering process (see next Section, Fig. 11.5 and compare also Chapter B.2).

11.5 Radio versus X-ray luminosity and black hole mass

All seven observed NUGA galaxies (except NGC 5953) appear to be sub-Eddington systems fulfilling thus the criterion for ADAFs as possible mechanisms for their radio core emission. The strong correlation between X-ray luminosity, black hole mass and radio luminosity has been proven for many systems, among them X-ray binaries and also (strongly) active galaxies. In Fig. 11.6, our observed 5 GHz are compared VLBI luminosities ($L_{5.0}$) with published ROSAT X-ray luminosities (Roberts & Warwick 2000, Fabbiano et al. 1992) and black hole masses (McElroy et al. 1995) of the 7 objects. As expected, one finds for both, M_{bh} and L_x , a strong correlation with $L_{5.0}$. Yi & Boughn (1998) have proposed an equation including all three independent quantities based on theoretical

⁶Please note, that the assumed emission areas for the stellar and the dust part are different (due to different angular resolutions etc.) so that, despite of Wien's law, the stellar black body at the higher temperature is located at lower fluxes, however

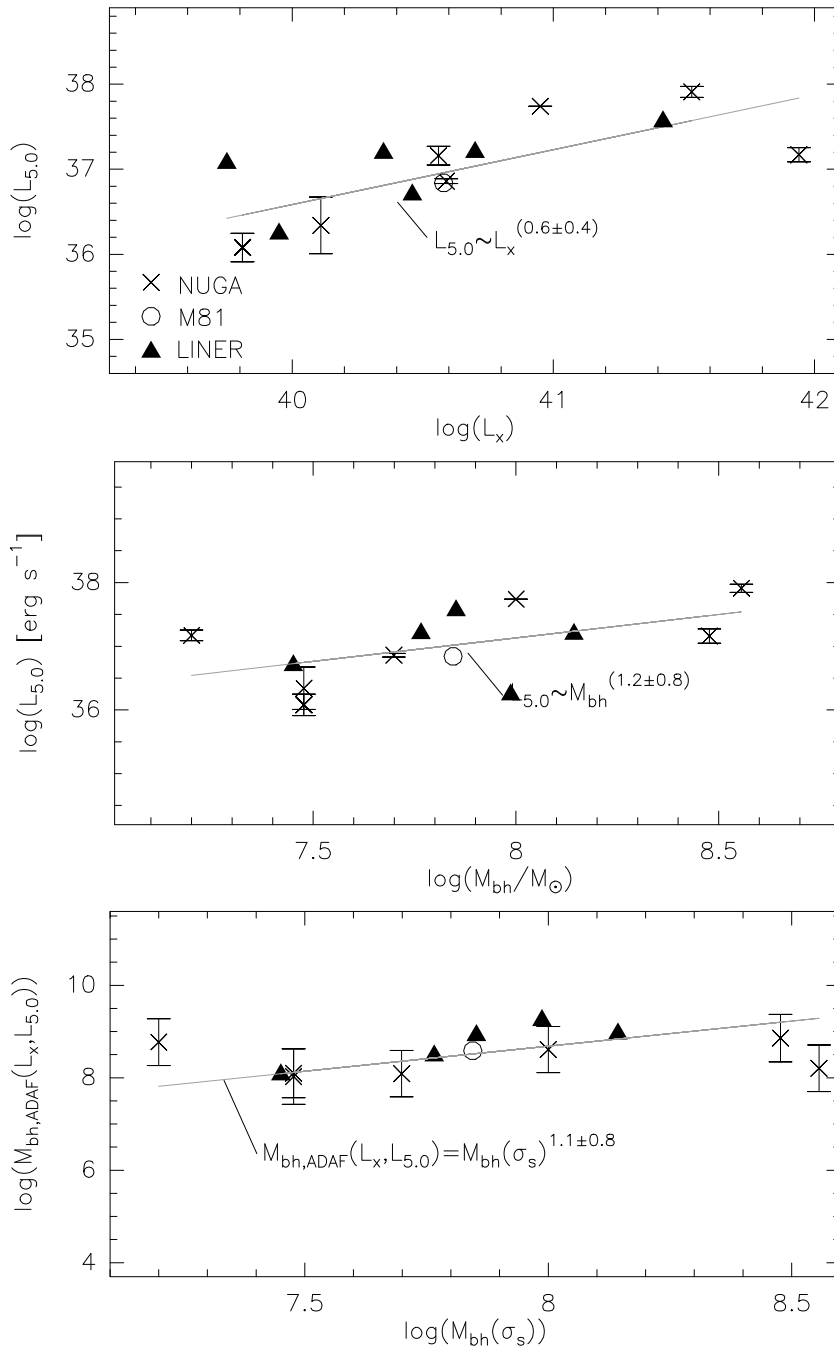


Figure 11.6: Comparison of radio with X-ray luminosities (*upper panel*), radio luminosity with black hole masses (*middle panel*), and of the black hole masses derived via X-ray and radio fluxes with the one determined via the stellar velocity dispersion (*lower panel*). NGC 1068 was included, while NGC 5953 was excluded since no X-ray flux is so far published. Filled triangles symbolise LINER galaxies taken from VLBA observations carried out by Falcke et al. (2000). *Upper & Middle panel*: Errors are statistical errors of the EVN 5.0GHz luminosity. *Lower panel*: Errors are from statistical errors for the radio luminosity and the given errors for the equation published by Yi & Boughn (1998); see text for more details.

considerations for ADAFs. In contrast to the authors, who confronted their theoretical results to radio data for LLAGN, mostly obtained with the VLA or MERLIN array, i.e. at lower angular resolutions, their equation can be empirically confirmed within the errors with our radio sample at much higher angular resolution and of even much weaker radio sources (see lower panel of Fig.11.6). The higher angular resolution of our new data allow to better separate the compact core emission from extended emission coming from a jet for instance. Moreover, our sample consists of mJy to sub-mJy sources. Previous studies were funded on much stronger objects. Thus, even for these weak radio sources, a strong correlation between radio and X-ray radiation can be proven as well. This correlation can be traced back to scattering processes. The compact radio emission is produced by accelerated electrons in a magnetic field, i.e. (optically thick) synchrotron processes. A photon, that is radiated by such an electron, can be later scattered by another electron and gain energy⁷, i.e. undergo an inverse Compton scattering process. This relation can also be seen in Fig. 11.5, where the X-ray fluxes can be roughly extrapolated from the radio fluxes by assuming a turnover of the synchrotron radiation at frequencies 100-400GHz followed by $P_\nu \propto \nu^{-1}$ ($P_\nu = 4\pi D^2 \cdot S_\nu$) and scattering processes.

The ADAF theory works hence also for the core emission in these LLAGN. However, as the MERLIN maps indicate as well, ADAFs are not the only answer for the origin of the radio emission in this kind of objects. Also jets seem to play an important role in LLAGN following hence their “bigger brothers”, the HLAGN.

11.6 Summary and Conclusion

This chapter presents first results of snapshot radio observations of a sample of seven LLAGN taken from the NUGA survey with MERLIN and EVN. Besides compact emission, also extended emission in form of jets is found in these weak radio sources. The radio fluxes decrease significantly with increasing angular resolution at the respective wavelength indicating extended and diffuse emission. The radio core components appear to have mostly flat to inverted spectra (within the errors) with only one exception (NGC 2782) which can, however, be traced back to resolution effects. NGC 3147 and NGC 1068 show both indications for a turn-over in their SED from cm to mm-wavelengths. Additionally, their global CO morphology is very similar as well, indicating that these two systems might be in comparable evolutionary stages, i.e. that they might be “twins”. Comparing all NUGA sources with each other, one finds that the individual SEDs are very similar with respect to each other and reveal nicely the different emission mechanisms, such as the optically thick synchrotron radiation of the compact radio cores or the thermal black body distribution of the stars and the dust. Moreover, the X-ray fluxes can be extrapolated from the radio part of the SED by assuming Synchrotron self (inverse) Compton scattering. A more detailed comparison of the observed radio luminosities to the X-ray luminosities published by Roberts & Warwick (2000), and to the black hole mass, estimated via the respective stellar velocity dispersions, reveals a tight correlation between this quantities. As six of the seven NUGA sources may be classified to radiate at sub-Eddington rates, ADAF theory can be used to explain the origin of the (core) radio emission in these sources. Moreover, the found correlations are in excellent agreement with predictions coming from ADAF theory. Only NGC 5953 seems to hold a special role since it almost radiates at Eddington luminosities. Unfortunately no X-ray luminosity is published for this source so that no comparison can be done with the radio flux of its black hole mass. However, ADAFs alone are not enough to disentangle the whole mechanism that is at play for the non-thermal radio emission in these active galaxies. Rather combined ADAF+jet models have to be considered to unveil the nature of these objects. Our results of the radio observations of this (limited) sample of LLAGN clearly draw many similarities to HLAGN boosting and nourishing the interpretation of LLAGN as scaled down versions of HLAGN. Thus, the processes at play are consistent with accretion onto a supermassive black hole excluding SNRs as alternative source for the radio emission.

⁷by a factor of γ^2 , where γ is the Lorentz-factor ($= (1 - v^2/c^2)^{-1/2}$).

Part VI

Summary, Conclusions and future prospects

Chapter 12

Summary and Conclusions

In this thesis, molecular gas and non-thermal continuum emission was studied in several active galaxies from cm to mm wavelengths enabling different insights on the nature of their activity. The huge energetic production in active galaxies can be associated with accretion of matter onto a super-massive black hole in their centres as one likely explanation. While molecular gas, traced by carbon monoxide (CO), allows an investigation of the accretion mechanisms at different angular scales (i.e., from several kpc to ~ 50 pc in this study), radio continuum emission provides information on processes in the direct vicinity of the black hole (i.e., down to ~ 0.1 pc). Interferometric observations with the IRAM PdBI, currently the instrument with the highest sensitivity and at the same time highest available angular resolution for the analyses of CO, resulted in detailed maps of the distribution and kinematics of the molecular gas in five different types of active galaxies: NGC 3718, a LINER galaxy with a warped gas and dust disk at a distance of $D=13$ Mpc, NGC 1068, a Seyfert galaxy with a warped nuclear disk at $D=14.4$ Mpc, HE 1029-1831, one of the closest QSOs with a gas rich barred host at $D=180$ Mpc, 3C48, a likely merger at (angular size) distance of $D=850$ Mpc, and Q0957+561, a gravitationally lensed system at (angular-size) distance of $D=1.9 h_{65}^{-1} \text{ Gpc}^1$ ($z=1.414$). The first two targets belong to the NU(clei of)GA(laxy) project, an international collaboration that aims at analysing the distribution and kinematics of gas on the smallest available angular scales and with the highest sensitivity currently available. The NUGA survey includes a total of 30 Seyfert and LINER galaxies as well as transition objects (García-Burillo et al. 2003). HE 1029-1831 is part of the Cologne Nearby QSO sample, that aims at detecting and studying the molecular gas in these higher luminosity active galaxies (HLAGN). The results obtained for the molecular gas in these objects (see also Table 12.1) will be summarized in the following subsections.

Although CO is a good tracer for the molecular gas, it is, however, biased by the fact that it rather measures low to moderate gas densities ($n(\text{H}_2) \geq 200 \text{ cm}^{-3}$) and might thus miss further important information on the gas, which might be necessary to get a complete picture of the accretion mechanisms. Thus, IRAM 30 m observations have been conducted to search for HCN in the core NUGA sample. HCN is known to trace denser parts of the gas ($n(\text{H}_2) \sim 10^5 \text{ cm}^{-3}$). This is supposed to be the first step for follow-up interferometric observations.

The radio continuum emission was studied with MERLIN and VLBI at sub- and milliarcsecond angular resolution. 7 NUGA galaxies were chosen to conduct first snap-shot observations at two different wavelengths, 6 cm and 18 cm. The information gained here will also be briefly summarized.

12.1 NGC 3718

NGC 3718 is a peculiar galaxy with a LINER type 1.9 nucleus at a distance of 13 Mpc. Its host galaxy has a prominent dust lane and its atomic and molecular gas disc appears to be strongly warped from large scales ($\simeq 20$ kpc; Schwarz 1985) over moderate scales ($\simeq 1$ kpc, Pott et al. 2004) down to small scales ($\simeq 200$ pc, Krips

¹see Table 12.1

et al. 2004c, 2005a). The new interferometric data unveil mainly six different source components within the dust lane: one associated with the nucleus, four symmetrically positioned on either side of the nucleus at galactocentric distances of about 1.3kpc and 4.0kpc from the center, and a sixth on the western side at ~ 3 kpc with only a very weak eastern counterpart. Based on a kinematic model using tilted rings to simulate the warp, the five symmetric source components are interpreted as locations of strong orbit crowding points. Besides the sixth feature on the western side, the lower flux (a factor of ~ 2) of the eastern components compared to the western ones indicates an intrinsic large scale asymmetry in NGC 3718 that cannot be explained by the warp alone. Indications for a small scale asymmetry are also seen in the central 200-300pc evoked by a dominance of the redshifted emission on these scales. These asymmetries might be evidence for a tidal interaction with the companion galaxy (*large scales*) and gas accretion onto the nucleus (*small scales*).

12.2 NGC 1068

NGC1068 is a barred spiral galaxy at a distance of 14.4 Mpc with a Seyfert nucleus. The $^{13}\text{CO}(1-0)$, $^{12}\text{CO}(2-1)$ and continuum emission of this object were observed with the IRAM PdBI in the framework of this PhD thesis. The continuum emission was detected at 3 mm and for the first time also at 1 mm. Besides strong core emission, also emission coming from the jet was found at both wavelengths. The 3 mm results for the jet and the core are in excellent agreement with other radio studies. The 1 mm continuum emission at the core indicates a turn-over in the SED similar to what is found for Sgr A*, while the 1 mm jet component is still consistent with a spectral index of -1 ($f_\nu \propto \nu^\alpha$) derived from lower radio frequencies. The $^{13}\text{CO}(1-0)$ emission is much stronger correlated with the bar than with the spiral arms with respect to the $^{12}\text{CO}(1-0)$ emission similar to other galaxies. Schinnerer et al. (2000) report on very compact and strongly rotating $^{12}\text{CO}(2-1)$ gas near the centre but lack enough sensitivity (detection only within $\sim 3\sigma$) to exclude all doubts. The new observations independently support such a nuclear gas component within $\sim 4 - 5\sigma$. Also, the new observations indicate much clearer the ring structure of the $^{12}\text{CO}(2-1)$ line emission. The molecular gas masses are determined to $1.6 \times 10^9 M_\odot$ for the total gas mass, and to $\sim 2.5 \times 10^8 M_\odot$ for the gas mass of the inner ring.

12.3 HE 1029-1831

HE 1029-1831 is one of the closest known QSOs at a redshift of $z=0.039$ (corresponding to an angular size distance of 150 Mpc) and was included in the so called Cologne nearby QSO sample. It was first detected in CO with SEST and then mapped with the IRAM PdBI in all available configurations. HE 1029-1831 is rich in molecular gas ($M_{\text{gas}} = 7.6 \times 10^9 M_\odot$) which appears to be subthermally excited and cold (Krips et al., 2004c). Most of the emission can be associated with a bar that is clearly visible at optical wavelengths and only a very small fraction with the southern spiral arm. A striking velocity gradient across the bar is also found in the CO data indicating a bar driven gas inflow based on a model of Roberts et al. (1979).

12.4 3C48

3C48 is one of the first detected quasars and has evoked many studies due to its unusually large and bright host galaxy. This fact, the existence of a second bright compact component labeled 3C48A about $1''$ North-East to the QSO (Stockton & Ridgway 1991, Zuther et al. 2004), a tail-like extension to the North-West (Canalizo & Stockton 2000), and its richness in molecular gas (Scoville et al. 1993; Wink et al. 1997) are the main arguments leading to the conclusion that 3C48 might be the remnant of a recent merger event. Our new interferometric observations of the CO(1-0) line and mm continuum emission in the bright host galaxy around 3C48 give new evidences for a second nucleus and thus for the merger hypothesis (Krips et al. 2004c, 2005b). The 3.5 mm and 1.2 mm continuum emission reveal an extension towards 3C48A and as well a second one in elongation of the radio jet. Thus, 3 different sources are suggested to power the mm continuum - the QSO, 3C48A and a jet. Moreover, the CO(1-0)

line clearly shows two different velocity systems: a very compact one directly located on the QSO with a very steep velocity gradient in South-East to North-West direction, and a more extended one with a flatter velocity gradient perpendicular to the first and centered closer to 3C48A. The total integrated CO(1–0) emission is also in agreement with recent multi-particle simulations of the star and gas dynamics by using a setup similar to that one taken for the Antennae galaxies but seen from a different viewing angle (Scharwächter et al. 2004, PhD thesis of Scharwächter 2005). The simulations do not only propose a solution for the missing counter-tidal tail which would lie in this scenario just in front of the host galaxy and remain hence undetectable, but also predicts a northern gas tail and one in SouthWest direction as it is seen in the observed gas emission. Thus, a merger event in 3C48 becomes more and more likely.

12.5 Q0957+561

Q0957+561 is a well known gravitationally lensed system at a redshift of $z=1.41$ (Walsh et al. 1979). Based on additional interferometric PdBI observations, the CO(2-1) and 3mm continuum emission of Q0957+561 were reanalysed (Krips et al. 2004a,b,c). The emission in the CO(2-1) lines reveals a gas rich host galaxy with a peculiar double-peaked profile at one of the two lensed images. The new interferometric CO maps of the host galaxy agree well with HST images obtained by Keeton et al. (2000) and the double-peaked line profile is thus interpreted as two velocity components arising from rotating molecular gas in the disk of the host galaxy. This hypothesis is further supported by detailed simulations with a gravitational lensing program (Krips 2001).

12.6 Dense gas in 12 NUGA galaxies

IRAM 30m observations of the HCN emission in 12 galaxies from the NUGA core sample have been successfully conducted. In 7 galaxies, a significant amount of HCN could be detected in the central $\sim 20''$. A determination of the global ratio between the HCN(1–0) and CO(1–0) luminosity results in a value of ~ 0.2 on average. This is consistent with values found for other LINER and Seyfert galaxies (Curran et al. 2000; Curran et al. 2001). Furthermore, a strong correlation between the HCN luminosities, tracing the amount of dense gas, to the FIR luminosities, probing star formation, is found. The comparison of the star formation efficiency, i.e. the efficiency of the transformation of molecular gas into OB stars (Solomon et al. 1992), and the fraction of dense gas also results in a strong correlation. This is in excellent agreement with previous works by other groups (e.g. , Curran et al. 2001, Solomon et al. 1992). However, the 30m observations do not yet allow to analyse the distribution of the HCN with respect to the ^{12}CO emission. Thus, further IRAM PdBI observations are in preparation (see Section 12.8).

12.7 Radio emission in 7 NUGA galaxies

Radio snapshot observations of seven NUGA galaxies with MERLIN and VLBI at 18cm and 6cm were recently finished (Krips et al., 2004d, 2005c). Besides compact emission, also extended components such as jets are found. The data reveal an “onionskin”-like behaviour with respect to the fluxes: they decrease with increasing angular resolution indicating hence further extended emission. Most of the sources are found to have flat to inverted spectra of the radio core emission with only one exception showing a very steep spectrum. A comparison of the 6cm VLBI with published X-ray luminosities of the seven galaxies unveils a strong correlation between both values. This is not surprising since studies of HLAGN have already proven such a tight correlation. Previous studies of LLAGN have shown such a tendency but they were either based on observations with much lower angular resolution or contained not more than 3 objects or were conducted only at one frequency. Six of the seven NUGA galaxies from this radio sub-sample are sub-Eddington systems and fulfill thus the criterion for Radiatively Inefficient Accretion Flows (RIAFs), or more particular Advection Dominated Accretion Flows (ADAFs), as source for the non thermal radio emission. The tight correlation between the radio core and X-ray luminosities on the one hand, and a further

Name	Angular Size	Distance	Nuclear Type	$M_{\text{gas}} [10^8 M_{\odot}]$	Gas morphology	
NGC 3718	13 Mpc		LINER	1.9	~ 2.4	warped gas disk, large and small scale asymmetries
NGC 1068	14 Mpc		Seyfert 1		~ 16	2 spiral arms, bar and nuclear ring
HE 1029-1831	150 Mpc		QSO		~ 76	bar
3C48	850 Gpc		QSO		~ 400	two distinct kinematical gas reservoirs
Q0957+561	$1.9 h_{65}^{-1}$ Gpc ^a		Quasar		$\sim 500 h_{65}^{-2}$	disk

Table 12.1: Summary of all objects observed with the IRAM PdBI in the framework of this thesis. ^a Please note that in Chapter 9 a Hubble constant of $H_0 = 65 \text{ km s}^{-1} \text{ Mpc}^{-1}$ was used to be consistent with (Krips 2001, diploma thesis), while for the other sources $H_0 = 75 \text{ km s}^{-1} \text{ Mpc}^{-1}$ was used to be able to compare the results with other publications. Thus, a factor of $h_0 = H_0/65 \text{ km s}^{-1} \text{ Mpc}^{-1}$ has to be applied here, which is $h_0 \approx 1.2$ $H_0 = 75 \text{ km s}^{-1} \text{ Mpc}^{-1}$.

tight correlation between the radio core luminosity and black hole mass on the other hand agree in an excellent way with predictions from ADAF theory. However, as the extended emission in these objects also shows, ADAFs are not fully adequate to explain the radio emission in these galaxies. Therefore, combined ADAF-jet models have to be considered also for LLAGN as already proposed for HLAGN, their bigger brothers. This radio study nourishes the interpretation of LLAGN as scaled down HLAGN.

12.8 General remarks and future prospects

The IRAM PdBI observations of the NUGA core sample were recently finished but are not yet fully analysed, except in the cases of NGC 4826, NGC 7217 and NGC 3718. Thus, general conclusions for the NUGA sample remain speculative at this point. The first two objects have given rather evidence for a hampered accretion at the current epoch (García-Burillo et al. 2003, Combes et al. 2004), while the results for NGC 3718 are still consistent with and even support an ongoing accretion, at least at a radius of $\sim 200 \text{ pc}$. Also, in the case of NGC 1068, the apparent highly rotating nuclear gas component seen in the position-velocity diagrams might be interpreted as or at least associated with an accretion disk, even if this has still to be regarded as very speculative with the current information. Interestingly, NGC 1068 seems to have a “twin”, namely NGC 3147, within the NUGA sample (compare Fig. 6.8 and 3.2). Both have a larger spiral/ring structure as well as double peaked CO emission indicative for a ring in their nuclear region. Not only that the CO-morphologies of NGC 1068 and NGC 3147 are very similar, but they both reveal a turnover in the SEDs from cm to mm-wavelengths. It will be a matter of future work to find out to what extent this “twin-pair” is comparable. In particular, does NGC 3147 and also the other NUGA sources show signs for a strongly rotating nuclear component as well?

Based on the IRAM 30m results of the HCN emission and its low gas mass, NGC 3718 appears to represent rather the role of an outsider within the NUGA sample concerning its CO characteristics, on the one hand. On the other hand, besides NGC 1068, NGC 3147 and NGC 4579, it is one of the strongest radio emitter in the NUGA radio sub-sample. A possible but still speculative explanation for this “discrepancy” between low gas mass and “strong” radio emission might be that a gravitational interaction with its companion galaxy NGC 3729 induces an accretion onto the nucleus and thus nuclear activity but no material such as gas might be exchanged at the current epoch due to the distance between both galaxies (NGC 3729 is at a distance of 18 Mpc, i.e. 5 Mpc farther away than NGC 3718) so that the gas mass of NGC 3718 does not significantly change. However, compared to the QSOs/quasars in this study, the NUGA sources appear rather as gas-poor (Table 12.1). In this study, the gas masses increase significantly with redshift². Each of the two dynamical gas systems in 3C48, for instance,

²However, one has to keep in mind that only the brightest galaxies at higher redshift are observable. Objects comparable to NGC 3718 are



Figure 12.1: Artist images of ALMA and LOFAR (taken from the respective official homepages).

already contain 100 times more gas mass respectively than the entire galaxy NGC 3718. The difference in mass between Q0957+561 and 3C48 is, however, roughly the same but, of course, no conclusions can be drawn from this fact. Although the gas masses are comparable and both apparently host the same type of AGN, the two systems might, otherwise, differ significantly from each other. 3C48 is most likely a merger and the nature of Q0957+561 remains still a puzzle although its apparent gas disk makes it more “familiar” to less redshifted galaxies and could help to increase our knowledge about the evolution of these galaxies. However, more systems have to be detected and studied in CO at this redshift range of 1-2 to gain statistically relevant results. The nature of the mm-continuum emission in 3C48 has to be also investigated further, above all of the emission connected with the second apparent nucleus to disentangle between thermal dust emission and non thermal radio emission. The detection of a second transition of CO in 3C48 as well as in Q0957+561 would allow to reveal further gas properties and also to substantiate the previous findings of the two distinct gas systems in 3C48 or the double-peaked line towards the northern lensed image in Q0957+561.

Simulations are a powerful tool to gain new insights of and find further answers for the complexity of the observed properties in the galaxies studied in this PhD thesis, such as the strongly rotating nuclear component in NGC 1068. Previous models (e.g., Schinnerer et al. 2000) did not account for this feature. Further, detailed simulations of the barred CO distribution in HE 1029-1831 would also help to increase the understanding of the gas kinematics in this system.

So far, only snap-shot observations of seven NUGA galaxies were carried out with EVN and MERLIN. For the most interesting sources, such as NGC 2782 for instance, higher sensitivity observations are a logical next step. For the remaining NUGA sources, which were not yet observed in their radio emission, snap-shot observations have still to be carried out. Besides the continuum emission, the study of the HCN emission in the NUGA galaxies is not yet finished and needs interferometric maps to enable a more detailed comparison between the rather lower gas density regions traced by CO and the denser gas regions measured via HCN.

Many of these studies can be carried out with current instruments, such as the IRAM PdBI, VLBI but also new instruments such as the Sub-Millimeter Array (SMA) in Hawaii. The latter provides the possibility to observe at sub-millimeter frequencies and so higher transitions of CO, for instance. The NUGA project could thus gain new information of the gas properties, i.e. of hotter gas components, and so better separate starburst from nuclear activity. Another useful array which will start its operation most likely next year is the new CARMA array being the merger of the old OVRO and BIMA interferometers. It will be a direct concurrent to the IRAM PdBI for the next years in the northern hemisphere. ALMA, the Atacama Large Millimeter Array in Chile (Fig. 12.1), covering the southern hemisphere, will be also accesible in the next ~ 5 years. The work of this PhD thesis can be regarded as basis for future, possible projects with ALMA that will provide a huge jump in terms of angular

not detectable with current instruments at a redshift similar to Q0957+561 for instance

resolution ($\sim 0.01''$) and sensitivity (in total 64 antennae of 12m-diameter are planned). It will also cover a much larger frequency range - from $350\mu\text{m}$ to 10mm - than any other current mm-/submm-interferometer. At the radio domain, i.e. at cm-wavelengths, new challenging instruments are in preparation as well, such as the SKA, the Square Kilometer Array, and the european pendant LOFAR (Fig. 12.1), meaning LOw Frequency ARray. They both will operate at frequencies below 250 MHz with a large bandwidth enabling for instance to search for the turnover frequency in radio jet spectra. These outstanding future instruments will allow to further unpuzzle the nature of active galaxies in general and also to give answer to questions which cannot be settled with the current technology at cm-, mm- and submm-wavelengths.

Appendix

Appendix A

Warps

How warps can be modelled will be briefly discussed in this section including the main assumptions. The description used by Quillen et al. (1993) will thereby be taken. The gas disk with inclination ϑ (Fig. A.1) is here divided into several rings of which some are inclined out of the disk plane by another angle $\omega(r)$ assuming that the gas in the respective rings rest on circular orbits and the rings do not intersect with each other. This produces a warp that changes through precession of an angle $\alpha(r)$. Following Quillen et al. (1993), i.e. assuming a elliptical, galactical potential which is spherically-symmetric, $\alpha(r)$ is determined by the following equation:

$$\frac{d\alpha(r, t)}{dt} = \left(1 - \frac{1}{q}\right) \frac{v(r)}{r} \quad (\text{A.1})$$

$$= \text{constant in time} \quad (\text{A.2})$$

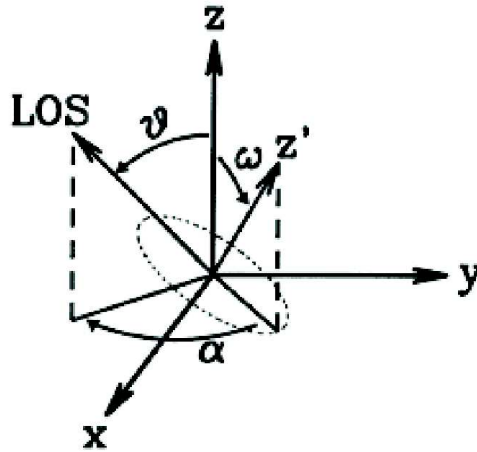


Figure A.1: The coordinate system describing the basic parameters for the tilted-ring model. X, and Y are referred to the galactic plane. ϑ is the inclination of the reference ring while ω represents the angle about which a ring at radius r is tilted out of the galactic plane. LOS means Line-Of-Sight. Figure taken from Quillen et al. (1993).

where $v(r)$ denotes the rotation curve of the gas disk, i.e. $\frac{v(r)}{r}$ is equivalent to the angular velocity, and q is the ratio of the axis in the potential. Integrating yields

$$\alpha(r, t) = \left(1 - \frac{1}{q}\right) \frac{v(r)}{r} \times t + \alpha_0 \quad (\text{A.3})$$

(A.4)

By given initial $\omega(r)$, $v(r)$ and intensity distribution $I(r)$ and by variation of $\left(1 - \frac{1}{q}\right) \cdot t$ and α_0 , the warp can be modelled. The function $\omega(r)$ is generally defined with a finite number of rings, i.e. discretely sampled. The points within two rings are then linearly interpolated.

Appendix B

Emission processes in the radio and X-ray domain

In this chapter, the main process of the non-thermal emission at radio and X-ray wavelengths will be briefly summarized. A more detailed description can be found in Harwit (2000).

B.1 Synchrotron radiation

Synchrotron radiation is produced by a charged particle (e.g., electron) that moves at relativistic velocities across a magnetic field. Assuming the particle orbit to be in the plane perpendicular to the magnetic field lines (Fig. B.1), the Lorentz force can be transformed into

$$\Delta p_y = \frac{evB}{c} \Delta t_0 \quad (\text{B.1})$$

with p_y being the relativistic momentum in y -direction, e the charge of the electron, v the velocity and c the speed of light. With

$$p_x = \frac{m_0 v}{\sqrt{1 - \frac{v^2}{c^2}}} \quad (\text{B.2})$$

(m_0 is the particle's rest mass) the angular deflection during time interval Δt_0 can be calculated via

$$\delta = \frac{\Delta p_y}{p_x} \quad (\text{B.3})$$

$$= \frac{eB}{m_0} \sqrt{1 - \frac{v^2}{c^2}} \Delta t_0 \quad (\text{B.4})$$

$$= \frac{eB \Delta t_0}{m_0 c \gamma(v)} \quad (\text{B.5})$$

To obtain the gyrofrequency ω_g , δ must be 1, i.e.

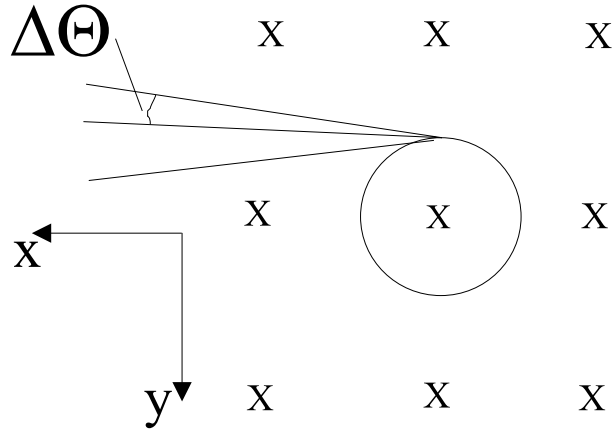


Figure B.1: Orbit of a relativistic charged particle in a magnetic field. The direction of the magnetic field lines is into the paper.

$$\omega_g = \frac{1}{\Delta t_0} \quad (\text{B.6})$$

$$= \frac{eB}{m_0 c} \gamma(v)^{-1} \quad (\text{B.7})$$

Considering relativistic effects (in time *and* space; i.e. highly relativistic particles ($v/c \simeq v^2/c^2$)), the time interval Δt at the observer's rest frame will be different from Δt_0 , i.e.

$$\Delta t = \left(1 - \frac{v}{c}\right) 2\gamma(v)^{-1} \Delta t_0 \quad (\text{B.8})$$

$$\simeq \gamma(v)^{-2} \Delta t_0 \quad (\text{B.9})$$

$$(\text{B.10})$$

This results in the maximum frequency of the synchrotron radiation,

$$\omega_m = \gamma(v)^2 \omega_g \quad (\text{B.11})$$

$$(\text{B.12})$$

The spectrum of the synchrotron radiation (of monenergetic electrons) will be a composite of very thin lines at high harmonics of the gyrofrequency. Ginzburg & Syrovatskii (1964) and Shklovskii (1960) provide a relation for the emitted energy

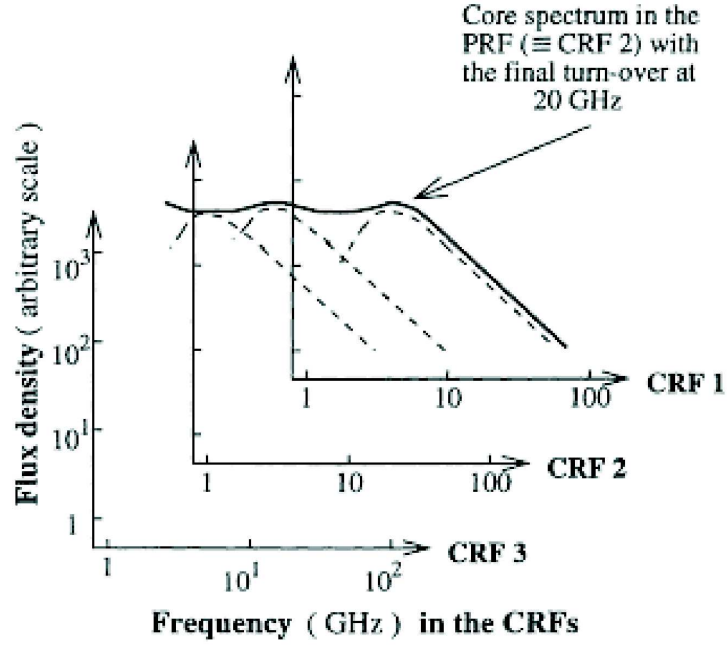


Figure B.2: Model of a flat core spectrum in the cosmological rest frame (CRF) and plasma rest frame (PRF). The core spectrum is marked by the thick solid line being the superposition of the individual synchrotron spectra at different frequencies. The 3 cosmological rest frames CRFs1,2, and 3 are Doppler shifted by factors of 0.2, 1 and 5, with respect to the plasma rest frame. Image taken from Athreya et al. (1997).

$$P(\nu, \epsilon) = 2\pi P(\omega, \epsilon) \quad (\text{B.13})$$

$$= \frac{16e^3 B}{m_0 c^2} p\left(\frac{\omega}{\omega_m}\right) \quad (\text{B.14})$$

$$p\left(\frac{\omega}{\omega_m}\right) \propto \left(\frac{\omega}{\omega_m}\right)^{1/3}, \quad \omega \ll \omega_m \quad (\text{B.15})$$

$$p\left(\frac{\omega}{\omega_m}\right) \propto \left(\frac{\pi\omega}{\omega_m}\right)^{1/2} \exp\left(-\frac{2\omega}{3\omega_m}\right), \quad \omega \gg \omega_m \quad (\text{B.16})$$

$$(\text{B.17})$$

where ϵ is the energy of the particle. Fig. B.2 indicates the expected Spectral Energy Distribution (SED).

Active galaxies often reveal different types of radio emission. Extended jets and lobes and also compact cores can be identified. While the first are associated with optically thin synchrotron emission, having thus steep spectra (i.e. $f_\nu \propto \nu^{-1}$ and lying in general at frequencies above ν_m), the core emission is correlated with optically thick synchrotron emission. Thus, the fluxes follow rather a flat to inverted spectrum and also self-absorption processes have to be considered. However, also relativistic effects can simulate such a flat spectrum. This is illustrated in Fig. B.2. One has to take into account different rest frames for the emitting plasma, i.e. the frequencies of each individual emitting cosmological rest frame of the source (crf) are Doppler shifted in the plasma rest frame (prf). Thus, the composite of the respective spectra yield a flat spectrum.

B.2 Compton scattering

Compton scattering takes place when a high-energy photon is scattered by a charged particle (e.g., electron). If a highly energetic particle transfers momentum to a low-energy photon, the process is called inverse Compton scattering. Both processes are equivalent.

Assuming 1.) conservation of mass-energy, i.e.

$$m_0c^2 + h\nu = m_0\gamma v c^2 + h\nu' \quad (\text{B.18})$$

with h the Planck constant and the other values as defined above, 2.) conservation of momentum along the direction of the incoming photon

$$\frac{h\nu}{c} = \frac{h\nu'}{c} \cos(\theta) + m_0\gamma(v)v \cos(\Phi) \quad (\text{B.19})$$

and 3.) the same for the transverse momentum

$$0 = \frac{h\nu'}{c} \sin(\theta) - m_0\gamma(v)v \sin(\Phi) \quad (\text{B.20})$$

one finds with $\lambda = c/\nu$, and $\lambda' = c/\nu'$, that

$$\lambda' - \lambda = 2 \frac{h}{m_0c} \sin\left(\frac{\theta}{2}\right) \quad (\text{B.21})$$

For inverse Compton scattering this changes to

$$\lambda' = 2 \frac{h}{m_0c} \sin\left(\frac{\theta}{2}\right) + \lambda_D \quad (\text{B.22})$$

$$\lambda_D = \lambda \sqrt{\frac{c-v}{c+v}} \quad (\text{B.23})$$

Then, the back-scattered photon ($\theta = 180^\circ$) will have (from a stationary reference system) a wavelength λ_s of

$$\lambda_s = 2 \frac{h}{m_0c} \sqrt{\frac{c-v}{c+v}} + \lambda \left(\frac{c-v}{c+v} \right) \quad (\text{B.24})$$

While Compton scattering at optical wavelengths does not significantly contribute to the emission, it has to be considered at X-rays where it amounts to 10% (for an electron $\frac{h}{m_0c} = 2.4 \times 10^{-10}$ cm; X-rays are at 5×10^{-9} cm).

The cross section of a Compton scattering process has to be calculated with the Klein-Nishina formula depending the classical electron radius $r_e = \frac{e^2}{m_0c^2}$ and the ratio of the photon to electron energy $\alpha = \frac{h\nu}{m_0c^2}$. For low energies, this equation can be approximated by

$$\sigma_c = \sigma_e (1 - 2\alpha + O(\alpha^2)), \quad \alpha \ll 1 \quad (\text{B.25})$$

i.e., becomes at very low energy equal to the Thomson cross section $\sigma_e = \frac{8\pi}{3} r_e^2$. For high energies, one finds

$$\sigma_c = \frac{3}{8} \sigma_e \frac{1}{\alpha}, \quad \alpha \ll 1 \left(\ln(2\alpha) + \frac{1}{2} \right) \quad (\text{B.26})$$

Appendix C

Velocity channel maps of HE1029-1831

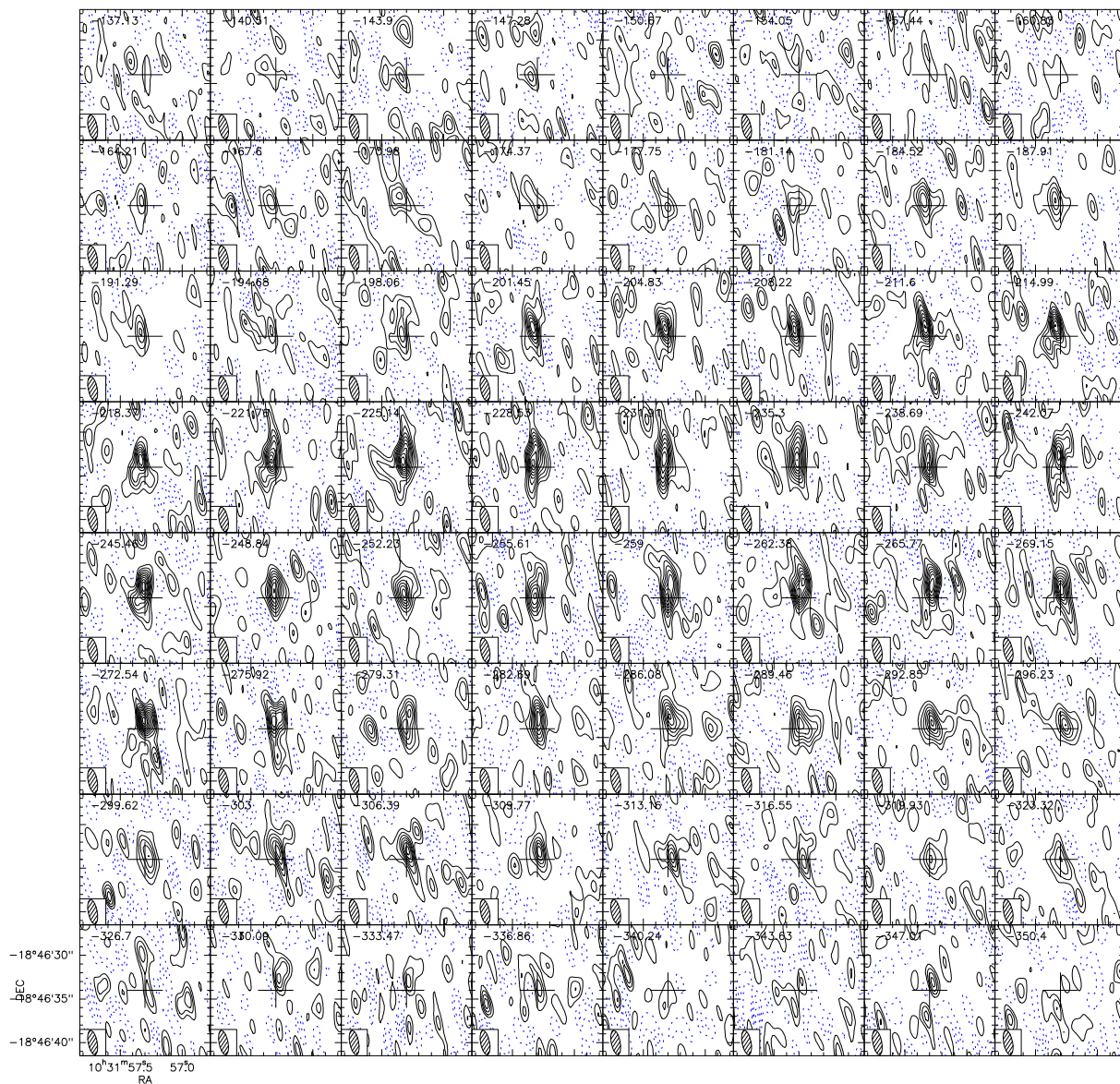


Figure C.1: Velocity channel maps of the CO(1–0) line emission in HE 1029-1831. Contours are in steps of $1\sigma=6\text{mJy}$. The synthesized beam is shown in the lower left corners.

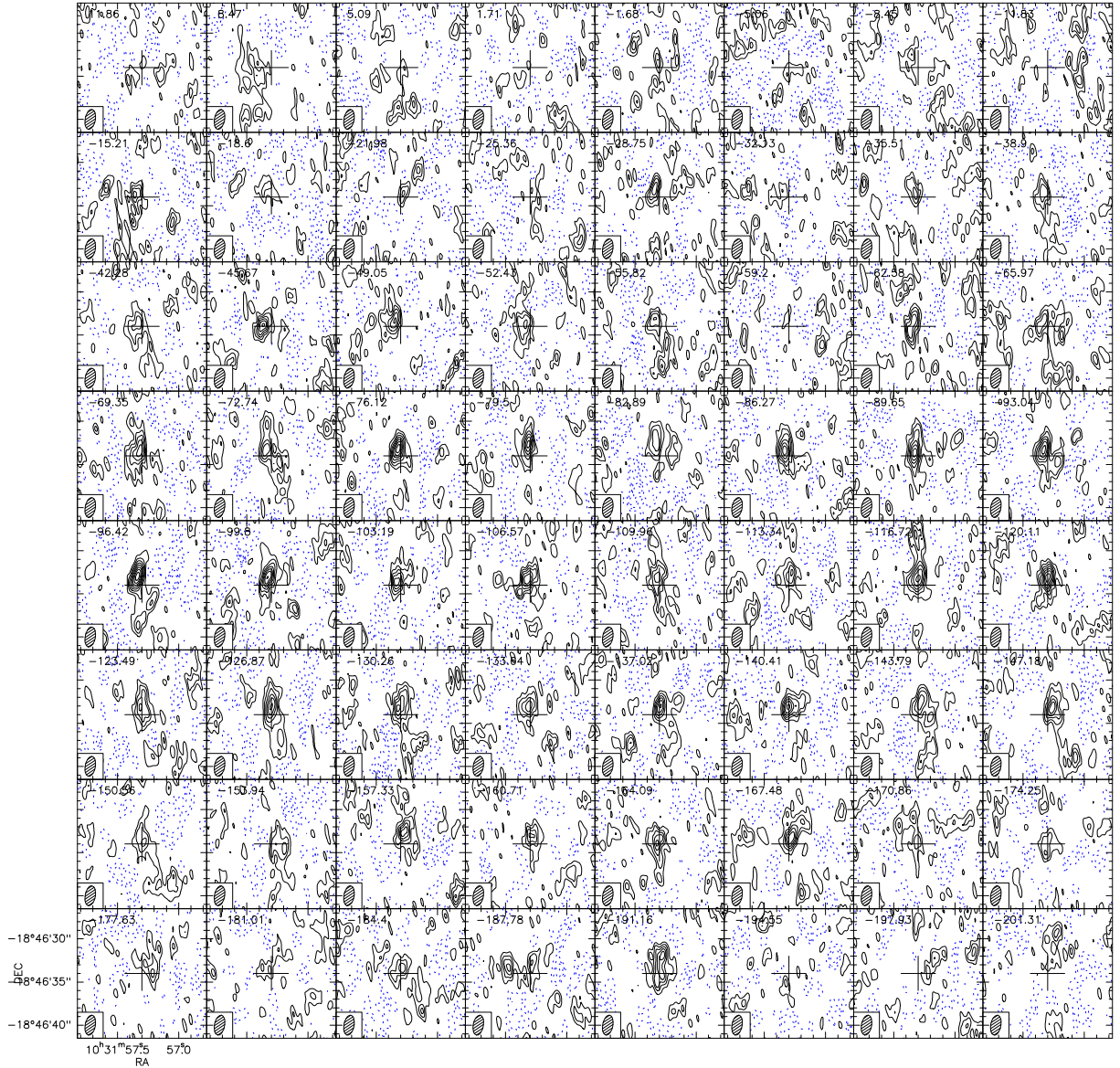


Figure C.2: Velocity channel maps of the CO(2-1) line emission in HE 1029-1831. Contours are in steps of $1\sigma=18\text{mJy}$. The synthesized beam is shown in the lower left corners.

Appendix D

HCN and $^{12}\text{CO}(1-0)$ spectra of the NUGA core sample

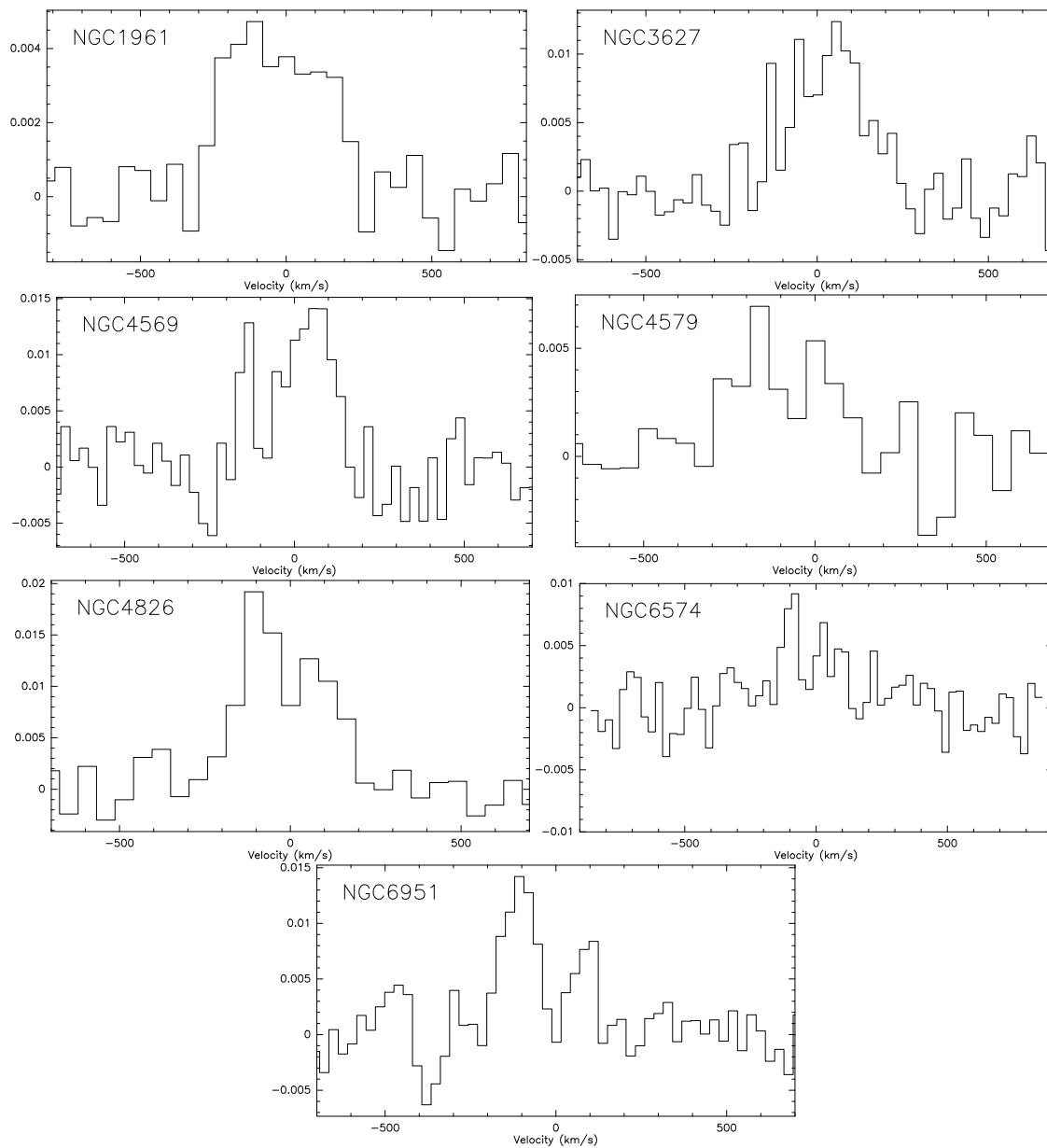


Figure D.1: Central HCN(1-0) spectra of the 6 NUGA sources observed with the IRAM 30m telescope. The y-axis is in units of T_a^* ; HPBW=27.5''

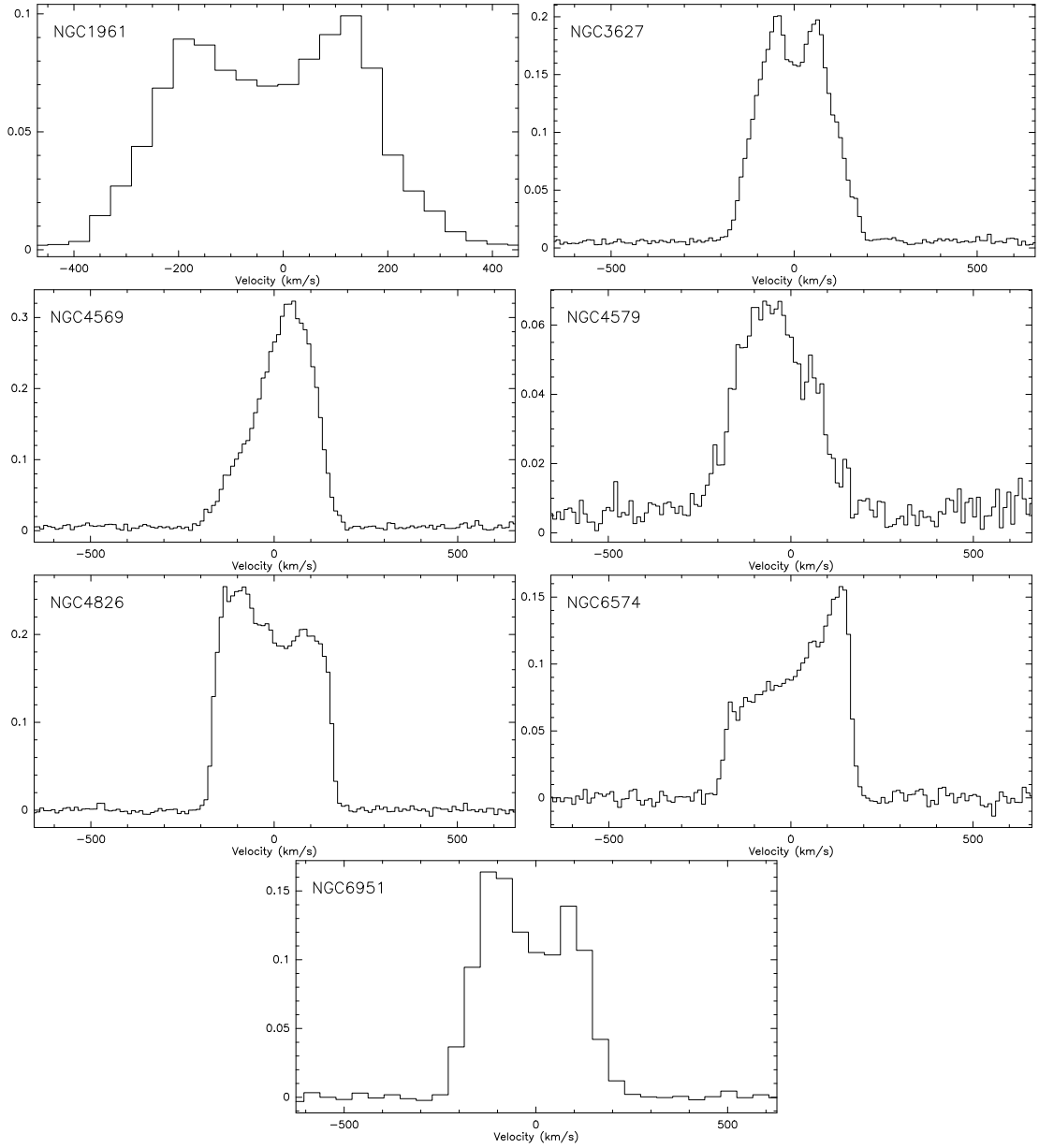


Figure D.2: "Global" $^{12}\text{CO}(1-0)$ spectra of the 6 NUGA sources observed with the IRAM 30m telescope. All $^{12}\text{CO}(1-0)$ spectra were summed up and averaged. The y-axis is in units of T_{mb} ; HPBW=21''

Bibliography

- [1] Almaini, O. & Fabian, A.C., 1997, MNRAS, 288, 19
- [2] Aitken, D.K., Greaves, J., Chrysostomou, A., Jenness, T., Holland, W., Hough, J.H., Pierce-Price, D., and Richer, J., 2000, ApJ, 534, 173
- [3] Andreani, P., Cimatti, A., Loinard, L., 2000, A&A 354, L1
- [4] Angonin-Willaime, M.-C., Soucail, G., Vanderriest, C., 1994, A&A, 291, 411
- [5] Antonucci, R.R.J. & Miller, J.S., 1985, ApJ, 297, 621
- [6] Athreya, R.M., Kapahi, V.K., McCarthy, P.J., van Breugel, W., 1997, MNRAS, 289, 525
- [7] Bahcall, J.N., Kirhakos, S., Saxe D.H., Schneider, D.P., 1997, ApJ, 479, 642
- [8] Baker, J., 1998, AAS, 193 (5706), Vol. 30, p.1333
- [9] Ball, G.H., Narayan, R., and Quataert, E., 2001, ApJ, 552, 221
- [10] Barkana, R., Lehár, J., Falco, E.E., Grogin, N.A., Keeton, Ch.R., Shapiro, I.I., 1999, ApJ, 520, 479
- [11] Barth, A. J., Ho, L. C., Filippenko, A. V., Sargent, W. L. W., 1998, ApJ 496, 133
- [12] Beasley, A.J. & Conway, J.E., 1995, in ASP Conf. Ser. 82, Very Long Baseline Interferometry and the VLBA, ed. J.A. Zensus, P.J. Diamond & Napier (San Francisco: ASP), 327
- [13] Becker, T. & Duschl, W.J., 1997, A&A, 328, 95
- [14] Bernstein, G.M., Fischer, P., Tyson, J.A., Rhee G., 1997, AJ, 483, L79
- [15] Blandford, R.D., 1993 in Astrophysical Jets, ed. D. Burgerella, M. Livio & C.P. O’Dea (Cambridge Univ. Press), 15
- [16] Blandford, R.D. & Begelman, M.C. 1999, MNRAS, 303, 1
- [17] Bower, G.C., Wright, M.C.H., Falcke, H., and Backer, D.C., 2003, ApJ, 588, 331
- [18] Bradley, M.P., "An Introduction to Active Galactic Nuclei", Cambridge University Press
- [19] Burke, B. F., Miley, G. K., 1973, A&A 28, 379
- [20] Canalizo, G. & Stockton, A., 2000, ApJ 528, 201
- [21] Casoli, F., Dickey, J., Kazes, I., Boselli, A., Gavazzi, G., and Jore, K., 1996, A&AS, 116, 193
- [22] Chae, K.-H., 1999, ApJ, 524, 582

- [23] Chartas, G., Chuss, D., Forman, W., Jones, C., Shapiro, I., 1998, *ApJ*, 504, 661
- [24] Collin, S. & Huré, J.-M., 2001, *A&A*, 372, 50
- [25] Combes, F., 1988, in *Galactic and Extragalactic Star Formation*, ed. Pdriz & Fich (Dordrecht: Kluwer), 475
- [26] Combes, F., Boisseé, Mazure, A., and Blanchard, A., 1995, "Galaxies and Cosmology", *A&A Library*, Springer Verlag, Berlin Heidelberg
- [27] Combes, F., García-Burillo, S., Boone, F. et al., 2004, *A&A* 414, 857
- [28] Downes, D., Solomon, P.M. & Radford, S.J.E., 1993, *ApJ* 414, L13-L16
- [29] Downes, D. & Solomon, P.M., 1998, *ApJ* 507, 615
- [30] Duric, N. & Seaquest, E.R., 1986, *CaJPH* 64, 531
- [31] Duschl, W.J., Strittmatter, P.A. & Biermann, P.L., 2000, *A&A* 357, 1123
- [32] Eckart, A. & Downes D., 2001, *ApJ* 551, 730
- [33] Eckart, A., Schödel, R., and Straubmeier, Ch., 2004, "The Exploration of the Supermassive Black Hole at the center of the Milky Way" (manuscript), to appear in Imperial College Press, London
- [34] Evans, S.A., Mazzarella, J.M., Surace, J.A. & Sanders, D.B., 2002, *ApJ* 580, 749
- [35] Eisenhauer, F., Schödel, R., Genzel, R., Ott, T., Tecza, M., Abuter, R., Eckart, A., and Alexander, T., 2003, *ApJ*, 597, 121
- [36] Fabbiano, G., Kim, D.-W. & Trinchieri, G., 1992, *ApJ* 80, 531
- [37] Falcke, H., 1996, *ApJ* 464, L67
- [38] Falcke, H., Nagar, N.M., Wilson, A.S. et al., 2000a, *ApJ* 267, L5
- [39] Falcke, H. & Markoff, S., 2000b, *A&A* 362, 113
- [40] Falcke, H., Lehar, J., Barvainis, R., Nagar, N.M., Wilson, A.S., 2001, in *ASP Conf. Ser. 224, Probing the Physics of Active Galactic Nuclei*, ed. B.M. Peterson, R.W. Pogge, and R.S. Polidan (San Francisco: Astronomical Society of the Pacific), 265
- [41] Falcke, H., Lehar, J., Barvainis, R., Nagar, N.M. & Wilson, A.S., 2001, in *ASP Conf. Ser. 224, Probing the Physics of Active Galactic Nuclei by Multiwavelength Monitoring*, ed. B.M. Peterson, R.S., Polidan & R.W. Pogge (San Francisco: ASP), 265
- [42] Falco, E.E., Gorenstein, M.V., Shapiro, I.I., 1985, *ApJ*, 289, L1
- [43] Ferrarese, L. & Merritt, D., 2000, *ApJ*, 539, 9
- [44] Filippenko, A.V., Sargent, W.L.W., 1985, *ApJS* 57, 503
- [45] Francis, P.J., Hewett, P.C., Foltz, C.B., Chaffee, F.H., Weymann, R.J., and Morris, Simon L., 1991, *ApJ*, 373, 465
- [46] Gallimore, J.F.; Baum, S.A., and O'Dea Ch.P., 1996, *ApJ*, 458, 136
- [47] Gallimore, J.F.; Baum, S.A., and O'Dea Ch.P., 2004, *ApJ*, 613, 794
- [48] García-Burillo, S., Sempere, M.J., Combes, F., Hunt, L.K., Neri, R., 2000 *A&A* 363, 869

- [49] García-Burillo, S., Combes, F., Eckart, A., et al., 2003a, in *Active Galactic Nuclei: From Central Engine to Host Galaxy*, ed. S. Collin, F. Combes & I. Shlosman, ASP Conf. Ser., 290, 423
- [50] García-Burillo, S., Combes, F., Hunt, L.K., Boone, F. et al., 2003b, *A&A* 407, 485
- [51] Gao, Yu, Lo, K. Y., Lee, S.-W., & Lee, T.-H., 2001, *ApJ* 548, 172
- [52] Gebhardt, K., Bender, R., Bower, G., Dressler, A., Faber, S.M.; Filippenko, A.V.; Green, R., Grillmair, C., Ho, L.C.; Kormendy, J., Lauer, T.R., Magorrian, J., Pinkney, J., Richstone, D., and Tremaine, S., 2000a, *ApJ*, 539, 13
- [53] Gebhardt, K., Kormendy, J., Ho, L.C., Bender, R., Bower, G., Dressler, A., Faber, S.M., Filippenko, A.V., Green, R., Grillmair, C., et al., 2000, *ApJ*, 543, 5
- [54] Genzel, R., Schdel, R., Ott, T., Eisenhauer, F., Hofmann, R., Lehnert, M., Eckart, A., Alexander, T., Sternberg, A., Lenzen, R., Clénet, Y., Lacombe, F., Rouan, D., Renzini, A., and Tacconi-Garman, L. E., 2003a, *ApJ*, 594, 812
- [55] Genzel, R., Baker, A.J., Tacconi, L.J., Lutz, D., Cox, P., Guilloteau, St., and Omont, A., 2003b, *ApJ*, 584, 633
- [56] Graham, J.R., Matthews, D.P., Neugebauer, G., Soifer, B.T. & Wilson, T.D. 1990, *ApJ* 354, L5
- [57] Greenhill, L.J., Gwinn, C.R., 1997, *Ap&SS*, 248, 261
- [58] Greenstein, J.L. & Schmidt, M., 1964, *ApJ*, 140, 1
- [59] Grogin, N.A., Narayan, R., 1996, *ApJ*, 464, 92
- [60] Groves, B.A., Cecil, G., Ferruit, P., Dopita, M.A., 2004, *ApJ*, 611, 786
- [61] Guesten, R., Genzel, R., Wright, M. C. H., Jaffe, D. T., Stutzki, J., Harris, A. I., 1987, *ApJ* 318, 124
- [62] Guilloteau, S., Delannoy, J., Downes, D., et al. 1992, *A&A* 262, 624
- [63] Guilloteau, S. & Lucas, R. 2000, in *Imaging at Radio Through Submillimeter Wavelengths*, ed. J. G. Mangum & S. J. E. Radford (San Francisco: ASP), 299
- [64] Haas, M., Mller, S.A.H., Bertoldi, F., Chini, R., Egner, S., Freudling, W., Klaas, U., Krause, O., Lemke, D., Meisenheimer, K., Siebenmorgen, R., and van Bemmell, I., 2004, *A&A*, 424, 531
- [65] Hartwich, M., Eckart, A., Leon, S., 2002, *AGM* 18, P136
- [66] Harwit, M., 200, *Astrophysical Concepts*, Astronomy and Astrophysics Library, Springer
- [67] Harvanek, M., Stocke, J.T., Morse, J.A., Rhee, G., 1997, *AJ*, 114, 2240
- [68] Heckmann, T.M., Smith, E.P., Baum, S.A., van Breugel, W.J.M., Miley, G.K. et al., 1986, *ApJ* 311, 526
- [69] Heckman, T.M., Blitz, L., Wilson, A.S., Armus, L., and Miley, G.K., 1989, *ApJ*, 342, 735
- [70] Helfer, T.T. & Blitz, L., 1997, *ApJ*, 478, 162
- [71] Ho, L.C., 1999a, *ApJ* 516, 672
- [72] Ho, L.C., 1999b, *Observational Evidence for the Black Holes in the Universe*, Conference held at Calcutta, January 11-17th, 1998, p.157

- [73] Hummel, E., van Gorkom, J.H., Kontanyi, C.G., 1983, ApJ 267, L5
- [74] Hummel, E. & van der Hulst, J. M., 1986, A&A 155, 151
- [75] Irwin, J.A. & Seaquest, E.R., 1988, ApJ 335, 658
- [76] Igumenshchev, I.V., Chen, X., and Abramowicz, M.A., 1996, MNRAS, 278, 236
- [77] Igumenshchev, I.V. & Abramowicz, M.A., 1999, MNRAS, 303, 309
- [78] Igumenshchev, I.V. & Abramowicz, M.A., 1999, ApJS, 130, 463
- [79] Jorstad, S.G., Marscher, A.P., Mattox, J.R., Wehrle, A.E., Bloom, S.D., Yurchenko, A.V., 2001, ApJS, 134, 181
- [80] Kaldare, R., Colless, M., Raychaudhury, S., and Peterson, B.A., 2003, MNRAS, 339, 652
- [81] Kaspi, S., Smith, P.S., Netzer, H., Maoz, D., Jannuzi, B.T., and Giveon, U., 2000, ApJ, 533, 631
- [82] Khachikian, E.Y., Weedman, D.W., 1974, ApJ, 192, 581
- [83] Keene, J., Stern, D., Lawrence, C., Eisenhardt, P., Gorjian, V., Stapelfeldt, K., Werner, M., and Charmandaris, V., 2004, AAS, 204, 4122 (see also: <http://www.spitzer.caltech.edu/Media/releases/ssc2004-09/release.shtml>)
- [84] Keeton, C.R., Falco, E.E., Impey, C.D., et al., 2000, ApJ 542, 74
- [85] Kellermann, K.I. & Pauliny-Toth, I.I.K., 1981, ARA&A, 19, 373
- [86] Kenney, J.D. & Young, J.S., 1988, ApJS, 66, 61
- [87] Kneib, J-P., Alloin, D., Pelló, R., 1998, A&A, 339, L65
- [88] Kohno, K., Kawabe, R., Vila-Vilaró, B. 1999, ApJ 511, 157;
- [89] Kohno et al. 2002, astro-ph/0206398;
- [90] Kohno et al. 2003 PASJ 55 L1;
- [91] Kormendy, J. & Richstone, D., 1995, ARA&A, 339, L65
- [92] Kormendy, J. & Bender, R., 1999, ApJ 522, 772
- [93] Kormendy, J. & Gebhardt, K., 2001, AIPC, 586, 363
- [94] Krichbaum, Th., Alef, W., Witzel, A., Zensus, J.A., Booth, R.S., Greve, A., and Rogers, A.E.E., 1998, A&A, 329, 873
- [95] Krips, M., diploma thesis at University of Cologne, "The gravitationally lensed quasar at millimeter wavelengths"
- [96] Krips, M., Pott, J.-U., Eckart, A., Leon, S., Neri, R., Straubmeier, C., 2003, Ap&SS 284, 511
- [97] Krips, M., Neri, R., Eckart, A., Downes, D., Martín-Pintado, J., and Planesas, P., 2004a, accepted for publication in A&A, astro-ph/0411138
- [98] Krips, M., Neri, R., Eckart, A., Martín-Pintado, J., Planesas, P. and Colina L. 2004, "The quasar Q0957+561: Lensed CO emission from a disk at $z \sim 1.4$?", appeared in "Proceedings of the 4th Cologne-Bonn-Zermatt-Symposium", ed. S. Pfalzner, C. Kramer, C. Straubmeier, and A. Heithausen (Springer Verlag Berlin Heidelberg), p.23-26

- [99] Krips, M., Eckart, A., Neri, R., Pott, J.-U., Zuther, J., Scharwächter, J. and Bertram, Th., “Feeding monsters - a study of active galaxies”, in “Dense Molecular Gas around Protostars and in Galactic Nuclei”, Eds. Y.Hagiwara, W.A.Baan, H.J.van Langevelde, 2004, a special issue of ApSS, Kluwer, in press
- [100] Krips, M., Eckart, A., Neri, R., Pott, J.-U., Combes, F. and García-Burillo, S., 2004d, “Active galaxies - parsec scale radio emission and the surrounding ISM”, in “The Interplay among Black Holes, Stars and ISM in Galactic Nuclei”, Proceedings of IAU Symposium, No. 222, eds. Th. Storchi-Bergmann, L.C. Ho & H.R. Schmitt, in press
- [101] Krips, M., Eckart, A., Neri, R., Pott, J.U., Leon, S., Combes, F., García-Burillo, S., Hunt, L.K., Baker, A.J., Tacconi, L.J., Englmaier, P., Schinnerer E., and Boone F., 2005a, “Molecular Gas in Nuclei of GALaxies (NUGA) III. The warped LINER NGC 3718”, submitted to A&A
- [102] Krips, M., Eckart, A., Neri, R., Zuther, J., Downes, D., and Scharwächter, J., 2005c, “Gas and continuum emission in 3C48: Evidences for two merger nuclei?”, almost ready for submission
- [103] Krips, M., Eckart, A., Pott, J.-U., Leon, S., Neri, R., García-Burillo, S., Combes, F., Boone F., Hunt, L.K., Baker, A.J., Tacconi, L.J., Schinnerer E., and Englmaier, P., 2005d, “Radio emission in 7 NUGA sources”, in prep.
- [104] Krolik, J.H. & Kallman, T.R., 1987, ApJ, 320, 5
- [105] Kundic, T., Turner, E.L., Colley, E.N. et al., 1997, ApJ, 482, 75
- [106] van der Laan, H. & Perola, G.C., 1969, A&A, 3, 468
- [107] Ma, C., Arias, E. F., Eubanks, T. M., Fey, A. L., Gontier, A.-M., Jacobs, C. S., Sovers, O. J., Archinal, B. A., Charlot, P. 1998, AJ 116, 516
- [108] Magorrian, J., Tremaine, S., Richstone, D., Bender, R., Bower, G., Dressler, A., Faber, S.M., Gebhardt, K., Green, R., Grillmair, C., Kormendy, J., and Lauer, T., 1998, AJ, 115, 2285
- [109] Martini, P. & Pogge, R.W., 1999, AJ, 118, 2646
- [110] Matthews, T.A., Bolton, J.G., Greenstein, J.L., Munch, G. & Sandage, A.R., 1961, Sky and Telescope 21, 148
- [111] Mediavilla, E., Serra-Ricart, M., Oscoz, A., et al., 2000, ApJ 531, 635
- [112] Meisenheimer, K., Haas, M., Müller, S.A.H., Chini, R., Klaas, U. & Lemke D., 2001, A&A 372, 719
- [113] Meixner, M., Pulchasky, R., Blitz, L., Wright, M., and Heckman, T., 1990, ApJ, 354, 158
- [114] Melia, F. & Falcke, H., 2001, ARA&A, 39, 309
- [115] Miller, J.S. & Antonucci, R.R.J, 1983
- [116] Mirabel, I. F., Vigroux, L., Charmandaris, V., Sauvage, M., Gallais, P., Tran, D., Cesarsky, C., Madden, S. C., Duc, P.-A., 1998, A&A 333, 1
- [117] McElroy, D.B., 1995, ApJSS 100, 105
- [118] Nagar, N.M., Falcke, H., Wilson, A.S. & Ho, L.C., 2000, ApJ 542, 186
- [119] Nagar, N.M., Wilson, A.S. & Falcke, H., 2001, ApJ 559, L87
- [120] Nagar, N. M., Falcke, H., Wilson, A. S., Ulvestad, J. S., 2002, A&A, 392, 53

- [121] Narayan, R., Yi, I., and Mahadevan, R., 1995, *Nature*, 374, 623
- [122] Narayan, R., Mahadevan, R. & Quataert, E., 1998, in *Theory of Black Hole Accretion Disks*, ed. M.A. Abramowicz, G. Björnsson & J.E. Pringle (Cambridge: Cambridge Univ. press.), 148
- [123] Narayan, R., Igumenshchev, I.V., and Abramowics, M.A., 2000, *ApJ*, 539, 798
- [124] Neff, Susan G. & Ulvestad, James S., 2000, *AJ* 120, 670
- [125] Nelson, C.H., 2000, *ApJ* 544, 91
- [126] Netzer, H. & Peterson, B.M., 1997, *Astronomical Time Series*, Eds. Maoz, D., Sternerber, A., and Leibowitz, (Dordrecht: Kluwer), p.85
- [127] Norris, R.P., 1985, *MNRAS* 216, 701
- [128] Papadopoulos, P., Ivison, R. et al., 2001, *Nature* 409, 58
- [129] Pedlar, A., Kukula, M.J., Longley, D.P.T., et al., 1993, *MNRAS* 263, 471
- [130] Perley, R.A., Dreher, J.W., and Cowan, J.J., 1984, *ApJ*, 285, 35
- [131] Perley, R.A., Schwab, F.R., and Bridle, A.H., 1994, *A.S.P. Conf. Ser.*, Vol. 6, *Synthesis Imaging in Radio Astronomy*
- [132] Planesas, P., Martín-Pintado, J., Neri, R., Colina L., 1999, *Science*, 286, 2493 (P99)
- [133] Pott, J.-U., Hartwich, M., Eckart A., Leon. S., Krips, M., Straubmeier, Ch., 2004, *A&A* 415, 27
- [134] Pringle, J.E., 1993, in *Astrophysical Jets*, ed. D. Burgerella, M. Livio & C.P. O’Dea (Cambridge Univ. Press), 1
- [135] Quataert, E., 2001, in *ASP Conf. Ser. 224, Probing the Physics of Active Galactic Nuclei by Multiwavelength Monitoring*, ed. B.M. Peterson, R.S., Polidan & R.W. Pogge (San Francisco: ASP), 71
- [136] Quataert, E. & Gruzinov, A., 2000, *ApJ*, 545, 842
- [137] Quataert, E., 2003, *Astronomische Nachrichten Supplement*, 324, 435
- [138] Quillen, A.C., Graham, James R., and Frogel, Jay A., 1993, *ApJ*, 412, 550
- [139] Richstone, D., Gebhardt, K., and Pinkney, J., 1999, *AAS*, 195, 9906
- [140] Richter, O.-G., Sancisi, R., 1994, *A&A* 290, L9
- [141] de Robertis, M.M., Hayhoe, K., Yee, H.K.C., 1998, *ApJS*, 115, 163
- [142] Roberts, W.W., Huntley, J.M., and van Albada, G.D., 1979, *ApJ*, 233, 67
- [143] Roberts, T.P. & Warwick, R.S., 2000, *MNRAS*, 315, 98
- [144] Sakamoto, K., Okumura, S. K., Ishizuki, S., & Scoville, N.Z., 1999a, *ApJ* 525, 691
- [145] Sakamoto, K., Scoville, N.Z., Yun, M.S., Corsas, M., Genzel, R. & Tacconi, L., 1999b, *ApJ* 514, 68
- [146] Sakamoto, K., Scoville, N.Z., Yun, M.S., Corsas, M., Genzel, R., and Tacconi, L., 1999c, *ApJ*, 525, 691
- [147] Sanders, D. B. & Mirabel, I. F., 1996, *ARA&A* 34, 749

- [148] Scharwächter, J., Eckart, A., Pfalzner, S., Zuther, J., Krips, M. & Straubmeier, Ch., 2004, A&A 414, 497
- [149] Schinnerer, E., Eckart, A. & Tacconi, L.J., 2000a, ApJ 533, 826
- [150] Schinnerer, E., Eckart, A., Tacconi, L.J., Genzel, R. & Downes, D., 2000b, ApJ 533, 850
- [151] Schmidt, M., 1961, Nature, 197, 1040
- [152] Schneider, P., Ehlers, J., Falco, E.E., 1992, *Gravitational lenses*, New York, Springer
- [153] Schwarz, U.J., 1985, A&A 142, 273
- [154] Scoville, N.Z., Padin, S., Sanders, D.B., Soifer, B.T. & Yun, M.S., 1993, ApJ 415, L75
- [155] Scoville, N. Z., Evans, A. S., Dinshaw, N., Thompson, R., Rieke, M., Schneider, G., Low, F. J., Hines, D., Stobie, B., Becklin, E., Epps, H., 1998, ApJ 492, L107
- [156] Sempere, M.J., Combes, F., and Casoli, F., 1995, A&A, 299, 371
- [157] Shakura, N.I., Sunyaev, R.A., 1973, A&A 24, 337
- [158] Shields, G.A., Gebhardt, K., Salviander, S., Wills, B.J., Xie, B., Brotherton, M.S., Yuan, J., and Dietrich, M., 2003, ApJ, 583, 124
- [159] Shlosman, I., Frank,, J. & Begelman, M.C. 1989 Natur 338 45
- [160] Shlosman, I. & Noguchi, M., 1993, ApJ, 414, 474
- [161] Slee, O.B., Sadler, E.M., Reynolds, J.E. & Ekers, R.D., 1994, MNRAS, 269, 928
- [162] Soifer, B.T., Sander, D.B., Madore, B.F., Neugebauer, G., Danielson, G.E., Elias, J.H., Lonsdale, C.J. & Rice, W.L., 1987, ApJ 320, 238
- [163] Solomon, P. M. & Barrett, J. W., 1991, IAUS 146, 235
- [164] Solomon, P.M., Downes, D., Radford, S.J.E. & Barret, J.W., 1997, ApJ 478, 144
- [165] Stockton, A. & Ridgeway, S.E., 1991 AJ 102, 488
- [166] Surace, J.A., Sanders, D.B., and Evans, A.S., 2001, AJ, 122, 2791
- [167] Tacconi, L.J., Genzel, R., Blietz, M., Cameron, M., Harris, A.I., Madden, S., 1994, ApJ, 426, 77
- [168] Tacconi, L.J., Blietz, M., Cameron, M., Downes, D., Genzel, R., Krabbe, A., Sternberg, A., Tacconi-Garman, L.E., and Weitzel, L., 1996, *Vitas in Astronomy*, vol.40, Issue 1, p.23
- [169] Tacconi, L.J., Schinnerer, E., Gallimore, J.F., Genzel, R., Tacconi-Garman, L.E., and Downes, D., 1997, AAS, 191, 7803
- [170] Thornley, M., Regan, M., Helfer, T., Sheth, K., Vogel, S., Harris, A., Wong, T., Blitz, L., and Bock, D., 1999, Ap&SS, 269, 391
- [171] Thompson, A.R., Moran, J.M., and Swenson, G.W.jr., 1986, Krieger publishing company, *Interferometry and Synthesis in Radio Astronomy*
- [172] Toomre, A. & Toomre, J., 1972, ApJ 178, 623
- [173] Ulvestad, J.S. & Wilson, A.S., 1984, ApJ 278, 544

- [174] Ulvestad, J.S. & Ho, Luis C., 2001, *ApJ* 562, L133
- [175] Urry, C.M. & Padovani, P., 1995, *ASP*, 107, 803
- [176] Usero, A., García-Burillo, S., Fuente, A., Martín-Pintado, J., and Rodríguez-Fernández, N.J., 2004, *A&A*, 419, 897
- [177] Vila-Vilarò, B., Taniguchi, Y., and Nakai, N., 1998, *AJ*, 1553
- [178] Wandel, A., 1999, *ApJ*, 519, 39
- [179] Walsh, D., Carswell, R.F., Weynman, R.J., 1979, *Nature*, 279, 381
- [180] Whitmore, B. C., Zhang, Q., Leitherer, C., Fall, S. M., Schweizer, F., Miller, B. W., 1999, *AJ* 118, 1551
- [181] Wild, W., Eckart, A., 2000, *A&A* 359, 483
- [182] Wilkes, B. J., Schmidt, G.D., Smith, P.S., Mathur, S., McLeod, K.K., 1995, *ApJ*, 455, 13
- [183] Wilkinson, P.N., Tzioumis, A.K., Benson, J.M., Walker, R.C., Simon R.S. & Kahn, F.D., 1991, *Nature* 352, 313
- [184] Wink, J.E., Guilloreau, S. & Wilson, T.L., 1997, *A&A* 322, 427
- [185] Wrobel, J.M. & Heeschen, D., 1991, *AJ*, 101, 148
- [186] Yi, I. & Boughn, S.P., 1998, *ApJ*, 499, 198
- [187] Young, J.S., Xie, S., Tacconic, Knezek, et al., 1995, *ApJS*, 98, 219
- [188] Yuan, F., Markoff, S., and Falcke, H., 2002, *A&A*, 383, 854
- [189] Yun, M., Reddy, N.A., Scoville, N.Z., Frayer, D.T., Robson, E.I., and Tilanus R.P.J., 2004, *ApJ*, 601, 734
- [190] Zhu, M., Seaquist, E.R. & Kuno, N., 2004, *ApJ* 588, 243
- [191] Zhang, H., Xue, S., Burstein, D., Zhou, X., Jiang, Z., Wu, H., Ma, J., Chen, J., and Zou, Z., 2004, *AJ*, 127, 2579
- [192] Zuther, J., Eckart, A., Scharwächter, J., Krips, M., and Straubmeier, Ch., 2004, *A&A* 414, 919

List of Figures

1.1	Optical image of NGC 3718 and Q0957 superimposed with the integrated CO emission	16
1.2	Continuum map of NGC 1068 at 3 mm	17
1.3	IRAM PdBI picture	18
2.1	Representative SEDs of QSOs (radio to IR)	22
2.2	Mean QSO spectrum in the optical	23
2.3	Radio emission in Cygnus A	24
2.4	Optical spectrum of a Seyfert type 1 and type 2 galaxy	25
2.5	Schematic Model of Seyfert nuclei	27
2.6	Correlation between bulge and central black hole	29
3.1	IRAM PdBI CO maps of NUGA core survey	34
3.2	IRAM PdBI CO maps of NUGA core survey	35
3.3	IRAM PdBI CO maps of NUGA core survey	36
3.4	Optical images of some selected QSOs taken from the Cologne nearby QSO sample.	39
4.1	Pictures of the IRAM 30m telescope at the Pico Veleta in the Sierra Nevada, Spain.	44
4.2	Schematic picture of a two-element interferometer (taken from the IRAM Interferometry School).	45
4.3	Pictures of the IRAM Plateau de Bure Interferometer in the french Alps.	46
4.4	Transparency of the earth's atmosphere at different wavelengths	46
4.5	MERLIN telescopes	47
4.6	VLBI telescopes	48
5.1	Optical image of NGC 3718 superimposed with the integrated CO(1–0) emission	52
5.2	Positions of the IRAM 30 m observations are plotted with black crosses, and mosaic fields of the PdBI observations are shown as circles indicating the 42'' primary beam size for each observing field. The 30 m beamsize is shown in the upper left.	53
5.3	3 mm and 1 mm continuum maps of NGC 3718	55
5.4	SED of NGC 3718	56
5.5	Integrated CO(1–0) and CO(2–1) maps of NGC3718 (PdBI only)	57
5.6	Iso-velocity maps and position velocity diagrams of NGC 3718 (PdBI only)	58
5.7	Integrated CO(1–0) and CO(2–1) maps of NGC 3718 (PdBI+30m)	59
5.8	Position-velocity diagrams of NGC 3718 (PdBI vs. PdBI+30m)	60
5.9	Velocity integrated mosaic maps of CO(1–0) in NGC 3718 (PdBI only and PdbI+30m)	61
5.10	Tilt rings	62
5.11	Tilt angles of the warp model for NGC 3718	63
5.12	Velocity integrated intensity map of the model for NGC 3718	64
5.13	Model vs data in NGC3718 (PdBI only, PdBI+30m, 30m only)	65
5.14	Model versus data in NGC 3718 for three different velocity ranges (PdBI+30m)	66

5.15	Model versus data in NGC3718 (velocity integrated intensity maps, PdBI+30m)	67
5.16	First order moment maps plus position-velocity diagrams of mosaic data from NGC 3178 (PdBI+30m)	68
6.1	[OIII]map of NGC 1068	72
6.2	Model of the central engine in NGC 1068	73
6.3	Map of the maser disc in NGC 1068	74
6.4	Velocity integrated $^{12}\text{CO}(1-0)$ and $^{12}\text{CO}(2-1)$ line emission map of NGC 1068 (Schinnerer et al. 2000).	74
6.5	Continuum maps of NGC 1068 at 1 mm, 3 mm and 6cm	75
6.6	Overlay of the velocity integrated $^{12}\text{CO}(2-1)$ line emission with the 1.2 mm continuum of NGC 1068	76
6.7	Spectral index of the core emission in NGC 1068	78
6.8	Velocity integrated $^{13}\text{CO}(1-0)$ and $^{12}\text{CO}(2-1)$ line emission of NGC 1068	79
6.9	Velocity integrated $^{12}\text{CO}(2-1)$ line emission of NGC 1068 for the new and old data	79
6.10	Velocity integrated $^{12}\text{CO}(1-0)$ and $^{13}\text{CO}(1-0)$ line emission of NGC 1068	80
6.11	Spatially integrated $^{12}\text{CO}(1-1)$ and $^{13}\text{CO}(1-1)$ spectrum of NGC 1068.	81
6.12	Spatially integrated $^{12}\text{CO}(2-1)$ spectrum of NGC 1068.	82
6.13	Iso-velocity diagrams of the nuclear $^{12}\text{CO}(2-1)$ line emission in NGC 1068 (new and old data)	84
6.14	Position velocity diagrams of the nuclear $^{12}\text{CO}(2-1)$ line emission in NGC 1068 (new data)	85
6.15	Position velocity diagrams of the nuclear $^{12}\text{CO}(2-1)$ line emission in NGC 1068 (old data)	86
7.1	CO(1-0) and CO(2-1) spectrum of HE 1029-1831	91
7.2	Spatially integrated CO(1-0) and CO(2-1) spectrum of HE 1029-1831	92
7.3	Velocity integrated CO(1-0) and CO(2-1) emission in HE 1029-1831	93
7.4	Iso-velocity map of the CO(1-0) and CO(2-1) emission in HE 1029-1831	93
7.5	H-band image of HE1029-1831 superimposed with contours of the CO(2-1) line emission and compared with a model for NGC 5383.	95
7.6	Position velocity diagram of the CO(1-0) and CO(2-1) emission in HE 1029-1831	96
8.1	Continuum maps at 3.5 mm and 1.2 mm of 3C48	100
8.2	NIR-image of 3C48 overlaid with contours from the 3.5 mm and 1.2 mm	102
8.3	SED plot of 3C48	102
8.4	Continuum emission at 1.2 mm and 3mm vs. three Gaussian component model of 3C48	103
8.5	Channel maps of the CO(1-0) emission in 3C48	105
8.6	Spectrum at the position of the CO(1-0) centroid in 3C48	106
8.7	Integrated CO(1-0) emission of 3C48	107
8.8	Position velocity diagram of the CO(1-0) emission in 3C48	108
8.9	IR image overlaid with the integrated CO intensities of the different components in 3C48	109
8.10	IR map overlaid with integrated CO(1-0) emission (from -95 to $+35 \text{ km s}^{-1}$) and position-velocity map of 3C48	110
8.11	Channel maps of the CO(1-0) emission in 3C48 (new data)	111
8.12	Channel maps of the CO(1-0) emission in 3C48 (old data)	112
9.1	Optical and radio image of Q0957+561	118
9.2	3.1 mm, continuum and integrated CO(2-1) emission and CO(2-1) spectra of Q0957+561	120
9.3	Integrated emission of the blueshifted and redshifted CO(2-1) line in Q0957+561	121
9.4	χ^2 -test of Q0957+561	124
9.5	χ^2 -test of Q0957+561	125
9.6	χ^2 -test of Q0957+561	126
9.7	χ^2 -test of Q0957+561	127
9.8	χ^2 -test of Q0957+561	128

9.9	Best-fit model for an extended blueshifted line emission region centered on the nucleus for Q0957+561	129
9.10	Best-fit model for a rather compact blueshifted line emission region centered at an off-nuclear position for Q0957+561	129
9.11	Unlensed positions of the respective components from the line emission and radio continuum in Q0957+561	130
9.12	χ^2 -test for the red+blueshifted emission region in Q0957+561	131
9.13	Best-fit model for an extended emission region for the red- and blueshifted line centered on the position of the quasar in Q0957+561	131
9.14	The line-free continuum at 95 GHz and the $^{12}\text{CO}(2\rightarrow 1)$ line emission (<i>upper right panel</i>) in Q0957+561	132
9.15	HST image in the H-band of the host galaxy in Q0957+561 overlaid with contour levels of the integrated CO(2–1) emission	133
10.1	CO(1–0) and HCN(1–0) images of NGC 1097, NGC 6951 and NGC 1068	138
10.2	Comparison of the measured HCN(1–0) and CO(1–0) luminosities	143
10.3	Comparison of the measured HCN(1–0) and CO(1–0) luminosities with the FIR luminosities of the NUGA core sample	144
11.1	MERLIN and EVN/VLBI maps at 6cm and 18cm of 3 NUGA sources	154
11.2	MERLIN and EVN/VLBI maps at 6cm and 18cm of further 3 NUGA sources	155
11.3	MERLIN and EVN/VLBI maps at 6cm and 18cm of the remaining 7th NUGA source	156
11.4	SED for 7 NUGA core sources	157
11.5	SED of the 7 NUGA sources and NGC 1068	159
11.6	Comparison of radio with X-ray luminosities and of the black hole mass derived via X-ray and radio fluxes with the one determined via the stellar velocity dispersion for 7 NUGA core sources	160
12.1	ALMA and LOFAR	169
A.1	The coordinate system describing the basic parameters for the tilted-ring model	173
B.1	Orbit of a relativistic charged particle in a magnetic field.	176
B.2	Model of a flat core spectrum	177
C.1	Velocity channel maps of the CO(1–0) line emission in HE 1029-1831	180
C.2	Velocity channel maps of the CO(2–1) line emission in HE 1029-1831	181
D.1	Central HCN(1-0) spectra of the 7 NUGA sources	184
D.2	“Global” $^{12}\text{CO}(1-0)$ spectra of 7 NUGA sources	185

List of Tables

3.1	Basic properties of NUGA core survey	33
3.2	Molecular gas masses of NUGA core survey	37
3.3	Molecular gas morphology of the observed NUGA core sources	37
5.1	Fluxes and positions of the continuum emission in NGC 3718	54
5.2	CO(1–0) properties of NGC 3718	62
6.1	3 mm and 1 mm continuum parameters of NGC 1068	76
6.2	CO line parameters and gas as well as dynamical masses for NGC 1068	83
7.1	Line parameters for CO(1–0) and CO(2–1) in HE 1029-1831.	90
7.2	Fit parameters and gas mass of HE 1029-1831 derived from the CO(1–0) and CO(2–1) line spectrum. The latter shows the over the bar integrated line emission (Fig.7.2).	94
8.1	101
8.2	CO(1–0) data of 3C48	106
9.1	Basic properties of Q0957+561	119
9.2	Observational parameters of Q0957+561	120
9.3	Model parameter of Q0957+561	123
9.4	Apparent CO luminosity and molecular gas mass of Q0957+561	134
10.1	Basic observing parameters for HCN in the NUGA core survey	139
10.2	Central CO and HCN line temperatures of the NUGA core sources	141
10.3	FIR luminosities and luminosity ratios for the NUGA core sample	141
10.4	Integrated CO(1–0) intensities in the centre and averaged over the whole map in the NUGA core survey	142
10.5	Gas masses determined with the central CO(1–0) and HCN(1–0) luminosity in the NUGA core survey	143
11.1	Parameters of radio observations of 7 NUGA core galaxies	149
11.2	Radio positions of 7 NUGA sources	150
11.3	Results of the radio observations for 7 NUGA core sources	152
11.4	Spectral indices of 7 NUGA core sources	153
11.5	Black hole masses, bolometric and Eddington luminosities for 7 NUGA core galaxies	158
11.6	Some representative fluxes from radio, Far-Infra-Red (FIR) and optical frequencies to X-rays of the seven NUGA sources are given. ^a see caption of Table 11.5 for the references. ^b taken from NED. ^c taken from our IRAM PdBI observations. ^d taken from the EVN observations.	158
12.1	Summary of all observed objects	168

Table of Abbreviations

Jy	Jansky (1 Jy= 10^{-26} W m ⁻¹ Hz ⁻¹)
L_{\odot}	Solar luminosity ($=3.85 \cdot 10^{26}$ Watt= $3.85 \cdot 10^{33}$ erg s ⁻¹)
\mathcal{M}_{\odot}	Solar mass ($=1.99 \cdot 10^{30}$ kg)
pc	parsec (1 pc= $3.0856 \cdot 10^{16}$ m)
ADAF	Advection Dominated Accretion Flow
ADIOS	Advection Dominated Inflow-Outflow Solution
AGN	Active Galactic Nuclei
ALMA	Atacama Large Millimeter Array
BIMA	Berkeley-Illinois-Millimeter-Array
BLR	Broad Line Region
CDAF	Convection Dominated Accretion Flows
DSS	Digital Sky Survey
EVN	European VLBI Network
FCRAO	Five College Radio Astronomy Observatory
FIRST	
HLAGN	High Luminosity Active Galactic Nuclei
HST	Hubble Space Telescope
IRAM	Institute for Radio-Astronomy at Millimeter wavelengths
LLAGN	Low Luminosity Active Galactic Nuclei
LSB	Lower Side Band
LOFAR	LOW Frequency ARray
MERLIN	Multi-Element Radio Linked Interferometer Network
MPE	Max Planck institute for Extraterrestrial physics
NED	NASA/IPAC Extragalactic Database (http://nedwww.ipac.caltech.edu)
NLR	Narrow Line Region
NRO	Nobeyama Radio Observatory
OVRO	Owens Valley Radio Observatory
PdBI	Plateau de Bure Interferometer
QSO	Quasi-Stellar Object
Quasar	Quasistellar objects
RIAF	Radiatively Inefficient Accretion Flow
SgrA*	Sagittarius A*, compact radio source associated with the central black hole in our Milky Way
SKA	Square Kilometer Array
SMA	Sub-Millimeter-Array at Hawaii
USB	Upper Side Band
VLA	Very Large Array
VLBA	Very Large Baseline Array
VLBI	Very Long Baseline Interferometry

Acknowledgements

The first two people, I would like to thank, are Prof. Dr. Andreas Eckart and Dr. Roberto Neri, for giving me, among others, the opportunity to work in such an interesting research field. Their incessant enthusiasm for and their wide knowledge in astronomy has always been and still is an inspiration for me. At each moment, they provided the possibility for motivating and inspiring discussions about the projects of my PhD thesis.

I'm very grateful to Prof. Dr. Michael Grewing and IRAM, Grenoble, for giving me the opportunity to prepare an important part of my PhD thesis at their institute and to participate actively at observations with the IRAM Interferometer on the Plateau de Bure. The year, I spent in Grenoble, and above all the experiences as Astronomer on Duty helped to increase significantly my understanding and knowledge of mm-Interferometry providing a solid basis for future research.

A ce point, je voudrais exprimer mes sincères remerciements à l'équipe du Plateau de Bure grâce à qui chaque jours à Bure fut une belle experience. Les repas et les jeux de cartes et de boules étaient très amusants et aussi très jolis. Je voudrais aussi les remercier pour m'avoir aidée à améliorer mon "français pratique". Mon séjour au Plateau de Bure m'a donné la possibilité de rencontrer des personnes très intéressantes et aussi très différentes.

Furthermore, I owe a special thank to Dr. Dennis Downes for his useful comments concerning Q0957+561 and NGC 1068 improving the discussion and interpretation of the mm-data. I also want to thank Dr. Thomas Krichbaum and Dr. Walter Alef who patiently taught me how to reduce VLBI data. In this context, Dr. Tom Muxlow and Dr. Anita Richards have to be mentioned as well who helped me with useful comments and advices to reduce the MERLIN data. I thank Dr. Françoise Combes and Dr. Santiago García-Burillo for their remarks and comments about NGC 3718.

I would like to thank the staff of the IRAM 30m telescope in Spain for their help during the observations.

I'm also thankful to Dr. Stéphane Guilloteau, and Dr. Linda Tacconi for providing additional mm-data for 3C48 and NGC 1068.

Je voudrais remercier également toutes les personnes à l'IRAM et à Grenoble pour l'embellissement de mon séjour en France. En particulier, je remercie Dr. Roberto et Angelika Neri, Dr. Alessandro Navarrini (mille grazie per la tua amicizia), Anne-Laure Fontana, Patrice Serres, Fabrice Coq (merci pour les belles soirées de crêpes et la journée de catamaran), Dr. Jan-Martin Winters, Dr. Michael Bremer, Dr. Raphael Moreno et tous les autres astronomes ou personnes que j'ai oubliés maintenant. J'ai beaucoup apprécié chaque soir qu'on a passé ensemble. Merci beaucoup.

Danken möchte ich auch ganz besonders den Leuten aus der "Eckart"-Gruppe und genauso jedem weiteren aus dem I.Physikalischen Institut, die zu einer angenehmen Atmosphäre während meiner Doktorarbeit beigetragen haben. Hervorheben möchte ich dabei im Speziellen Dr. Rainer Schödel, meinen Zimmerleidensgenossen, der mich vor allem in der letzten Zeit tapfer ertrug und genauso geduldig meine Doktorarbeit Korrektur las, und Jens Zuther, der mir vor allem bei meinen diversen PC-Problemen ebenfalls geduldig und hilfreich zur Seite stand.

Zu guter Letzt gehört ein ganz besonderer und tiefer Dank natürlich meinen Eltern, die mir auf eine selbstverständliche Art und sicher unter manchen Opfern eine solche Ausbildung überhaupt erst ermöglichten. Meinem Bruder, seiner Frau Christina, meinem Patenkind Jenny und meinen Freunden möchte ich ebenfalls danken, für ihre Freundschaft und einfach, dass sie da sind.

Ich versichere, dass ich die von mir vorgelegte Dissertation selbständig angefertigt, die benutzten Quellen und Hilfsmittel vollständig angegeben und die Stellen der Arbeit - einschließlich Tabellen, Karten und Abbildungen -, die anderen Werken im Wortlaut oder dem Sinn nach entnommen sind, in jedem Einzelfall als Entlehnung kenntlich gemacht habe; dass diese Dissertation noch keiner anderen Fakultät oder Universität zur Prüfung vorgelegen hat; dass sie - abgesehen von unten angegebenen Teilpublikationen - noch nicht veröffentlicht worden ist sowie, dass ich eine solche Veröffentlichung vor Abschluss des Promotionsverfahrens nicht vornehmen werde. Die Bestimmungen dieser Promotionsordnung sind mir bekannt.

Die von mir vorgelegte Dissertation ist von Prof.Dr. Andreas Eckart betreut worden.

(Melanie Krips)

Teilpublikationen:

Krips, M., Pott, J.-U., Eckart, A., Leon, S., Neri, R., Straubmeier, C., 2003, *Ap&SS* 284, 511

Krips, M., Neri, R., Eckart, A., Downes, D., Martín-Pintado, J., and Planesas, P., 2004a, accepted for publication in *A&A*, astro-ph/0411138

Krips, M., Neri, R., Eckart, A., Martín-Pintado, J., Planesas, P. and Colina L. 2004, "The quasar Q0957+561: Lensed CO emission from a disk at $z \sim 1.4$?", appeared in "Proceedings of the 4th Cologne-Bonn-Zermatt-Symposium", ed. S. Pfalzner, C. Kramer, C. Straubmeier, and A. Heithausen (Springer Verlag Berlin Heidelberg), p.23-26

Krips, M., Eckart, A., Neri, R., Pott, J.-U., Zuther, J., Scharwächter, J. and Bertram, Th., "Feeding monsters - a study of active galaxies", in "Dense Molecular Gas around Protostars and in Galactic Nuclei", Eds. Y.Hagiwara, W.A.Baan, H.J.van Langevelde, 2004, a special issue of *ApSS*, Kluwer, in press

Krips, M., Eckart, A., Neri, R., Pott, J.-U., Combes, F. and García-Burillo, S., 2004, "Active galaxies - parsec scale radio emission and the surrounding ISM", in "The Interplay among Black Holes, Stars and ISM in Galactic Nuclei", Proceedings of IAU Symposium, No. 222, eds. Th. Storchi-Bergmann, L.C. Ho & H.R. Schmitt, in press

Krips, M., Eckart, A., Neri, R., Pott, J.U., Leon, S., Combes, F., García-Burillo, S., Hunt, L.K., Baker, A.J., Tacconi, L.J., Englmaier, P., Schinnerer E., and Boone F., 2005, "Molecular Gas in Nuclei of GALaxies (NUGA) III. The warped LINER NGC 3718", submitted to *A&A*

(Krips, M., Eckart, A., Neri, R., Zuther, J., Downes, D., and Scharwächter, J., 2005, "Gas and continuum emission in 3C48: Evidences for two merger nuclei?", ready for submission to *A&A*)

Curriculum Vitae

Name	Melanie Birgit Krips
Date of Birth	July 9th, 1977, Cologne (Germany)
Citizenship	German
Current address	Laudahnstrasse 6 50937 Köln Germany
Marital Status	Single

School Education

1983-1987	Elementary school, Pulheim, Germany
1987-1996	Grammar school "Geschwister Scholl", Pulheim, Germany
May 1996	Baccalaureate

University

1996-2001	Physics at the University of Cologne, Germany
September 1998	Pre-diploma ("Vordiplom") in physics
2000-2001	Diploma thesis in physics about: "The Gravitationally Lensed Quasar Q0957+561 at Millimeter Wavelengths"
December 2001	Diploma in physics
since January 2002	PhD in physics about: "High Resolution Multi-Wavelength Study of Active Galaxies"

Foreign stays

March-April 2000	Internship at IRAM, Grenoble, France
October-December 2000 & April-July 2001	IRAM, Grenoble (France), to work on diploma thesis
September 2002 - August 2003	IRAM, Grenoble (France), to work on PhD thesis (with DAAD fellowship)

German	Native
English	Fluent
French	Fluent
Latin	Latinum, good knowledge
Italian	Good knowledge
Spanish	Basic knowledge